INVESTIGATION OF THE SPIN STRUCTURE OF THE NUCLEON AT THE COMPASS EXPERIMENT

Dissertation
zur Erlangung des Grades
"Doktor
der Naturwissenschaften"

am Fachbereich 08 - Physik, Mathematik, Informatik
der JOHANNES GUTENBERG-UNIVERSITÄT
in Mainz

MALTE CHRISTIAN WILFERT
geboren in Darmstadt

Mainz, den 20. März 2017

ABSTRACT

The spin structure of the nucleon is studied at the COMPASS experiment. Their subject is of special interest since the surprising findings of the European muon collaboration (EMC) that the contribution from the quark spins to the nucleon spin is rather small. This finding started the search for the various contributions to the nucleon spin. Their contributions are given by the spins of the quarks and gluons and their orbital angular momenta, where the contribution from the quark spins is about 30%. At the COMPASS experiment, a polarised muon beam is scattered off a polarised fixed target made out of either lithium deuteride or ammonia. In such reactions, the longitudinal double spin asymmetry and the spin-dependent structure function are measured.

The longitudinal double spin asymmetry is obtained in two different kinematic regions. At low photon virtualities, $Q^2 < 1\,(\text{GeV}/c)^2$, precise results are obtained from the data taken in 2007 and 2011 using ammonia as a polarised proton target. The results show a small asymmetry of about 1%, which differs from zero, even at very small Bjorken-x. This is the first observation of spin effects at such low Bjorken-x. At high photon virtualities, $Q^2 > 1\,(\text{GeV}/c)^2$, the results for the asymmetry obtained from the 2006 and 2011 data taking are presented. The results from the 2006 data taking improve the statistical precision of the spin-dependent structure function of the deuteron. For the 2011 data taking, the nominal beam momentum was increased from $160\,\text{GeV}/c$ to $200\,\text{GeV}/c$. This extends the kinematic range towards lower Bjorken-x and higher photon virtualities. These results complete the previous results for the spin-dependent structure function of the proton using the data taken in 2007.

The results on the spin-dependent structure function are used together with the world data on the spin-dependent structure function of the proton, deuteron and neutron measured in deep inelastic scattering in a QCD fit to obtain the parton helicity distributions. They can be interpreted similar as the parton distribution function, which describe the momentum fraction carried by quarks within a certain Bjorken-x range dx. The parton helicity distributions describe the contribution from the quark spins to the total nucleon spin within dx. From the QCD fit, the contribution from the quark spins to the total spin of the nucleon is obtained as well as the the contributions from the various quark flavours.

The measured results on the spin-dependent structure functions are also used to evaluate their first moments, $\int_0^1 g_1(x, Q^2)\text{d}x$. They are used to test QCD sum rules like the Bjorken and the Ellis-Jaffe sum rule. A violation of the Ellis-Jaffe sum rule is already known since the surprising results from EMC and was confirmed by various experiments. The Bjorken sum rule is of special interest since it connects the non-singlet structure function, $g_1^{\text{NS}} = g_1^{\text{P}} - g_1^{\text{n}}$, with the ratio g_A/g_V. Further on the evolution of the non-singlet structure function is independent of the poorly known gluon helicity distribution. Here, the Bjorken sum rule is confirmed at the level of 9%. The first moment of the spin-dependent structure function of the deuteron allows for the determination of the singlet axial charge $a_0 = 0.32 \pm 0.02_{\text{stat}} \pm 0.04_{\text{syst}} \pm 0.05_{\text{evol}}$, which is identified with the contribution from the quark spins to the total nucleon spin in the $\overline{\text{MS}}$ scheme.

ZUSAMMENFASSUNG

Am COMPASS-Experiment wird die Spinstruktur des Nukleons untersucht. Diese ist von besonderen Interesse seit der überraschenden Entdeckung durch die europäische Myonkollaboration (EMC), dass nur ein kleiner Teil des Nukleonspins von den Spins der Quarks stammt. Mit dieser Entdeckung begann die Suche nach den verschiedenen Bestandteilen. Diese sind durch die Spins der Quarks und Gluonen sowie deren Bahndrehimpulsen gegeben, wobei der Beitrag der Quarks etwa 30% beträgt. Am COMPASS-Experiment wird für diese Untersuchung ein polarisierter Myonstrahl und ein polarisiertes Lithiumdeuterid- oder Ammoniaktarget genutzt. Aus diesen Messungen wurden die longitudinalen Doppelspinasymmetrien zusammen mit den spinabhängigen Strukturfunktionen bestimmt.

Die longitudinale Doppelspinasymmetrie wurde in zwei verschiedenen kinematischen Bereichen gemessen. Bei niedrigen Photonvirtualitäten, $Q^2 < 1 \, (\text{GeV}/c)^2$, wurde die Asymmetrie aus den Daten von 2007 und 2011 bestimmt, wobei Ammoniak als Target mit polarisierten Protonen verwendet wurde. Die Ergebnisse zeigen eine kleine, von null verschiedene Asymmetrie von 1% auch bei sehr kleinen Bjorken-x. Bei hohen Photonvirtualitäten, $Q^2 > 1 \, (\text{GeV}/c)^2$, wurde die spinabhängige Strukturfunktion des Deuterons aus den Daten von 2006 bestimmt. Diese Ergebnisse verbessern die statistische Genauigkeit der bisherigen COMPASS Messung. Für die Messung in Jahr 2011 wurde die Strahlenergie von 160 GeV auf 200 GeV erhöht. Dadurch konnte die spinabhängige Strukturfunktion des Protons bei noch kleineren Bjorken-x und größeren Photonvirtualitäten gemessen werden. Diese Messung vervollständigen die vorherige Messung bei 160 GeV.

Die Ergebnisse der spinabhängigen Strukturfunktionen wurden zusammen mit den Weltdaten zur spinabhängigen Strukturfunktion des Proton, des Deuteron und des Neutron in einem QCD fit verwendet, um die Partonhelizitätsverteilungen zu bestimmen. Diese können ähnlich wie die Partonverteilungen interpretiert werden, die den Impulsbruchteil, der von Quarks innerhalb eines bestimmten Bjorken-x Bereichs dx getragen wird, angeben. Die Partonhelizitätsverteilungen hingegen geben den Beitrag zum Nukleonspin in so einem Intervall dx an. Zudem wurde der gesamte Beitrag der Quarkspins sowie der der einzelnen Quark-Flavour zum Nukleonspin aus diesem Fit bestimmt.

Aus den Ergebnissen der spinabhängigen Strukturfunktionen wurden auch die ersten Momente, $\int_0^1 g_1(x, Q^2) dx$, der Strukturfunktionen bestimmt. Diese wurden zum Prüfen von QCD Summenregeln, wie der Bjorken- oder Ellis-Jaffe-Summenregel, verwendet. Eine Verletzung der Ellis-Jaffe-Summenregel ist bereits seit Ergebnissen von EMC bekannt und wurde seitdem durch weitere Messungen bestätigt. Die Bjorken-Summenregel verbindet die non-singlet Strukturfunktion, $g_1^{NS} = g_1^p - g_1^n$, mit dem Verhältnis g_A/g_V. Zusätzlich ist die Abhängigkeit von der Photonvirtualität dieser Strukturfunktion von der wenig bekannten Gluonhelizitätsverteilung unabhängig. Die Bjorken-Summenregel wurde mit einem Fehler von 9% bestätigt. Das erste Moment der spinabhängigen Strukturfunktion des Deuterons wurde auch verwendet, um die axiale singlet Ladung $a_0 = 0.32 \pm 0.02_{\text{stat}} \pm 0.04_{\text{syst}} \pm 0.05_{\text{evol}}$ zu bestimmen. Diese gibt im $\overline{\text{MS}}$ Schema den Beitrag der Quarkspins zum Nukleonspin an.

CONTENTS

THEORY AND INTRODUCTION

INTRODUCTION

The scattering of α particles off a thin gold foil lead to the interpretation of the atom as a large "electron cloud" and a dense and point-like nucleus by Rutherford [1] in 1911. This raised the interest in studying the structure of these nuclei. After the discovery of the neutron by Chadwick [2] in 1932, it was obvious that the nuclei consists of two types of nucleons, namely protons and neutrons. They were considered to be elementary particles first, which means that they do not have any substructure. More of these elementary particles were found in experiments involving cosmic radiation and early accelerator experiments. They soon exceeded a few hundreds. They were called hadrons. In order to organise this particle zoo, Gellmann [3] and Zweig [4] proposed a substructure of the hadrons composed of charged, point-like particles with spin-1/2. These are called quarks today. Three types of quarks were needed to explain all discovered particles. The three quarks are called up, down and strange quark. The hadrons consist either of three quarks (baryons) or of an quark antiquark pair (mesons). This model was widely accepted after the confirmation of the existence of the predicted fourth quark, called charm quark, in 1974 [5, 6]. Today six quark flavours are known including the bottom and top quark.

In order to explain the results found at SLAC [7] in 1969 in scattering of high energetic electrons off nucleons, Feynmann developed the parton model [8]. This model also assumes a substructure of nucleons. In this model, the scattering process is described as the interaction of a virtual photon with point-like partons with spin-1/2 inside the nucleon. These partons should have low masses. Soon, it became clear that partons and quarks are the same. This resulted in the development of the quark parton model, where the charged partons are identified with quarks. In the quark parton model, the nucleon consists of three valence quarks, which hold all quantum numbers of the nucleon. Similar to fluctuations of a photon into an electron-positron pair, also quarks and antiquarks are produced inside the nucleon. They are called sea quarks. Quantum chromodynamics (QCD) was developed in order to describe the interaction between quarks via a gauge boson called gluon. Its existence was confirmation by the TASSO experiment [9] in events with three hadron jets. Gluons are massless particles with spin-1 and interact with particles carrying a colour charge. They also carry a colour charge, which results in interactions among them.

In deep inelastic scattering of leptons off nucleons such as in the early SLAC experiments, the spin-independent structure functions F_1 and F_2 are measured. They allow to describe the intrinsic structure of the nucleon by so called parton distribution functions. They are interpreted as the number density for finding a quark with a certain momentum fraction inside a nucleon. Similar studies using a polarised lepton beam and a polarised target in order to study the spin structure of the nucleon started in 1978 at SLAC [10, 11]. They were continued later by the European Muon Collaboration at CERN. Their results on the violation of the Ellis-Jaffe sum rule is known as the beginning of the "spin crisis". As in the quark parton model the quantum numbers of the nucleon are given by the three valence quarks, the total nucleon spin is given by their spins. Two of the valence quarks

are expected to have their spin aligned parallel to the nucleon spin and one valence quark aligned antiparallel. This results in a total spin of 1/2. Taking into account relativistic effects, the quark spins contribute only about 60% to the total nucleon spin [12]. The measurement of EMC found a surprisingly small value of $(12 \pm 9 \pm 14)\%$ [13], which was even compatible with zero. This lead to further experiments studying the spin structure. All found a small contribution from the quark spins to the total spin of the nucleon in the order of 30%. A more realistic description of the nucleon spin includes in addition to the contribution from the quark spins, $\Delta\Sigma$, also contributions from the gluon spins, ΔG, and from their orbital angular momenta, L_q and L_g:

$$\frac{1}{2} = \frac{1}{2}\Delta\Sigma + \Delta G + L_q + L_g \ . \tag{1}$$

The COMPASS collaboration aims towards the measurement of the various contributions to the nucleon spin. The contribution from the spins of the quarks and gluons is measured in deep inelastic scattering of polarised muons off polarised nucleons. In order to perform a measurement with a good resolution, high beam energies are necessary. The polarised muon beam used at COMPASS is the polarised lepton beam with the highest energy in the world with energies between 100 GeV and 200 GeV.

In this thesis, the analysis of the data from the 2011 measurement using a polarised proton target are presented. Also, results from the 2006 measurement using a polarised deuteron target are presented. These results form together with the previous results from the 2002-2004 (deuteron) and 2007 (proton) measurement the final COMPASS results on the spin-dependent structure functions.

This thesis is organised in the following way: in Chapter 2 the theoretical background is summarised. This includes a brief description of deep inelastic scattering together with the important physical variables. Also the spin-independent and spin-dependent structure functions describing the structure of the nucleon are introduced. In addition, the Ellis-Jaffe and Bjorken sum rule are described and the extraction of the baryon decay constants is presented.

The experimental setup of the COMPASS spectrometer is presented in Chapter 3 for the measurement of deep inelastic scattering using a polarised muon beam scattering off a polarised fixed target. Here, the major detectors and the trigger system are described together with the polarised muon beam. In addition, the determination of the particle identification using the ring imaging Cherenkov detector is described.

In the following chapters, the results of this thesis are presented together with the methods and quantities needed for the extraction of the longitudinal double spin asymmetry. The calculation of the longitudinal double spin asymmetry is explained in Chapter 4 together with the necessary inputs for its calculation. Here, also the stability of the full spectrometer and reconstruction is tested in order to select only periods of stable data taking for the analysis.

The results for the longitudinal double spin asymmetry of the proton and the deuteron at high photon virtualities, $Q^2 > 1\,(\text{GeV}/c)^2$, are described in Chapter 5. In Chapter 6 the results for the longitudinal double spin asymmetry of the proton at low photon virtualities, $Q^2 < 1\,(\text{GeV}/c)^2$, are presented. In both cases, several studies are performed to study possible influences of false asymmetries on the results. In addition, the final results for the spin-dependent structure function are presented.

The results for the spin-dependent structure functions at high photon virtualities are used together with the world data on these structure functions in a next-to-leading order QCD fit. The QCD fit allows to extract the parton helicity distributions. The results of this QCD fit are presented in Chapter 7 together with the method used for this QCD fit. In addition, several studies on the functional forms and sources of systematic uncertainties are presented.

The results for the spin-dependent structure function of the proton and deuteron are also used to calculate the first moments of those structure functions. These allow to test the Bjorken sum rule and the Ellis-Jaffe sum rule. Using also the result for the first moment of the spin-dependent structure function of the deuteron, the contribution from the quark spins to the total nucleon spin is calculated. These results are presented in Chapter 8.

The thesis ends with a summary of all presented results and a conclusion in Chapter 9. The appendix contains tables with the values of the asymmetry and the structure functions presented before.

STRUCTURE OF THE NUCLEON

In this chapter, an overview of the theoretical description of the nucleon structure is given. First, the process of deep inelastic scattering is described. The results obtained in spin-independent and spin-dependent deep inelastic scattering are interpreted within the quark parton model. This model is extended using quantum chromodynamics to include gluons. Afterwards, the cross section asymmetry A_1 is described using forward scattering amplitudes.

Predictions for the first moment of the spin-dependent structure functions result in two sum rules, which are described in this chapter. These are the Bjorken sum rule and the Elis-Jaffe sum rule. Additionally, a short description of the spin-dependent structure function at low Bjorken-x is given.

2.1 DEEP INELASTIC SCATTERING

The structure of the nucleon is studied in inelastic scattering of leptons by nucleons. In first order quantum electro dynamic (QED), this process is described by the exchange of a virtual photon between the lepton and the nucleon. Also the exchange of a Z-boson is possible. But this exchange is suppressed due to the mass of the Z-boson. The process $\ell + N \rightarrow \ell' + X$ is shown in Figure 1. The process is characterised by the four-momenta of the particles. These are k and k' for the incoming and the scattered lepton and P and q for the nucleon and the virtual photon.

At the COMPASS experiment, muons are used, which are scattered off nucleons inside a fixed target. In fixed target experiments, the nucleons in the target have no momentum in the laboratory frame. Therefore, their energy is given by the mass of the nucleon.
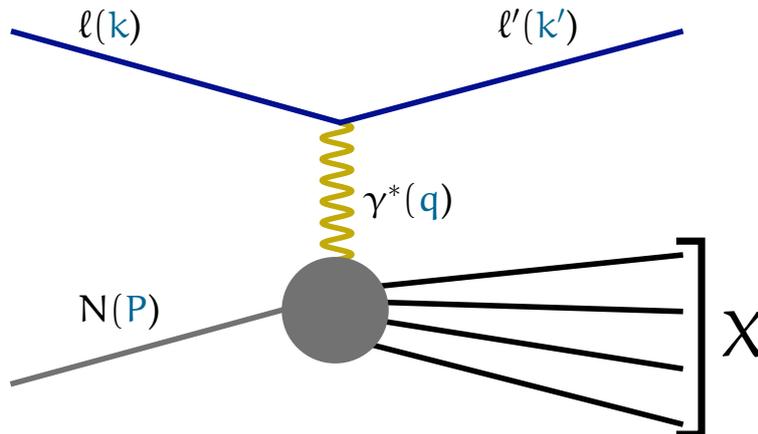
Figure 1: Feynman diagram of the deep inelastic scattering process $\ell N \rightarrow \ell' X$ in the one photon exchange. The four-momenta of each particle are shown.

2.2   KINEMATICS OF DEEP INELASTIC SCATTERING

In an inclusive measurement of inelastic lepton nucleon scattering, only the scattered lepton is detected. Therefore, in addition to the four-momentum of the incoming lepton $k = (E, \mathbf{k})$ also the one of the scattered lepton $k' = (E', \mathbf{k}')$ is known. The energy of the incoming and scattered lepton are given by E and E'. The corresponding momentum vectors of the lepton are $\mathbf{k}$ and $\mathbf{k}'$. The four-momentum of the target nucleon is $P = (M, \mathbf{o})$. Here, M is the mass of the nucleon. The interaction is described via the exchange of one virtual photon with the four-momentum q as shown in Figure 1. The process is described by two independent kinematic variables. Two commonly used variables are the photon virtuality Q^2 and the Bjorken-x variable. The photon virtuality is given by the negative square of the four-momentum of the virtual photon

$$Q^2 = -q^2 = -\left(k - k'\right)^2 \overset{\text{lab.}}{=} -2m^2c^2 + 2\left(\frac{EE'}{c^2} - |\mathbf{k}||\mathbf{k}'|\cos\theta\right) \, . \tag{2}$$

As the virtual photon is space-like, positive values of the photon virtuality are obtained due to the minus sign. Here, the mass m of the lepton is used in addition to the scattering angle θ of the lepton. The photon virtuality describes the resolution with which the nucleon is probed and gives the scale of the interaction. The Bjorken-x variable is given by

$$x = \frac{Q^2}{2P \cdot q} \overset{\text{lab.}}{=} \frac{Q^2}{2M(E - E')} \, . \tag{3}$$

It can be interpreted as the elasticity of the process. For $x = 1$ an elastic scattering took place. In the case of inelastic scattering, Bjorken-x is smaller than one. In addition, other variables can be used like the energy transferred by the virtual photon in the laboratory frame

$$\nu = \frac{P \cdot q}{M} \overset{\text{lab.}}{=} E - E' \, . \tag{4}$$

The dimensionless variable

$$y = \frac{P \cdot q}{P \cdot k} \overset{\text{lab.}}{=} \frac{\nu}{E} \tag{5}$$

is the relative energy transferred from the virtual photon to the nucleon. The characterisation of the process as elastic, inelastic or deep inelastic is made using the invariant mass W of the hadronic final state. It is given by

$$W^2c^2 = (P + q)^2 \overset{\text{lab.}}{=} M^2c^2 + Q^2\left(\frac{1}{x} - 1\right) \, . \tag{6}$$

In the case of elastic scattering, W is equal to the mass of the nucleon. The process is called inelastic if W is larger than the nucleon mass and it is called deep inelastic if W is larger than the mass of individual nucleon resonances, $W^2 > 5\,(\text{GeV}/c^2)^2$. The cross section as a function of W is shown in Figure 2 as it was measured at SLAC [14] using various beam energies. For $W > 2.5\,\text{GeV}/c^2$ no individual nucleon resonances are visible. This is already fulfilled at the kinematics of the COMPASS experiment. Using the 200 GeV/c
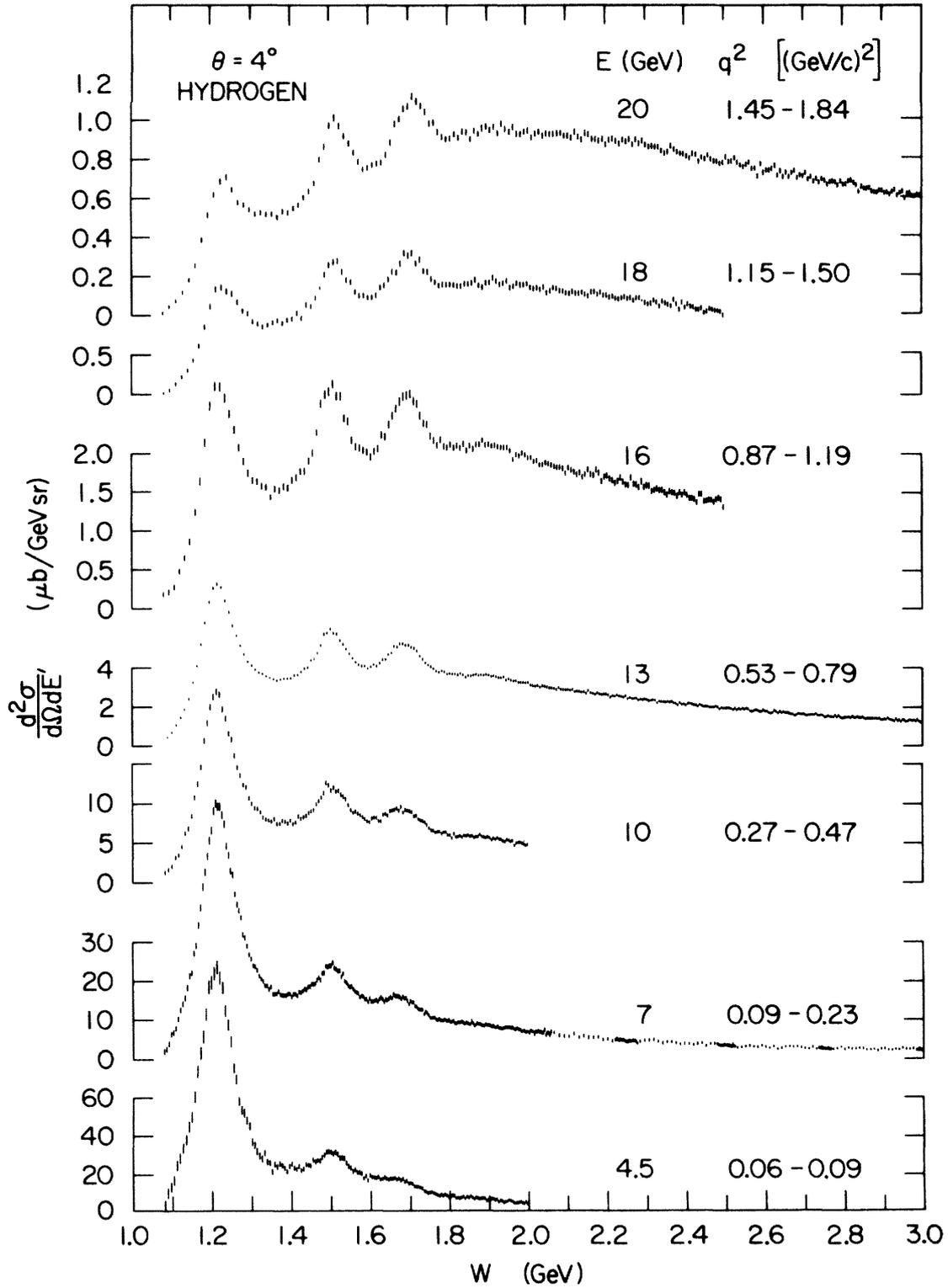
Figure 2: Measured cross section for electron proton scattering as a function of the invariant mass of the hadronic final state W. The cross section was measured using various beam energies E. At low W the individual nucleon resonances are visible. (Taken from [14])

muon beam, at $x = 0.0025$ the invariant mass of the hadronic final state is $18.4\,\text{GeV}/c^2$ and at $x = 0.7$ it is between $3.5\,\text{GeV}/c^2$ and $10.1\,\text{GeV}/c^2$. The invariant mass in the centre of mass system is given by

$$s = (k + P)^2 \overset{\text{lab.}}{=} \frac{Q^2}{xy} + M^2c^4 + m^2c^4 \,. \tag{7}$$

At the COMPASS experiment, the invariant mass is $\sqrt{s} = 19\,\text{GeV}/c^2$ in the case of the $200\,\text{GeV}/c$ muon beam.

2.3   CROSS SECTION FOR DEEP INELASTIC SCATTERING

The differential cross section for inclusive deep inelastic scattering of leptons by nucleons is given by the product of the leptonic tensor, $L_{\mu\nu}$, and the hadronic tensor, $W_{\mu\nu}$ [15]:

$$\frac{d^2\sigma}{d\Omega dE'} = \frac{\alpha^2}{Q^4} \frac{E'}{ME} L^{\mu\nu} W_{\mu\nu} \,. \tag{8}$$

Here, α is the electromagnetic fine-structure constant. Only the contribution from the one photon exchange is taken into account. Contributions from the exchange of a Z boson can be neglected at the energies used at the COMPASS experiment. They are suppressed by a factor $Q^2/(Q^2 + M_Z^2)$, depending on the mass M_Z of the Z boson.

The leptonic tensor describes the emission of the virtual photon by the lepton. As leptons are point-like particles, the leptonic tensor can be calculated using quantum electrodynamics (QED). The tensor can be split into two parts, a symmetric (S) one and an antisymmetric (A) one,

$$L_{\mu\nu}(s, k, k') = L_{\mu\nu}^{(S)}(k, k') + i L_{\mu\nu}^{(A)}(s, k, k') \,. \tag{9}$$

Here, already a summation over the spins of the scattered lepton is performed and only a dependence on the spin s of the incoming lepton remains. This corresponds to the case where the polarisation of the scattered lepton is not measured. The symmetric term in the tensor is independent of the spin of the incoming lepton and describes the spin-independent scattering. It is given by

$$L_{\mu\nu}^{(S)}(k, k') = 2(k_\mu k'_\nu + k'_\mu k_\nu) - 2g_{\mu\nu}(k \cdot k' - m^2) \,. \tag{10}$$

On the contrary, the asymmetric term depends on the spin of the incoming lepton and describes the spin-dependent scattering. It is given by

$$L_{\mu\nu}^{(A)}(s, k, k') = 2m\epsilon_{\mu\nu\alpha\beta} s^\alpha q^\beta \,. \tag{11}$$

Here, $g_{\mu\nu}$ is the metric tensor and $\epsilon_{\mu\nu\alpha\beta}$ the antisymmetric Levi-Civita tensor.

The hadronic tensor cannot be calculated using quantum electrodynamics. It describes the absorption of the virtual photon by the nucleon. Similar to the leptonic tensor, the hadronic tensor can be split into a symmetric and an antisymmetric contribution

$$W_{\mu\nu}(S, P, q) = W_{\mu\nu}^{(S)}(P, q) + i W_{\mu\nu}^{(A)}(S, P, q) \,, \tag{12}$$

where S is the spin of the target nucleon. Even though it is not possible to calculate the hadronic tensor, a generalised expression for both contributions can be obtained. They

are obtained by taking into account the properties of quantum electrodynamics for time and parity invariance. In addition, the expressions have to conserve the electromagnetic current and be Lorentz invariant. For a nucleon with spin-1/2, the symmetric contribution describing spin-independent scattering is given by

$$\frac{1}{2M}W_{\mu\nu}^{(S)}(P,q) = \left(-g_{\mu\nu} + \frac{q_\mu q_\nu}{q^2}\right)W_1 + \left[\left(P_\mu - \frac{P\cdot q}{q^2}q_\mu\right)\left(P_\nu - \frac{P\cdot q}{q^2}q_\nu\right)\right]\frac{W_2}{M^2}. \quad (13)$$

The antisymmetric contribution, which describes the spin-dependent scattering, is given by

$$\frac{1}{2M}W_{\mu\nu}^{(A)}(S,P,q) = \epsilon_{\mu\nu\alpha\beta}q^\alpha\left\{MS^\beta G_1 + \left[(P\cdot q)S^\beta - (S\cdot q)P^\beta\right]\frac{G_2}{M}\right\}. \quad (14)$$

Here, the unknown structure of the nucleon is parametrised in four so called structure functions. For the spin-independent scattering of leptons, the functions W_1 and W_2 are introduced and for the spin-dependent scattering the functions G_1 and G_2. These four functions all depend on q^2 and the product $P\cdot q$, which is proportional to the variables ν.

2.4 STRUCTURE FUNCTIONS

The newly introduced structure functions W_i and G_i describing the unknown structure of the nucleon are not dimensionless. They can be replaced by dimensionless expressions:

$$\begin{aligned} MW_1(\nu,Q^2) &= F_1(x,Q^2)\,, \\ \nu W_2(\nu,Q^2) &= F_2(x,Q^2)\,, \end{aligned} \quad (15)$$

$$\begin{aligned} M^2\nu G_1(\nu,Q^2) &= g_1(x,Q^2)\,, \\ M\nu^2 G_2(\nu,Q^2) &= g_2(x,Q^2)\,, \end{aligned} \quad (16)$$

yielding the dimensionless structure functions F_1, F_2, g_1 and g_2. The differential cross section is obtained from the contraction of the leptonic and hadronic tensor. The spin-independent and spin-dependent contribution to the differential cross section are now expressed by the dimensionless structure functions and kinematic variables. The expression for the spin-independent contribution is

$$\frac{d^2\sigma}{dxdQ^2} = \frac{4\pi\alpha^2}{Q^2x}\left[\left(1 - \frac{Q^2}{2MEx} - \frac{Q^2}{4E^2}\right)F_2(x,Q^2) + \frac{Q^4}{4M^2E^2x}F_1(x,Q^2)\right]. \quad (17)$$

The spin-dependent cross section $\Delta\sigma$ is given for the difference between the cross sections for reactions where the lepton spin and the nucleon spin are antiparallel and reactions where they are parallel:

$$\Delta\sigma = \sigma^{\uparrow\downarrow} - \sigma^{\uparrow\uparrow}. \quad (18)$$

Therefore, a polarised target together with a polarised beam is needed for the measurement. The differential cross section for this spin-dependent contribution is given by

$$\frac{d^2\Delta\sigma}{dxdQ^2} = \frac{4\pi\alpha^2}{MEQ^2x}\left[\left(2 - \frac{Q^2}{2MEx} - \frac{Q^2}{2E^2}\right)g_1(x,Q^2) + \frac{2Mx}{E}g_2(x,Q^2)\right]. \quad (19)$$

2.5   FIRST CROSS SECTION MEASUREMENT

A first measurement of the spin-independent cross section was performed at the linear accelerator at Stanford (SLAC) [7] in 1969. They used an electron beam with energies between $3\,\text{GeV} - 17\,\text{GeV}$ scattering off protons. The results for the ratio of the inelastic cross section to the Mott cross section, which describes the scattering of a point-like spin-$1/2$ particle by a point-like nucleon, are shown in Figure 3. The results for three different masses of the hadronic final state are shown together with the already well known behaviour for elastic scattering. A surprisingly weak dependence of the cross section ratio on
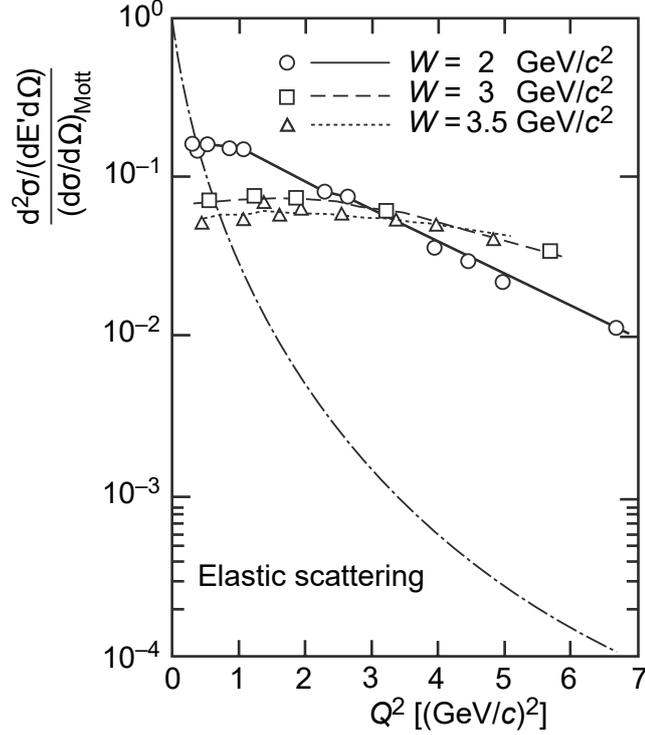
Figure 3: Ratio of the inelastic cross section to the Mott cross section as a function of the photon virtuality for different values of the invariant mass of the hadronic final state. (Taken from [16])

the photon virtuality was observed for $W > 2\,\text{GeV}/c^2$. This cross section ratio is given by the two spin-independent structure functions:

$$\frac{d\sigma}{d\Omega dE'} \bigg/ \left(\frac{d\sigma}{d\Omega}\right)_{\text{Mott}} = W_2(Q^2, \nu) + 2W_1(Q^2, \nu)\tan\frac{\theta}{2} \ . \tag{20}$$

Therefore, the two spin-independent structure functions are nearly independent of the photon virtuality at fixed invariant masses of the hadronic final state. This is an indication of point-like substructures in the proton.

2.6   QUARK PARTON MODEL

The first findings at SLAC were confirmed also with deuteron targets and led to the development of the quarks parton model for the interpretation of the results. In the

parton model, which was developed by Feynman and Bjorken [8, 17], the interpretation of deep inelastic scattering is performed in a fast moving reference frame. In this frame, the nucleon has a very large longitudinal momentum, $P_z \to \infty$. Therefore, all partons inside the nucleon move collinearly and all masses and transverse momenta can be neglected. In addition, the time for the interaction between the virtual photon and the parton is considered to be short. Using these assumptions, the interaction between the lepton and the nucleon is described by an incoherent sum of all interactions on the different partons. In this reference frame, Bjorken-x is interpreted as the momentum fraction of the nucleon carried by the parton.

The combination of the parton model with the already existing quark model from Gell-man and Zweig [3, 4] lead to the quark parton model. In the quark parton model, partons are identified as quarks and the nucleon consists of three valence quarks, which are responsible for all quantum numbers of the nucleon. In the extended quark parton model, also pairs of quarks and antiquarks exist inside the nucleon. They are called sea quarks. The valence quarks of the proton are two up quarks and one down quark and the ones of the neutron are two down quarks and one up quark. Table 1 lists some properties of the quarks.

Table 1: Summary of the properties of the quarks [18].

	UP	DOWN	STRANGE	CHARM	BOTTOM	TOP
Electric charge	$\frac{2}{3}e$	$-\frac{1}{3}e$	$-\frac{1}{3}e$	$\frac{2}{3}e$	$-\frac{1}{3}e$	$\frac{2}{3}e$
Isospin	$\frac{1}{2}$	$-\frac{1}{2}$	0	0	0	0
Mass (MeV/c^2)	$2.2^{+0.6}_{-0.4}$	$4.7^{+0.5}_{-0.4}$	96^{+8}_{-4}	1270 ± 30	4180^{+40}_{-30}	$173210 \pm 510 \pm 710$

The interpretation of the structure functions within the quark parton model is given by the parton distribution functions $q(x)$. These represent the number of quarks with a certain flavour (up, down, strange ...) with a momentum fraction in the interval $[x, x + dx]$. Therefore, the integrals of these functions for the valence quarks of a proton are given by

$$\int_0^1 dx\, u_v(x) = 2 \,,$$
$$\int_0^1 dx\, d_v(x) = 1 \,,$$

(21)

which represent the number of up and down valence quarks. For the neutron, these relations can be obtained by assuming a SU(2) symmetry for up and down quarks called isospin symmetry. This results in proton and neutron being isospin partners with opposite isospin. Therefore, the relations for the neutron can be obtained by interchanging the up and down quarks distribution. Using the parton distribution functions, the spin-independent structure functions are given by summing over all flavours:

$$F_1(x) = \frac{1}{2} \sum_q e_q^2 \left(q(x) + \bar{q}(x) \right) \,,$$

(22)

$$F_2(x) = x \sum_q e_q^2 \left(q(x) + \bar{q}(x) \right) \,.$$

(23)

Here, e_q is the charge of a quark of a particular flavour. A confirmation of the quarks being spin-1/2 particles was obtained from the Callan-Gross relation [19] connecting the spin-independent structure functions:

$$F_2(x) = 2x \cdot F_1(x) \, . \tag{24}$$

This relation is only valid for quarks with a spin of 1/2. In the case of quarks with spin 0, F_1 is zero. The result of the measurement is shown in Figure 4 for the ratio $2xF_1/F_2$. The measured ratio is in good agreement with the prediction for a spin of 1/2.
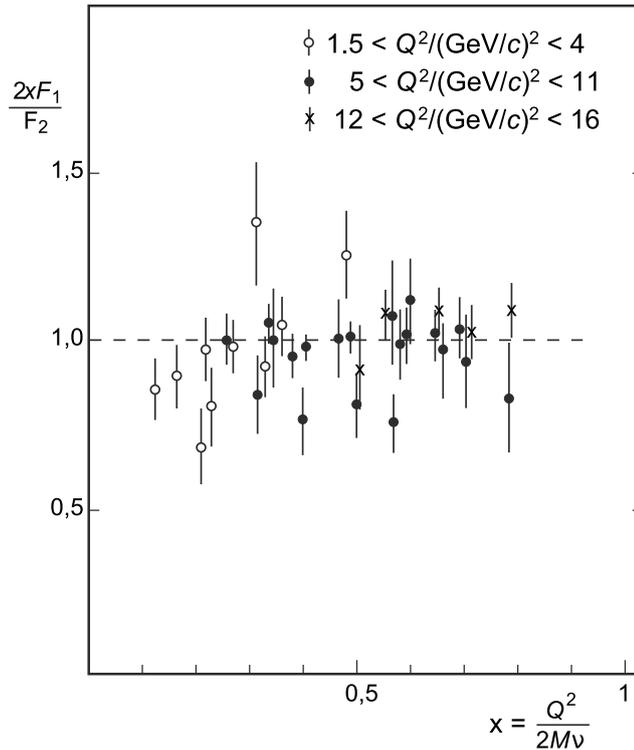
Figure 4: Measurement of the ratio of the two spin-independent structure functions $2x \cdot F_1$ and F_2. The results were obtained at the SLAC. (Taken from [16])

In the quark parton model, also the spin-dependent structure functions can be calculated. The structure functions are expressed by the quark helicity distributions $\Delta q(x)$. They are connected to the parton distribution function by taking into account the helicity of the quarks inside the nucleon. The function q^+ denotes the number density of quarks with their spins parallel to the one of the nucleon and q^- the ones with their spins antiparallel. The parton distribution functions $q(x)$ are given by the sum of those two:

$$\begin{aligned} q(x) &= q^+(x) + q^-(x) \\ \bar{q}(x) &= \bar{q}^+(x) + \bar{q}^-(x) \, , \end{aligned} \tag{25}$$

whereas the helicity ones are given by the difference of the two functions

$$\begin{aligned} \Delta q(x) &= q^+(x) - q^-(x) \\ \Delta \bar{q}(x) &= \bar{q}^+(x) - \bar{q}^-(x) \, . \end{aligned} \tag{26}$$

Thus, the quark helicity distributions contain information on the contributions from the quarks to the spin of the nucleon. Using the parton helicity distributions, the spin-dependent structure functions are given by:

$$g_1(x) = \frac{1}{2} \sum_q e_q^2 \left(\Delta q(x) + \Delta \bar{q}(x) \right) , \tag{27}$$

$$g_2(x) = 0 . \tag{28}$$

Here, only g_1 is related to the quark helicity distributions. A interpretation of g_2 is not possible in the quark parton model.

From Equations 22, 23 and 27, a simple interpretation of the structure functions is possible. The structure function F_1 describes the number density of quarks, F_2 the momentum distribution of the quarks and g_1 the spin distribution of the quarks inside the nucleon. Thus the integral over the full Bjorken-x range of F_2 is connected to the contribution from the quarks to the momentum of the nucleon. Their contribution is about 50%. Similar, the contribution from the quark spins to the total spin of the nucleon is connected to the integral of g_1.

2.7 QCD IMPROVED PARTON MODEL

The precision of the measurements of the spin-independent structure functions was improved since the early SLAC experiments and today a large kinematic range is covered by the different measurements on fixed targets and at a lepton nucleon collider. The results for the structure function F_2^p are shown in Figure 5. The measurements show a clear dependence on the photon virtuality, which was already observed by the early SLAC experiments. At low values of Bjorken-x, the structure function shows an increase with increasing photon virtualities, whereas at higher values of Bjorken-x, the structure function decreases. Only for values of Bjorken-x around 0.2, the initially observed independence on the photon virtuality is present. In order to explain this behaviour, the quark parton model has to be extended taking into account binding effects, which are described by the exchange of gluons in quantum chromodynamics.

2.7.1 *Gluons and the coupling constant*

The interaction of quarks is described by a non-Abelian gauge theory called quantum chromodynamics (QCD). This theory describes the interaction of quarks via a colour field transmitted by gluons. The gluons couple to the charge of the strong force called colour. In contrast to the electromagnetic interaction, where only one charge exists (plus or minus), three charges exists in quantum chromodynamics called red (r), blue (b) and green (g) together with their anticolour. Quarks always carry one of the three colours and the antiquarks always carry an anticolour. A major difference between strong and electromagnetic interactions is that gluons also carry charge, which is a certain combination of a colour and a anticolour charge. The possible combinations are described by a SU(3) symmetry of the three colour and anticolour. Therefore, all independent combinations
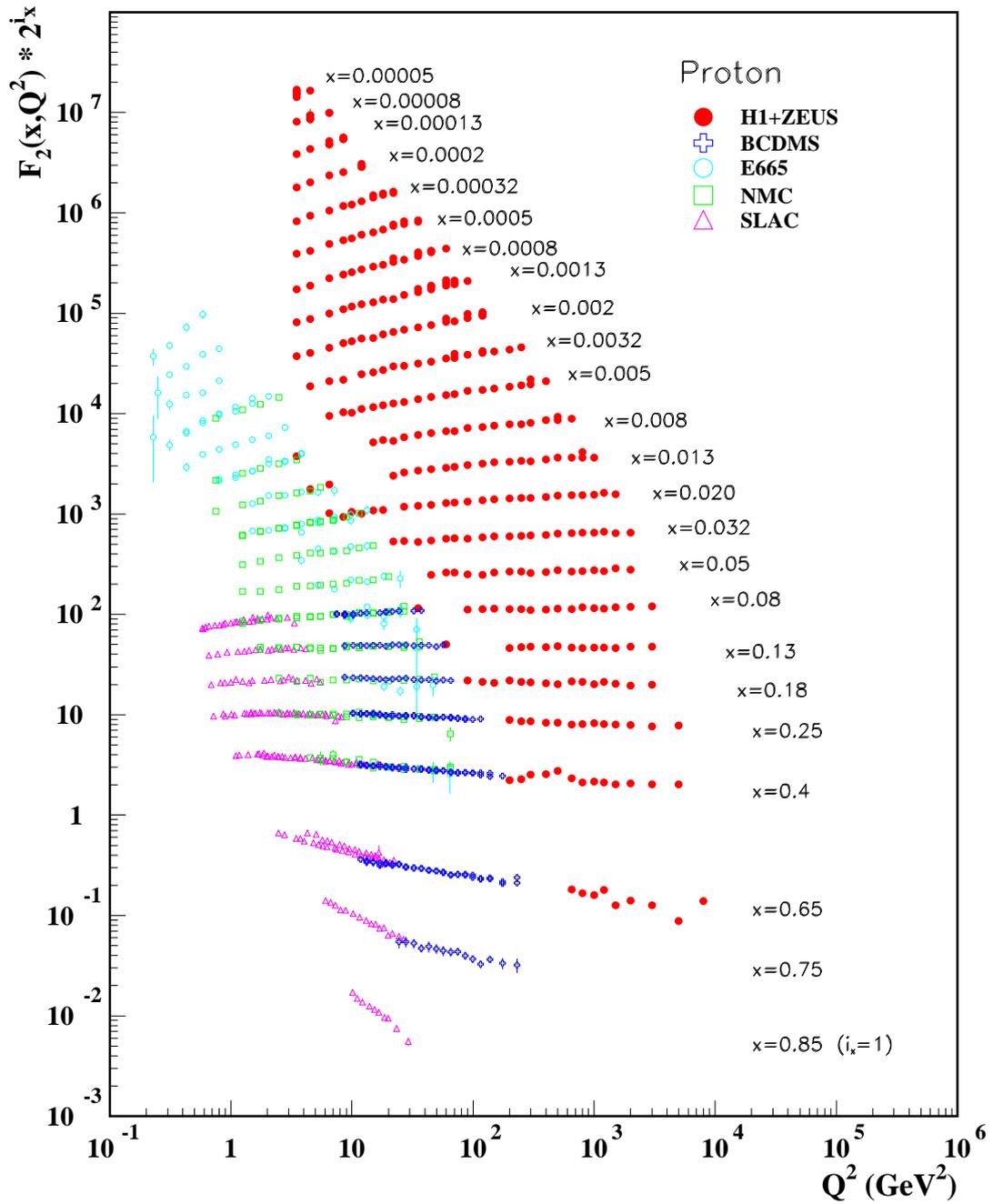
Figure 5: The structure function F_2^p measured at fixed target experiments using electrons (SLAC [20]) or muons (BCDMS [21], E665 [22], NMC [23]) and measured at collider experiments (H1 and ZEUS [24]). The measurements are shown with an offset depending on the Bjorken-x bin. (Taken from [18])

are grouped in a antisymmetric octet and a symmetric singlet. The singlet combination is colourless:

$$\frac{1}{\sqrt{3}}\left(r\bar{r} + g\bar{g} + b\bar{b}\right) \ . \tag{29}$$

The combinations of the octet are given by:

$$r\bar{g}, \quad r\bar{b}, \quad g\bar{b}, \quad g\bar{r}, \quad b\bar{r}, \quad b\bar{g}, \quad \frac{1}{\sqrt{2}}\left(r\bar{r} - g\bar{g}\right), \quad \frac{1}{\sqrt{6}}\left(r\bar{r} + g\bar{g} - 2b\bar{b}\right) \ . \tag{30}$$

The combinations from the octet are not colourless. Gluons, which are colourless, do not interact with other particles carrying a colour. Therefore, only gluons carrying a colour combination from the octet can interact. As gluons carry a colour, they interact with one another. This results in a strong dependence of the strong coupling constant α_s on the photon virtuality. At leading order, the dependence of the strong coupling constant on the scale given by the photon virtuality is [25]:

$$\alpha_s(Q^2) = \frac{12\pi}{(33 - 2n_f) \cdot \ln\left(Q^2/\Lambda^2\right)} \ . \tag{31}$$

Here, n_f is the number of active quark flavours, which can contribute at a given scale and Λ is interpreted as the scale at which non-perturbative effects dominate. For $n_f = 3$ the measured value of this constant is $\Lambda = 332\,\text{MeV}$ [18]. The dependence is shown in Figure 6 together with measurements of the strong coupling constants. The shown range includes results with $n_f = 3, 4, 5$ and also results with $n_f = 6$.
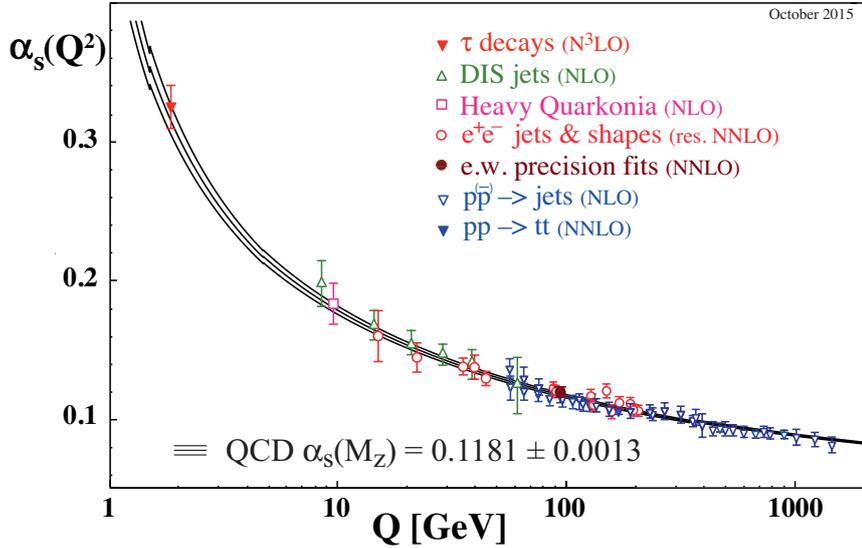
Figure 6: Results for the strong coupling constant as a function of Q obtained from various reactions. (Taken from [18])

At high virtualities, which corresponds to small distances, the strong coupling constant is small. Therefore, the quarks behave like free particles. This is also the behaviour assumed in the naive quark parton model. It is called "asymptotic freedom". Due to the small value of the coupling constant, calculations of interactions can be performed using techniques from perturbation theory. Processes at this scale are called "hard" processes.

The behaviour at small virtualities is called "confinement". In this region the strong coupling constant becomes large and calculations using perturbation theory are not possible. The name "confinement" describes the observation that no free quarks or gluons exist. They are confined inside of colourless particles. Processes at this scale are called "soft".

2.7.2 *Evolution equations*

For the calculation of the cross section for virtual photon nucleon interactions, the factorisation Ansatz is used. It allows to split the contributions to the cross section into a contribution from the "hard" process and one from the "soft" process. Here, the "hard" process is the interaction between the virtual photon and the parton. This can be calculated using quantum electrodynamics. The "soft" process describes the nucleon and includes the parton distribution functions, which cannot be calculated in quantum chromodynamics. The factorisation introduces the factorisation scale μ_f, which separates both parts. Therefore, the parton distribution functions and the strong coupling constant are scale dependent.

Different schemes exist for the factorisation of "soft" and "hard" processes. The obtained cross section is independent of the scheme as long as the same scheme is used in the calculation of the "soft" and the "hard" contribution. A commonly used scheme is the modified minimal subtraction scheme, $\overline{MS}$ [26].

In deep inelastic scattering, usually the photon virtuality is used as a scale. Often a scale of $Q^2 > 1\,(GeV/c)^2$ is used, which is considered to be large enough to allow perturbative calculations. The scale dependence of the parton distribution functions is illustrated by the interpretation of the photon virtuality as a resolution, which is illustrated in Figure 7. At low scales, for example, only the interaction between the virtual photon and a quark is resolved. At larger scales, which are large photon virtualities, also a possible emission of a gluon from a quark is resolved. The emission results in a change of the kinematics of the process.

(a) Scale Q_0^2 (b) Scale $Q^2 > Q_0^2$
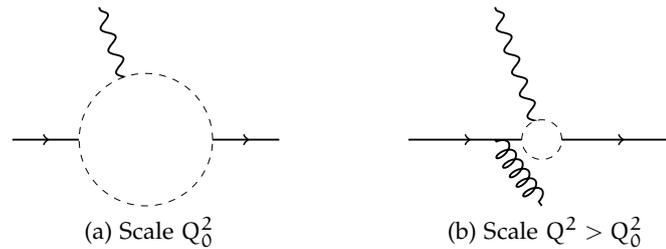
Figure 7: Illustration of the scale dependence for two different scales Q_0^2 (left) and $Q^2 > Q_0^2$ (right). The resolution is connected to the photon virtuality as indicated by the dashed circle. At higher scales the additional radiation of a gluon is resolved.

The scale dependence of a parton distribution function is given by:

$$\frac{d}{d\ln Q^2}q_i(x,Q^2) = \frac{\alpha_s(Q^2)}{2\pi}\int_x^1 \frac{dy}{y}\left[q_i(y,Q^2)P_{qq}\left(\frac{x}{y}\right) + g(y,Q^2)P_{qg}\left(\frac{x}{y}\right)\right], \quad (32)$$

$$\frac{d}{d\ln Q^2}g(x,Q^2) = \frac{\alpha_s(Q^2)}{2\pi}\int_x^1 \frac{dy}{y}\left[\sum_i q_i(y,Q^2)P_{gq}\left(\frac{x}{y}\right) + g(y,Q^2)P_{gg}\left(\frac{x}{y}\right)\right]. \quad (33)$$

In this equations, the evolution of a quark distribution function q_i is coupled to the parton distribution function of the gluon g. The contribution from the gluons to the evolution of each quark flavour is given by the same term in Equation 32. It describes the contribution from gluon splitting into quark and antiquark pairs. The first term in Equation 32 involving the quark distribution function describes the emission of a gluon from the quark. Also, all quark distribution functions contribute to the evolution of the gluon distribution function in Equation 33 via the emission of a gluon. The second term in Equation 33 describes the emission of a gluon from the gluon. The emission of gluons/quarks from quarks or other gluons is described by the splitting functions $P_{ij}(x/y)$. They represent the probability of a parton j carrying the momentum fraction x to emit a parton i with the momentum fraction y. For example, $P_{qq}(x/y)$ is the probability of a quark with the momentum fraction x to emit a gluon and become a quark with the momentum fraction y. The processes described by the splitting functions are shown in Figure 8. The splitting

(a) $P_{qq}(z)$ (b) $P_{gq}(z)$ (c) $P_{qg}(z)$ (d) $P_{gg}(z)$
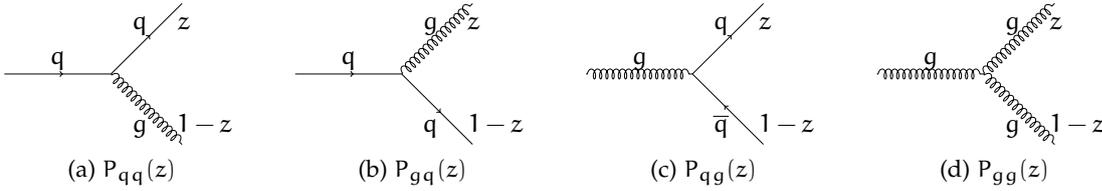
Figure 8: Illustration of the processes described by the splitting functions.

functions are calculated in perturbation theory. In leading order of the strong coupling constant α_s they are given by [25]:

$$P_{qq}(z) = \frac{4}{3}\left[\frac{1+z^2}{(1-z)_+}\right] + 2\delta(1-z), \quad (34)$$

$$P_{qg}(z) = \frac{1}{2}\left[z^2 + (1-z)^2\right], \quad (35)$$

$$P_{gq}(z) = \frac{4}{3}\left[\frac{1+(1-z)^2}{z}\right], \quad (36)$$

$$P_{gg}(z) = 6\left[\frac{1-z}{z} + z(1-z) + \frac{z}{(1-z)_+}\right] + \left[\frac{11}{2} - \frac{n_f}{3}\right]\delta(1-z). \quad (37)$$

Here, the $+$ denotes the plus distribution, which is defined for any sufficiently regular function g by

$$\int_0^1 dx\, g(x)\left[f(x)\right]_+ = \int_0^1 dx\, (g(x) - g(1))\, f(x). \quad (38)$$

As the evolution of all quark distribution functions involves the same contribution from the gluon distribution function, its contribution cancels in the evolution of differences between the quark distribution functions, named non-singlet distribution functions. Therefore, the evolution equations can be reformulated to describe the evolution of the gluon distribution together with the sum off all quark distribution functions, which is given by

$$q^S(x, Q^2) = \sum_{i=1}^{n_f} q_i(x, Q^2) \, . \tag{39}$$

It is named singlet distribution function. In addition to these two equations, several non-singlet combinations q^{NS} exist, which are described by the same evolution equation independent of the gluon distribution function. Introducing the convolution of two functions $f \otimes g = \int_x^1 f(x/y)g(y)dy/y$ the evolution equation are

$$\frac{d}{d \ln Q^2} \, q^{NS} = \frac{\alpha_s(Q^2)}{2\pi} \qquad P_{qq}^{NS} \qquad \otimes \, q^{NS} \, , \tag{40}$$

$$\frac{d}{d \ln Q^2} \begin{pmatrix} q^S \\ g \end{pmatrix} = \frac{\alpha_s(Q^2)}{2\pi} \begin{pmatrix} P_{qq}^S & 2n_f P_{qg} \\ P_{gq} & P_{gg} \end{pmatrix} \otimes \begin{pmatrix} q^S \\ g \end{pmatrix} \, . \tag{41}$$

The set of evolution equation is called Dokshitzer-Gribov-Lipatov-Altarelli-Parisi equations or short DGLAP equations [27]. In the context of SU(2) and SU(3) flavour symmetry, two non-singlet combination appear. These are the isospin combination $q_3 = (u + \bar{u}) - (d + \bar{d})$ and the octet combination $q_8 = (u + \bar{u}) + (d + \bar{d}) - 2(s + \bar{s})$.

The DGLAP equations also describe the scale dependence for the parton helicity distributions. This is done by introducing new splitting functions ΔP_{ij}. These new splitting functions are interpreted as the probability for a particle to have the same helicity as the parent particle. In leading order of the strong coupling constant α_s they are given by [25]:

$$\Delta P_{qq}(z) = \frac{4}{3} \left[\frac{1 + z^2}{(1 - z)_+} \right] + 2\delta (1 - z) \, , \tag{42}$$

$$\Delta P_{qg}(z) = \frac{1}{2} \left[z^2 - (1 - z)^2 \right] \, , \tag{43}$$

$$\Delta P_{gq}(z) = \frac{4}{3} \left[\frac{1 - (1 - z)^2}{z} \right] \, , \tag{44}$$

$$\Delta P_{gg}(z) = 3 \left[(1 + z^4) \left(\frac{1}{z} + \frac{1}{(1 - z)_+} \right) - \frac{1 - z^3}{z} \right] - \left(\frac{11}{2} - \frac{n_f}{3} \right) \delta (1 - z) \, . \tag{45}$$

The splitting functions P_{qq} and ΔP_{qq} are the same in leading order. Therefore, the evolution of the non-singlet distributions is the same for the spin-independent and spin-dependent case. Due to the emission of soft gluons, the splitting functions P_{gg} and P_{gq} are different in the spin-independent and spin-dependent case. In the spin-independent case, these result in singularities at small Bjorken-x, whereas in the spin-dependent case the gluon splits into a quark and antiquark pair with opposite spins, which results in helicity conservation. Calculations for the spitting function were also performed in higher order perturbation theory. For example, the next-to-leading order expressions for the spin-dependent case can be found in References [28, 29]. The differences between the splitting functions for the spin-independent and spin-dependent case result in a different dependence on the photon virtuality for the structure functions F_1 and g_1.

The scale dependence of the structure functions results in a modification of the Equations 22, 23 and 27 to include the dependence on the photon virtuality. At next-to-leading order, the influence from the gluons and effects from the running coupling constant has to be taken into account. This is done as follows (see, for example, in Reference [30]):

$$F_2 = x \langle e^2 \rangle \left[E_q^{NS} \otimes q^{NS} + E_q^{S} \otimes q^{S} + 2 n_f E_g \otimes g \right] , \tag{46}$$

$$g_1 = \frac{1}{2} \langle e^2 \rangle \left[C_q^{NS} \otimes \Delta q^{NS} + C_q^{S} \otimes \Delta q^{S} + 2 n_f C_g \otimes \Delta g \right] . \tag{47}$$

Here, the non-singlet combinations q^{NS} and Δq^{NS} depend on the target are given by

$$q^{NS}(x, Q^2) = \sum_{i=1}^{n_f} \left(\frac{e_i^2}{\langle e^2 \rangle} - 1 \right) q_i(x, Q^2) \tag{48}$$

with $\langle e^2 \rangle = \sum e_i^2 / n_f$. The factors E_q^{S}, E_q^{NS}, E_g and C_q^{S}, C_q^{NS}, C_g are called coefficient functions and are given as power series in α_s. In leading order, the coefficient functions are given by:

$$E_q^{S} = C_q^{S} = \delta(1 - x) , \tag{49}$$

$$E_q^{NS} = C_q^{NS} = \delta(1 - x) , \tag{50}$$

$$E_g = C_g = 0 . \tag{51}$$

This results in the already known expressions shown in Equations 23 and 27. The next-to-leading order expressions for the spin-dependent coefficient functions can be found in References [31, 32].

2.8 VIRTUAL PHOTON NUCLEON INTERACTION

The cross section for deep inelastic scattering can be described using the cross section for absorption of a virtual photon. The absorption cross section is expressed as the imaginary part of the forward virtual photon nucleon scattering amplitude of the process $\gamma(h) +$ nucleon$(H) \rightarrow \gamma(h') +$ nucleon(H') [33]. Here, $h(h')$ and $H(H')$ denote the helicity of the photon and the target nucleon before (after) the interaction. This connection is done using the optical theorem, which is illustrated in Figure 9.
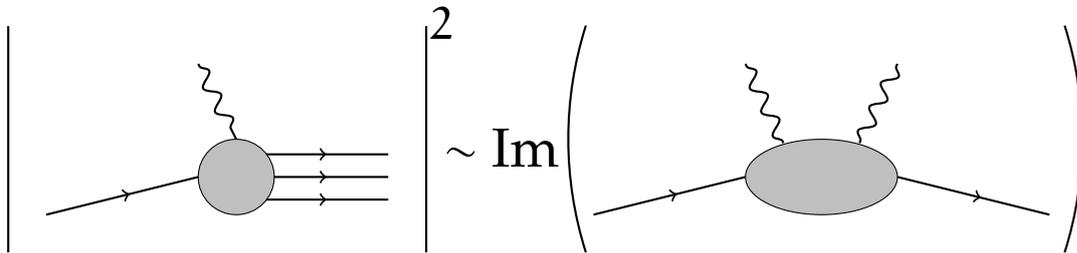
Figure 9: Illustration of the optical theorem connecting the virtual photon absorption cross section to the imaginary part of the forward Compton scattering amplitude.

In the case of a spin-1/2 target, only four independent amplitudes exists. They are connected to cross sections and therefore also to structure functions. The number of amp-

litudes is obtained by requiring helicity conservation as well as time and parity symmetry to be valid. The resulting cross sections are [34]:

$$\sigma^T_{1/2} = \frac{4\pi^2\alpha}{MK}\mathcal{A}(1,\frac{1}{2};1,\frac{1}{2}) \quad = \frac{4\pi^2\alpha}{MK}\left(F_1 + g_1 - \frac{2Mx}{\nu}g_2\right) , \tag{52}$$

$$\sigma^T_{3/2} = \frac{4\pi^2\alpha}{MK}\mathcal{A}(1,-\frac{1}{2};1,-\frac{1}{2}) = \frac{4\pi^2\alpha}{MK}\left(F_1 - g_1 + \frac{2Mx}{\nu}g_2\right) , \tag{53}$$

$$\sigma^L_{1/2} = \frac{4\pi^2\alpha}{K}\mathcal{A}(0,\frac{1}{2};0,\frac{1}{2}) \quad = \frac{4\pi^2\alpha}{K}\left(\frac{F_2}{\nu}\left(1+\frac{\nu^2}{Q^2}\right) - \frac{1}{M}F_1\right) , \tag{54}$$

$$\sigma^{TL}_{1/2} = \frac{4\pi^2\alpha}{K}\mathcal{A}(0,\frac{1}{2};0,-\frac{1}{2}) = \frac{4\pi^2\alpha}{K}\frac{\sqrt{Q^2}}{M\nu}(g_1 + g_2) . \tag{55}$$

Here, the helicity amplitudes $\mathcal{A}$ are given as a function of the different helicities h, h', H and H'). The symbol $T(L)$ denotes the scattering of a transverse (longitudinal) virtual photon by a nucleon and $\sigma^{TL}_{1/2}$ represents the interference term. The subscripts $1/2$ ($3/2$) denotes the total spin of the system of virtual photon and nucleon. The kinematic factor K, which appears in the nominator of the non-physical cross sections for virtual photon in Equations 52-55, is given using the Hand convention [35]

$$K = \nu - \frac{Q^2}{2M} . \tag{56}$$

It cancels in the calculation of physical cross sections. For convenience, the cross section for transverse virtual photon absorption to introduced as

$$\sigma^T = \frac{1}{2}\left(\sigma^T_{1/2} + \sigma^T_{3/2}\right) = \frac{4\pi^2\alpha}{MK}F_1 , \tag{57}$$

which depends only on the spin-independent structure function F_1. The cross section ratio R is given by the ratio of the longitudinal and transverse virtual photon absorption cross sections:

$$R = \frac{\sigma^L}{\sigma^T} = \frac{(1+\gamma^2)F_2}{2xF_1} - 1 . \tag{58}$$

Here $\gamma = \sqrt{2Mx/\nu}$ is a kinematic factor.

2.9   CROSS SECTION ASYMMETRY

For the determination of the spin-dependent structure function g_1, the spin-dependent part of the cross section is measured (see Equations 18 and 19). Instead of measuring the cross section difference between parallel ($\sigma^{\uparrow\uparrow}$) and antiparallel spin directions ($\sigma^{\uparrow\downarrow}$) of the nucleon and the lepton directly, the longitudinal double spin asymmetry A_{LL} is measured, which is related to these cross sections by:

$$A_{LL} = \frac{\sigma^{\uparrow\downarrow} - \sigma^{\uparrow\uparrow}}{\sigma^{\uparrow\downarrow} + \sigma^{\uparrow\uparrow}} = D(A_1 + \eta A_2) . \tag{59}$$

Here, D is the depolarisation factor, which takes into account the spin transfer from the lepton to the virtual photon. It is explained in Section 4.4.4. The factor

$$\eta = \frac{\gamma(1 - y - \gamma^2 y^2/4 - y^2 m^2/Q^2)}{(1 - \gamma^2 y/2)(1 - y/2) - y^2 m^2/Q^2} \tag{60}$$

denotes a kinematic factor, where $\gamma = 2Mx\sqrt{Q^2}$. This kinematic factor is small for the kinematics of the COMPASS experiment. The two photon nucleon asymmetries, A_1 and A_2, can be expressed via the cross sections that were introduced before in Section 2.8:

$$A_1 = \frac{\sigma_{1/2}^T - \sigma_{3/2}^T}{\sigma_{1/2}^T + \sigma_{3/2}^T} = \frac{g_1 - \gamma^2 g_2}{F_1} \, , \tag{61}$$

$$A_2 = \frac{\sigma_{1/2}^{TL}}{\sigma^T} = \gamma \frac{g_1 + g_2}{F_1} \, . \tag{62}$$

Using this expression for A_1, its shape can be described. At a Bjorken-x close to one, the struck quark carries nearly the full momentum of the nucleon. As the virtual photon can only interact with quarks with the opposite helicity, the cross section $\sigma_{3/2}$ disappears. In this case, the asymmetry is large, $A_1 \sim 1$. In the region of the valance quarks, $x \sim 1/3$, two out of the three valence quarks have their spin correctly aligned to interact with the virtual photon, which results in an asymmetry of $A_1 \sim 1/3$. In the region of the sea quarks, i.e. at low Bjorken-x, the quark-antiquark pairs are expected to be produced with opposite spin orientations. This causes both cross sections to have a similar size, which results in an asymmetry close to zero.

For the asymmetry A_2, an upper limit of

$$|A_2| < \sqrt{(1 + A_1)R/2} \tag{63}$$

is obtained from the so called Soffer limit [36]. Measurements of A_2 from various experiments are shown in Figure 10 together with the Soffer limit and a calculation from the Wandzura-Wilczek relation [37]. The figure shows that the asymmetry A_2 is small for the proton and close to zero in the case of the deuteron. For both measurements, the asymmetry is much smaller than indicated by the Soffer limit. More information is given in Reference [38].

From the expression of the asymmetries in Equation 62, the relation to the spin-dependent structure function g_1 is obtained:

$$g_1 = \frac{F_1}{1 + \gamma^2} (A_1 + \gamma A_2) = \frac{F_2}{2x(1 + R)} (A_1 + \gamma A_2). \tag{64}$$

Here, the relation between the unpolarised structure functions from Equation 58 is used. The contribution from A_2 is neglected in the analysis of COMPASS data since it is small. The largest contribution from the proton measurement is $A_2^p \approx 0.1$ for $x \geqslant 0.5$. A contribution to the the systematic uncertainty takes into account a possible contribution from A_2, see Section 5.2.7.2.

2.10 MODIFICATIONS FOR DEUTERON

The helicity amplitudes in Section 2.8 are discussed for a spin-1/2 particle. In the case of the deuteron, which is a spin-1 particle, it is necessary to modify them. From the symmetry arguments given before, eight independent amplitudes are obtained [43]. For the asymmetry A_1, only cross sections connected to the absorption of a transverse photon contribute. They are related to the cross sections for a total spin of 0, 1 and 2 of the virtual photon nucleon system:

$$\sigma^T = \frac{1}{3} \left(\sigma_0^T + \sigma_1^T + \sigma_2^T \right) \, . \tag{65}$$
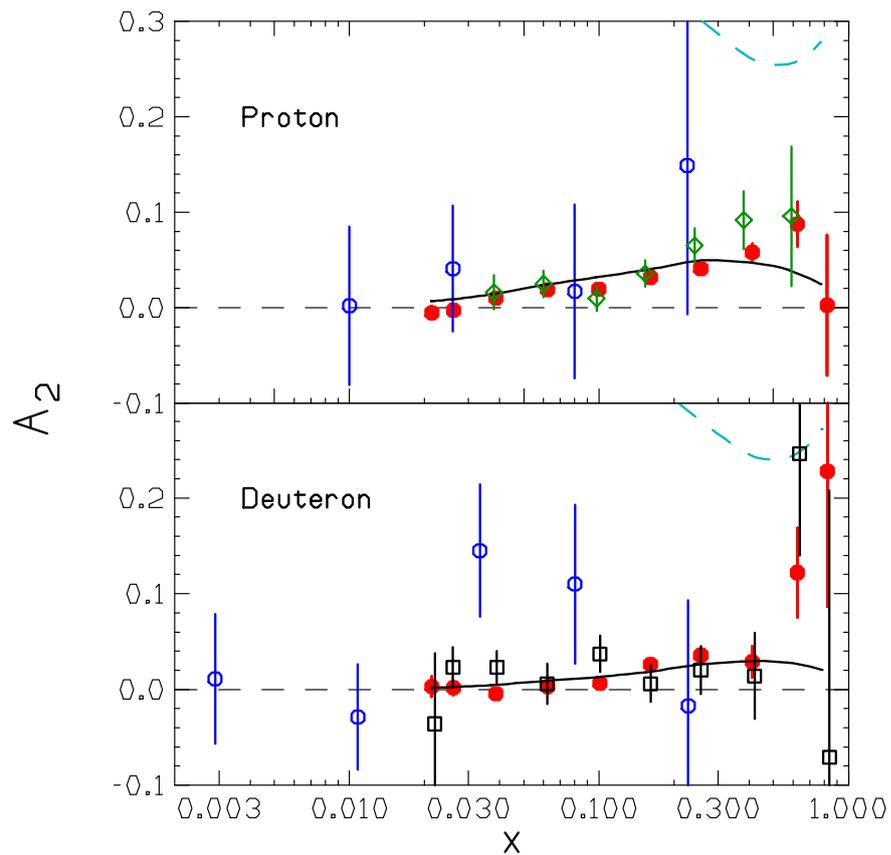
Figure 10: Measurements of the asymmetry A_2 for protons and deuterons. Shown are the measurements from E155 [38] (full circle) and [39] (open square), E143 [40] (open diamond), and SMC [41, 42] (open circle). The dashed line shows the Soffer limit and the solid line is a calculation from the Wandzura-Wilczek relation. (Taken from [38])

From the cross sections for the different total spins, the asymmetries are obtained as:

$$A_1 = \frac{3}{2} \frac{\sigma_0^T - \sigma_2^T}{\sigma_0^T + \sigma_1^T + \sigma_2^T} = \frac{g_1 - \gamma^2 g_2}{F_1} \ , \tag{66}$$

$$A_2 = \frac{3}{2} \frac{\sigma_0^{TL} - \sigma_1^{TL}}{\sigma_0^T + \sigma_1^T + \sigma_2^T} = \gamma \frac{g_1 + g_2}{F_1} \ . \tag{67}$$

In the case of A_2, also the cross sections connected to the interference between the absorption of a transverse and longitudinal photon (σ_i^{TL}) have to be considered similar to the spin-1/2 case. The relations between the asymmetries and the structure functions are the same as in the case of spin-1/2 particles. Therefore, similar arguments hold for the expected shape of the asymmetry as described in Section 2.9.

2.11   SUM RULES IN SPIN-DEPENDENT DEEP INELASTIC SCATTERING

Sum rules for the first moment of the spin-dependent structure function

$$\Gamma_1 = \int_0^1 dx\, g_1(x) \tag{68}$$

can be obtained from Equations 27 by introducing the first moment Δq of a quark helicity distribution, for example:

$$\Gamma_1^p(Q^2) = \frac{1}{2} \left[\frac{4}{9} \left(\Delta u + \Delta \bar{u} \right) + \frac{1}{9} \left(\Delta d + \Delta \bar{d} \right) + \frac{1}{9} \left(\Delta s + \Delta \bar{s} \right) \right] \ . \tag{69}$$

Using isospin symmetry the first moment of the spin-dependent structure function of the neutron is obtained by exchanging Δu and Δd. The Δq_i are described by the projection operator $(1 \pm \gamma_5)/2$ for a proton with the momentum P and spin S by introducing the covariant spin vector S^μ

$$2MS_\mu \Delta q = \langle P, S | \bar{q} \gamma_\mu \gamma_5 q | P, S \rangle \ . \tag{70}$$

Here, the proton matrix elements a_0 and a_i, which are also called axial charges, can be introduced using the flavour-singlet axial-vector current $J_{5\mu}^0$ and the octet of axial-vector current $J_{5\mu}^i$ with $i = 1, 2, \ldots, 8$, which are given by

$$J_{5\mu}^0 = \bar{\psi} \gamma_\mu \gamma_5 \psi \qquad \text{with} \quad \psi = \begin{pmatrix} \psi_u \\ \psi_d \\ \psi_s \end{pmatrix} \ , \tag{71}$$

$$J_{5\mu}^i = \bar{\psi} \gamma_\mu \gamma_5 \frac{\lambda_i}{2} \psi \ . \tag{72}$$

Here, the matrices λ_i are the generators of flavour SU(3) in the Gell-Mann standard representation. Using the axial vector currents the proton matrix elements are given by:

$$\langle P, S | J_{5\mu}^0 | P, S \rangle = 2MS_\mu a_0 \ , \tag{73}$$

$$\langle P, S | J_{5\mu}^i | P, S \rangle = MS_\mu a_i \ . \tag{74}$$

The axial vector currents also describe the β decay of the hyperons in the spin-1/2 baryon octet, which consist of neutron, proton, $\Sigma^{\pm}, \Sigma^0, \Lambda, \Xi^-$ and Ξ^0. Using the SU(3) flavour symmetry, all matrix elements are connected to two decay constants, F and D. The constraints on the decay constants are given in Table 3.

The two non-singlet charges are given by

$$a_3 = F + D = \frac{g_A}{g_V} \, , \tag{75}$$

$$a_8 = 3F - D \, , \tag{76}$$

where g_A/g_V is determined from the the neutron β decay. The axial charges are identified in the parton model with the first moments of the quark helicity distributions

$$a_0 = (\Delta u + \Delta \bar{u}) + (\Delta d + \Delta \bar{d}) + (\Delta s + \Delta \bar{s}) \tag{77}$$

$$a_3 = (\Delta u + \Delta \bar{u}) - (\Delta d + \Delta \bar{d}) \tag{78}$$

$$a_8 = (\Delta u + \Delta \bar{u}) + (\Delta d + \Delta \bar{d}) - 2(\Delta s + \Delta \bar{s}) \, . \tag{79}$$

These are used to express the first moment of the proton and neutron spin-dependent structure function by

$$\Gamma_1^{p(n)}(Q^2) = \frac{1}{12}\left(\pm a_3 + \frac{1}{3}a_8\right) + \frac{1}{9}a_0 \, , \tag{80}$$

where the expression for the neutron is given by the negative term including a_3, which is obtained from isospin symmetry. The singlet charge cannot be fixed by hyperon decays. It is identified with the total contribution from the quark spins to the spin of the nucleon in the $\overline{\text{MS}}$ scheme. Using other schemes, this relation is not necessarily valid. For example, in the AB scheme [44] a contribution from gluons has to be taken into account:

$$a_0 = \Delta\Sigma^{AB} - n_f \frac{\alpha_s}{2\pi}\Delta G^{AB} \, . \tag{81}$$

Here, $\Delta\Sigma^{AB}$ is the contribution from the quarks to the nucleon spin and ΔG^{AB} the one from the gluons. In this scheme, $\Delta\Sigma^{AB}$ is scale independent.

In higher order perturbation theory, the Fourier transforms of the coefficient functions introduced in Equation 47 [15] are used in the calculation of the first moments. Their Fourier transforms are the Wilson coefficients C_1^{NS} and C_1^{S}. For the first moments, one obtains:

$$\Gamma_1^{p(n)}(Q^2) = \frac{1}{12}C^{NS}(Q^2)\left(\pm a_3 + \frac{1}{3}a_8\right) + \frac{1}{9}C^S(Q^2)a_0 \, . \tag{82}$$

The Wilson coefficients are available in perturbative QCD up to order α_s^3 in References [45, 46]. For the non-singlet contribution a calculation in order α_s^4 exists [47]. The coefficients up to the order α_s^2 are:

$$C^S = 1 - \frac{\alpha_s}{\pi} - 1.0959\left(\frac{\alpha_s}{\pi}\right)^2 \, , \tag{83}$$

$$C^{NS} = 1 - \frac{\alpha_s}{\pi} - 3.5833\left(\frac{\alpha_s}{\pi}\right)^2 \, . \tag{84}$$

2.11.1 *Bjorken sum rule*

The Bjorken sum rule predicts the first moment of the difference of the spin-dependent structure function of the proton, g_1^p, and the neutron, g_1^n, which is also called non-singlet spin-dependent structure function, g_1^{NS}. This sum rule relies on the SU(2) or isospin symmetry, which is more fundamental than the SU(3) symmetry. Using the axial charges defined in Equations 77-79 and Equations 75 and 76, the first moment of the non-singlet structure function is related to the axial charge a_3. The first moment of the non-singlet structure function can be calculated from Equation 82:

$$\Gamma_1^{NS}(Q^2) = \int_0^1 dx \left(g_1^p(x, Q^2) - g_1^n(x, Q^2) \right) = \frac{1}{6} C^{NS}(Q^2) \left| \frac{g_A}{g_V} \right| . \tag{85}$$

This relation is called Bjorken sum rule [48]. It only depends on the axial charge $a_3 = g_A/g_V$, which is given by the ratio of the weak coupling constants from the neutron β decay.

2.11.2 *Ellis-Jaffe sum rule*

The Ellis-Jaffe sum rule predicts the size of the first moment of the proton and neutron spin-dependent structure function. These predictions are obtained using Equation 82. The axial charges a_3 and a_8 are known, whereas the singlet charge is not known from the SU(3) symmetry. It can be expressed via the axial charge a_8 and the first moment of the strange quark helicity distribution $\Delta s + \Delta \bar{s}$. This results in a modified expression for the first moments of the spin-dependent structure function:

$$\Gamma_1^{p(n)}(Q^2) = \frac{1}{12} C^{NS}(Q^2) \left(\pm a_3 + \frac{1}{3} a_8 \right) + \frac{1}{9} C^S(Q^2) \left(a_8 + 3 \left(\Delta s + \Delta \bar{s} \right) \right) . \tag{86}$$

Assuming that the contribution from strange quarks vanishes results in the Ellis-Jaffe sum rule [49]

$$\Gamma_1^{p(n)}(Q^2) = \pm \frac{1}{12} C^{NS}(Q^2) a_3 + \left(\frac{1}{36} C^{NS}(Q^2) + \frac{1}{9} C^S(Q^2) \right) a_8 . \tag{87}$$

This is not a strict sum rule due to its assumptions. Ellis and Jaffe already state in their paper that they do not expect this sum rule to be exact [49]. The sum rule is of historical interest since first measurements of the spin-dependent structure function were only available using a polarised proton target and a considerable violation was observed already by EMC [13].

2.12 DETERMINATION OF THE DECAY CONSTANTS

The baryon decay constants used up to now were obtained in a fit from AAC [50], which used the data from Reference [51]. Today, new measurements of the hyperon β decays were performed. The value for the neutron β decay has changed and in addition also the measurement of the Ξ^0 decay is available. Assuming SU(3) flavour symmetry, the decay constants are extracted in a two parameter fit to neutron and hyperon β decays. The different decays used in the two parameter fit are shown in Table 2 together with

Table 2: Inputs from Reference [18] to the two parameter fit of the baryon decay constants. The values from the fit are given in the last column.

DECAY	COMBINATION	MEASUREMENT	THIS FIT
$n \to pe^- \bar{\nu}$	$F + D$	1.2723 ± 0.0023	1.272 ± 0.011
$\Lambda \to pe^- \bar{\nu}$	$F + \frac{D}{3}$	0.718 ± 0.015	0.7338 ± 0.0083
$\Sigma^- \to ne^- \bar{\nu}$	$F - D$	-0.340 ± 0.017	-0.343 ± 0.011
$\Xi^- \to \Lambda e^- \bar{\nu}$	$F - \frac{D}{3}$	0.25 ± 0.05	0.1956 ± 0.0083
$\Xi^0 \to \Sigma^+ e^- \bar{\nu}$	$F + D$	1.22 ± 0.05	1.272 ± 0.011

their measured values. The two parameter fit to the neutron and hyperon β decays is performed by χ^2 minimisation. The parameters obtained from this fit are shown in Table 3 together with the χ^2 value of the fit and are compared to the ones from AAC. Introducing the new data to this fit results in a very small change of the decay constants below the statistical precision of the fit. Due to the more precise measurement of the neutron β decay the χ^2 value is slightly increased but still represents a good fit with a χ^2 probability of 33%. In Figure 11 the result of the two parameter fit is shown together with the constraints

Table 3: Results of the two parameter fit of the hyperon decay constants. The results are compared to the ones of a previous fit by AAC.

PARAMETER	THIS FIT	AAC
F	0.4647 ± 0.0078	0.463 ± 0.008
D	0.8073 ± 0.0079	0.804 ± 0.008
χ^2/NDF	$3.4/3 = 1.1$	0.98

from the neutron and hyperon β decays. In addition the $1\sigma, 2\sigma$ and 3σ confidence level are shown. The shape of the confidence levels shows that the fit is mainly constraint by the very precise measurement of the neutron β decay.

2.13 STRUCTURE FUNCTIONS AT LOW BJORKEN-X

The kinematic range of low Bjorken-x is interesting as a new regime. In this kinematic range, no measurements exist in the perturbative region at $Q^2 > 1 \, (\text{GeV}/c)^2$. Currently only measurements at fixed target experiments were performed, where low Bjorken-x correspond to low photon virtualities. The kinematic region of low photon virtualities is of interest since non perturbative mechanisms dominate and the transition between "soft" and "hard" processes can be studied.

In the photoproduction limit, $Q^2 \to 0$, the spin-dependent structure function should be given by a finite function of the squared invariant hadronic final state mass. In the Regge limit, which correspond to $x \to 0$ or $Q^2 \ll W^2$, the Regge model can be used. It predicts that the spin-dependent structure function is given at any fixed photon virtuality as [52]

$$g_1^i \sim \beta(Q^2) x^{-\alpha_i(0)} . \tag{88}$$
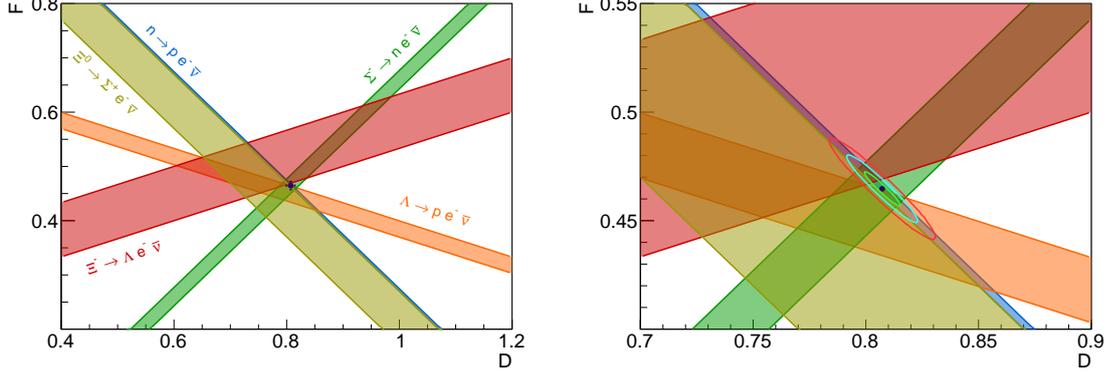
Figure 11: Left: Constraints from the various hyperon decays on the decay constants together with the result from the two parameter fit. Right: Zoom in to the result of the two parameter fit together with the $1\sigma, 2\sigma$ and 3σ confidence level.

Here, the α is different for the singlet and non singlet combinations.

At low photon virtualities, the generalised vector meson dominance model (GVDM) [53, 54] describes the spin-independent electroproduction quite well. Therefore, it is reasonable to use this model to also describe the spin-dependent case. In such models, the spin-dependent structure function has two contributions:

$$g_1(x, Q^2) = g_1^{part}(x, Q^2) + g_1^{VMD}(x, Q^2) \,. \tag{89}$$

Here, g_1^{part} is the partonic contribution, which given by the QCD improved parton model using suitable extrapolations towards low photon virtualities, and g_1^{VMD} is the contribution from the GVMD model. The term g_1^{VMD} sums up contributions from the light vector mesons with masses $M_\nu < 1\,\text{GeV}/c^2$. Its contribution is given by

$$g_1^{VMD}(x, Q^2) = \frac{M\nu}{4\pi} \sum_V \frac{M_V^4 \Delta\sigma_V(W^2)}{\gamma_V^2(Q^2 + M_V^2)^2} \,, \tag{90}$$

where γ_V^2 are determined from the leptonic width of the vector mesons and $\Delta\sigma_V$ are the spin-dependent vector-meson nucleon cross sections, which are unknown and have to be parametrised. These parametrisations depend only on one parameter. It can be estimated using the Drell-Hearn-Gerasimov-Hosoda-Yamamoto (DHGHY) sum rule [55–57], which relates the first moments of the spin-dependent structure function in the photoproduction limit to the anomalous magnetic moment of the nucleon. In such an calculation the parameter was found to be negative resulting in a negative contribution of g_1^{VMD}.

THE COMPASS EXPERIMENT

THE COMPASS EXPERIMENT AT CERN

The COMPASS (COmmon Muon and Proton Apparatus for Structure and Spectroscopy) experiment is located at the M2 beamline of the super proton synchrotron (SPS) at CERN (Conseil Européen pour la Recherche Nucléaire). It is a two-staged magnetic spectrometer with a fixed target, which can either be a polarised solid-state lithium deuteride or ammonia target, an unpolarised liquid hydrogen target or different kinds of nuclear targets. The type of target depends on the physics program. The main physics program is the study of the nucleon structure using a polarised muon beam. Due to the fixed target kinematics, it is sufficient to cover only the forward direction with detectors, which correspond to an almost 4π coverage in the centre of mass system of the scattering process for the scattered muon. The spectrometer is divided into two stages. The first stage is called large angle spectrometer (LAS) and can detect particles with low momenta and large angles, whereas the second stage is called the small angle spectrometer (SAS), which detects particles with larger momenta and smaller angles. These two stages allow for a good momentum reconstruction over a large momentum range. Each stage has its own magnet for the momentum determination and various tracking detectors. In each stage, also a hadron and electromagnetic calorimeter is present, which allows for the detection of neutral particles.

In the following sections the most important parts of the detector for this analysis are described. A complete description of the setup can be found in References [58, 59]. An isometric view of the spectrometer is shown in Figure 12.
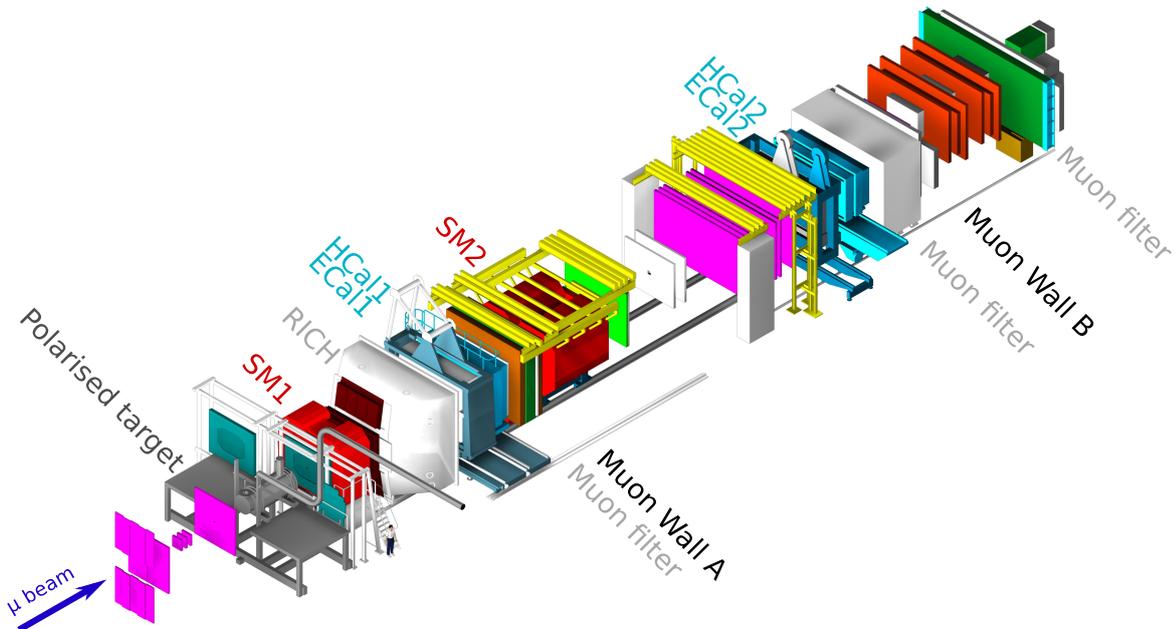
Figure 12: Isometric view of the COMPASS experiment.

3.1   THE M2 BEAMLINE AND THE POLARISED MUON BEAM

The M2 beamline [59, 60] is capable of delivering a high intensity polarised muon beam or unpolarised hadron beam to the COMPASS experiment. For calibration purposes, also a low intensity electron beam can be obtained. In the case of spin physics, the polarised positive muon beam is used. This beam is produced by extracting the 400 GeV/c proton beam from the SPS slowly over a period of 4.8 s onto the T6 production-target. Here, various target thicknesses can be chosen to obtain various intensities of the beam afterwards. The target can either be empty or beryllium with various length of up to 500 mm. A full overview of the beamline is shown in Figure 13.
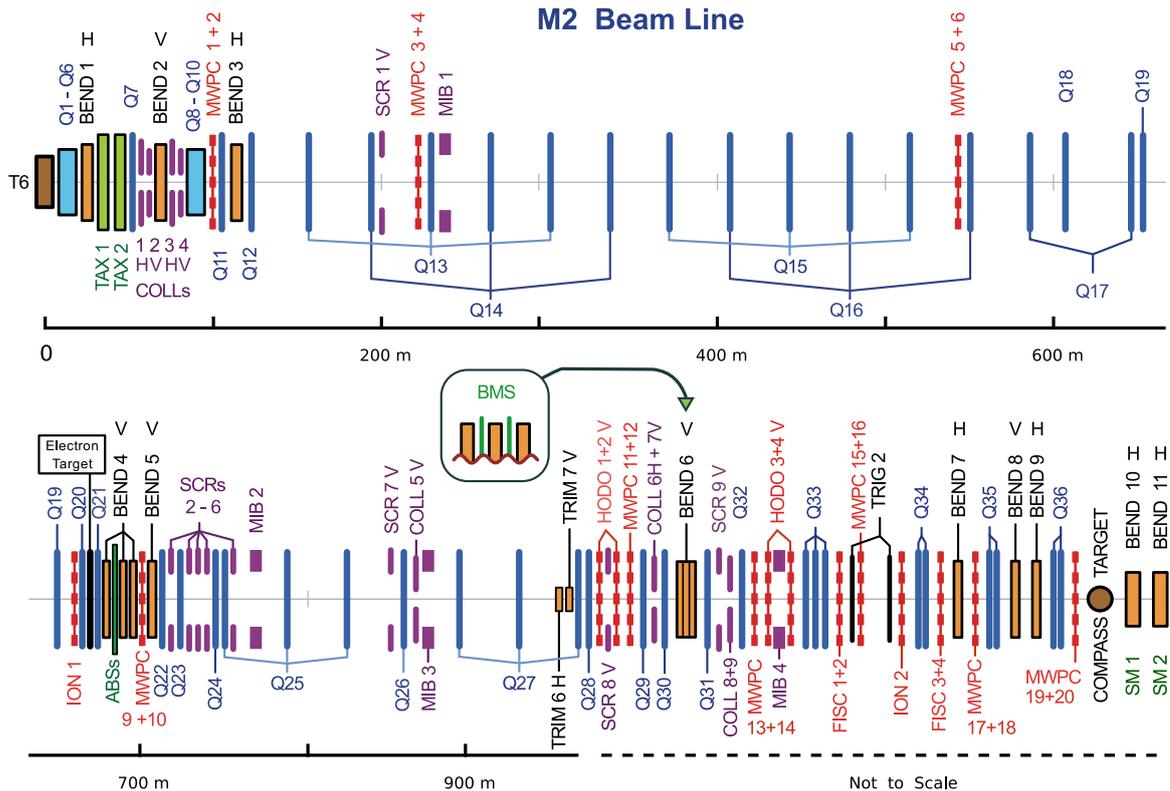
Figure 13: Overview of the CERN M2 beamline including the various magnets, absorber, scrapers and collimators. (Taken from [59]).

The beamline consists of many elements including bending magnets, quadrupole magnets, collimators, scrapers and absorbers. The bending magnets are dipole magnets, which are used to change the direction of the beam, whereas the quadrupole magnets are used to focus the beam. One quadrupole is not enough for this task as it can only focus the beam in one plane, whereas it is defocused in the perpendicular plane. With at least two quadrupole magnets, effective focusing can be obtained. The collimators in the beamline are used to define the angular and momentum acceptance. The scrapers are used to reduce the halo component of the beam and the absorbers are used for removing hadrons from the beam. The halo component consist of muons, which are, for example, not significantly deflected in the magnets.

The hadrons produced at the T6 target pass six high-gradient quadrupole magnets designed for high acceptance to collect as many produced hadrons as possible and a set of

three dipole magnets to define the momentum of the hadron beam. They are followed by a 430 m long decay section equipped with alternating focusing and defocusing quadrupole magnets (FODO). Along this path, parts of the produced pions and kaons decay into muons:

$$\pi^+ \longrightarrow \mu^+ \nu_\mu \quad \text{Branching ratio: } (99.98770 \pm 0.00004\%) \tag{91}$$

$$K^+ \longrightarrow \mu^+ \nu_\mu \quad \text{Branching ratio: } (63.56 \pm 0.11)\% . \tag{92}$$

The muons are polarised due to parity violation in these weak decays. After the decay section, a set of four bending magnets is positioned. In between those magnets, nine absorber can be placed. Each of them is a 1.1 m long block of beryllium. They are moved into the beam to remove remaining hadrons and allow only muons to pass. Afterwards, the beam enters a second FODO section with an length of 250 m in order to perform the final focusing for the experiment. The collimators in this section are used to define the momentum of the beam. At the end of the FODO section, the beam passes again a set of bending magnets to bend the beam horizontally into the experimental hall. They are surrounded by six scintillator hodoscopes. This array is called the beam momentum station (BMS) and is used to measure the momentum of each beam particle. Afterwards, the beam is focused onto the COMPASS target. The muon flux achieved per spill is about $2.5 \cdot 10^7 \, \text{s}^{-1}$. The possible muon flux, which can be achieved, is shown in Figure 14 (left) as a function of the ratio of the momentum of hadron and muon. The highest flux can be achieved at $p_\mu/p_h \approx 0.9$. In addition, the average muon polarisation is shown in Figure 14 (right) as a function of the momentum ration.
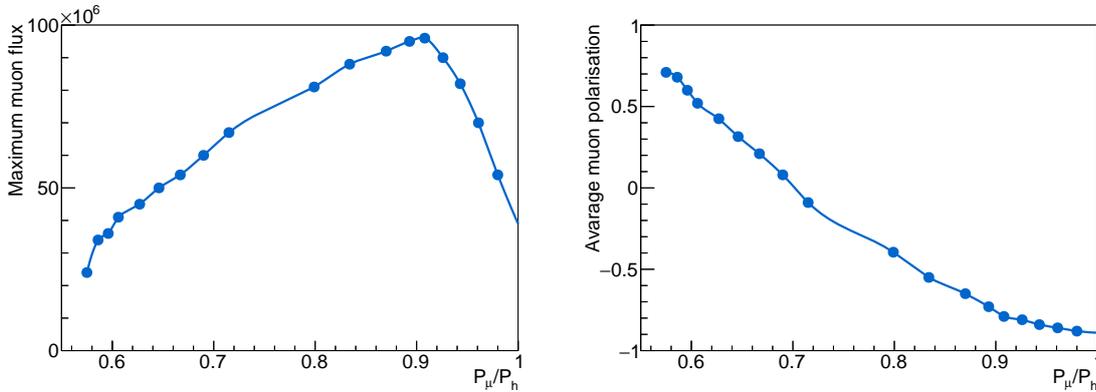
Figure 14: Left: Maximum muon flux as a function of the ratio of the momentum of the decaying hadron and the muon. Right: Average muon polarisation as a function of the ratio of the momentum of the decaying hadron and the muon. (Taken from [61])

3.1.1 *Momentum measurement*

In order to use the most of the incident muon flux, a large momentum spread of the beam of 5% is used. This spread is given by the beam optics. Due to the momentum spread, the momentum of each incoming particle is measured in the beam momentum station. A overview of the BMS is given in Figure 15. It consists of a bending magnet surrounded by six scintillator hodoscopes (BM01 - BM06), which consist of 64 elements

(BM01-BM05) or 128 elements (BM06) with different width to limit the flux per element. The beam momentum is parametrised based on the coordinates of a track passing through
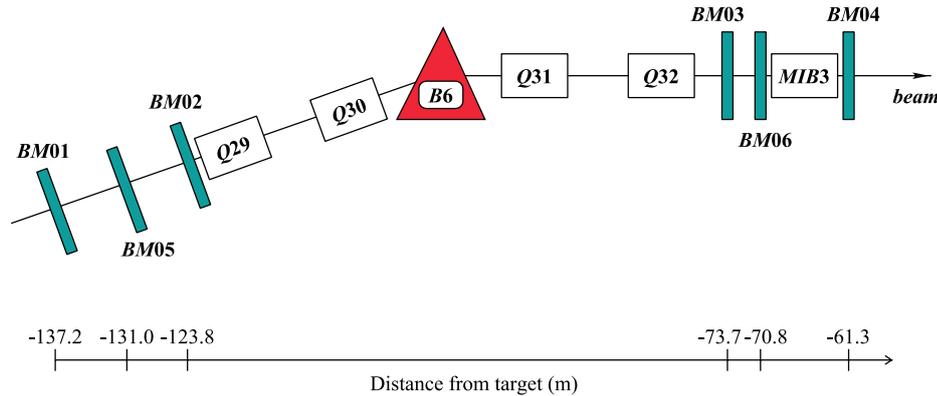
Figure 15: Overview of the beam momentum station used for the COMPASS experiment. (Taken from [59])

those detectors, which were obtained using a simulation of the full beam line. Thus the precision of the momentum measurement is $\leqslant 1\%$. The information from the BMS is used together with the information from the detectors in front of the target at the COMPASS experiment to reconstruct the incoming muon tracks during the reconstruction.

3.1.2 *Beam polarisation*

The muon beam is naturally polarised. The polarisation can be obtained in the case of a mono energetic beam from the helicity of a muon after the decay of a hadron. In the laboratory frame this corresponds to a longitudinal polarisation of the muon, given by

$$P_{\mu^\pm} \approx \mp \frac{m_h^2 + \left(1 - 2\frac{E_h}{E_\mu}\right) m_\mu^2}{m_h^2 - m_\mu^2} \; . \tag{93}$$

Here, the E_i are the energy of the decaying hadron and the muon in the laboratory frame and the m_i are their masses. The polarisation achieved from pions and kaons is shown in Figure 16 (left) as a function of the ratio of the momentum of hadron and muon. High polarisation can be obtained by selecting either $E_\mu/E_\pi = 0.57$ or $E_\mu/E_\pi = 1$. The muons from the decay of kaons are polarised in opposite direction compared to muons from the decay of pions in the case of $E_\mu/E_K = 0.57$. This results in a reduced overall muon polarisation. In the case of $E_\mu/E_K = 1$ the muons from both decay are polarised in the same direction. Therefore, a momentum ratio close to $E_\mu/E_h = 1$ is preferred. The best momentum ratio is chosen from the statistical factor of merit, which is given by the beam intensity and the squared muon polarisation. This factor is shown in Figure 16 (right). The best choice of the momentum ratio is $p_\mu/p_h = 0.9$.

3.2 POLARISED TARGET

In addition to a polarised beam also a polarised target is needed to measure longitudinal double spin asymmetries. For the polarised target not only a high polarisation is import-
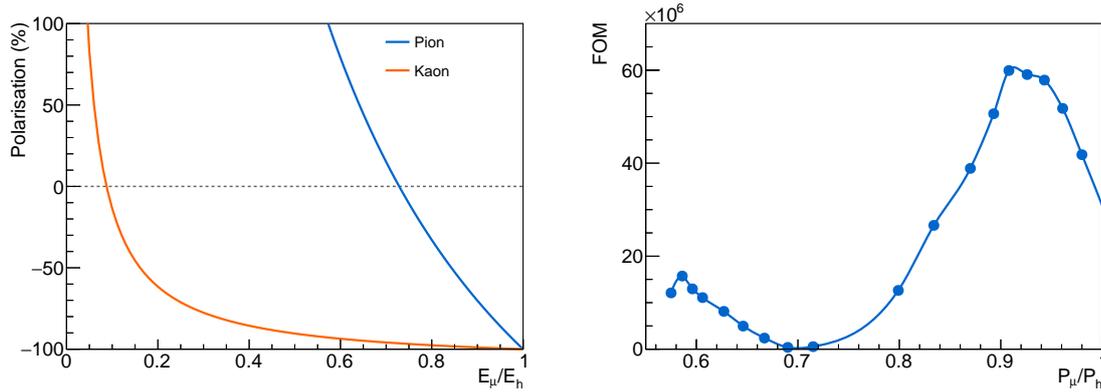
Figure 16: Left: Muon polarisation for a fixed hadron energy. Right: Statistical factor of merit given by the beam intensity and the squared muon polarisation. (Taken from [61])

ant but also a high amount of polarisable material inside the target in order to obtain high luminosities. At the COMPASS experiment a 1.2 m long solid state target is used. In order to obtain high proton and deuteron polarisations dynamic nuclear polarisation (DNP) is used. This requires a low temperature of the target material and a high magnetic field. The magnetic field is produced by a superconducting solenoid, which defines the acceptance of the spectrometer. The geometrical acceptance for the most downstream part of the target is ± 180 mrad.

3.2.1 *Target material*

Two different materials are used for the COMPASS polarised target. For measurements on polarised deuterons, isoscalar lithium deuteride (^{6}LiD) is used [62]. This material allows for a reasonable deuteron polarisation and has a good composition with a large amount of polarisable material (see Table 4), since ^{6}Li can be described as a ^{4}He (spin-0) nucleus and a deuteron [63]. In the case of measurements on polarised protons, ammonia (NH_3) is used as a target material [64]. It allows for a very high proton polarisation. But it has a smaller amount of polarisable material (see Table 4).

Table 4: Properties of the target materials.

	LITHIUM DEUTERIDE	AMMONIA
Polarisation	$> 40\%$	$> 80\%$
Fraction of polarisable material	$\sim 35\%$	$\sim 15\%$

3.2.2 *Polarisation build up*

The polarisation achieved with a magnetic field of 2.5 T for electrons at the conditions inside of the COMPASS target at temperatures of T = 50 mK is high. It is generated by the Zeeman splitting of the magnetic sublevels in a magnetic field. At these conditions, only
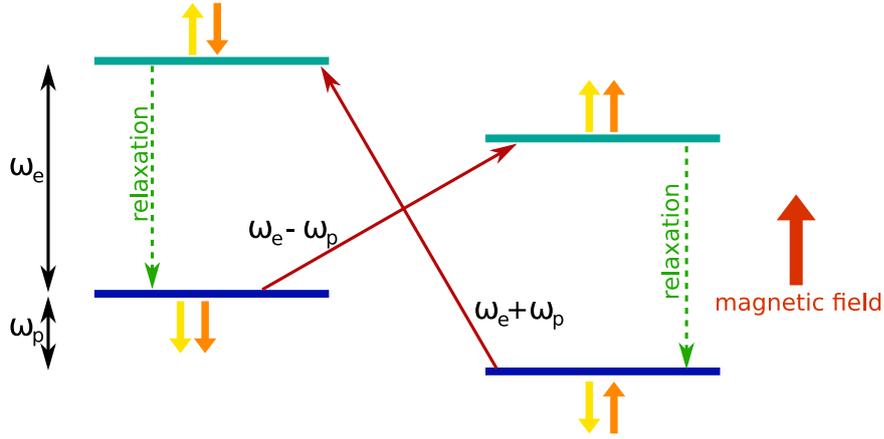
Figure 17: Illustration of the energy levels in an electron proton system. The yellow arrows indicate the direction of the electron spin and the orange ones the direction of the proton spin. Transitions between the different levels are possible using the correct frequencies.

a very small polarisation is achieved for protons or deuterons. Using the Curie law, this polarisation can be calculated for spin-1/2 particles

$$P_{1/2} = \frac{N_\uparrow - N_\downarrow}{N_\uparrow + N_\downarrow} = \tanh\left(\frac{\mu B}{2kT}\right) \tag{94}$$

and spin-1 particles

$$P_1 = \frac{N_\uparrow - N_\downarrow}{N_\uparrow + N_0 + N_\downarrow} = \frac{4\tanh\left(\frac{\mu B}{2kT}\right)}{3 + \tanh^2\left(\frac{\mu B}{2kT}\right)} \ . \tag{95}$$

Here, μ is the magnetic moment of the particle and k is the Boltzmann constant. At $B = 2.5\,T$ and $T = 50\,mK$ the polarisation for electrons is $> 99.9\%$, whereas the polarisation for protons is 5.1% and for deuterons only 1.0%. Therefore, another method is necessary to achieve a high polarisation of protons and deuterons. This method is called dynamic nuclear polarisation (DNP)[65, 66].

The DNP transfers the polarisation of the electrons to the protons. This process can be illustrated in the case of an electron proton pair in an external magnetic field as shown in Figure 17. At low temperatures, only the two lower levels are populated with the electron spin aligned with the magnetic field. Using microwaves with the correct frequency ($\omega_e + \omega_p$) the transition $|\downarrow\Uparrow\rangle \rightarrow |\uparrow\Downarrow\rangle$ is stimulated or by using the frequency ($\omega_e - \omega_p$) the transition $|\downarrow\Downarrow\rangle \rightarrow |\uparrow\Uparrow\rangle$. These transitions are followed by a relaxation of the spins. This takes place within milliseconds in the case of electrons, whereas the relaxation for the proton spin is 10^6 times slower due to the lower magnetic moment. This leads to an increase in the proton polarisation. The polarisation can be kept after the polarisation process by operating the target in the so called "frozen spin" mode, which means without further microwave irradiation. This is achieved by cooling the material down to $T \sim 50\,mK$.

In order to use the effect, paramagnetic centres are needed in the case of real materials. In ammonia these centres are produced by irradiating the material once with a particle beam and keeping the material at temperatures of liquid nitrogen afterwards. The proton polarisation is produced at these positions and transferred via spin diffusion to protons not close to the centres.

3.2.3 *Magnets*

In order to build up and keep the polarisation in the target cells, a large magnetic field is needed. It is provided by a superconducting solenoid with a magnetic field of up to 2.5 T along the beam axis with a homogeneity better than $4 \cdot 10^{-5}$. This homogeneity is achieved with sixteen additional correction coils (see Figure 19-11,12) along the target. The solenoid was designed such that the geometrical acceptance of the most upstream part of the target is ± 180 mrad. This defines the acceptance of the spectrometer. The length of the magnet is about 2.6 m with an outer diameter of about 1.2 m.

In order to perform a rotation of the polarisation in each target cell an dipole magnet is needed in addition to the solenoid. The dipole magnet used in the target produces a magnetic field of 0.6 T. The rotation of the polarisation of the target cells is performed by changing simultaneously the magnetic field of the solenoid and dipole magnet. The rotation of the polarisation direction is possible since the direction of the nucleon spin follows the direction of the external magnetic field as long as the change is performed adiabatically. The changes in the magnetic fields are shown in Figure 18 as a function of the time. Such an operation takes about 30 minutes. This is much faster compared to a repolarisation of the target cells, which takes several hours. More information can be found in Reference [67].
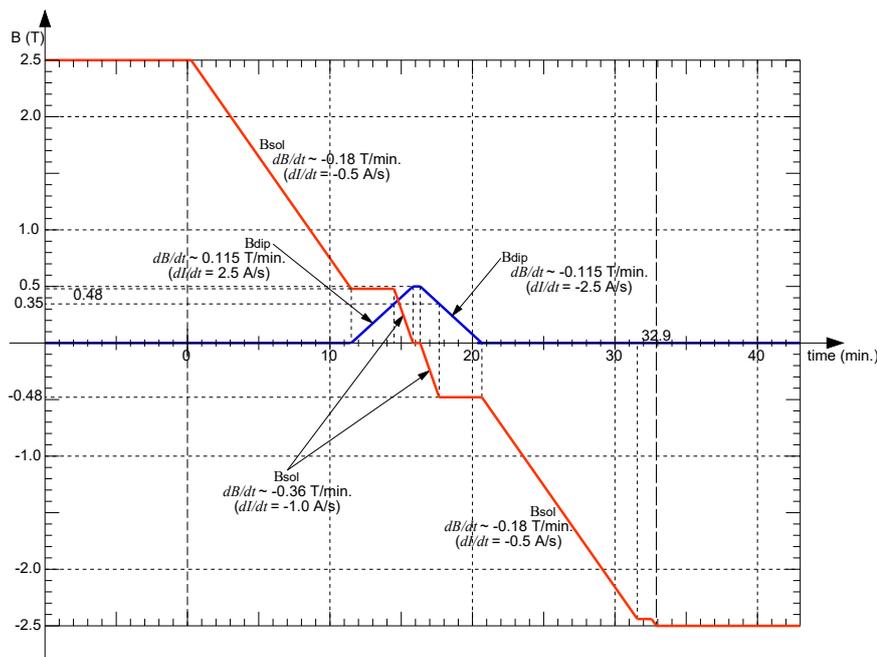
Figure 18: Changes in the magnetic fields of the target in order to perform a change of the polarisation direction. (Taken from [67])

3.2.4 *Cooling system*

In order to keep the target material at very low temperatures, the target is cooled using a ^{3}He/^{4}He dilution refrigerator. It utilises a phase transition at low temperatures to reach very low temperatures. The refrigerator is filled with liquid helium from the gas/liquid

separator (see Figure 19-8). Cold gas is used for the thermal shielding, which is kept at 4 K and 80 K. Liquid helium is used to fill the ^{4}He evaporator (see Figure 19-7), which is typically at a temperature of 1.3 K. It is also used for cooling the microwave cavity down to a temperature of 3 K. The dilution cryostat is filled with a mixture of ^{4}He and ^{3}He. The ^{3}He evaporator (see Figure 19-6) is kept at a temperature of 0.6 K, which is below 0.87 K, at which the helium mixture performs a phase transition into two phases. One is low in ^{3}He and the other rich in ^{3}He. ^{3}He is moved from the ^{3}He rich phase to the ^{3}He poor phase, thus removing energy from the system. Using this technique it is possible to cool down the target material to temperatures below 50 mK.

3.2.5 *Target cells*

A technical drawing of the target with its cooling system is shown in Figure 19. The target material is arranged in three cells (see Figure 19-1,2,3). The central cell (60 cm) is twice as long as the two outer cells (30 cm) and polarised in the opposite direction. The advantage of this three cell configuration is that the mean geometrical acceptance for the central cell is the same as for the combined outer cells. In order to improve the acceptance cancellation, the polarisation of each cell is changed regularly. This is done using the solenoid and dipole magnet as described before.

The target cells are located inside a microwave cavity, which is divided into three sections by microwave stoppers. They also separate the three target cells by 5 cm. The target cells are made of a polyamid mesh, which allows for an good heat exchange with the surrounding liquid helium. The diameter of the target cells is 4 cm. These cells are fixed inside an aramid fibre epoxy tube.

3.2.6 *Polarisation measurement*

The polarisation of the target material is measured by continuous wave nuclear magnetic resonance (NMR) [68, 69]. For this system, ten coils are mounted along the target (3 on each outer cell and 4 on the central cell). The NMR signal is obtained from a frequency sweep around the proton Larmor frequency. The area covered by the the NMR signal is proportional to the polarisation of the target. In order to convert this measurement to an absolute polarisation value, a thermal equilibrium measurement is necessary. For this measurement the NMR signal is measured at temperatures in the range of $1.0 - 1.6$ K and a magnetic field of 2.5 T without microwave irradiation. After reaching the thermal equilibrium the polarisation is given by the Curie law from Equations 94 and 95. Due to the small polarisation this measurement has to be corrected for a measurement without the target material to account for the polarisation in the surrounding material. The result for a polarisation measurement is shown in Figure 20 for the target polarisation during the polarisation build up.

3.3   SPECTROMETER

The two stages of the COMPASS spectrometer have different acceptances. The LAS section is the first stage and has an polar acceptance of ±180 mrad. Particles emitted with up to 30 mrad and a momentum larger than 5 GeV/c are detected in the SAS section.
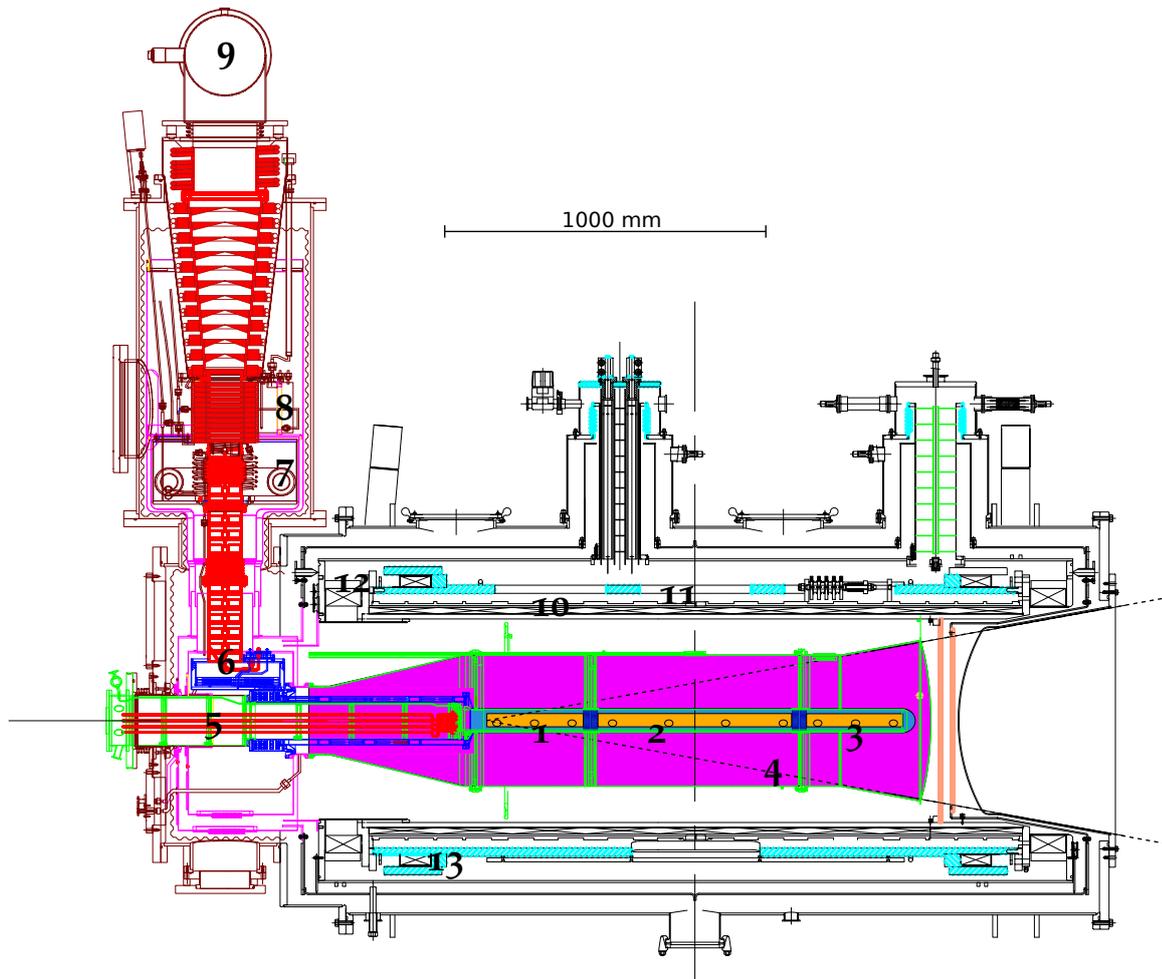
Figure 19: Technical drawing of the polarised target of the COMPASS experiment. 1-3: target cells (U, C, D), 4: microwave cavity, 5: target holder, 6-9: ^{3}He-^{4}He dilution refrigerator, 10: solenoid coil, 11 and 12: correction coils, 13: dipole coil. The muon beam enters from the left side.
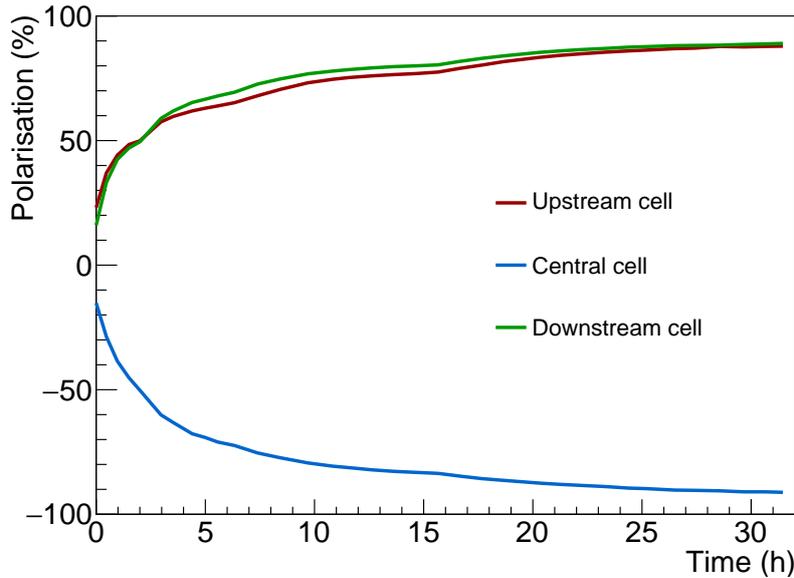
Figure 20: Build up of the polarisation of each target cells during the 2011 run. The measurement was performed on 10./11. July 2011.

The complete COMPASS setup is shown in Figure 21. In addition to the two spectrometer stages, the beam telescope is locate in front of the target to measure the incoming particles. The beam telescope also includes the BMS. The setup is described in detail in References [58, 59].

3.3.1 *Spectrometer magnets*

The COMPASS setup includes two spectrometer magnets for the momentum measurements called SM1 and SM2. The first dipole magnet, SM1, has a length of 110 cm and an integrate magnetic field of $\int Bdl = 1$ Tm bending in horizontal direction. It is used for the momentum measurement in the LAS stage. The aperture in the middle has a width of 229 cm and a height of 152 cm. This matches the opening of the target solenoid, which defines the geometrical acceptance of the LAS of 180 mrad

The second dipole magnet, SM2, has a larger integrate magnetic field than the first one so that higher momenta can be measured. It has a length of 4 m and an opening of 2×1 m^2, which is smaller than the one of SM1. The integrated magnetic field is $\int Bdl = 4.4$ Tm bending in horizontal direction. The position of both spectrometer magnets is shown in Figure 21.

3.3.2 *Tracking detectors*

In the COMPASS spectrometer many stations of tracking detectors are used for the detection of charged particles. They are distributed over the entire length of the spectrometer. In order to deal with the different requirements on the rate capability depending on the distance to the beam and the requirements on the size of the active area of the detector, various detector technologies are used. These can be separated in three different groups.
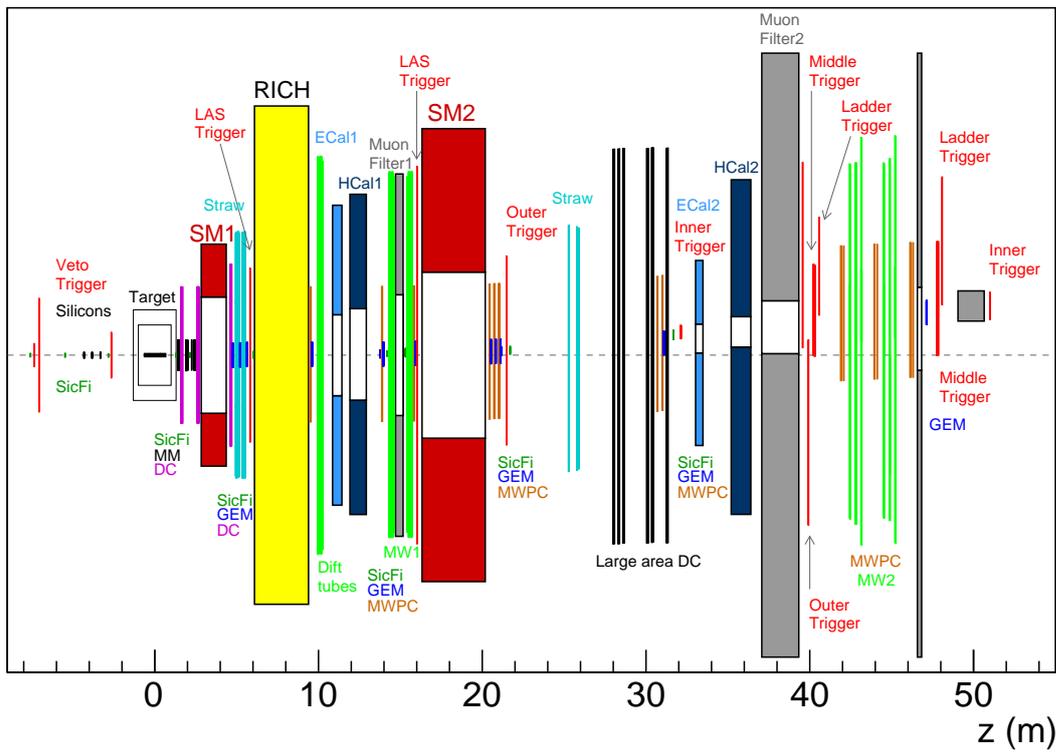
Figure 21: Setup of the COMPASS spectrometer with each detector element as it has been used in 2011. The muon beam enters from the left.

Detectors, which cover the beam region, have to withstand very high rates. Therefore, an excellent time or spatial resolution is required. Detector technologies fulfilling this requirement are silicon microstrip detectors (Si) and scintillating fibre detectors (SciFi). At smaller distances to the beam, a high rate capability together with a good spatial resolution is required. In this region micro mesh gaseous structure detector (MM) and gas electron multiplier detectors (GEM) are used. In the outer regions with an reduced particle flux, a large active region is needed. In this region, multi wire proportional chambers (MWPC), drift chambers (DC) and straw tube detectors (STRAW) are used. The position of all those detectors is shown in Figure 21.

The detector stations consist of several planes in order to measure different projections of the penetration point perpendicular to the beam axis. The term X- and Y-plane are used for detector planes measuring the horizontal and vertical coordinate. Using only two projections is not enough to determine the exact position of a track if more than one particle passes the detector. In such a case ambiguities in the possible position arise. Therefore, also inclined U- and V-planes are used. The properties of the various detectors are shortly discussed in the following sections.

3.3.2.1 *Multi wire proportional chamber*

Multiwire proportional chambers consist of several parallel anode wires in between cathode foils. The volume of the detector is filed with gas. At COMPASS a gas mixture of Ar, CO_2 and CF_4 is used. A charged particle traversing the detector will ionise the gas along its path. Due to the electric field produced by the high potential difference, the electrons will produce an avalanche of electrons, which is detected. In total 34 wire layers are used at COMPASS in 11 detectors with 1 m long wires, which have an diameter of 20 μm. The gap between the cathode foils is about 8 mm. The distance between the wires is 2 mm.

Three different kinds of MWPCs are used at COMPASS. The A-type ones consist of a X-, U- and V-plane. The U- and V-plane are inclined by $\pm 10.14°$. In addition also the A*-type is in use with an addition Y-plane. The size of these chambers is $178 \times 120 \, \text{cm}^2$ with a central dead zone of $16 - 20 \, \text{cm}$ in diameter. The B-type chambers are a little bit smaller and have a size of $178 \times 90 \, \text{cm}^2$ with a central dead zone of $22 \, \text{cm}$ in diameter. They consist of a X-plane and a U- or V-plane, which is inclined by $10.14°$. The spatial resolution of these detectors is 1.6 mm.

3.3.2.2 *Drift Chambers*

Drift chambers are a further development of MWPCs. Instead of measuring only the current, the drift time of the avalanche to the anode wires is measured, which improves the spatial resolution. The drift chambers consist of two cathodes foils together with anode and potential wires. The cathode and the potential wires are kept at $-1700 \, \text{V}$ and the anode wires are at $0 \, \text{V}$. The potential wires are used to form the electric field inside of the detector. In order to solve left-right ambiguities, two drift cells are staggered with shifted wires as illustrated in Figure 22. The detector volume is filled with an gas mixture of Ar, CF_4 and C_2H_6 or CO_2. Each drift chamber has a insensitive dead zone in the centre for the passage of the beam in order to avoid the high counting rate. One station consists of several layers of drift cells, whereby two layers are used for each projection. They are

staggered to measure all four projections. The U- and V-planes are inclined between $10°$ and $30°$. The spatial resolution of these detectors is $110\,\mu m - 170\,\mu m$.
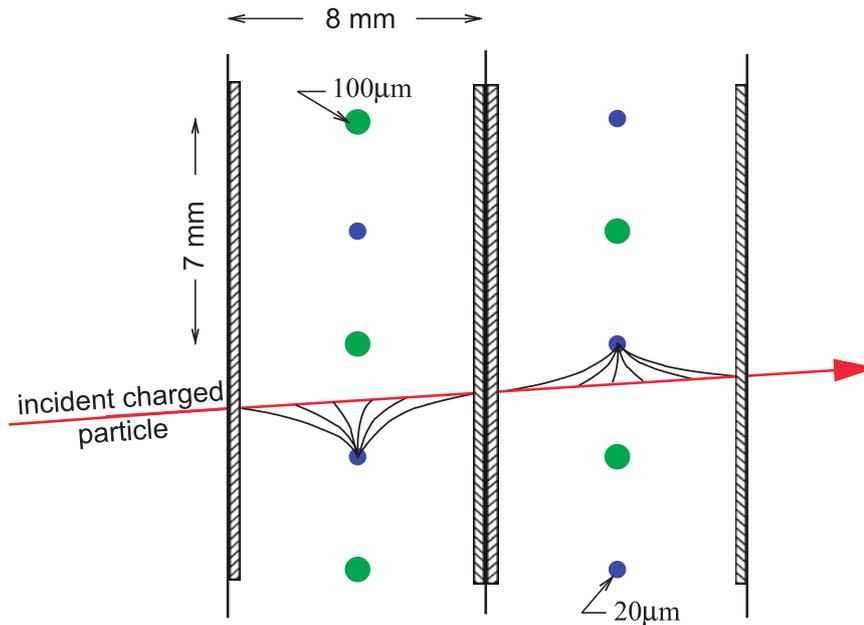
Figure 22: Drift cell geometry used at COMPASS. (Taken from [58])

3.3.2.3 *Straw tube detectors*

Straw tube detectors are very large area detectors made of straw drift tubes. Each tube is similar to a small drift cell. Several of these tubes are glued together to form a detector plane. In order to avoid left-right ambiguities, again a second layer is added. This forms one straw tube detector. A drift tube consists of a gold plated tungsten anode wire surrounded by a thin foil consisting of two layers. The inner layer is aluminised and used as cathode. The diameter of the tubes is $6.14\,mm$ for the tubes in the central part and $9.65\,mm$ in the outer part. They are filled with a gas mixture of Ar, CO_2 and CF_4. One station consists of three straw tube detectors to measure the X- and Y-projection together with a plane inclined by $10°$. The central part of the detector contains a $20 \times 20\,cm^2$ hole for the beam. The total active area of this detector is about $3.2 \times 2.8\,m^2$. Still the spatial resolution of this detector is $190\,\mu m$ at a moderate counting rate.

3.3.2.4 *Micro mesh gaseous structure detector*

The micro mesh gaseous structure (MicroMegas) detectors are another further development of the MWPCs for high rates. This is achieved by separating the detection and the amplification volumes. The principle is shown in Figure 23. The detector is filled with a gas mixture. At COMPASS a mixture of Ne, C_2H_6 and CF_4 is used. The detection volume, which is also called conversion gap, and the amplification volume are separated by a thin copper micro mesh foil. A traversing charged particle produces the primary electrons inside the detection volume. A moderate electric field of less than $1\,kV/cm$ is applied to guide the primary electrons into the amplification volume. In this part, a stronger electric field of $40\,kV/cm$ is applied. Here, the primary electrons produce an avalanche, which

produces a signal at the anode. The anode is divided into strips, which are smaller in the central region than in the outer region.

The MicroMegas used at COMPASS have an size of $40 \times 40\,cm^2$ with an central dead zone with a diameter of $5\,cm$. One station consists of two doublets of those detectors. A doublet consist of two MicroMegas with their strips perpendicular to one another forming the X- and Y-plane. The second doublet is rotated by $45°$ forming the U- and V-planes. The spatial resolution achieved with those detectors is $90\,\mu m$ with a time resolution of $9.3\,ns$.
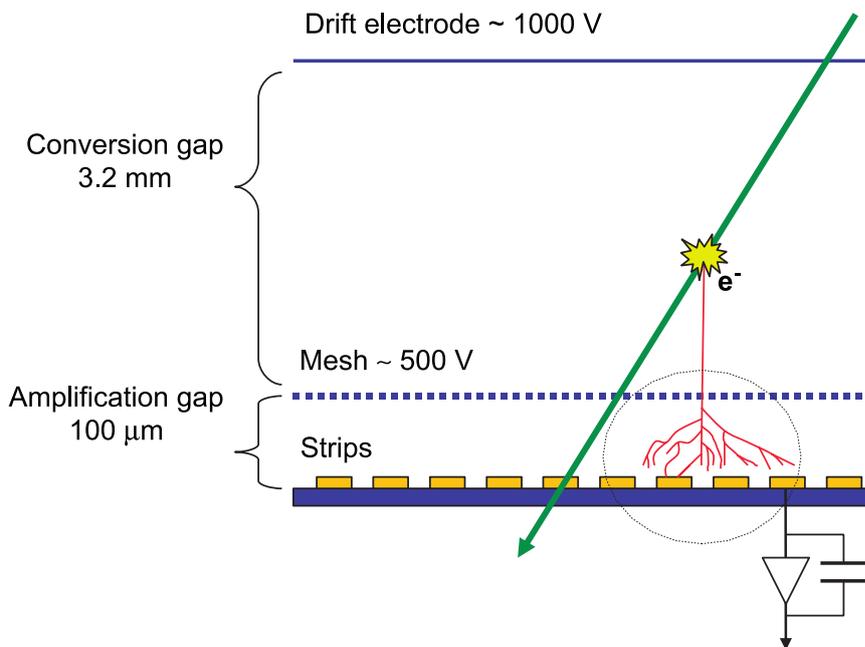
Figure 23: Illustration of the principle of a MicroMegas detector. (Taken from [58])

3.3.2.5 *Gas electron multiplier detector*

The gas electron multiplier detector (GEM) is a second type of high resolution, high rate gaseous detector used at COMPASS. In contrast to MicroMegas detectors, the amplification is not done near the strips. Instead, it is performed in steps in a thin polyimide foil of $50\,\mu m$ with a copper cladding on both sides. The setup of one GEM with three amplification stages, as it is used at COMPASS, is shown in Figure 24. The foil has a large number of micro holes. It is placed between two parallel electrodes in a gas volume, which is filled with a mixture of Ar and CO_2. By applying an electric field of a few $100\,V$ across the foil, the primary electrons passing these holes are multiplied. The electric field guides these electrons to the next amplification stage or to the detection stage, which consist of two layers of strips orthogonal to one another. The active area of this detector is $31 \times 31\,cm^2$ with a dead zone of $5\,cm$ in diameter in the centre.

Two of those detectors are mounted back to back, where the second one is inclined by $45°$. This allows to measure all four projections. These detectors have an spatial resolution of $70\,\mu m$ and a time resolution of $12\,ns$.
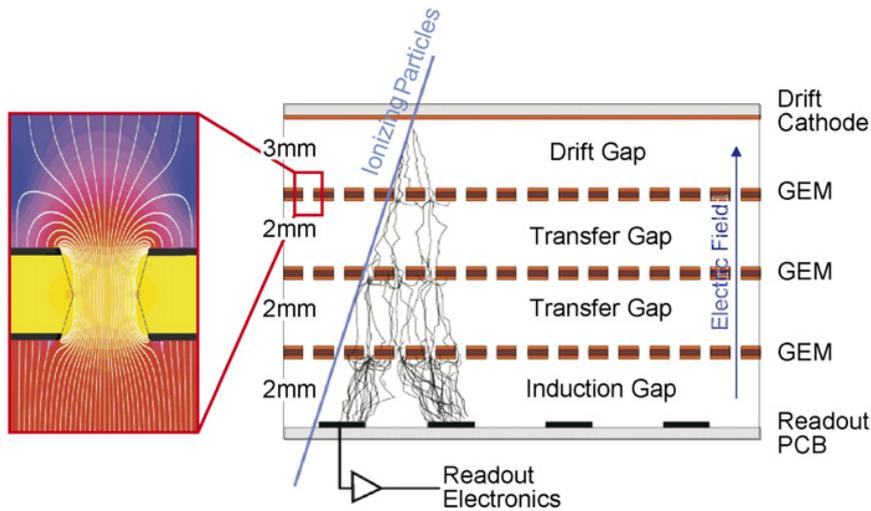
Figure 24: Illustration of the principle of a GEM detector. (Taken from [58])

3.3.2.6   *Scintillating fibre detector*

These detector consist of layers of scintillating fibres. A traversing charged particle produces scintillation light in these fibres, which is detected. The layers are staggered (see Figure 25), allowing a large enough overlap between the fibres for good detection efficiency. A column of fibres lined up in beam direction is read out by one channel of a multi-anode photomultiplier tube. In each station, at least a X- and a Y-plane is used. For some stations also a U-plane is added, which is inclined by 45°.

Here, the properties of the two SciFi stations in the beam telescope are listed as an example. In the case of those two stations, the diameter of a fibre is 0.5 mm and the active area is 4 cm^2. The ones behind the target are larger. Due to the high hit rate in the beam, the hits of incoming muons are assigned based on the time correlation as spatial correlation would result in ambiguities. The time resolution of these detectors is about 350 ps with a spatial resolution of 130 μm.
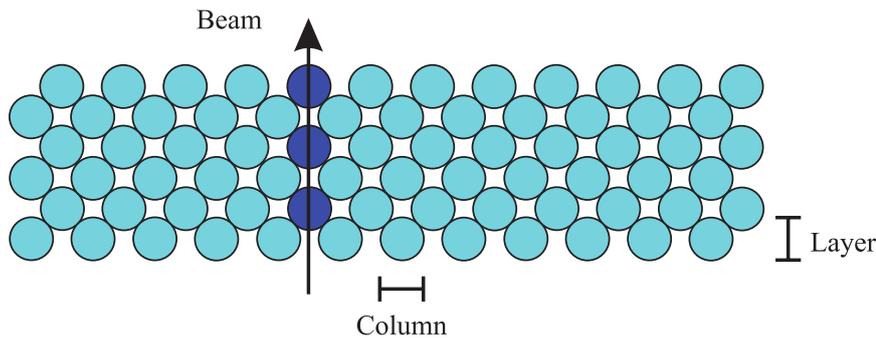
Figure 25: Illustration of the staggering of one SciFi plane. (Taken from [58])

3.3.2.7   *Silicon micro strip detector*

The silicon micro strip detectors are used to improve the spatial resolution for the reconstruction of the incoming muon in addition to the scintillating fibre detectors, which

provide an excellent time resolution. The silicon micro strip detectors were originally designed for the use at HERA [70] and optimised for high fluxes. They consist of a 300μm thick n-type wafer with an active area of $5 \times 7\,cm^2$. The signals are read out from strips on both sides. On one side 1280 strips are used and on the other side 1024 strips, which are orthogonal to the first ones. This allows to measure the X- and Y-projection using one detector. One detector station is formed by two of those detectors mounted back to back, where the second one is inclined by 5° in order to measure the U- and V-projection. This detector is operated at low temperatures around 130 K to reduce noise and to improve the time and spatial resolution. These detectors have an excellent spatial resolution of $4 - 6\,\mu m$ and a time resolution of 2.5 ns.

3.3.2.8 *Muon identification*

Muon identification at COMPASS is done using a set of tracking stations before and after an absorber. The purpose of the absorber is to absorb most of the hadrons. Therefore, only muons are detected behind the absorber. Those arrangements are located at the end of both spectrometer stages behind the calorimeter, which already absorb most hadrons.

In the first stage, the detector system is called muon wall 1 (MW1). It consists of eight planes of mini drift tubes, which are used for the particle detection. They are split in two groups consisting of four planes each. They are separated by a 60 cm thick iron absorber (MF1). Each of the two groups has two planes to measure the X-projection and two planes to measure the Y-projection. The stations and the absorber have an hole in the centre matching the acceptance of the second spectrometer stage. Mini drift tubes are similar to the straw tube tracker. They are made of a 50 μm thick gold plated tungsten wire surrounded by a 0.6 mm thick aluminium cell. One module is shown in Figure 26. Each cells is filled with a Ar and CO_2 gas mixture.
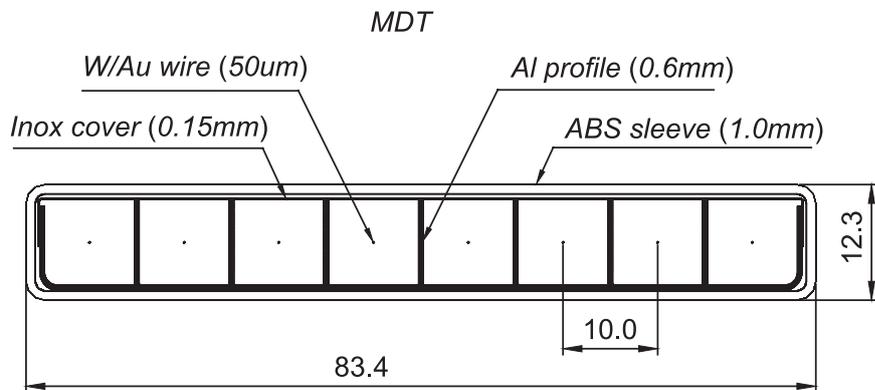
Figure 26: Illustration of one module of a mini drift tube used in MW1. (Taken from [58])

In the SAS, the muon identification is done using the tracking detectors before the 2.4 m long concrete absorber and two stations of muon wall 2 (MW2) after the absorber, together with three MWPCs. The muon wall 2 stations consists of six planes of drift tubes arranged in two X-planes, two Y-planes and two by −15° inclined planes. The drift tubes are made of stainless steal tubes with an inner diameter of 29 mm and a gold plated tungsten anode wire. The diameter of the wire is 50 μm. The tubes are filled with a Ar and CH_4 gas mixture. The stations have a rectangular hole around the beam.

Two other absorbers are present in the second spectrometer stage. These absorber are located at the end of the spectrometer in front of the trigger hodoscopes and consist of iron. The position of the absorbers and the muon wall detectors in the COMPASS setup are shown in Figure 21.

3.3.3 *Calorimeter*

In the LAS and SAS stage of the spectrometer an electromagnetic (ECal) and a hadron calorimeter (HCal) are present. They allow to measure the energy of hadrons and electrons in addition to the momentum and position measured by the other detectors. Using the calorimeter, also photons and neutrons can be detected. The electromagnetic calorimeter is always placed in front of the hadron calorimeter.

3.3.3.1 *Electromagnetic Calorimeter*

Both electromagnetic calorimeters are build out of lead glass modules. High energetic gamma rays and electrons entering these modules form an electromagnetic shower. The light produced by the shower is proportional to the amount of energy deposited in the calorimeter and is detected with photomultipliers. The length of the calorimeters correspond to more than 16 radiation length, which is enough to contain the full electromagnetic shower. The assembly of the modules of both calorimeters is shown in Figure 27. The electromagnetic calorimeter (ECal1) in the first stage is made out of 1500 modules and the one (ECal2) in the second stage out of 2972. ECal1 consist of three types of modules with different dimensions due to availability and cost. These calorimeters are calibrated at least once per year using an electron beam.
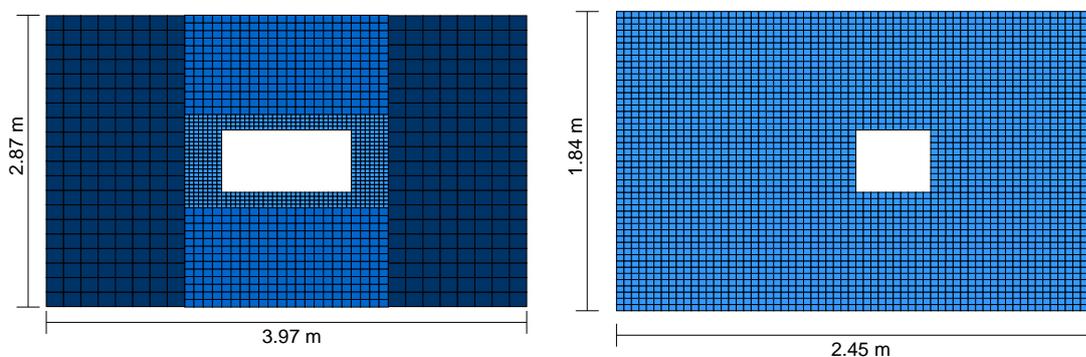
Figure 27: Assembly of the modules in both electromagnetic calorimeters. Left: ECal1. Right: ECal2.

3.3.3.2 *Hadron Calorimeter*

The hadron calorimeters are sampling calorimeter build out of several modules. Each module has a modular structure. They consist of alternating layers of iron and scintillator plates. The iron plates are used to slow down the incident particles and to create a hadron shower. The scintillator plates detect the shower. Due to the large size of hadron showers,

the modules of the hadron calorimeters are much larger in cross section than in the electromagnetic calorimeters. In the first hadron calorimeter (HCal1) 480 modules are used; in the second one (HCal2) 220 are used. The assembly of modules of both calorimeters is shown in Figure 28.
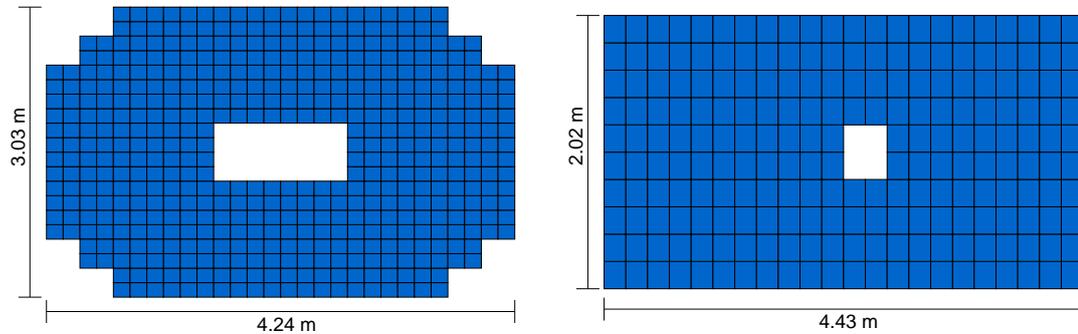
Figure 28: Assembly of the modules in both hadron calorimeters. Left: HCal1. Right: HCal2.

3.4 HADRON IDENTIFICATION

The LAS section of the COMPASS spectrometer contains a ring imaging Cherenkov detector (RICH), which is used for the identification of charged particles up to a momentum of 50 GeV/c. The detector uses the Cherenkov effect to measure the velocity of a particle. Together with the measured momentum, the mass of a particle can be determined.

3.4.1 *RICH-1 detector*

The RICH detector is illustrated in Figure 29. It is basically a large gas volume. The vessel is 5.3 m height, 6.6 m wide and has a length of 3.3 m. This size is large enough to cover the full acceptance of the LAS. A steal pipe is mounted in the central part of the vessel to separate the beam particles without interaction in the target from the active area. The volume of about $80 \, \text{m}^3$ is filled with the highly purified radiator gas C_4F_{10}. It has a reflective index of about 1.0015 and high transparency in the very ultra violet (VUV) region. Particles traversing the radiator gas can emit Cherenkov light, which is mainly ultra violet light. This light is focused via two spherical mirror systems to the photon detectors, which are located outside of the acceptance of the first spectrometer stage. Two different kinds of detectors are used for the detection of the photons. In the central region fast multi-anode photomultiplier tubes are used that are able to cope with high occupancies. In the outer region CsI-coated MWPCs behind quartz windows are used.

3.4.2 *Basic principle*

The Cherenkov effect describes the emission of light under a certain angle with respect to the direction of the particle when it travels faster than the speed of light within the
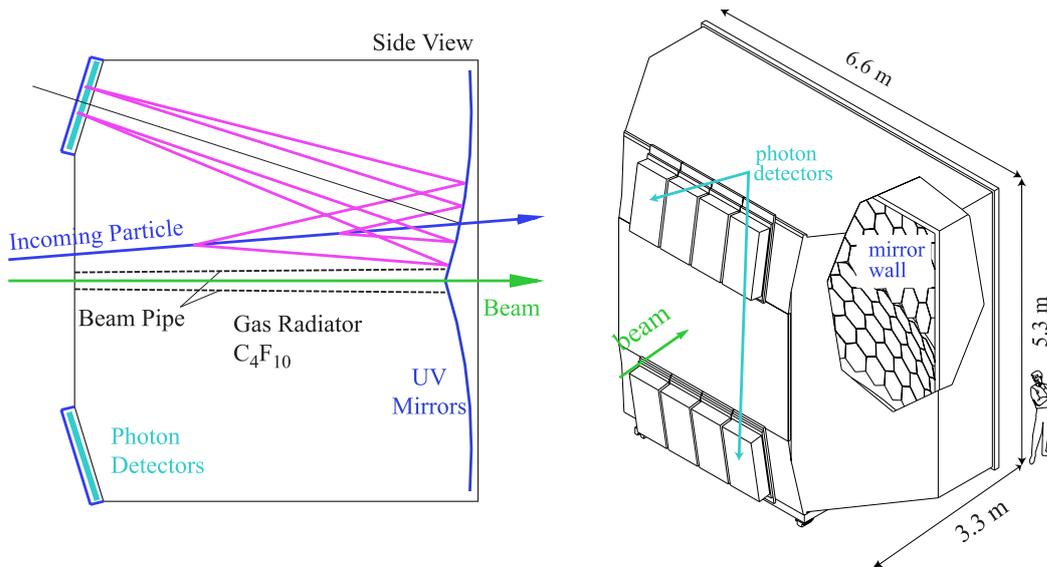
Figure 29: Layout of the COMPASS RICH detector. Left: Illustration of a particle crossing the detector and emitting Cherenkov light, which is focused on the photon detectors. Right: Dimensions of the detector. (Taken from [58])

medium. This angle only depends on the refractive index n of the material and the relative velocity β of the particle:

$$\cos\theta = \frac{1}{n\beta} \; . \tag{96}$$

Therefore, measuring the Cherenkov angle provides a measurement of the speed of a particle. This equation also explains that the Cherenkov angle saturates at about 55 mrad for all particle types at high momenta. The reconstructed Cherenkov angle is shown as a function of the momentum of a particle in Figure 30. Certain bands for electrons, muons, pions, kaons and protons are visible with a certain threshold. These depend on the mass of the particle. From Equation 96, a requirement on the relative velocity is obtained, $\beta > 1/n$. From this requirement, the threshold can be calculated. In the case of C_4F_{10}, pions can be identified starting at a momentum of 2.5 GeV/c, kaons starting at 9 GeV/c and protons starting at 17 GeV/c. The threshold for electrons is at a momentum of 9 MeV/c and for muons at 1.9 GeV/c. It is not possible to distinguish between pions and muons using the RICH, but muons can be identified by the amount of radiation length passed.

3.4.3 *Particle identification using likelihoods*

The particle identification at COMPASS is not performed by reconstructing the full Cherenkov ring (see Figure 31 left). Instead, the information from the reconstructed track is used to determine the centre of the ring. Therefore, only the radial distribution of the photons around the track projection is used (see Figure 31 right). This distribution can be described by a Gaussian distribution for the Cherenkov photons and a background contribution taking into account electronic noise of the photon detectors. Using these
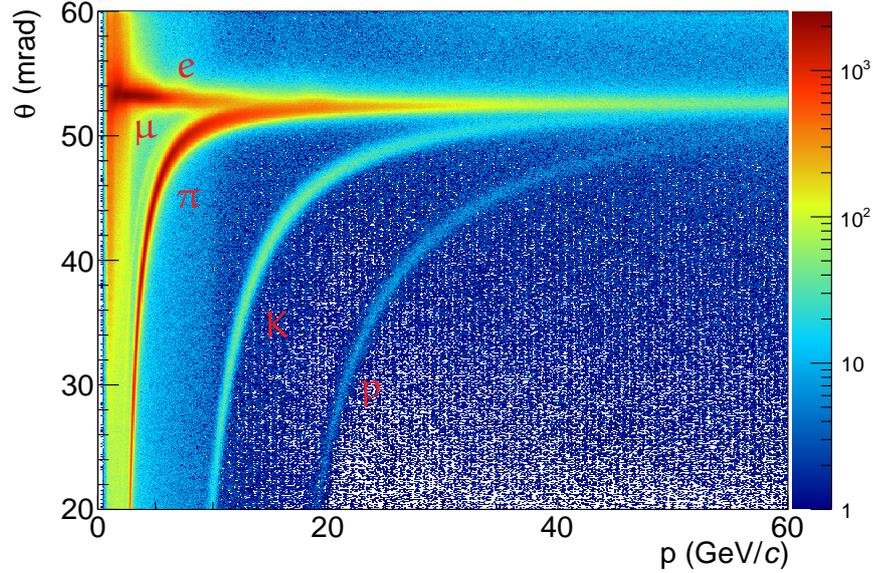
Figure 30: Reconstructed Cherenkov angle as a function of the momentum

assumption, a likelihood can be calculated for each particle taking into account different mass hypotheses:

$$L = \prod_{k=1}^{N} (1 - \epsilon) G(\theta_k, \phi_k) + \epsilon B(\theta_k) \, , \tag{97}$$

where $\epsilon = N_B / (N_S + N_B)$ is the background fraction given by the number N_S of photons in the Gaussian peak and the number N_B of photons in the background. B and G are the normalised background and signal distribution given by:

$$G(\theta_k, \phi_k) = \frac{1}{\sigma_k \sqrt{2\pi}} \exp \left(-\frac{1}{2} \left(\frac{\theta_k - \theta_{mass}}{\sigma_k} \right)^2 \right) \frac{\theta_k}{\theta_{mass}} \tag{98}$$

$$B(\theta_k) = \frac{2}{\theta_{max}} \theta_k \, . \tag{99}$$

Here, θ_{mass} is the Cherenkov angle corresponding to a particular mass, θ_{max} is the upper limit for the angular range and σ_k is the uncertainty on the angle θ, which depends on the relative velocity β and the azimuthal angle ϕ with respect to the particle trajectory. A more detailed description can be found in [71].

3.5   TRIGGER

COMPASS data is recorded event wise. This requires a trigger system to start the readout process. The trigger system is based on signals from muons. The trigger decision is made from hodoscope signals, energy depositions in the hadron calorimeter and a veto system. The trigger system consists of various hodoscopes consisting of scintillator strips. The signals from at least two hodoscopes, which are at different positions in the spectrometer
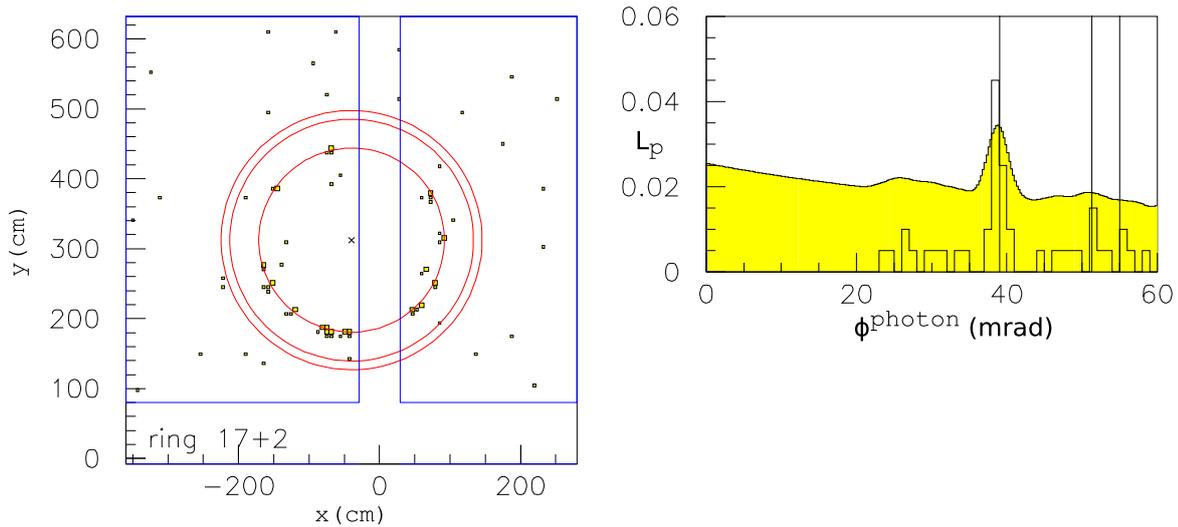
Figure 31: Left: Distribution of reconstructed photons together with the expected Cherenkov rings for pion, kaons and proton (also indicated by the black lines on the right). Right: Likelihood distribution for an identified proton. (Taken from [71])

and at least one of them is behind an absorber allowing only muons to pass, are used in a special coincidence to obtain the trigger signal. This coincidence is build as a matrix in order to create the coincidence signal for all possible combinations of the strips. The trigger system is described in References [72, 73].

In the case of the trigger based on hodoscope signals, two different methods are used: The target-pointing method and the energy-loss method. In order to cover different kinematic regions due to the variation of rates, five different trigger systems are build. These systems are called inner trigger (IT), ladder trigger (LT), middle trigger (MT), outer trigger (OT) and LAS trigger (LAST). The position of the different hodoscopes in the spectrometer are shown in Figure 32 together with the position of the hodoscopes of the veto system.
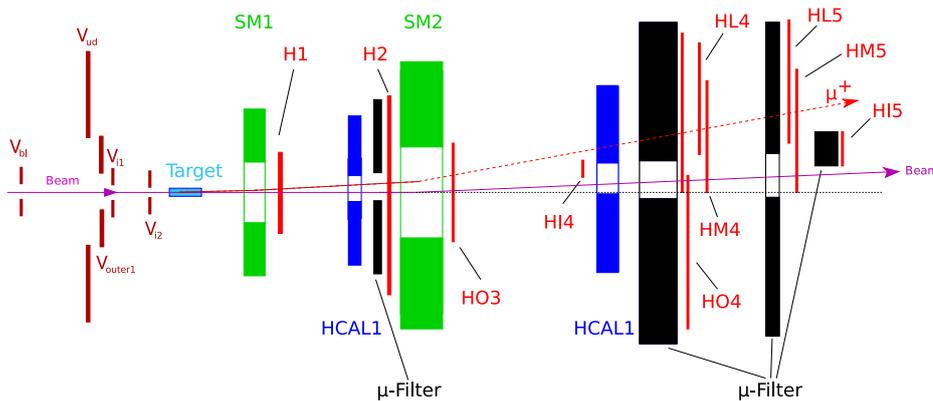
Figure 32: Overview of the relevant trigger elements in the spectrometer. (Taken from [73])

3.5.1   *Target-pointing trigger*

The target-pointing method utilises the fact that the spectrometer magnets deflect charged particles only in the horizontal plane. In the vertical plane, the angle of the muon remains the same and can be measured. This is done via pairs of hodoscope stations with horizontal strips. Only certain combinations of elements from both stations correspond to a possible interaction inside of the target, whereas other combinations, which belong for example to halo muons do not point to an interaction inside of the target. This principle is illustrated in Figure 33 for two kinds of tracks, one with interaction in the target and one passing outside the target. In order to form all possible combinations of the signals from two hodoscope planes coincidence matrices are used. The final trigger decision is formed by selecting only pixels in this matrix, which correspond to interactions inside of the target. The pixels form the diagonal of a matrix. Using the central strips, the position of the interaction cannot be determined. This results in a singularity in the matrix. This principle is used in the LAS, outer and middle trigger.
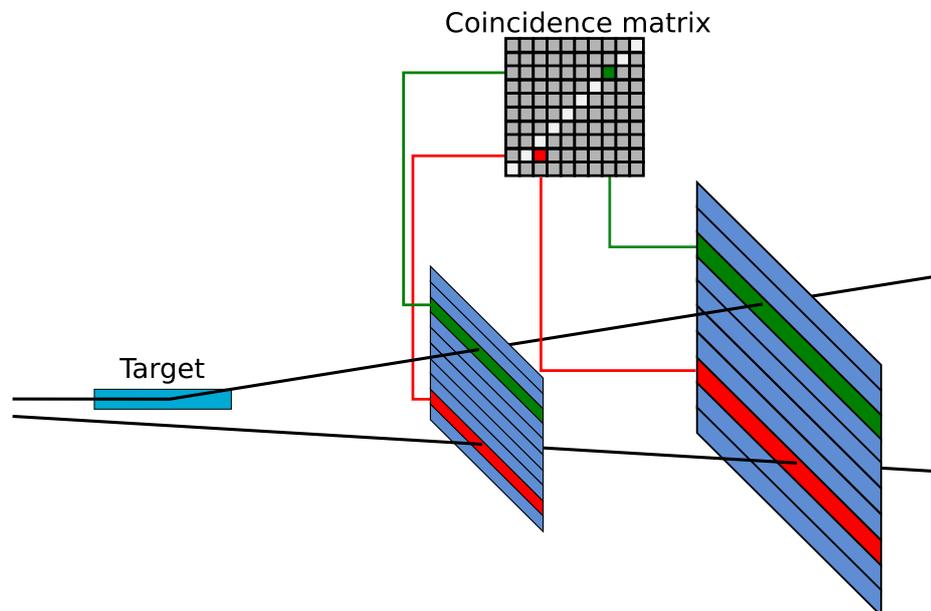
Figure 33: Illustration of the target-pointing method. A scattered muon results in a coincidence between the two strips of the hodoscopes pointing in direction of the target. A halo muon fails to produce such an coincidence.

3.5.2   *Energy-loss trigger*

The target-pointing method can only be used if the scattering angle is large enough. In order to trigger on events with small scattering angles, a different method is used. It utilises the energy loss in an interaction and a magnetic field. The loss of energy results in larger deflection in the magnetic fields compared to the case where no interaction took place. In order to trigger on the energy loss, two hodoscope stations are used, which consist of vertical strips. Again, all possible combinations from two hodoscope planes are used to form a coincidence matrix. This time, the allowed combinations form a triangular

shape due to different scattering angles at different energies. The rejected pixel correspond to an minimal amount of energy lost in the interaction. This principle is illustrated in Figure 34 for a muon with no energy loss passing the target and a muon, which lost energy due to an interaction in the target. This principle is used for the inner, middle and ladder trigger.
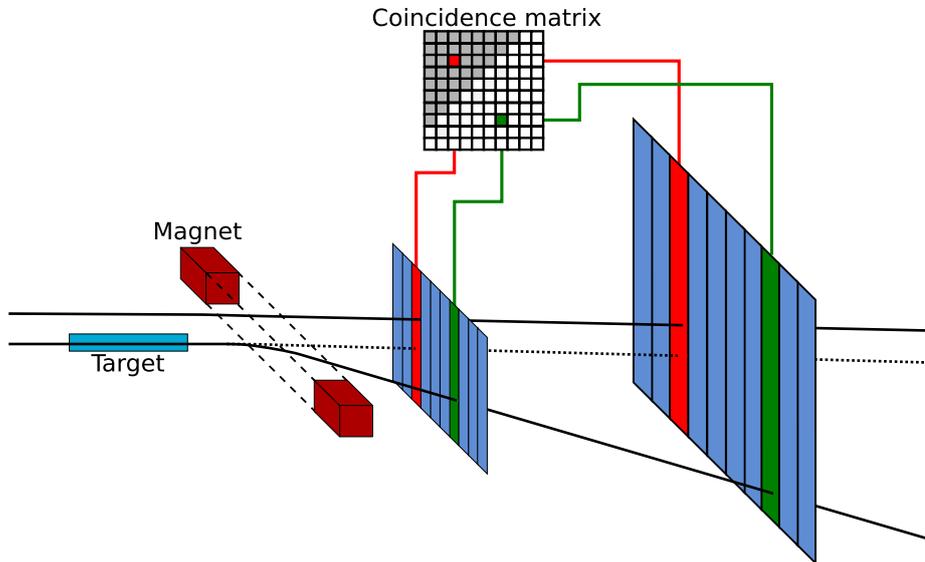
Figure 34: Illustration of the energy-loss method. A scattered muon results in a coincidence between the two strips of the hodoscopes in agreement with an interaction inside the target. A halo muon fails to produce such an coincidence.

3.5.3 *Veto system*

The muon beam used at COMPASS is surrounded by a halo component and also has a sizeable divergence. Both reflect the origin of the beam. This results in trigger signals produced by muons without interaction inside the target. They can be reduced by introducing a veto system in front of the target. The veto systems consists of five scintillator hodoscope stations with an central hole for the beam. Their position in the beamline is shown in Figure 32. They are positioned at different distances to the beam to suppress different unwanted contributions. Two large veto hodoscopes suppress halo components further away from the beam and three veto hodoscopes are build to suppress the part of the beam that does not pass the target. The final veto signal is formed by an "or" of all veto hodoscopes [74]. An illustration of the veto system is shown in Figure 35. The advantage of such an system is the reduction of wrong trigger signals. This results in a lower amount of events, which have to be treated by the data acquisition system and therefore reduce its dead time. On the other hand, a new dead time is introduced due to the time needed to produce a coincidence between the veto system and the trigger system.
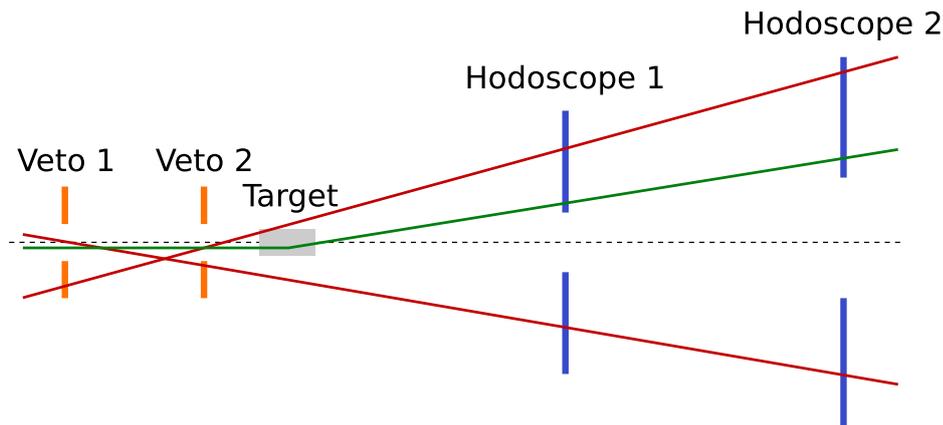
Figure 35: Illustration of the veto system. Muons passing the veto detector are rejected (red). Only incoming muons with a possible interaction in the target can produce a trigger signal (green). (Taken from [72])

3.5.4   Calorimeter trigger

The pure calorimeter trigger (CT) is the only trigger system not triggering on muons. Instead, it triggers on the energy deposition of particles inside the calorimeter (HCal1, HCal2 and ECal1). Therefore, it is used to extend the kinematic range of the trigger system towards larger photon virtualities and to trigger on events with a scattered muon outside of the acceptance of the scintillating hodoscope triggers. Additionally, it can be used for studying the efficiency of the other trigger systems. In order to distinguished between muons and hadrons, the energy threshold of the trigger is set to an energy higher than the one of a muon passing thorough the calorimeter. The muon only deposits energy corresponding to a minimal ionising particle. Typically, this threshold is larger than three times the energy deposition of such a particle. In order to trigger only on a cluster produced by hadrons 2×2 cells are summed up, which is the typical shower size in the calorimeter.

For the calorimeter trigger (CT), a high threshold, which suppresses 90% of clusters produced by single muons, is used. In parallel also a lower threshold is used. This signal is used in coincidence with the signals from a hodoscope trigger to form a "semi-inclusive" trigger. This is used for the inner, ladder and LAS trigger.

3.5.5   Summary

The various trigger systems used in the COMPASS experiment are located at different positions in the spectrometer. At least one hodoscope of each trigger system is located behind an absorber, which provides the muon identification. Based on their distance to the beam, they cover different kinematic regions. An overview of the kinematic region covered by the various hodoscope based trigger is shown in Figure 36 as a function of the photon virtuality and the relative virtual photon energy.

The properties of the various hodoscope based trigger systems is summarised in Table 5. Here, the middle trigger has a unique property compared to the other triggers used for physics data. It is used as an "inclusive" and "semi-inclusive" trigger and makes use of both triggering methods.
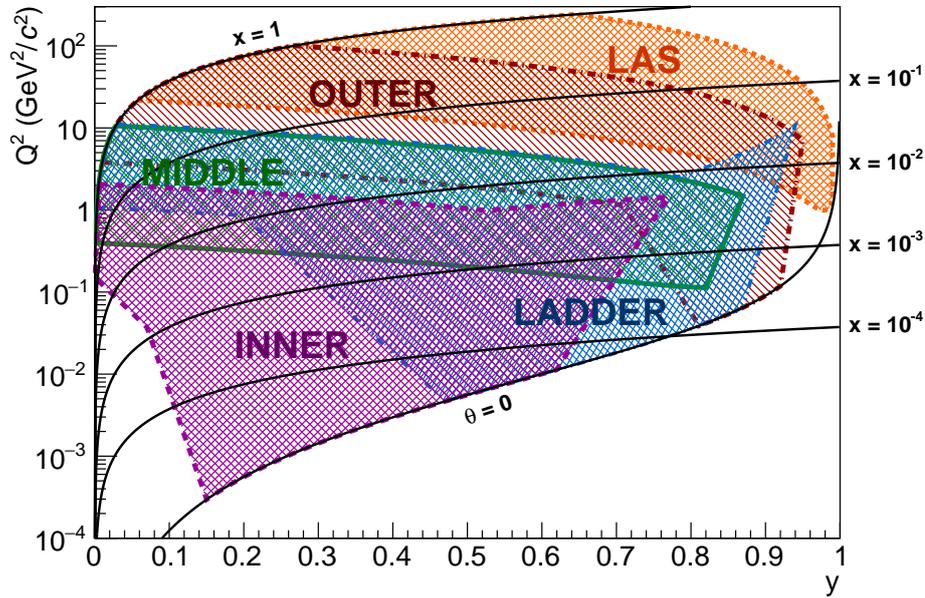
Figure 36: Kinematic coverage of the different trigger systems as a function of the photon virtuality and the relative photon energy. The coverage is shown for the muon beam with a nominal momentum of 200 GeV/c.

Table 5: Overview of the different Hodoscope trigger.

TRIGGER	PRINCIPLE	TYPE
Inner (IT)	energy loss	"semi-inclusive"
Middle (iMT/MT)	energy loss, target pointing	"inclusive" and "semi-inclusive"
Ladder (LT) (before 2010)	energy loss	"semi-inclusive"
Ladder (LT) (since 2010)	energy loss	"inclusive"
Outer (OT)	target pointing	"inclusive"
LAS (LAST) (2011)	target pointing	"semi-inclusive"

3.6   DATA ACQUISITION AND RECONSTRUCTION

The data recording is managed by the data acquisition system (DAQ) on an event-by-event basis. Each event corresponds to at least one trigger signal. The DAQ is able to handle high trigger rates as well as a large data flow. The recorded data from each detector is reconstructed offline in order to extract tracks, vertices and physics quantities.

3.6.1   *Data acquisition*

The structure of the COMPASS data acquisition system is shown in Figure 37. It is controlled by the trigger control system (TCS). The detector data is collected using time to digital converter (TDC) and sampling analogue to digital converter (SADC). Their data are transferred to the concentrator modules, which are either CATCH (COMPASS accumulate, transfer and control hardware) [75] mainly used for TDC information or GeSiCa (GEM and silicon control and acquisition module) for SADC information. They collect and merge the detector data before sending them to the readout buffer computers (ROB). These computers are equipped with so called spill buffer cards, which collect the data from the connected concentrator modules and store them on SDRAM cards during the spill before being saved on the PC. The readout buffer computers are connected to all event builder computers (EB). Their task is the creation of events using all available data from the readout buffers. The data is split into files of 1 GB each. These files are stored on the event builders before being transferred to the CERN computer centre for storage on a tape system [76]. The event builders also run an online filter, which is used for data filtering and quality monitoring.

3.6.2   *Event reconstruction*

The reconstruction of events is done using a software called CORAL[1] (COMPASS reconstruction and analysis). It uses in addition to the raw data from the detectors (or inputs from Monte Carlo simulations) files containing the position and calibration parameters of all detectors, as well as maps of the magnetic fields and material maps. The information is used for track, momentum and vertex reconstruction as well as particle identification and calorimeter cluster reconstruction. The output of the reconstruction is stored into a tree like structure based on ROOT [77] and is called mini data summary tapes (mDST). These files are used for further physics analysis using PHAST[2] (physics analysis software tool), which can access the mDST files and includes tools for filtering and processing the data. It is also capable of creating mDST files.

3.6.2.1   *Track reconstruction*

The track reconstruction is done in three steps, which are described in Reference [58]. In the first step, pattern recognition is used to find clusters consistent with track segments. This is done by dividing the spectrometer into different zones, in which tracks are expected to be straight lines. The zones are separated by the spectrometer magnets, the target

---

1 https://twiki.cern.ch/twiki/bin/viewauth/Compass/DataReconstruction/CoralSoftware
2 http://ges.home.cern.ch/ges/phast/index.html
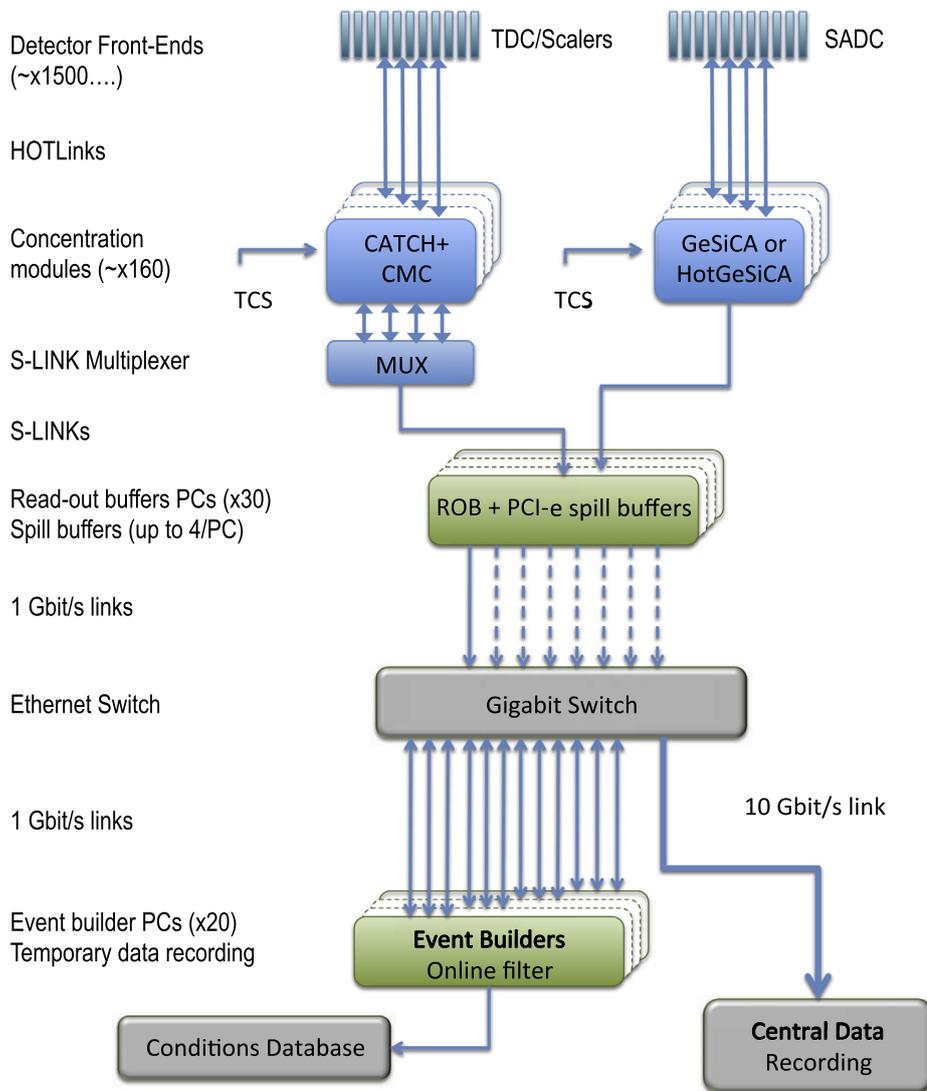
Figure 37: Layout of the data acquisition system used at COMPASS with the different steps of handling the detector information. (Taken from [59])

and the second muon filter. A reconstructed event is shown in Figure 38 together with the different zones. The track finding procedure is done starting with projections using the detectors sensitive to this direction. For each combination of possible tracks, a path with a width is build. The width is given by the detector resolution. The path is used to find further hits along a possible track. Afterwards, the information from all projections are combined to determine the tracks in the three dimensional space. These tracks are compared to entries in a dictionary of possible tracks to speed up the fitting procedure.

In a second step, the full tracks are build. First, a straight line fit is performed in each zone. Afterwards adjacent zones for straight tracks are connected by bridging. The combination of track segments is done based on the best χ^2 for a pair of segments. Combinations with a bad χ^2 or ones containing segments already used for an accepted combination are rejected.

In the last step, the magnetic field and material maps are used to estimate the best parameters of a track. This is done using a Kalman fit method [78, 79], twice. One iteration starting at the first measured position and one starting at the last measured position.
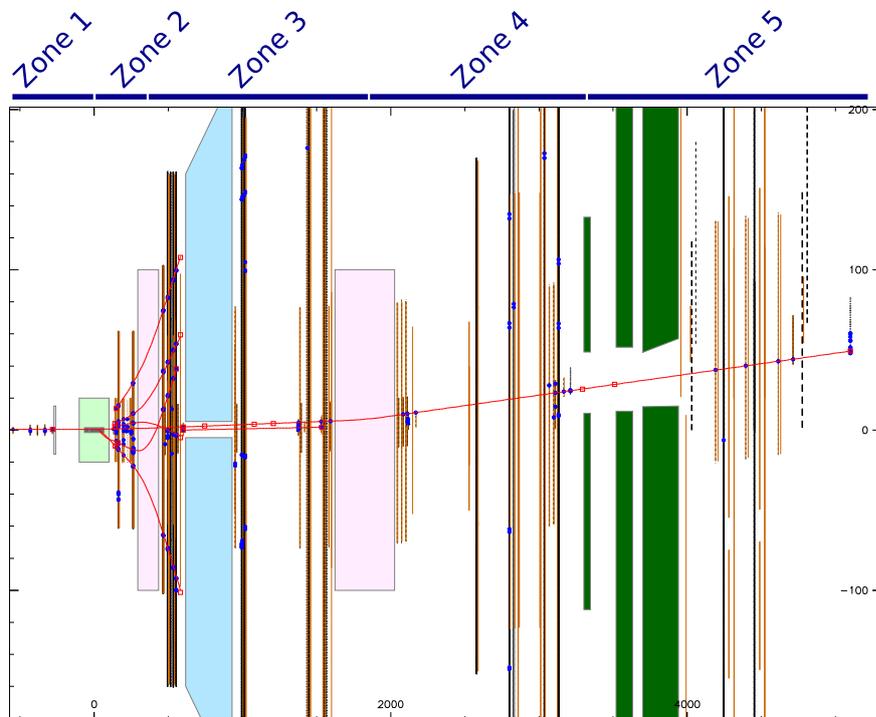
Figure 38: One event reconstructed by CORAL. The blue points correspond to hits in the detectors and the red lines are the reconstructed tracks. The different zones used for the straight line fits are indicated on top.

3.6.2.2 *Vertex reconstruction*

During the event reconstruction two kinds of vertices are determined. Primary vertices have a incoming particle (muon) and one or more outgoing tracks connected to it. The distribution of reconstructed primary vertices is shown in Figure 39. The secondary vertices only take into account possible decays of neutral particles into two oppositely charged

particles. Therefore, secondary vertices have only two outgoing particles and no incoming one.

The reconstruction of primary vertices starts by finding the point of closes approach between the incoming track and tracks found in the spectrometer. Tracks, which are too far away from this point, are rejected. The selected tracks are used in an inverse Kalman fit to calculate the χ^2 contribution for each track. Tracks with too large contributions are removed and the fit is repeated. A recovery algorithm is implemented for the case that this procedure fails. As an event can contain more than one incoming beam track, more than one possible primary vertex can be found.

The secondary vertices are reconstructed by combining all pairs of tracks with opposite charge and searching for a possible decay position. This is done using again Kalman filter techniques to find positions of close approach. Tracks can be connected to several secondary vertices and also to a primary one.
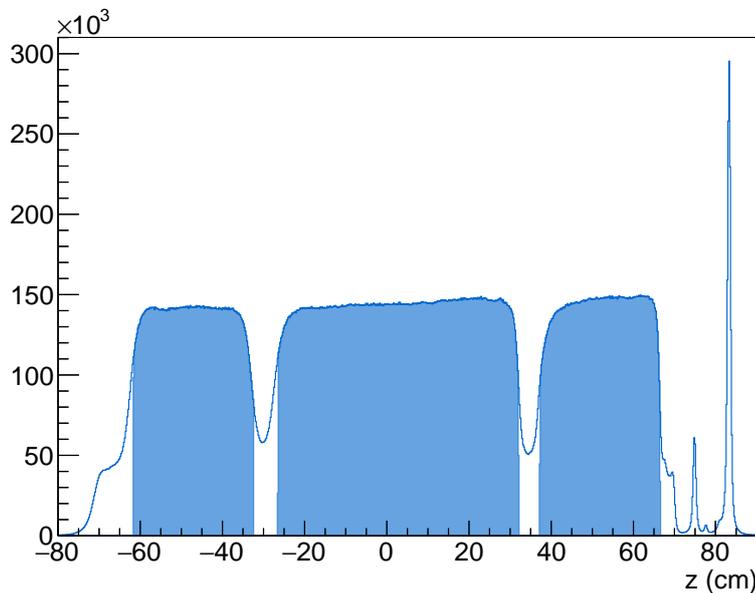
Figure 39: Distribution of primary vertices along the Z-axis for events with $Q^2 > 1\,(\mathrm{GeV/c})^2$. The blue area correspond to one of the three target cells.

3.7 DETERMINATION OF THE RICH PARTICLE IDENTIFICATION EFFICIENCY

In this section, the method and results of the evaluation of the RICH performance for the 2011 data taking are presented. The identification and misidentification probabilities are evaluated for pions, kaons and protons as a function of the entrance angle θ of the particle into the RICH and its momentum. The same method was used before in the determination of the RICH efficiency for the 2006 data taking as described in Reference [80].

In previous analysis on the RICH particle identification efficiency, "exclusive" ϕ mesons were used. These are ϕ meson produced in an exclusive reaction. Therefore, only three particles are detected in the spectrometer. These are the scattered muon and the two kaons from the decay of the ϕ meson. Such events do not represent typical events at COMPASS from deep inelastic scattering where also more than three particles are detected. Therefore,

so called "inclusive" φ mesons are used for the analysis. These are φ mesons produced in deep inelastic scattering. Such events contain not only the scattered muon and the decay kaons from the φ meson but might also contain additional particles.

3.7.1   *Data selection*

For the determination of the RICH efficiency, it is necessary to have a source of events where the true kind of the particle passing the RICH is known. That kind of events is obtained using two body particle decays, namely the decay of a K^0 into two pions $(K^0 \to \pi^+\pi^-)$, the φ decay into two kaons $(\phi \to K^+K^-)$ and the Λ decay into a pion and a proton $(\Lambda \to p\pi^-)$. In order to select events, which represent events used in later analysis, deep inelastic scattering events with a scattered muon are selected. Therefore, the typical cuts are applied to the data:

1. Exclude bad spills

2. Select best primary vertex with incoming and scattered muon [3]

3. Check if primary vertex is inside one of the target cells (PaAlgo::InTarget)

4. Extrapolated track of the incoming muon should cross all target cells (PaAlgo::CrossCells)

5. $0.1 \leqslant y \leqslant 0.9$

Different selection criteria have to be used for K^0, Λ and φ decays. In the case of K^0 mesons and Λ baryons, the particles have to decay by the weak force. Therefore, the decay length is long enough to produce a secondary vertex, which can be separated from the primary one. The φ mesons has to decay by the strong force. This results in a very short decay length and it is not possible to separate the secondary vertex from the primary one.

3.7.1.1 K^0 *and* Λ *selection*

For K^0 meson the decay into π^+ and π^- with a branching ration of $(69.20 \pm 0.05)\%$ [18] and in the case of Λ and $\bar{\Lambda}$ baryons the decay into a proton and a pion with an branching ration of $(63.9 \pm 0.5)\%$ [18] is selected. In both decays the reconstruction of the secondary vertex is possible. The following cuts are applied to select these decays:

1. Selection of good secondary vertex
   - Loop over all vertices
   - Vertex is not a primary one
   - Exactly two oppositely charged outgoing particles
   - The tracks should not be connected to any other primary vertex
   - Primary and secondary vertex separated by more than 2σ

2. Select good hadron tracks
   - Both particles should not have crossed more than 10 radiation length

---

3 Phast.7.136

- Last measured position (Z_{Last}) behind SM1
- Transverse momentum with respect to the mother particle larger than $23\,\text{MeV}$ to suppress electrons
- Check that the decaying particle is connected to the primary vertex ($\theta \leqslant 0.01$)

3. Additional cuts

- $p_h > 1\,\text{GeV/c}$
- Mass difference smaller than $150\,\text{MeV/c}^2$ between the K^0/Λ mass and the invariant mass of the two decay hadrons assuming the correct masses

The same cuts except for the mass cuts are used for K^0 and Λ candidates. For the selected candidates, the RICH likelihoods of the two decay particles are stored for further analysis. During the first selection step, good secondary vertices are selected with only two outgoing tracks. In order to ensure that the two tracks belong to this secondary vertex, the vertex is skipped if a track is assumed to originate from a primary vertex. In addition, the primary and secondary vertex should be separated from one another. Therefore, the distance between both should be larger than two times the reconstruction accuracy.
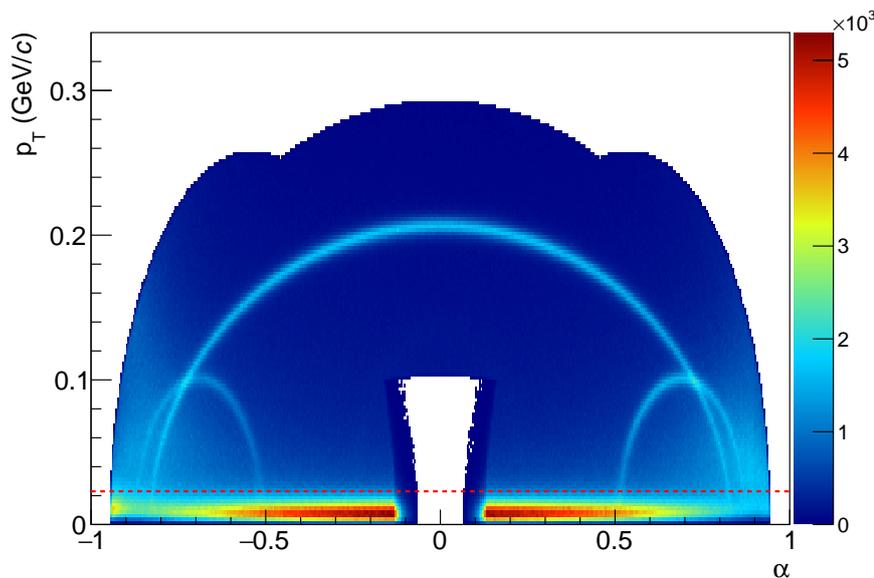
Figure 40: Armenteros plot showing the effect of the cut on the transverse momentum, which is illustrated by a red line.

During the second selection step, good hadron tracks are selected. In order to suppress tracks from muon, tracks which have passed a large amount of material are rejected. In addition, only tracks with a measured momentum are selected. This is ensured by a last measured position behind the first spectrometer Magnet. In addition, it is ensured that the K^0 meson or Λ baryon is produced in the primary vertex by comparing the angle θ between their momentum vector and the vector connecting the primary and secondary vertex. Tracks from electrons are suppressed by removing particles with low transverse momenta with respect to the mother particle. This is shown in Figure 40. Here, the

transverse momentum of a particle is shown as a function of the ratio of the longitudinal momentum ratio of two particles:

$$\alpha = \frac{p_{L,1} - p_{L,2}}{p_{L,1} + p_{L,2}} \ . \tag{100}$$

The three visible arcs are produced by the decay of the K^0 mesons and the Λ baryons. The decay of K^0 mesons in two particles with the same mass results in the symmetric arc, whereas the decay of Λ baryons into two particles with different masses result in the two smaller arcs on the left and right side. The band at the bottom is produced by electrons from pair production. These are removed by the cut on the transverse momentum. This is also shown in Figure 41 for the transverse momentum of the particles from possible decays of K^0 mesons or Λ baryons.
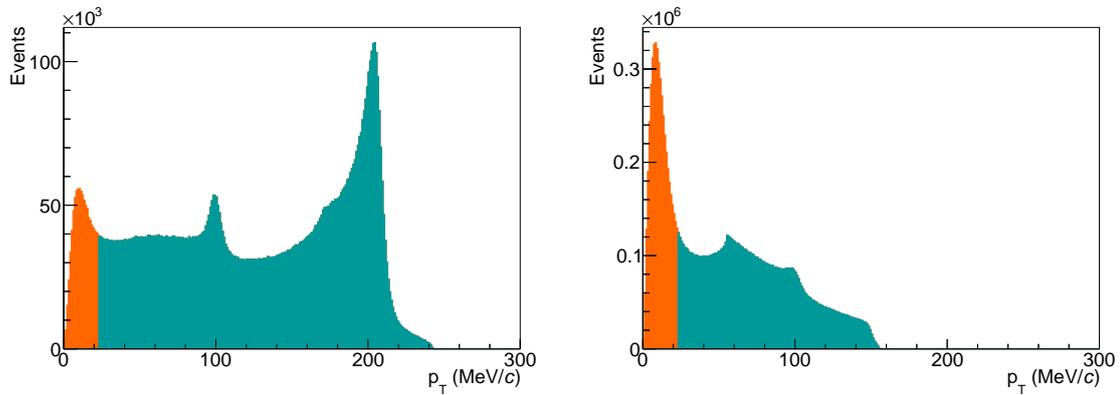
Figure 41: Distribution of the transverse momentum for K^0 (left) and Λ (right) candidates. The orange area corresponds to the removed events.

During the third selection step, events, which will not be used in the later analysis, are removed. Therefore, a minimal momentum of the particle is required and only a mass range of $150\,\mathrm{MeV}/c^2$ around the K^0 or Λ mass is selected.

The effect of the cuts on the invariant mass of the K^0 and Λ candidates is shown in Figure 42 in the range of their mass. The strongest reduction is achieved by requiring the production of the K^0 meson or Λ baryons at the primary vertex. In addition, also the effect of the Likelihood cuts for the particle identification, which are applied later one, is shown.

3.7.1.2 φ selection

The φ meson decay length is too short to separate the primary and decay vertex. Therefore, all outgoing particles from a primary vertex are taken into account for the search of possible φ mesons. The branching ratio of the decay into two kaons is $(48.9 \pm 0.5\%)$ [18].

1. Select possible event with φ mesons
   - At least 3 outgoing particles (includes scattered muon)
   - Loop over all outgoing particles
   - Oppositely charged pairs of hadrons (none is a muon)
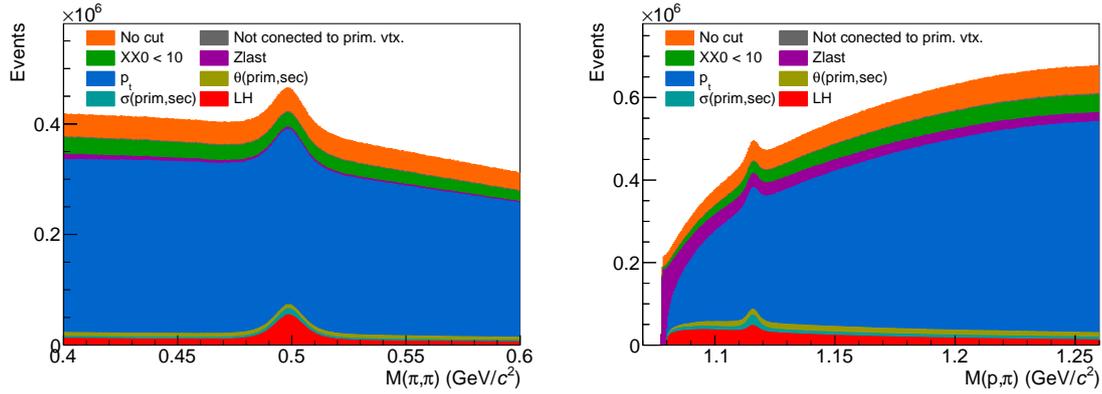
Figure 42: Invariant mass for K^0 (left) and Λ (right) candidates after the application of various cuts.

2. Select good hadron tracks

   - Last measured position behind SM1

   - Transverse momentum with respect to the mother particle larger than $23\,\mathrm{MeV}$ to suppress electrons

3. Additional cuts

   - $9\,\mathrm{GeV}/c < p < 55\,\mathrm{GeV}/c$

   - Mass difference between ϕ mass and the invariant mass of the two hadrons smaller than $120\,\mathrm{MeV}/c^2$ assuming the kaon mass

The selection steps are similar the the selection of the K^0/Λ candidates. In the first step, primary vertices with oppositely charged hadron pairs are selected. During the second selection step, only particles with a measured momentum are kept and possible electrons are removed by removing particles with a too low transverse momentum. During the third step additional cuts are applied to remove events, which will not be used in the later analysis. The effect of the various cuts is shown in Figure 43. The selection of ϕ meson candidates results in a large combinatorial background. During the selection the largest suppression is achieved by the removal of electrons. By also applying the Likelihood cuts to identify the kaons a large suppression can be achieved.

3.7.2 *RICH particle identification*

The goal of the selection is a clean pion and kaon sample. Due to the larger amount of pions compared to kaons stricter selection cuts are imposed for kaons. The identification of these particles is done using likelihood cuts. The calculation of those is described in Section 3.4. Using the likelihood values, the particle identification is done by comparing these values with one another. In the simplest case, the highest one determines the particle type. This method is used in the case of pions. In the case of kaons, stricter likelihood cuts are applied to suppress misidentified pions. These stricter cuts are an improvement compared to previous COMPASS analysis. The likelihood cuts are listed in Table 6. A further improvement is the inclusion of protons in the RICH particle identification efficiency determination.
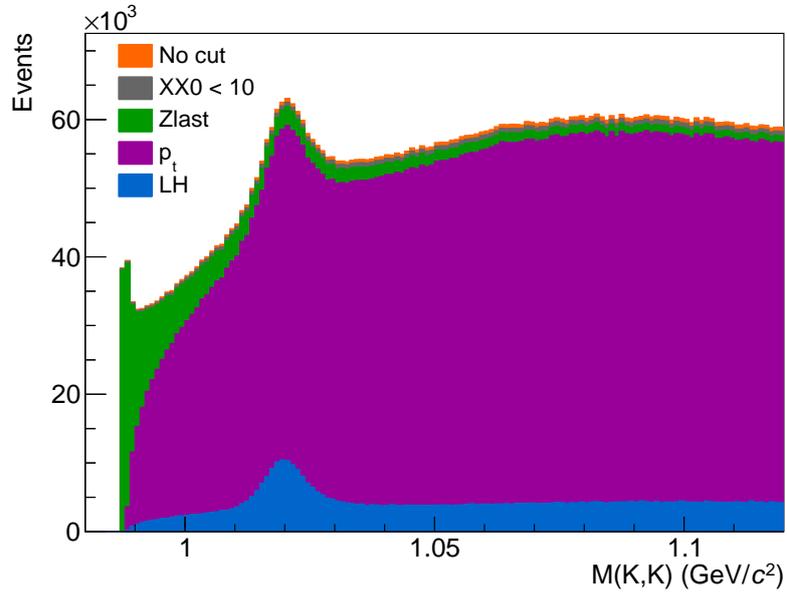
Figure 43: Invariant K^+K^- mass after the application of various cuts. Also the effect of the identification of one kaon is shown.

Table 6: Likelihood cuts for pion, kaon and protons.

	PION	KAON	PROTON	
Momentum	$p > p_{\pi,\text{thr}}$	$p > p_{K,\text{thr}}$	$p \leqslant p_{p,\text{thr}}$	$p > p_{p,\text{thr}}$
Likelihood type i	π	K	bg	p
$\text{LH}(i)/\text{LH}(\pi)$	—	> 1.08	> 1.0	> 1.0
$\text{LH}(i)/\text{LH}(K)$	> 1.0	—	> 1.0	> 1.0
$\text{LH}(i)/\text{LH}(p)$	> 1.0	> 1.00	—	—
$\text{LH}(i)/\text{LH}(bg)$	> 1.0	> 1.24	—	> 1.0

The RICH particle identification efficiency is studied in the momentum range of $10\,\mathrm{GeV/c} \leqslant$ $p \leqslant 50\,\mathrm{GeV/c}$. In this range, pions and kaons are emitting Cherenkov light, while up to $\sim 17\,\mathrm{GeV}$ protons are still below the threshold of

$$p_{\mathrm{thr},i} = m_i \cdot \frac{1}{\sqrt{n^2 - 1}} \, , \tag{101}$$

where n is the refractive index. This is shown in Figure 44 where the reconstructed Cherenkov angle is shown as a function of the hadron momentum. As the momentum range
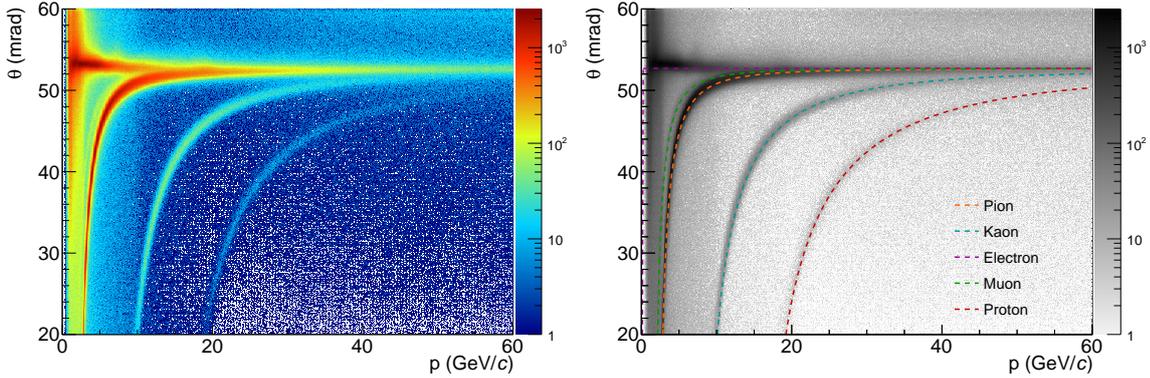
Figure 44: Left: Reconstructed Cherenkov angle as a function of the momentum. Right: Comparison with the calculated Cherenkov angle for each particle type using the refractive index of the RICH gas.

is restricted to momenta larger than $10\,\mathrm{GeV/c}$, no electron rejection can be performed. In this momentum range the Cherenkov angle for pions and electrons are to close to one another. Muons can also be not rejected using likelihood cuts as the Cherenkov angle for muon and pion is too close to one another. But they can be identified by cuts on the radiation length passed by a particle. The identification of pions, kaons and protons above the momentum threshold is done by comparing the likelihood values with one another. The likelihood cuts for protons require its likelihood to be the largest one. These cuts are also given in Table 6. Below the momentum threshold, protons do not emit Cherenkov light. Therefore, the likelihood values are used to test whether the detected light is consistent with random noise in the detector (background). In order to avoid possible problems due to the uncertainty on the reconstructed momentum or the uncertainty of the refractive index of the RICH gas, a region of $\pm 5\,\mathrm{GeV/c}$ around the proton threshold is used, where both hypothesis are applied for proton identification.

3.7.3 *Efficiency determination*

The particle identification efficiency of the RICH is studied as a function of the hadron phase space, which is given by the hadron momentum and its polar angle at the entrance of the RICH. This was already studied before, for example in References [81] and [82]. The binning used for this study is similar to a previous analysis described in Reference [80]. A fine binning is used for the momentum dependence since the Cherenkov effect depends on this variable. For the dependence on the polar angle, a coarse binning is used, since only a weak dependence is observed. The binning is given by:

- Momentum p (GeV/c) = $(10, 11, 12, 13, 15, 17, 19, 22, 25, 27, 30, 35, 40, 50)$

- Angle θ (rad) = $(0.0, 0.01, 0.04, 0.12, 0.3)$

For each bin, the elements of the efficiency matrix M_{RICH} are determined separately for positive and negative particles. The elements of this matrix contain the probability for a particle i to be identified as a particle of type j, for example a pion that is correctly identified as pion or wrongly as a kaon. The full matrix is given by:

$$M_{RICH} = \begin{pmatrix} \epsilon(\pi \to \pi) & \epsilon(\pi \to K) & \epsilon(\pi \to p) & \epsilon(\pi \to noID) \\ \epsilon(K \to \pi) & \epsilon(K \to K) & \epsilon(K \to p) & \epsilon(K \to noID) \\ \epsilon(p \to \pi) & \epsilon(p \to K) & \epsilon(p \to p) & \epsilon(p \to noID) \end{pmatrix} \tag{102}$$

The different elements are determined by $\epsilon(i \to j) = N(i \to j)/N(i)$ where $N(i)$ is the total number of particles i and $N(i \to j)$ is the number of particles i, which are identified as particle j. These numbers are evaluated using samples, where the particle type is known, as in the case of the selected decays.

In the case of positive pions, the events from the K^0 sample are used where the negative hadron is identified as a pion using the likelihood cuts shown in Table 6. Therefore, the second particle has to be a pion too, if the decaying particle was a K^0. Using the RICH, the particle type is determined for the second particle, which results in the number $N(\pi^+ \to j)$. An equivalent procedure is used for positive kaons and protons using the ϕ and Λ samples. In order to obtain these numbers for the negative particles, the same samples are used but this time performing the identification of the positive particle in the first place.

The numbers $N(i \to j)$ are extracted using a fit, which is described here for the K^0 sample, where the negative pion is already identified. The events are put into five different groups, depending on the particle type determined by the RICH:

1. All events (RICH not used for second particle)

2. Events where π^+ is identified as π^+

3. Events where π^+ is identified as K^+

4. Events where π^+ is identified as p

5. Events where π^+ is not identified

For each of these groups, the invariant K^0 mass spectra are shown in Figure 45, for example, and the number of events in the peak and the background are determined by a simultaneous fit of all five spectra. These spectra are described using two Gaussian distributions with the same mean for the signal, f_{Sig}, and a polynomial to describe the background, f_{BG}. Their expressions are given in Table 7. The two Gaussian distributions account for the different resolutions of the two stages. The fitted function for each of the groups is given by:

$$f(x) = N_{Sig} \cdot f_{Sig} + N_{BG} \cdot f_{BG} , \tag{103}$$

where N_{Sig} is the amount of K^0 and N_{BG} the amount of background events. Here, the same width, σ_1 and σ_2, of the two Gaussian distributions was used for all five spectra. Also

Table 7: Functional form for the description of the the mass spectra for K^0, ϕ and Λ candidates. The symbol G represents a Gaussian distribution and the symbol BW a Breit-Wigner distribution.

SAMPLE	SIGNAL	BACKGROUND
K^0	$\delta G(\mu, \sigma_1) + (1 - \delta) G(\mu, \sigma_2)$	$1 + ax + b(2x^2 - 1) + c(4x^3 - 3x)$
ϕ	$BW(\mu, \sigma_1) \otimes G(\mu, \sigma_2)$	$(x - t)^n \cdot \exp(-a(x - t))$ with $t = 2 \cdot m_K$
Λ	$\delta G(\mu, \sigma_1) + (1 - \delta) G(\mu, \sigma_2)$	$(x - t)^n \cdot \exp(-a(x - t))$ with $t = m_p + m_\pi$

the ratio δ of the amount of events in both Gaussian distributions is the same. The shape of the background is the same for all spectra except the one where the pion is identified as a proton. In this case, a possible background due to decays from Λ baryons decaying in a pion and an proton can be enriched. This results in a slightly different background shape. The integral of the background remains a independent parameter in all five cases. In order to ensure that the sum of all efficiencies ($\epsilon(\pi^+ \to \pi^+) + \epsilon(\pi^+ \to K^+) + \epsilon(\pi^+ \to$

(a) All   (b) Identified as pion   (c) Identified as kaon   (d) Identified as proton   (e) No identification
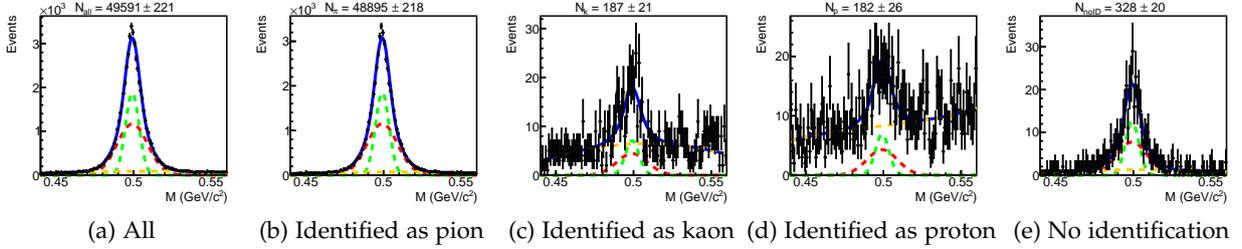
Figure 45: Mass spectra for K^0 candidates with an identified π^- for various hypothesis for the second hadron. The momentum of the positive hadron is in the range of ($25 \, \text{GeV}/c^2 < p < 27 \, \text{GeV}/c^2$) and the angle in the range of ($0.01 < \theta < 0.04$).

$p) + \epsilon(\pi^+ \to \text{noID})$) is 100%, an additional constraint is introduced to the fit.

$$N^{\text{all}}(K^0) = N^\pi(K^0) + N^K(K^0) + N^p(K^0) + N^{\text{noID}}(K^0) \,, \tag{104}$$

where $N^i(K^0)$ ($i = \pi, K, p, \text{noID}$) is the number of K^0 obtained from the histogram where the pion is identified as i. This results in 16 free parameters of the fit. The same method is used in the case of kaons and protons. The main difference between those fits and the one for the K^0 sample is the description of the signal and the background. The functions describing both are also given in Table 7. Again the parameters describing the shape are the same in all five spectra and the fit parameters describing the integrals of the functions are used as free parameters, except for the parameter of the mass spectrum including all events. This results in 15 free parameters for the fit of the ϕ sample and in 15 free parameters for the fit of the Λ sample.

Examples of the fits performed for the ϕ and Λ samples are shown in Figures 46 and 47. The fits show the results for one momentum bin ($25 \, \text{GeV}/c^2 < p < 27 \, \text{GeV}/c^2$) and angular bin ($0.01 < \theta < 0.04$), which was also shown for the K^0 sample.

(a) All   (b) Identified as pion   (c) Identified as kaon   (d) Identified as proton   (e) No identification
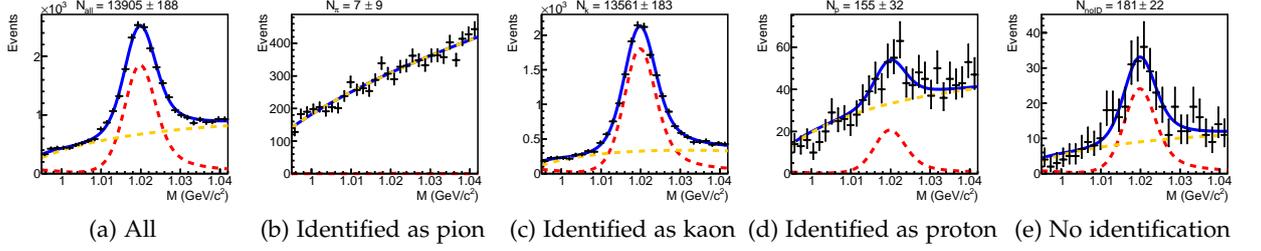
Figure 46: Mass spectra for ϕ candidates with an identified K^- for various hypothesis for the second hadron. The momentum of the positive hadron is in the range of $(25\,\text{GeV}/c^2 < p < 27\,\text{GeV}/c^2)$ and the angle in the range of $(0.01 < \theta < 0.04)$.

(a) All   (b) Identified as pion   (c) Identified as kaon   (d) Identified as proton   (e) No identification
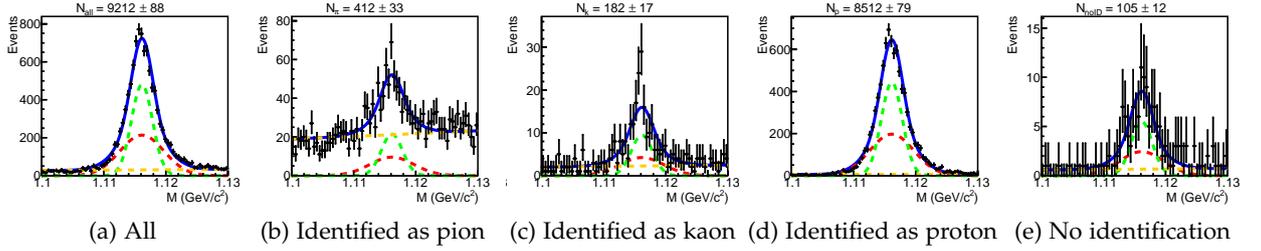
Figure 47: Mass spectra for Λ candidates with an identified π^- for various hypothesis for the second hadron. The momentum of the positive hadron is in the range of $(25\,\text{GeV}/c^2 < p < 27\,\text{GeV}/c^2)$ and the angle in the range of $(0.01 < \theta < 0.04)$.

3.7.4 *Calculation of the efficiencies and uncertainties*

The elements of the efficiency matrix M_{RICH} are determined from fitted numbers of signal events,

$$\epsilon(i \to j) = N(i \to j)/N(i) \,. \tag{105}$$

Here, $N(i)$ is given by the sum of all $N(i \to j)$. As the nominator and denominator are correlated, the uncertainty can be determined via error propagation taking into account the covariance matrix of the fit,

$$\Delta\epsilon = \sqrt{\sum_{j=1}^{m} \left(\frac{\partial\epsilon}{\partial N(i \to j)} \right)^2 \cdot u_j + 2 \sum_{j=1}^{m-1} \sum_{k=j+1}^{m} \left(\frac{\partial\epsilon}{\partial N(i \to j)} \frac{\partial\epsilon}{\partial N(i \to k)} \cdot u(j,k) \right)} \,. \tag{106}$$

Here, u_j are the diagonal elements of the covariance matrix, $u(j,k)$ are the off diagonal elements and ϵ is one of the elements of the efficiency matrix. The summations are done over all possible particle types, which are pion, kaon, proton and no identification in this case.

3.7.5 *Results*

The result for the RICH particle identification efficiency is shown in Figures 48 to 53 for the various particles and their charges. In each figure, the momentum dependence for the

various angular bins are shown. The weak dependence on the angle as well as the strong dependence on the momentum especially near the threshold is visible.

The RICH performs a correct identification of pions in more than 95% of the cases for momenta below $30\,\mathrm{GeV/c^2}$ and the probability for a misidentification of a pion as a kaon is below $\sim 1\%$. For kaons, near the threshold a strong dependence on the momentum is visible. At higher momenta the correct identification is given in $\sim 95\%$ of the cases. For protons, the momentum dependence at the threshold is even stronger. Below the threshold, protons are identified correctly in about 50% of the cases. Above the threshold, the efficiency rises up to $\sim 95\%$. For the future analysis of hadron asymmetries, the inverse of the efficiency matrix will be needed.

(a) Pion

(b) Kaon

(c) Proton

(d) No identification
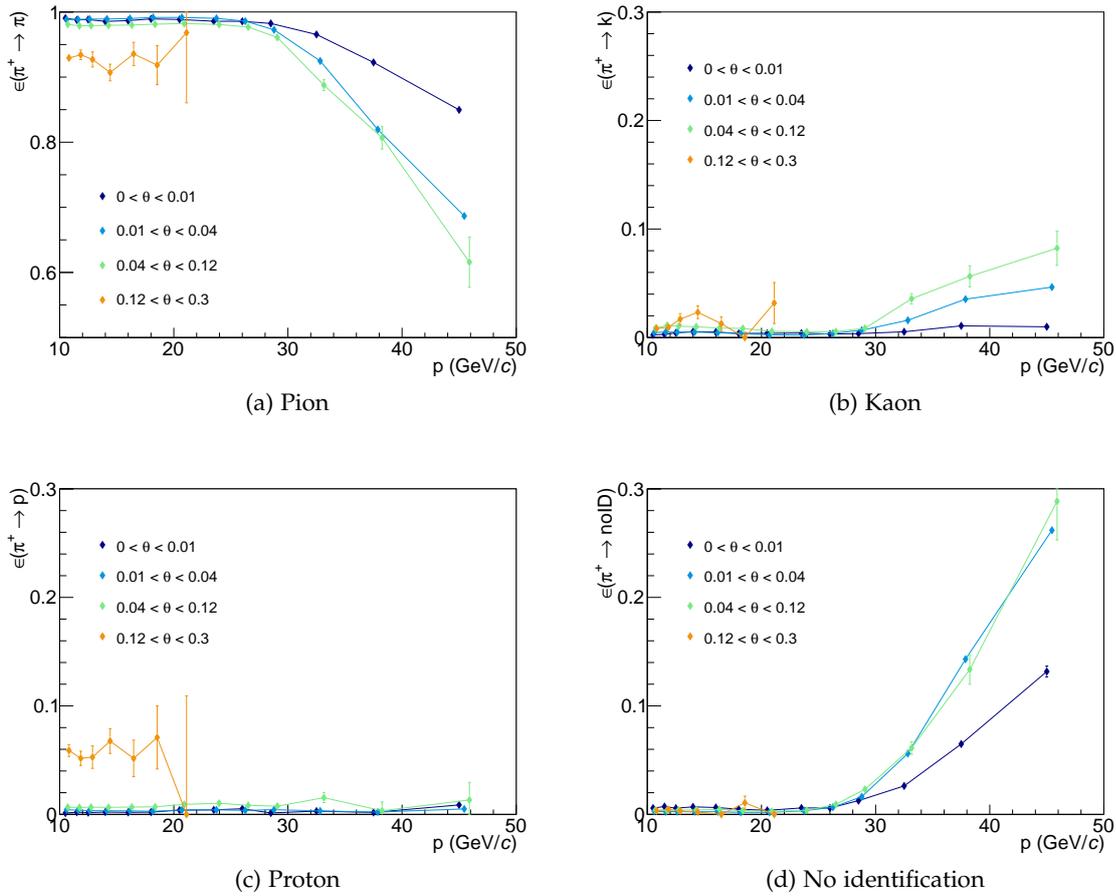
Figure 48: Identification probabilities $\epsilon(\pi^+ \to j)$ for positive pions. The results for the different θ bins are slightly shifted to the right to avoid an overlap.

(a) Pion

(b) Kaon

(c) Proton

(d) No identification
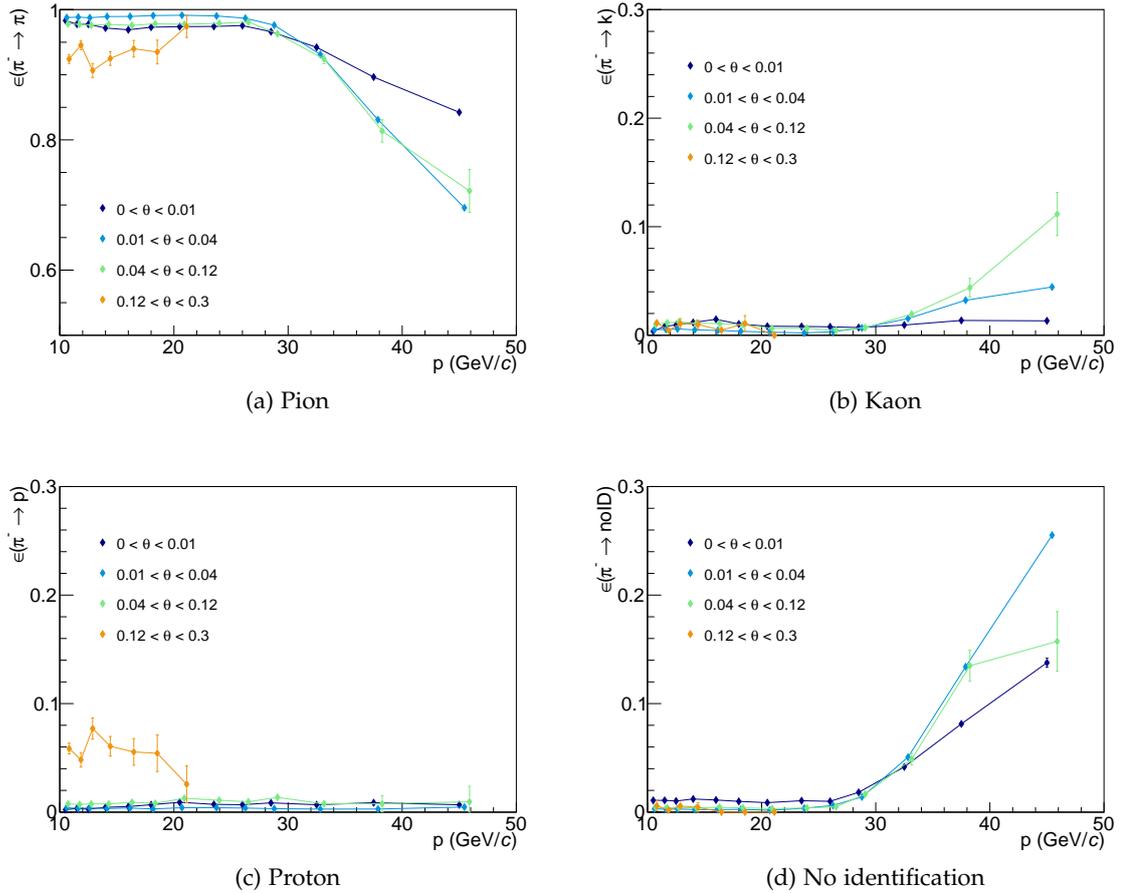
Figure 49: Identification probabilities $\epsilon(\pi^- \to j)$ for negative pions. The results for the different θ bins are slightly shifted to the right to avoid an overlap.

(a) Pion

(b) Kaon

(c) Proton

(d) No identification
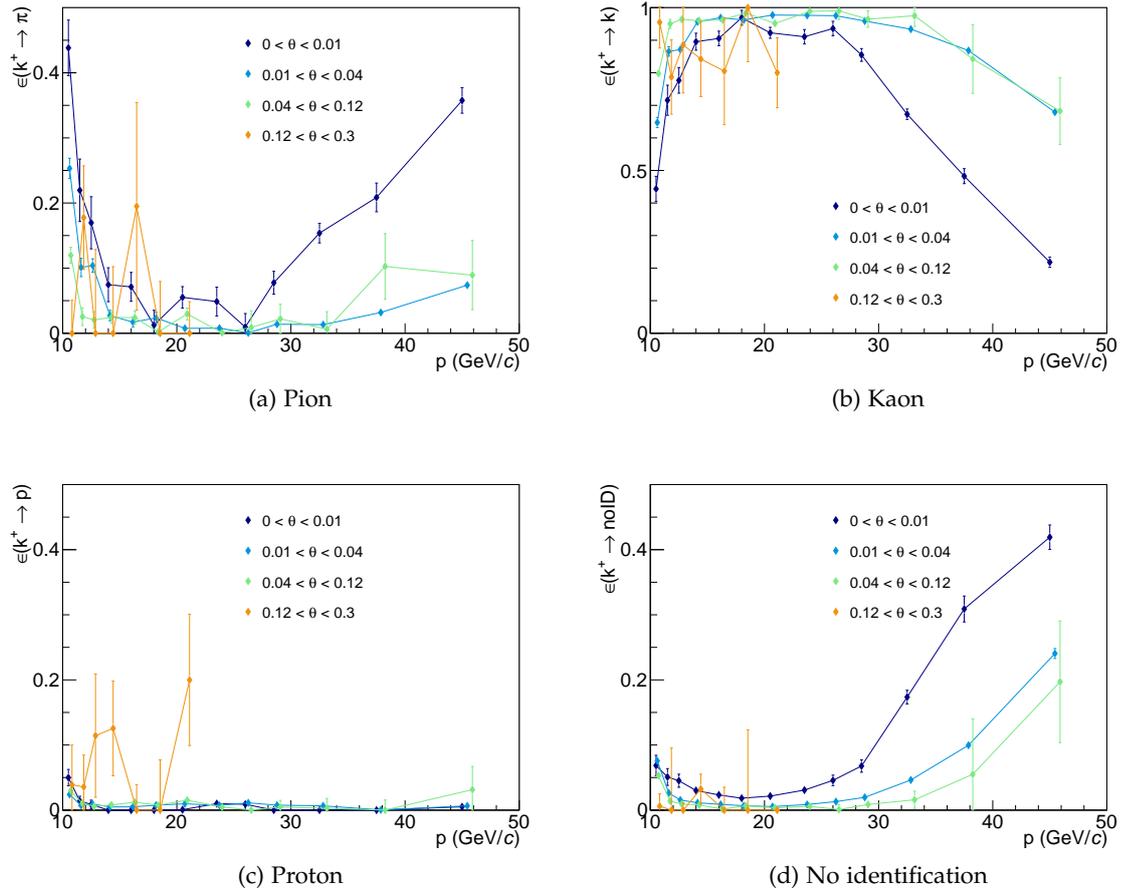
Figure 50: Identification probabilities $\epsilon(K^+ \rightarrow j)$ for positive kaons. The results for the different θ bins are slightly shifted to the right to avoid an overlap.

(a) Pion

(b) Kaon

(c) Proton

(d) No identification
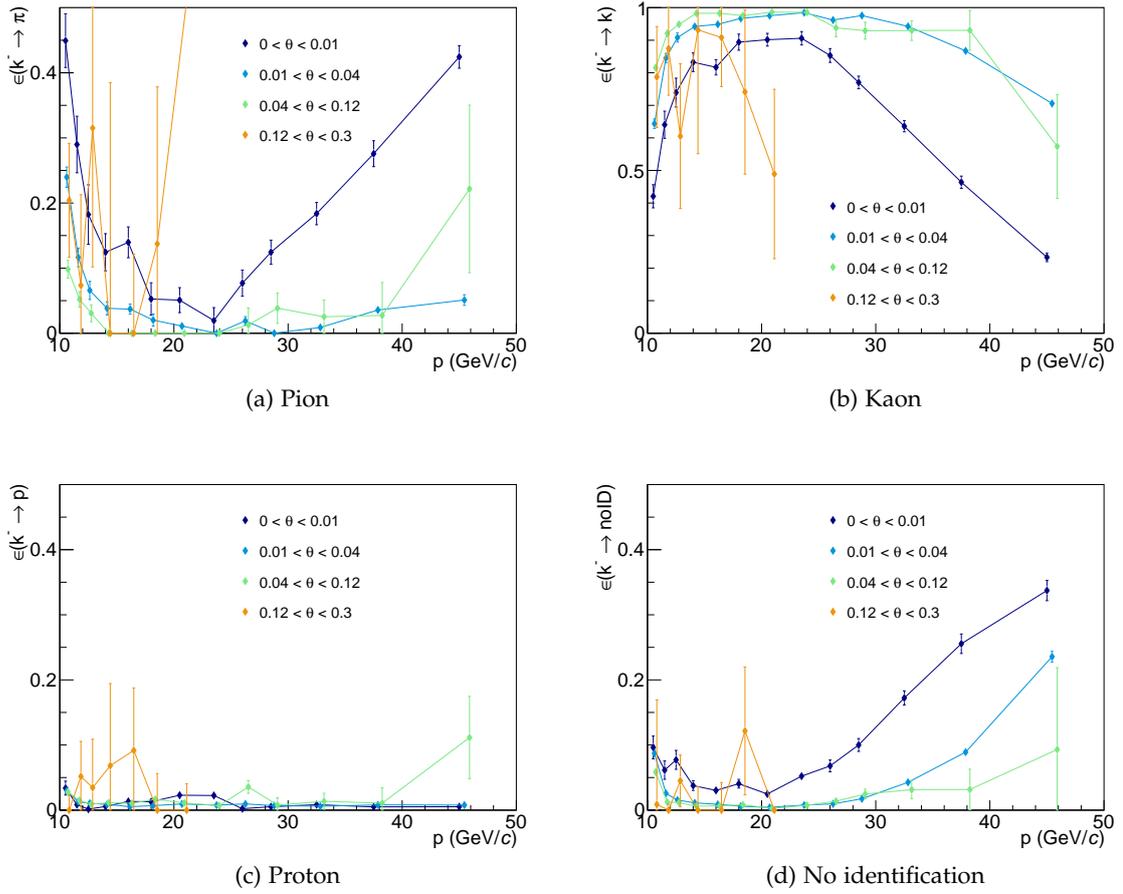
Figure 51: Identification probabilities $\epsilon(K^- \to j)$ for negative pions. The results for the different θ bins are slightly shifted to the right to avoid an overlap.
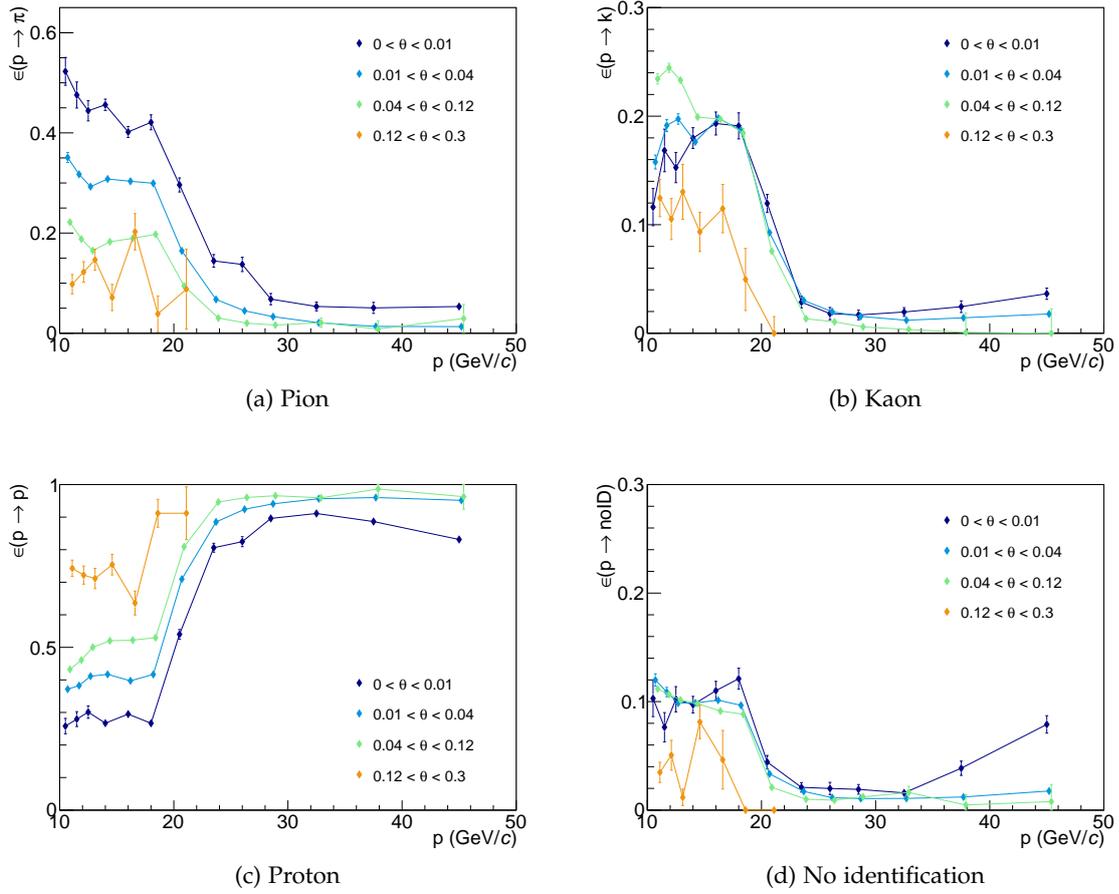
Figure 52: Identification probabilities $\epsilon(p \to j)$ for protons. The results for the different θ bins are slightly shifted to the right to avoid an overlap.

(a) Pion

(b) Kaon

(c) Proton

(d) No identification
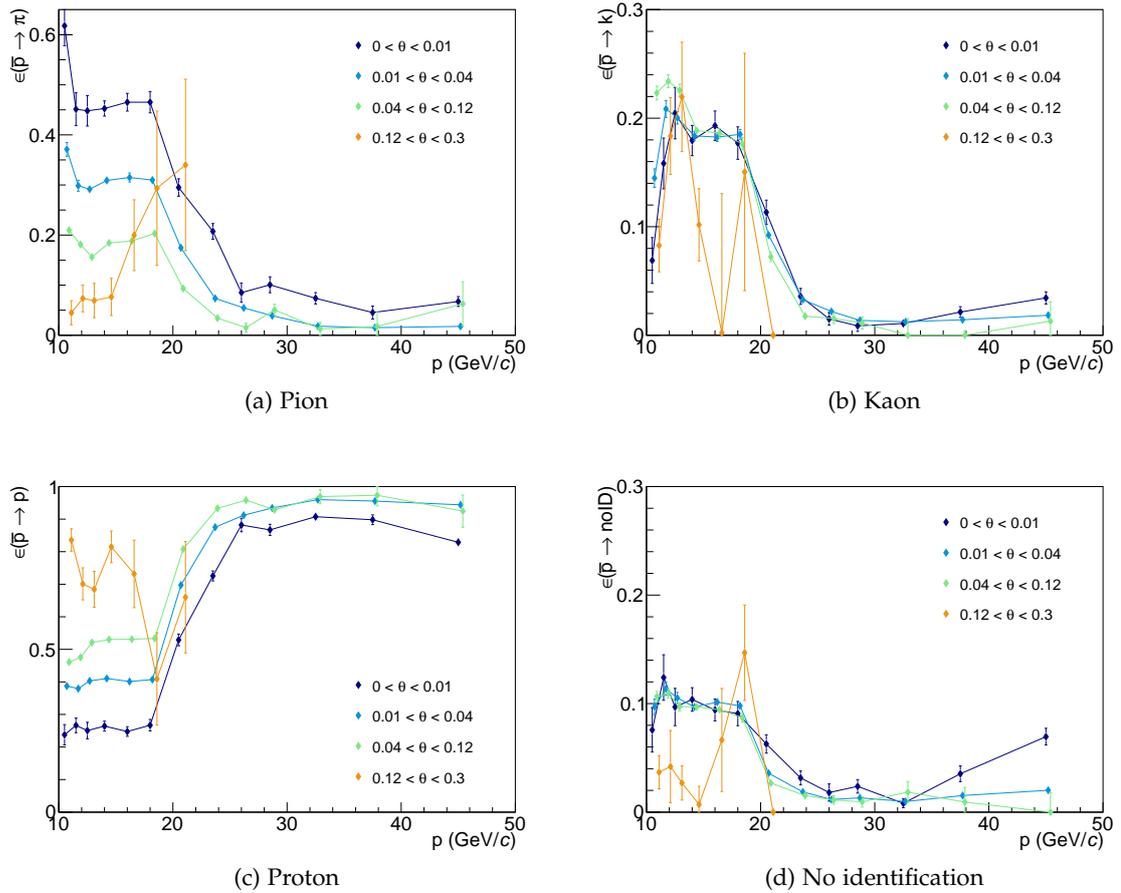
Figure 53: Identification probabilities $\epsilon(\bar{p} \to j)$ for antiprotons. The results for the different θ bins are slightly shifted to the right to avoid an overlap.

THE LONGITUDINAL DOUBLE SPIN ASYMMETRY

EXTRACTION OF ASYMMETRIES

In this chapter, the COMPASS method for the extraction of longitudinal double spin asymmetries from data is described. Also, the test of the data stability for the full data from the 2011 data taking is described. In addition, the necessary external inputs for the asymmetry calculation are explained. These external inputs are, for example, the beam and target polarisation, the depolarisation factor, the dilution factor and the parametrisation of the spin-independent structure function. Also the corrections to the longitudinal double spin asymmetry are described. These corrections take into account radiative effects and offsets to the longitudinal double spin asymmetry due to the presence of nitrogen-14 or lithium-7 inside the target material.

4.1 ASYMMETRY CALCULATION

The original method for the calculation of the longitudinal double spin asymmetries from data was developed by SMC and was further improved by the COMPASS collaboration. The method is described in References [83, 84]. For calculating the longitudinal double spin asymmetry, the data is divided into four sets. They contain the data from the two different target cells. These are the upstream (u) and downstream (d) cell in the case of the two cell target or the central (c) and the two outer cells (o) in the case of the three cell target. These two data sets are divided once more depending on the polarisation direction before and after a solenoid field reversal ($u = u^\uparrow, d = d^\downarrow, u' = u^\downarrow, d' = d^\uparrow$). The solenoid field reversal is described in Section 3.2.

The number of events in each target cell for the two possible solenoid field directions can be expressed as a function of different variables

$$N_u = \int d\vec{x} a_u \Phi_u n_u \overline{\sigma} \left(1 + P_B P_T f D A_1\right) = \alpha_u \left(1 + \beta_u A_1\right) , \tag{107}$$

$$N_d = \int d\vec{x} a_d \Phi_d n_d \overline{\sigma} \left(1 + P_B P_T f D A_1\right) = \alpha_d \left(1 + \beta_d A_1\right) , \tag{108}$$

$$N'_u = \int d\vec{x} a'_u \Phi'_u n_u \overline{\sigma} \left(1 + P_B P_T f D A_1\right) = \alpha'_u \left(1 + \beta'_u A_1\right) , \tag{109}$$

$$N'_d = \int d\vec{x} a'_d \Phi'_d n_d \overline{\sigma} \left(1 + P_B P_T f D A_1\right) = \alpha'_d \left(1 + \beta'_d A_1\right) . \tag{110}$$

Here, the prime indicates the quantities after a rotation of the solenoid field. The integral over $\vec{x}$ takes into account all variables (x, Q^2...), a_i is the acceptance, Φ_i the incoming muon flux, n_i the number of target nucleons and $\overline{\sigma}$ is the spin-independent cross section. The term connected to the asymmetry A_1 depends on the beam polarisation P_B, the target polarisation P_T, the dilution factor f and the depolarisation factor D. These equations can be simplified by introducing the factors α and β, which are given by:

$$\alpha_i = a_i \Phi_i n_i \overline{\sigma} , \tag{111}$$

$$\beta_i = P_B P_T f D . \tag{112}$$

Here, the index $i = \{u, d, u', d'\}$ denotes the corresponding target cell before or after a solenoid field reversal. The equations for the number of events in one target cell can be reformulated by introducing the mean acceptance factor

$$\langle a_i \rangle = \frac{\int d\vec{x} \, a_i \Phi_i n_i \bar{\sigma}}{\int d\vec{x} \, \Phi_i n_i \bar{\sigma}} \tag{113}$$

and the mean β

$$\langle \beta_i \rangle = \frac{\int d\vec{x} \, \alpha_i \beta_i}{\int d\vec{x} \, \alpha_i} \ . \tag{114}$$

Using these two factors, the double ratio δ of the number of events per target cell and solenoid field direction is given by:

$$\delta = \frac{N_u N'_d}{N_d N'_u} \tag{115}$$

$$= \frac{\langle a_u \rangle \langle a'_d \rangle \int d\vec{x} \Phi_u n_u \bar{\sigma} \int d\vec{x} \Phi'_d n_d \bar{\sigma} \left(1 + \langle \beta_u \rangle A_1\right) \left(1 + \langle \beta'_d \rangle A_1\right)}{\langle a'_u \rangle \langle a_d \rangle \int d\vec{x} \Phi'_u n_u \bar{\sigma} \int d\vec{x} \Phi_d n_d \bar{\sigma} \left(1 + \langle \beta'_u \rangle A_1\right) \left(1 + \langle \beta_d \rangle A_1\right)} \ . \tag{116}$$

In this ratio, the integrals $\int d\vec{x} \Phi_i n_i \bar{\sigma}$ cancel hence the number of target nucleons and the spin-independent cross section do not depend on the the field direction. In addition, the muon flux per target cell can be equalised by cuts during the selection of the data. The double ratio of the mean acceptances also cancels, which has to be tested using the data. This leads to a second order equation for the asymmetry

$$aA_1^2 + bA_1 + c = 0 \ , \tag{117}$$

where the quantities a, b and c depend on the mean values of β and the double ratio δ:

$$a = \delta \langle \beta'_u \rangle \langle \beta_d \rangle - \langle \beta_u \rangle \langle \beta'_d \rangle \tag{118}$$

$$b = \delta \left(\langle \beta'_u \rangle + \langle \beta_d \rangle \right) - \left(\langle \beta_u \rangle + \langle \beta'_d \rangle \right) \tag{119}$$

$$c = \delta - 1 \ . \tag{120}$$

Solving this equation results in two solutions for the asymmetry depending on whether a is zero or not:

$$A_1 = \frac{\pm \sqrt{b^2 - 4ac} - b}{2a} \quad \text{if } a \neq 0 \tag{121}$$

$$A_1 = -\frac{c}{b} \quad\quad\quad\quad \text{if } a = 0 \ . \tag{122}$$

The uncertainty of the asymmetry is given by

$$\Delta A_1 = \sqrt{\frac{1}{\langle \beta^2 \rangle} \frac{1}{N}} \ , \tag{123}$$

where N is the total number of events. The mean value of kinematic variables X is calculated using all events from all cells

$$\langle X \rangle = \frac{\sum_j X_j}{N} \ . \tag{124}$$

Here, the X_j are the values of the variable for each event j. At this point, a weighting function $w(\vec{x})$ for each event can be introduced into this formalism by modifying the expression for N_i:

$$N_i \rightarrow p_i = \int d\vec{x}\, w(\vec{x}) N_i(\vec{x}) \approx \sum_j w_j \, . \tag{125}$$

This changes the expressions from Equations 113 and 114 for the mean acceptance and the mean β. Also, Equation 115 for the double ratio is modified:

$$\langle a_i \rangle = \frac{\int d\vec{x}\, a_i \Phi_i n_i \overline{\sigma} w(\vec{x})}{\int d\vec{x}\, \Phi_i n_i \overline{\sigma} w(\vec{x})} \, , \tag{126}$$

$$\langle \beta_i \rangle = \frac{\int d\vec{x}\, \alpha_i \beta_i w(\vec{x})}{\int d\vec{x}\, \alpha_i w(\vec{x})} \approx \frac{\sum_j w_j(\vec{x}) \beta_j}{\sum_j w_j(\vec{x})} \, , \tag{127}$$

$$\delta = \frac{p_u p'_d}{p_d p'_u} \, . \tag{128}$$

The second order equation for the asymmetry given in the Equations 121 and 122 remains the same together with the relations of the factors a, b and c given by Equations 118, 119 and 120. Using the weighting function results in a modification of the expression for the uncertainty

$$\Delta A_1 = \sqrt{\frac{\langle w^2 \rangle}{\langle w\beta \rangle^2} \frac{1}{N}} \, . \tag{129}$$

In addition, the expression for the calculation of mean values is modified. Now, the weighted mean is used

$$\langle X \rangle = \frac{\sum_j w_j^2 X_j}{\sum_j w_j^2} \, . \tag{130}$$

For the calculation of mean values always the kinematic variable is used, except for the photon virtuality. Here, the mean values is calculated for the logarithm of the photon virtuality Q^2 as the DGLAP equations (see Section 2.7.2) show a logarithmic dependence of the structure function g_1 on the photon virtuality.

The statistical optimal weight would be $w = P_B P_T fD$ to increase the contribution from events, which have large analysing powers for the asymmetry. In the case of real data, the target polarisation is removed from the weight as it is not known for each event and thus might introduce false asymmetries. Instead, only its mean value is known for a certain period in time, which can hide a time dependence and therefore introduces the false asymmetries.

4.2 DATA STABILITY

For the determination of the longitudinal double spin asymmetry A_1 only events from stable data taking should be used. Therefore, periods of unstable data taking conditions are excluded, for example such, which are affected by instabilities of detectors. Two different methods are used to search for those periods. The first method performs a search on the level of individual spills. The second one identifies runs, which are affected.

4.2.1 *Bad spill identification*

The identification of bad spills is performed on a spill by spill level. Its aim is the detection of spills, which are affected either by instabilities in the beamline or problems in the detectors. Those effects result in differences in the properties of reconstructed events.

In order to search for such spills, some basic variables for each spill are taken into account and studied as a function of the spill number (time). These variables are:

- Number of primary vertices per event

- Number of beam particles per primary vertex

- Number of tracks per primary vertex

- χ^2 of the primary vertex per vertex

- χ^2 of the tracks per track

- Number of hits per track

- Number of charged clusters per event

- Charged cluster energy per event

- Likelihoods per track

- Trigger rate

In the case of no problems in the spectrometer, the mean values for each parameter in all spills are close together and compatible within statistical fluctuations. The identification of bad spills utilises the assumption that the properties of a particular spill are similar to the neighbouring ones. For this reason, a spill is compared to its 1200 neighbours. A spill is marked as bad if the value of the observed quantity differs too much from the neighbouring spills. This is checked by using the root mean square of the distribution and counting the number of neighbours within a certain amount of root mean squares. Here, a distance of three root mean squares is chosen. For good spills with no problems, this number should be close to 1200 and in the case of bad ones, it will be close to zero. As an example, the distribution for the number of tracks per primary vertex as a function of the spill number is shown in Figure 54. Spills marked in red are considered to be bad ones. Two different kinds of bad spills are observed. Some single bad spills exist and groups of bad spills exists. The single ones are connected to the beam such as variations in the intensity or the spill structure. Groups of bad spills are connected to problems in the spectrometer. In such cases, the logbook is used to investigate the source of the problem. Here, the two groups marked in red are connected to timing problems in the case of the first sharp drop and to problems with one of the silicon micro strip detectors in the case of the second group. The spills marked as bad ones will not be used in the final analysis.

This analysis was performed for events of each physics trigger separately. In addition, the analysis is also performed using variables connected to the RICH detector and the calorimeters. This allows the use of individual bad spill list depending on the analysis. Here, the bad spill lists connected to the RICH detector and the calorimeters is not used. Table 8 shows the amount of rejected spills in the case of the asymmetry analysis, where
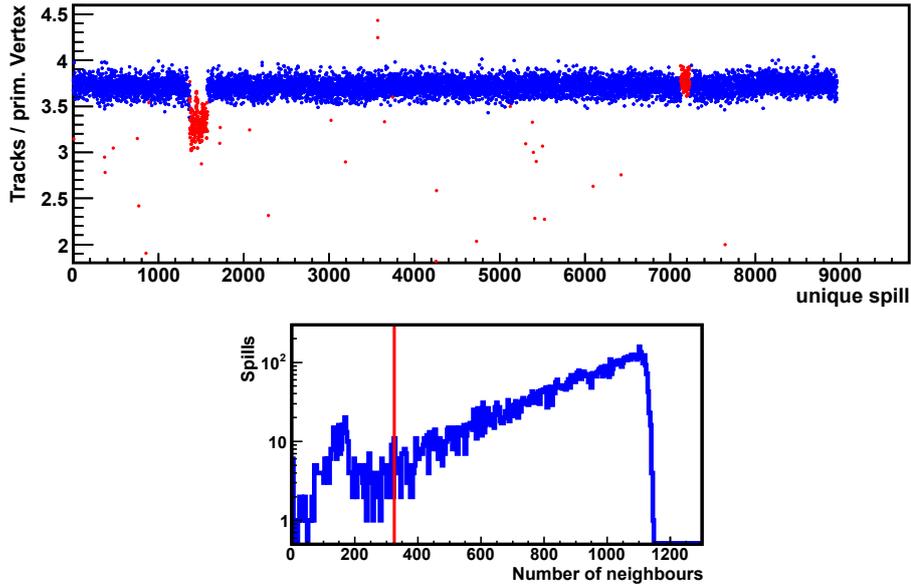
Figure 54: Top: Illustration of the bad spill identification using the number of tracks per primary vertex. Rejected spills are marked in red. Bottom: Distribution for the numbers of neighbours within three RMS. The red line indicates the threshold for a good spill.

only the bad spill lists for all triggers are used. The larger amount of rejected events in the period W25 is caused by an instability in the LAS trigger, which had impacts on the other ones. The larger amount of rejected spills in period W32 is caused by instabilities in the beam line due to problems with some quadrupole magnets.

Table 8: Amounts of rejected spills per data taking period.

PERIOD	REJECTED SPILLS	PERIOD	REJECTED SPILLS
W25	28.7%	W34	10.3%
W27	8.6%	W36	4.4%
W30	6.2%	W38	3.2%
W31	9.5%	W39	2.7%
W32	28.9%	W41	2.4%
W33	4.7%	W43	4.3%

4.2.2   *Bad run identification*

The search for bad runs is performed to test the performance of the reconstruction taking into account the whole detector. Therefore, events with reconstructed K^0 mesons were selected. In order to calculated the mean value of some parameter, the average has to be calculated over a full run.

4.2.2.1 *Data selection*

The selection of K^0 candidates is performed similar to the one described in Section 3.7.1. In order to keep as much K^0 candidates as possible, some cuts are weakened. The following cuts are applied:

1. Exclude bad spills

2. Best primary vertex with incoming and scattered muon [1]

3. Primary vertex is inside one of the target cells (PaAlgo::InTarget)

4. Selection of good secondary vertex

   - Loop over all vertices

   - Vertex is not a primary one

   - Exactly two oppositely charged outgoing particles

   - The tracks should not be connected to any other primary vertex

   - Primary and secondary vertex separated by more than 3σ

5. Select good hadron tracks

   - Both particles should not have crossed more than 10 radiation length

   - Last measured position behind SM1 (Momentum is measured)

   - Check that the decaying particle is connected to the primary vertex ($\theta \leqslant 0.04°$)

6. Additional cuts

   - Hadron momentum larger than $1\,\text{GeV/c}$

   - Mass difference between the K^0 mass and the invariant mass of the two decay hadrons smaller than $100\,\text{MeV/c}^2$ assuming the correct masses

At first, the already known bad spills are rejected and events with a primary vertex inside the target with an incoming and scattered muon attached are selected. These cuts are the same ones as used in the later analysis. Afterwards, a good secondary vertex is selected with good hadron tracks. It is also checked that the possible K^0 is produced at the primary vertex by applying a cut on the angle θ between the momentum vector of the K^0 candidate and the vector connecting the primary and secondary vertex. Some additional cuts are applied in the last step to remove events, which will not be used for the analysis.

4.2.2.2 *Results and method*

For each run, the invariant $\pi^+\pi^-$ mass is determined from the selected events. The obtained mass spectra are fitted using two Gaussian distributions with the same mean but different widths for the signal and a second order polynomial to describe the background. The two Gaussian distributions are used to account for the two different resolutions of the two spectrometer stages. An example of such a fit is shown in Figure 55 for the run 92204, which is part of the second data taking period of 2011. The difference between the K^0 mass obtained from the fit and the mass from the PDG [18] for all 2011 runs is shown

---

1 Phast.7.132
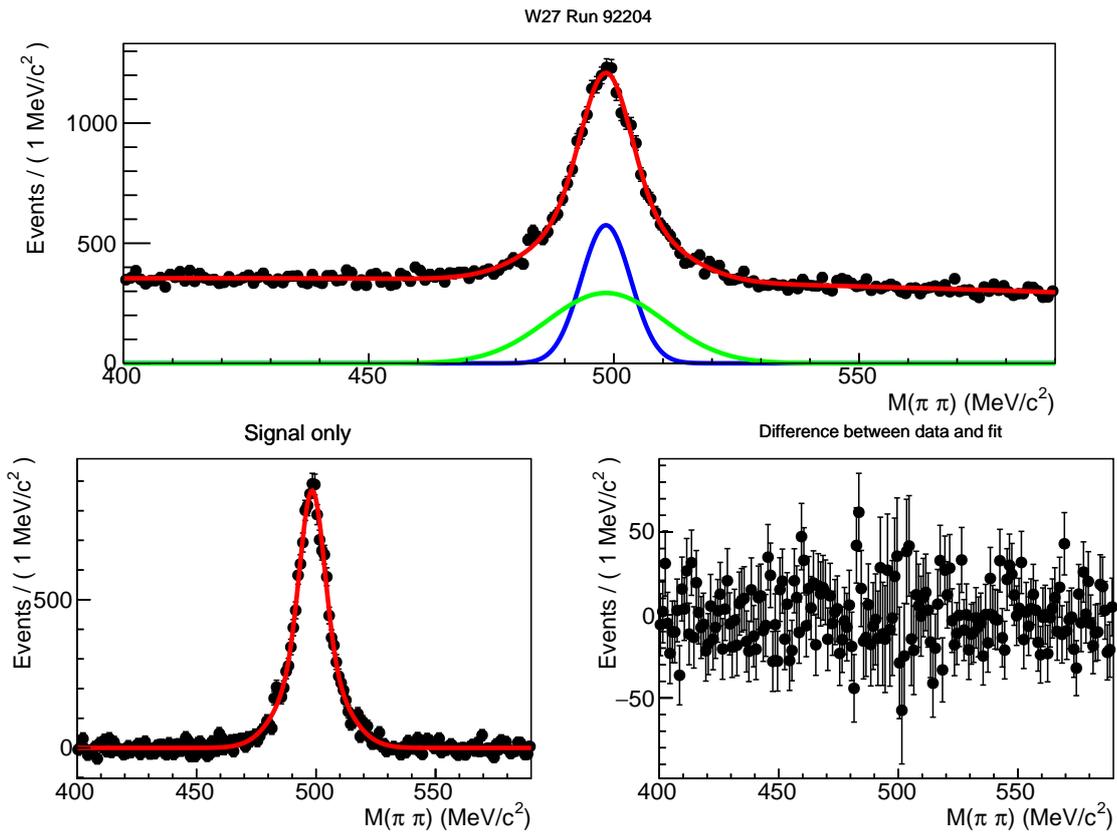
Figure 55: Fit of the invariant $\pi^+\pi^-$ mass for run 92204. Top: Full set of selected K^0 candidates with the result of the fit. Bottom left: Mass spectrum after subtracting the fitted background. Bottom right: Difference between data and fit.

in Figure 56. The difference is stable over the full year and shows only a small difference between the reconstructed mass and the one from the PDG of about 0.17%. In this figure, the beginning of a new data taking period is marked with blue lines indicating also a change in the alignment used for the detectors in the reconstruction. No runs are reject based on this study from the further analysis.
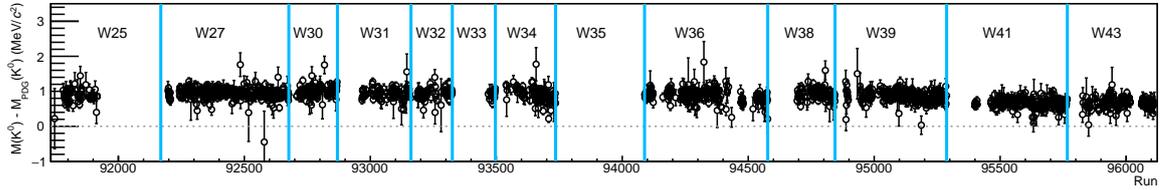
Figure 56: Difference between the reconstructed K^0 mass and the PDG value as a function of the run number.

4.3 DATA GROUPING

For the calculation of the asymmetries described in Section 4.1, it is necessary to divide the data in four different data sets (u, d, u', d'). Two possibilities are used to obtain these data sets. They can be obtained using the full data set and summing up all events belonging to each group. This method is called "global grouping". The other method utilises the daily reversal of the target solenoid field. Due to this reversal, the data taken before and after the reversal already form the four different data sets needed for the asymmetry calculation. Therefore, the asymmetry is calculated for all of such smaller groups and the weighted mean of the asymmetry from all those groups is calculated afterwards. This method is called "consecutive grouping". The advantage of this method is the reduction of false asymmetries connected to different data taking conditions throughout the year. If the data taking conditions do not change during the year, both methods will result in the same asymmetry. This comparison is part of the systematic studies on the longitudinal double spin asymmetry, which are described in Section 5.2.

4.4 INPUTS TO THE ASYMMETRY CALCULATION

The calculation of the asymmetry utilises the use of weights as described before. The additional inputs for the calculation of the weights are described in the following sections. Also, the parametrisations of the spin-independent structure function is discussed, which is needed for the calculation of the spin-dependent structure function from the asymmetry. In addition, corrections applied to the asymmetry are described.

4.4.1 *Beam and target polarisation*

The beam polarisation is calculated from a Monte Carlo simulation of the M2 beamline [85]. Using this simulation, a parametrisation of the polarisation depending on the momentum of the muon is obtained. Therefore, the polarisation can be calculated for each incoming muon. Figure 57 shows the beam polarisation as a function of the momentum for the the 160 GeV/c beam and the 200 GeV/c muon beam used in 2011. The uncertainty

on the beam polarisation is 5%. It is connected to the systematic uncertainties of the Monte Carlo simulation. These include possible misalignments of the beamline and the repeatability of the beam settings. The results of the Monte Carlo simulation were compared to measurements of the beam polarisation done by SMC [61, 86, 87]. These measurements were in agreement with the Monte Carlo simulation.
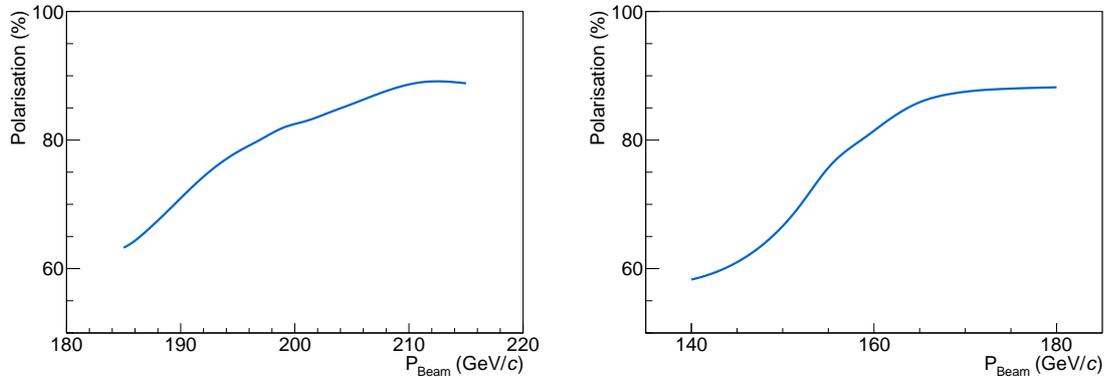
Figure 57: Beam polarisation of the COMPASS muon beam as a function of the beam momentum. Left: Beam polarisation for the muon beam used in 2011 $(200\,(\text{GeV}/c))$. Right: Beam polarisation for the muon beam used in 2006 and 2007 $(160\,(\text{GeV}/c))$.

The target polarisation cannot be determined for each event separately. It is determined for each run using the NMR system of the target (see Section 3.2). The target polarisation obtained for the 2011 data taking is shown in Figure 58 as a function of the run number. The relative uncertainty of the polarisation depends on the year and is connected to the uncertainty of the NMR measurement. This uncertainty takes into account the uncertainty on the thermal equilibrium calibration, with an empty and loaded target. Due to some problems with the target in 2011, a larger relative uncertainty of 3.5% on the target polarisation is obtained. In the case of the 2007 data where also ammonia was used as target material, the relative uncertainty is 2%. For the measurement using lithium deuteride in 2006, the relative uncertainty is 5%.

4.4.2 F_2 *parametrisation*

The spin-dependent structure function can be obtained from the measured asymmetry taking into account the spin-independent structure function F_2 (see Section 2.9). For the data at high photon virtualities, the parametrisation obtained by SMC [88] is used. SMC performed a fit to the world data on the structure functions F_2^p and F_2^d using in addition the precise determination of the ratio F_2^d/F_2^p by NMC [89]. The obtained parametrisation is valid for $3.5 \cdot 10^{-5} < x < 0.85$ and $0.2\,(\text{GeV}/c)^2 < Q^2 < 5000\,(\text{GeV}/c)^2$ in the case of the spin-independent structure function of the proton. In the case of the spin-independent structure function of the deuteron, it is valid for $9 \cdot 10^{-3} < x < 0.85$ and $0.2\,(\text{GeV}/c)^2 < Q^2 < 220\,(\text{GeV}/c)^2$. The results for the spin-independent structure function of the proton and deuteron are shown in Figure 59 as a function of Bjorken-x at the averaged Bjorken-x and photon virtuality of the various COMPASS data sets. In the case of the spin-independent structure of the proton (Figure 59 left) the results using the 160 GeV/c and 200 GeV/c muon beam are shown for the analysis at low (open points) and
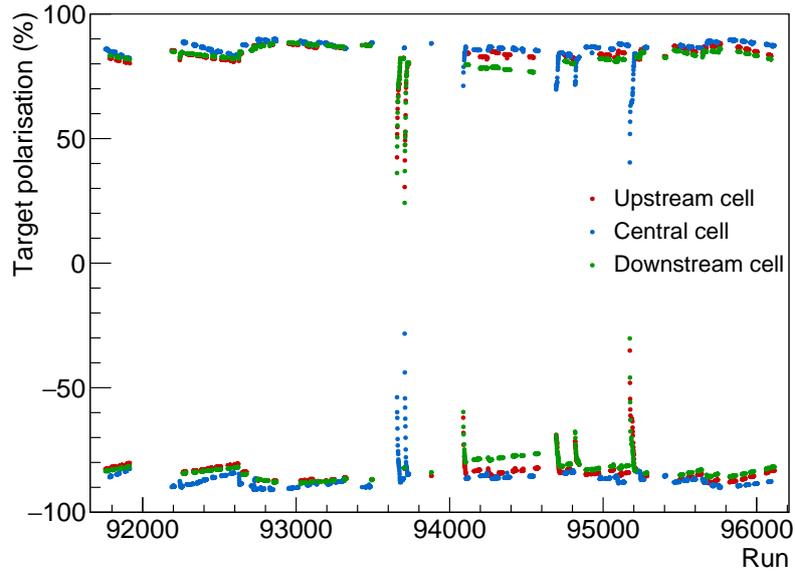
Figure 58: Target polarisation of all three target cells as a function of the run number in 2011.

high (full points) photon virtualities are shown. Therefore, at the same Bjorken-x different photon virtualities are used in the calculation of the spin-independent structure function. In the case of the spin-independent structure function of the deuteron, only the results at high photon virtualities are shown. The uncertainty of the spin independent structure function at high photon virtualities correspond to the uncertainty of the parametrisation, which is about 2%.
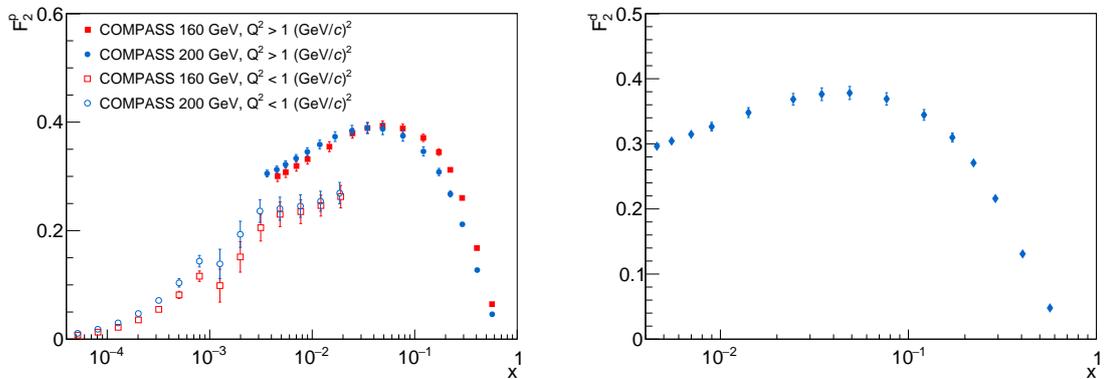
Figure 59: Left: Values of the F_2^p at the averaged Q^2 of the four COMPASS proton data sets. Right: Values of the F_2^d at the averaged Q^2 of the COMPASS deuteron data sets.

In the case of the analysis at low photon virtualities, three other parametrisations were considered in addition to the parametrisation obtained by SMC:

- A parametrisation based on the generalised vector meson dominance model [90, 91]. This parametrisation is valid for all Q^2 and for $10^{-5} < x < 0.1$.

- A parametrisation based on the saturation model [92], which is valid for $Q^2 < 100 \, (\text{GeV}/c)^2$ and for $10^{-6} < x < 0.1$.

- The ALLM parametrisation [93], which is obtained from a fit to the F_2 world data. The obtained parametrisation is valid for $Q^2 < 5000\,(\text{GeV}/c)^2$ and $3 \cdot 10^{-6} < x < 0.85$.

For the calculation of spin-dependent structure function at low photon virtualities, the parametrisation based on the generalised vector mesons dominance model was used for the kinematic range not covered by the SMC parametrisation. Here, the systematic uncertainty on the spin-independent structure function is obtained from the difference between the various available parametrisations:

$$\Delta F_2^i = \frac{F_2^{\text{ref}} - F_2^i}{2} \,,\tag{131}$$

where the F_2^{ref} is the value used in one bin and F_2^i are the values obtained for the various parametrisations. For the calculation of the systematic uncertainty the largest value of ΔF_2^i was used.

4.4.3 R *parametrisation*

The parametrisation of the transverse to longitudinal virtual photon absorption cross section ratio R is needed in the calculation of the asymmetry as it is part of the depolarisation factor (see Section 4.4.4). It is also needed to extract the spin-dependent structure function from the asymmetry (see Section 2.9), which partly cancels its contribution. This modifies the contribution to the systematic uncertainty of the spin-dependent structure function (see Section 5.2.8). The parametrisation was obtained by the E143 collaboration and is called R1998 [94]. They had extracted the cross section ratio by fitting the cross section data for scattering electrons off protons or off deuteron from various experiments. This parametrisation was modified by COMPASS to cover also lower value of the photon virtuality. For this reason, the behaviour for $Q^2 < 0.5\,(\text{GeV}/c)^2$ was modified [95]. This includes the behaviour of the cross section ratio $R \sim Q^2$ at $Q^2 = 0\,(\text{GeV}/c)^2$. The modification was done as follows:

$$R\left(Q^2 < 0.5\,(\text{GeV}/c)^2, x\right) = R_{1998}\left(0.5\,(\text{GeV}/c)^2, x\right) \cdot \beta \left(1 - \exp\left(-Q^2/\alpha\right)\right) \,.\tag{132}$$

Here, $\alpha = 0.2712\,(\text{GeV}/c)^2$ and $\beta = 1/\left(1 - \exp\left(0.5\,(\text{GeV}/c)^2/\alpha\right)\right)$ was used. Over the full Bjorken-x range, this modified function and its first derivative are continuous. The uncertainty on the cross section ratio at low photon virtualities was assumed to be 0.2. This covers the result obtained in the photoproduction limit ($R = 0$) and also the measured values at higher photon virtualities at HERA ($R = 0.4$) [96]. The resulting parametrisation is shown in Figure 60 as a function of Bjorken-x for the kinematics of the COMPASS data. The increased uncertainty at low photon virtualities is visible.

4.4.4 *Depolarisation factor*

The depolarisation factor describes the polarisation transfer from the lepton to the virtual photon. It is given by

$$D = \frac{y\left(\left(1 + \gamma^2 y/2\right)\left(2 - y\right) - 2y^2 m^2/Q^2\right)}{y^2\left(1 - 2m^2/Q^2\right)\left(1 + \gamma^2\right) + 2\left(1 + R\right)\left(1 - y - \gamma^2 y^2/4\right)} \,,\tag{133}$$
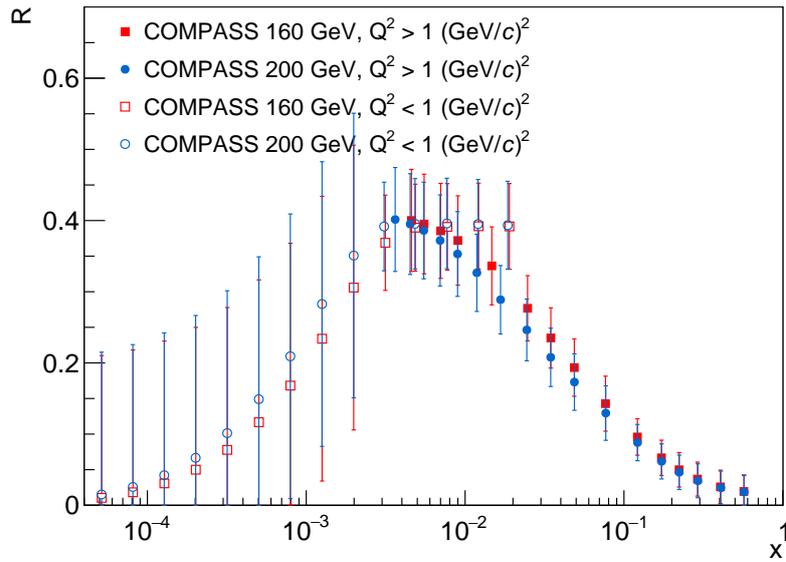
Figure 60: Values of R from the parametrisation of E143 including the COMPASS modifications as a function of Bjorken-x. The cross section ratio is shown for the kinematics of the four COMPASS proton data sets.

where $\gamma = 2Mx/\sqrt{Q^2}$ is a kinematic factor. It depends on the cross section ratio R described before. The depolarisation factor is shown in Figure 61 as a function of Bjorken-x for the kinematics of the COMPASS proton data. The increased uncertainty at low Bjorken-x is connected to the increased uncertainty of R at low photon virtualities.
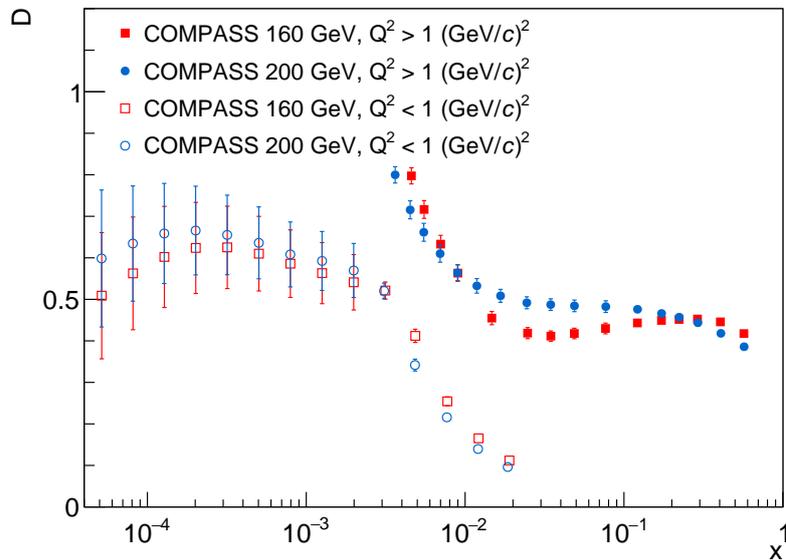
Figure 61: Values of the depolarisation factor as a function of Bjorken-x. It is shown for the kinematics of the four COMPASS proton data sets.

4.4.5 *Dilution factor*

The dilution factor takes into account that not all nucleons inside the target material can be polarised. A description of the dilution factor used at COMPASS is given in References [97, 98]. In a naive way, it is given by:

$$f = \frac{\text{Number of polarisable nucleons}}{\text{Number of all nucleons}} \ . \tag{134}$$

Using this relation, a dilution factor of $3/17 = 0.18$ is obtained for ammonia and of $4/8 = 0.5$ for lithium deuteride. In the case of lithium deuteride, the number of polarisable nucleons takes also into account that in addition to the deuteron the lithium nucleus can be described as a ^{4}He nucleus plus a deuteron.

The calculation of the dilution factor has to take into account the cross sections for scattering off the different contributions

$$f = \frac{n_{p(d)}\sigma_{p(d)}}{n_{p(d)}\sigma_{p(d)} + \sum_A n_A \sigma_A} = \frac{n_{p(d)}}{n_{p(d)} + \sum_A n_A \frac{\sigma_A}{\sigma_{p(d)}}} \ . \tag{135}$$

Here, n is the number of nuclei of either proton, deuteron or a element with atomic weight A and σ the spin-independent double differential total scattering cross section per nucleus. The additional deuteron inside of ^{6}Li is not taken into account here. It is considered by a correction factor. The cross sections include radiative processes and are not the ones for the one photon exchange. The difference between the cross section for scattering off a proton/deuteron and off the other material result in a Bjorken-x dependence of the dilution factor. This difference originates at high Bjorken-x mainly from the EMC effect and at low Bjorken-x mainly from radiative processes. A list of materials, which are present in the target, are given in Table 9 for the 2011 data taking and in Table 10 for the 2006 data taking. The cross section ratios are obtained from the ratio of the spin-independent structure function F_2. As these F_2 ratios were obtained by applying the radiative corrections to the measured cross section ratios, this needs to be undone [99]

$$\frac{F_2^A}{F_2^{p(d)}} = \frac{A}{A_{p/d}} \frac{\sigma_A}{\sigma_{p(d)}} \frac{\rho_A}{\rho_{p(d)}} \ . \tag{136}$$

Here, the factor $A/A_{p(d)}$ takes into account that the structure function F_2 is defined per nucleon and the ρ_i are the radiative corrections to the cross section for interactions on the nucleus i, which are calculated using TERAD [100–102].

4.4.6 *Additional corrections for ammonia*

The longitudinal double spin asymmetry has to be corrected due to the presence of spin-1 nuclei inside the ammonia target or due to the presence of spin-1/2 nuclei inside the lithium deuteride target. These materials result in an offset to the asymmetry. In addition also other spin-1/2 nuclei are present inside the ammonia target or other spin-1 nuclei inside the lithium deuteride target. These result in an increased amount of polarisable material inside the target. An example for such an contribution is the additional deuteron inside of lithium-6. Here, a calculation of those two correction factors is shown in the case of the ammonia target.

Table 9: Composition of the target material for each cell during the 2011 data taking.

	UPSTREAM (mol)	CENTRAL (mol)	DOWNSTREAM (mol)
Hydrogen	28.663 ± 0.265	59.835 ± 0.388	29.670 ± 0.335
Deuteron	0.003 ± 0.001	0.007 ± 0.001	0.003 ± 0.001
Helium-3	0.295 ± 0.035	0.563 ± 0.066	0.284 ± 0.035
Helium-4	6.357 ± 0.354	12.144 ± 0.642	6.128 ± 0.354
Nitrogen-14	9.520 ± 0.088	19.874 ± 0.129	9.855 ± 0.112
Nitrogen-15	0.035 ± 0.001	0.073 ± 0.001	0.036 ± 0.001

Table 10: Composition of the target material for each cell during the 2006 data taking.

	UPSTREAM (mol)	CENTRAL (mol)	DOWNSTREAM (mol)
Hydrogen	0.052 ± 0.006	0.100 ± 0.010	0.053 ± 0.006
Deuteron	10.261 ± 0.214	19.940 ± 0.329	10.558 ± 0.227
Helium-3	0.292 ± 0.040	0.599 ± 0.077	0.284 ± 0.040
Helium-4	3.633 ± 0.357	7.455 ± 0.667	3.536 ± 0.352
Lithium-6	9.859 ± 0.212	19.159 ± 0.329	10.144 ± 0.224
Lithium-7	0.454 ± 0.020	0.882 ± 0.035	0.467 ± 0.021

The counting rates for interactions inside the target with the two helicity states L and R can be expressed by

$$
\begin{aligned}
L(R) = a\Big[& (1-\eta_d)\, N_p \sigma_p \, (1 \pm A_p P_B P_p) && \text{Hydrogen} \\
& + \eta_d N_p \sigma_d \, (1 \pm A_d P_B P_d) && \text{Deuterium} \\
& + (1-\eta_{15})\, N_N \sigma_{14} \, (1 \pm A_{14} P_B P_{14}) && \text{Nitrogen-14} \\
& + \eta_{15} N_N \sigma_{15} \, (1 \pm A_{15} P_B P_{15}) && \text{Nitrogen-15} \\
& + \eta_3 N_3 \sigma_3 \, (1 \pm A_3 P_B P_3) && \text{Helium-3} \\
& + \sum_i N_i \sigma_i \Big] && \text{Unpolarised elements ,}
\end{aligned}
\tag{137}
$$

where a is the acceptance, P_B is the beam polarisation, η_i are the relative contributions of the element i or the element with $A = i$, η_{15}, for example, is the amount of nitrogen-15

inside of nitrogen, N_i are the number density of the different elements and P_i are the polarisations. From this expression the raw asymmetry can be obtained

$$A = \frac{L-R}{L+R} = P_p P_B f \left[A_p \left(1 - \eta_d\right)\right.$$

$$+ \eta_d \frac{P_d}{P_p} \frac{\sigma_d}{\sigma_p} A_d$$

$$+ \left(1 - \eta_{15}\right) \frac{N_{14}}{N_p} \frac{P_{14}}{P_p} \frac{\sigma_{14}}{\sigma_p} A_{14} \tag{138}$$

$$+ \eta_{15} \frac{N_{15}}{N_p} \frac{P_{15}}{P_p} \frac{\sigma_{15}}{\sigma_p} A_{15}$$

$$\left. + \eta_3 \frac{N_3}{N_p} \frac{P_3}{P_p} \frac{\sigma_3}{\sigma_p} A_3 \right] .$$

Using Equation 135 the dilution factor for the ammonia target is given by

$$f = \left(\left(1 - \eta_d\right) + \eta_d \frac{\sigma_d}{\sigma_p} + \eta_{15} \frac{N_N}{N_p} \frac{\sigma_{15}}{\sigma_p} + \eta_3 \frac{N_3}{N_p} \frac{\sigma_3}{\sigma_p} + \sum_i \frac{N_i}{N_p} \frac{\sigma_i}{\sigma_p} \right)^{-1} . \tag{139}$$

In order to relate the various asymmetries to known quantities, further assumptions on the asymmetries and the cross sections are used:

$$A_{15}\sigma_{15} = \beta_{15} g_{15} A_p \sigma_p , \tag{140}$$

$$A_{14}\sigma_{14} = \beta_{14} g_{14} \left(A_p \sigma_p + A_n \sigma_n\right) , \tag{141}$$

$$A_d \sigma_d = \gamma_d \left(A_p \sigma_p + A_n \sigma_n\right) , \tag{142}$$

$$A_3 \sigma_3 = \beta_3 g_3 A_p \sigma_p . \tag{143}$$

Here, β_i takes into account nuclear effects, for example, the polarisation of the deuteron inside lithium-6, g_i is the parametrisation of the EMC effect for an element and $\gamma_d = 1 - 1.5\omega_d$ takes into account that the deuteron can be in the $L = 2$ state. Using these assumptions, the longitudinal double spin asymmetry of the proton is calculated from Equation 138:

$$A_p = \frac{A}{P_p P_B f C_1} + C_2 \frac{\sigma_d}{\sigma_p} A_d . \tag{144}$$

Here, two new functions C_1 and C_2 are introduced. The function C_1 increases the amount of polarisable material inside the target due to the presence of other spin-1/2 nuclei, whereas the function C_2 accounts for the offset to the asymmetry due to the presence of spin-1 nuclei inside the target. The two functions are given by:

$$C_1 = \left(1 - \eta_d\right) + \eta_{15} \frac{N_N}{N_p} \frac{P_{15}}{P_p} \beta_{15} g_{15} + \eta_3 \frac{N_3}{N_p} \frac{P_3}{P_p} \beta_3 g_{15} , \tag{145}$$

$$C_2 = -\frac{1}{C_1} \left(\eta_d \frac{P_d}{P_p} + \left(1 - \eta_{15}\right) \frac{N_N}{N_p} \frac{P_{14}}{P_p} \frac{\beta_{14} g_{14}}{\gamma_d} \right) . \tag{146}$$

The factor C_1 is include into the dilution factor, whereas the correction including the function C_2 is applied as an correction to the asymmetry:

$$\Delta A_p = C_2 \frac{\sigma_d}{\sigma_p} A_d . \tag{147}$$

Here, the deuteron asymmetry enters in the correction, which is given by a parametrisation from JLAB [103]. The cross section ratio σ_p/σ_d is calculated using the ratio of the spin-independent structure functions F_2. In order to calculate the correction factors the following numbers are used (taken from [98]):

- Polarisations:

$$P_p = (89.0 \pm 2.5)\%$$
$$P_D = (29.2 \pm 2.8)\%$$
$$P_3 = (2.0 \pm 1.0)\%$$
$$P_{14} = (14.1 \pm 1.4)\%$$
$$P_{15} = (-4.1 \pm 1.5)\%$$

- Relative contributions:

$$\eta_{14NH_3} = 0.99621$$
$$\eta_{14ND_3} = 0.00011$$
$$\eta_{15NH_3} = 0.00368$$
$$\eta_{15ND_3} = 0.0$$
$$\eta_{3He} = 0.09081$$
$$\eta_{4He} = 0.90919$$

- Corrections for nuclear effects:

$$\beta_3 = 0.86 \pm 0.010$$
$$\beta_{15} = -0.3333 \pm 0.010$$
$$\beta_{14} = -0.3333 \pm 0.010$$

4.4.7 *Additional corrections for lithium deuteride*

In the case of lithium deuteride similar correction factors are obtained taking into account different materials. The factors are given by:

$$C_1 = (1 - \eta_p) + (1 - \eta_7)\frac{N_{Li}}{N_d}\frac{P_6}{P_d}\frac{\beta_6}{\gamma_d}g_6 , \tag{148}$$

$$C_2 = -\frac{1}{C_1}\left(\eta_p\frac{P_p}{P_d} + \eta_7\frac{N_{Li}}{N_d}\frac{P_7}{P_d}\frac{\beta_7 g_7}{\gamma_d}\right) . \tag{149}$$

The factor C_1 is included in the dilution factor, as in the case of ammonia. Here, C_1 account, for example, for the additional deuteron inside of lithium-6, which increases the amount of polarisable material. The factor C_2 will be used as an correction for the asymmetry due to the presence of spin-1/2 nuclei. This factor is included in a correction factor applied to the asymmetry. It is given by:

$$\Delta A_d = C_2\frac{\sigma_p}{\sigma_d}A_p , \tag{150}$$

where the cross section ratio σ_d/σ_p is calculated using the ratio of the spin-independent structure functions F_2 and the proton asymmetry is given by a parametrisation from JLAB [103]. The quantities needed to calculate the correction factors are (taken from References [97, 98]):

- Polarisations:

$$P_p = (100.0 \pm 1.0)\%$$
$$P_D = (40.6 \pm 0.3)\%$$
$$P_6 = (45.07 \pm 0.041)\%$$
$$P_7 = (90.0 \pm 0.9)\%$$

- Relative contributions:

$$\eta_p = 0.002$$
$$\eta_7 = 0.045$$

- Corrections for nuclear effects:

$$\beta_6 = 0.866 \pm 0.012$$
$$\beta_7 = 0.62 \pm 0.05$$

4.4.8 Radiative corrections

The structure function F_2 is is given for the one photon (1γ) exchange. Therefore, radiative corrections have to be applied to the measured cross section. The same is valid in the case of the spin-dependent structure function g_1 and also the asymmetry A_1. The cross section can be expressed as

$$\sigma = \nu\sigma^{1\gamma} + \sigma_{tail} \tag{151}$$

in the spin-independent case and in the spin-dependent case for the cross section difference between parallel and antiparallel orientation of the lepton and target spin as

$$\Delta\sigma = \nu\Delta\sigma^{1\gamma} + \Delta\sigma_{tail} . \tag{152}$$

The second term, which is either σ_{tail} or $\Delta\sigma_{tail}$, can be decomposed into various contributions. A contribution from elastic scattering off the nucleus, quasielastic scattering, which is elastic scattering on the nucleons inside the nucleus, and inelastic scattering:

$$\sigma_{tail} = \sigma_{tail}^{el} + \sigma_{tail}^{qel} + \sigma_{tail}^{inel} ,$$
$$\Delta\sigma_{tail} = \Delta\sigma_{tail}^{el} + \Delta\sigma_{tail}^{qel} + \Delta\sigma_{tail}^{inel} . \tag{153}$$

The factor ν is given by contributions from the vacuum polarisation and the vertex correction. It is found to be close to one. In Figure 62, the different contribution are illustrated in addition to the one photon exchange.

In the case of "inclusive" deep inelastic scattering, all contributions have to be taken into account. Events for elastic and quasielastic scattering can simulate deep inelastic scattering

(a) 1γ exchange   (b) Initial state radiation   (c) Final state radiation   (d) Vertex correction   (e) Vacuum polarisation
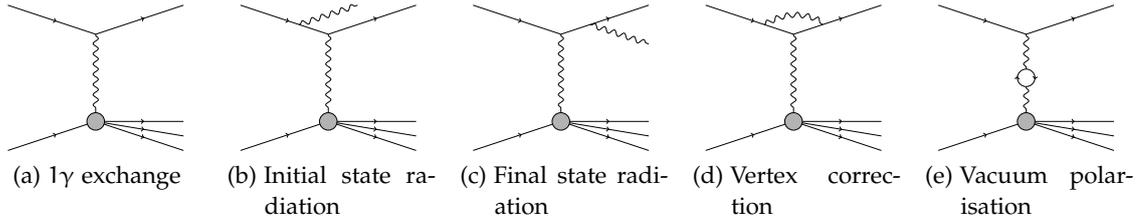
Figure 62: Various processes, which contribute to radiative corrections to the one photon exchange in inclusive deep inelastic scattering.

ones due to the emission of a photon, which changes the kinematics. In the case of "semi-inclusive" deep inelastic scattering, in addition to the scattered lepton also a hadron is detected. For this reason, the contributions from elastic and quasielastic scattering vanish as no hadron is emitted in such processes. Therefore, the dilution factor is different for "inclusive" and "semi-inclusive" measurements.

The expression for the measured asymmetry is modified by taking into account radiative corrections,

$$A_1^{\text{meas}} = \rho \left(A_1 + A_{\text{RC}} \right) . \tag{154}$$

Here, $\rho = \nu\sigma^{1\gamma}/\sigma$ takes into account the spin-independent radiative corrections. It is the same one used in Equation 136 for protons or deuterons ($\rho_{p(d)}$). The spin-dependent radiative corrections are included in

$$A_{\text{RC}} = \frac{\Delta\sigma_{\text{tail}}}{2\nu D\sigma^{1\gamma}} . \tag{155}$$

Here, D is the depolarisation factor. The spin-dependent contributions are calculated as corrections to the asymmetry using the program POLRAD [104]. They are shown in Sections 5.3.1 and 5.5.1 and compared to the statistical uncertainty of the COMPASS data sets. The factor ρ is included in the dilution factor forming an effective dilution factor including also the correction factor C_1

$$f' = \rho C_1 f . \tag{156}$$

These corrections are calculated using a program called TERAD [100–102], which takes into account also further corrections like corrections to the hadron not shown in Figure 62. The dilution factor including all modifications is shown in Figure 63 for the "inclusive" and "semi-inclusive" case. The difference between both results at low Bjorken-x is explained by the difference in the radiative corrections described before.
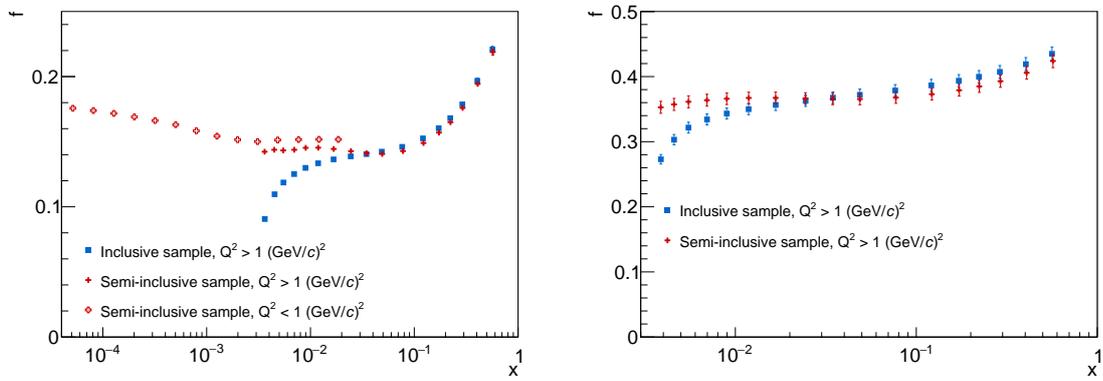
Figure 63: Values for the dilution factor as a function of Bjorken-x calculated for the kinematics of the four COMPASS proton data sets (left) and the COMPASS deuteron data set (right).

ASYMMETRY AT HIGH PHOTON VIRTUALITIES

The longitudinal double spin asymmetry A_1 is extracted in two different ranges of Q^2. Here, the analysis for the range $Q^2 > 1\,(\text{GeV/c})^2$ is described. This analysis uses the new data from the 2011 data taking and the one from the 2006 data taking. In the case of the data of the 2006 data taking, the asymmetry is studied using a deuteron target. For this measurement the nominal momentum of the beamline of $160\,\text{GeV/c}$ was used. Here, already results from COMPASS exist for the asymmetry from earlier data takings [105]. The 2006 data are used to improve the statistical accuracy of the asymmetry A_1^d and the structure function g_1^d.

In the case of the 2011 data taking, the nominal momentum of the muon beam was increased from $160\,\text{GeV/c}$ to $200\,\text{GeV/c}$ compared to 2006. This allows to reach higher photon virtualities and also lower values of the Bjorken scaling variable. Using the data from 2011 the asymmetry A_1 for protons is obtained, which complements the result from the 2007 data taking.

An overview of the years of data taking is given in Table 11. In this table the different targets and beam momenta used for the asymmetry measurement are listed together with the published papers. In this chapter the data selection is described in Section 5.1 and

Table 11: Overview on the years of data taking connected to the measurement of the asymmetry A_1

YEAR	NOMINAL BEAM MOMENTUM	TARGET	PUBLICATIONS
2002 - 2004	$160\,\text{GeV/c}^2$	Deuteron	[105], [95]
2006	$160\,\text{GeV/c}^2$	Deuteron	This work
2007	$160\,\text{GeV/c}^2$	Proton	[106]
2011	$200\,\text{GeV/c}^2$	Proton	This work

the systematic studies in Section 5.2. They are described independent of the two years of data taking. The results for the asymmetry and the structure function using the proton target are described in Sections 5.3 and 5.4, whereas the result using the deuteron target are described in Sections 5.5 and 5.6.

5.1 DATA SELECTION

The data selection for the extraction of A_1 at $Q^2 > 1\,(\text{GeV/c})^2$ is split into two parts. A preselection, which reduces the size of the data files significantly and a second selection step, at which the final event selection is performed. This allows for a quick reselection of events later on. This procedure is possible as only a small contribution ($\sim 10\%$) of the recorded events matches the condition on the photon virtuality.

5.1.1 *Preselection of the data*

The preselection is performed to reduce the size of the data set for the analysis. For this reason only basic cuts are applied. The first requirement on the events is the presence of a primary vertex that should have a scattered muon attached to it. For the scattered muon no quality checks are performed. Such tests are left for later data selections. Additionally a cut in the photon virtuality is applied. In the case of the 2006 data also a cut on the relative virtual photon energy y is applied to further reduce the size of the data set. The effect of the preselection is shown in Table 12. The larger amount of rejected events in 2011, for example, by the requirement of a primary vertex is connected to changes in the reconstruction program. Before only events with at least one reconstructed vertex were kept, whereas now all kinds of events are kept.

Table 12: Various cuts applied during the preselection of the data. The fraction of events left after each cut with respect to the initial sample is given.

	2006		2011	
CUT	EVENTS$/10^6$	(%)	EVENTS$/10^6$	(%)
Reconstructed Events	2558	100.0	12940	100.0
Primary vertex	2375	92.8	7921	61.2
Scattered muon	1409	55.1	1955	15.1
$Q^2 > 0.9\,(\text{GeV/c})^2$	123	4.8	202	1.6
$0.05 < y < 0.95$	102	4.0	-	-

5.1.2 *Selection for A_1 analysis*

The data selection for the A_1 analysis starts using the preselected data. Again the primary vertices with an incoming and scattered muon are selected. Now the quality options for the scattered muon are used. They reject events with more than one possible scattered muon and events, in which the track of the scattered muon does not cross the hodoscopes of the corresponding trigger. In addition, cuts on the incoming muon are applied. It was checked that the momentum of the incoming muon is measured and its momentum should be in the range of $\pm 20\,\text{GeV/c}$ around the nominal beam momentum. In the case of the 2011 data this range is narrowed down to $\pm 15\,\text{GeV/c}$ on the level of the asymmetry calculation due to a limited validity range of the parametrisation of the beam polarisation. In order to equalise the flux through the target cells, the extrapolation of the incoming muon track is required to pass all target cells. The primary vertex has to be inside of one of the target cells and the polarisation of this target cell should be known. Otherwise the event is discarded. In addition, kinematic cuts are applied to the data. The photon virtuality Q^2 should be larger than $1\,(\text{GeV/c})^2$ and the relative virtual photon energy y should be larger than 0.1 and smaller than 0.9. The lower limit removes events that are difficult to reconstruct due to the small energy transfer, while the upper limit removes events that have large radiative corrections. These cuts result in a Bjorken-x range of $x > 0.0025$ for the data taking in 2011 and of $x > 0.004$ for the data taking in 2006.

In addition the region with $x > 0.7$ is removed from the data due to the spectrometer acceptance. In order to ensure a good reconstruction of the event, the energy balance for the outgoing hadrons is checked by calculating the ratio $z = E_h/\nu$ of the energy of each outgoing hadron, assuming it is a pion, and the energy of the virtual photon. If this quantity is larger than one the event is discarded. In the asymmetry calculation, a distinction is made whether an event is triggered by an "inclusive" or a "semi-inclusive" trigger (see Section 3.5). For this reason, the number of those events is given in Table 13 in addition to the number of events passing the cuts used in the data selection.

Table 13: Effect of the data selection for the high Q^2 analysis. The last two rows show the size of the two kinds of event classes used for the asymmetry calculation.

	2006		2011	
CUT	EVENTS/10^6	(%)	EVENTS/10^6	(%)
Primary vertex with scattered muon	97	100.0	174	100.0
Measured target polarisation	96	99.4	174	99.9
Beam momentum cut	96	98.9	174	99.8
No particles with $z > 1$	95	98.7	173	99.4
Q^2 cut	88	90.9	162	93.0
y cut	71	73.7	101	58.1
Equalise beam flux	59	61.3	98	56.2
Primary vertex inside the target	46	47.9	79	45.3
Beam quality	46	47.9	77	44.2
x cut	46	47.9	77	44.2
"Inclusive" events	30	31.0	65	37.1
"Semi-inclusive" events	16	16.1	12	6.8

The classification of the events in "inclusive" and "semi-inclusive" ones is done as follows: If an "inclusive" trigger is present, the events is classified as an "inclusive" event. In the case of no "inclusive" trigger the "semi-inclusive" ones are checked. If they are present, the event is classified as a "semi-inclusive" one. If both "inclusive" and "semi-inclusive" trigger are present, the event still remains in the "inclusive" class. Events that are triggered by a pure calorimeter trigger are also part of the "semi-inclusive" class. The major difference between the classification for data taken in 2011 and 2006 is that the ladder trigger was changed to an "inclusive" trigger and that the LAS trigger was newly introduced. In addition, the inclusive middle trigger was prescaled in 2006. Therefore only every second trigger attempt was recorded and events with only a semi-inclusive middle trigger exist. In Figure 64, the relative contribution of the different classes of events is shown as a function of Bjorken-x and the photon virtuality for the data taken in 2011 and in Figure 65 for the data taken in 2006.

For each year of data taking, the relative contribution from "inclusive" triggers to the statistics of the different years is the dominant one over the full Bjorken-x range. As a function of the photon virtuality, it is visible that "inclusive" triggers contribute mainly
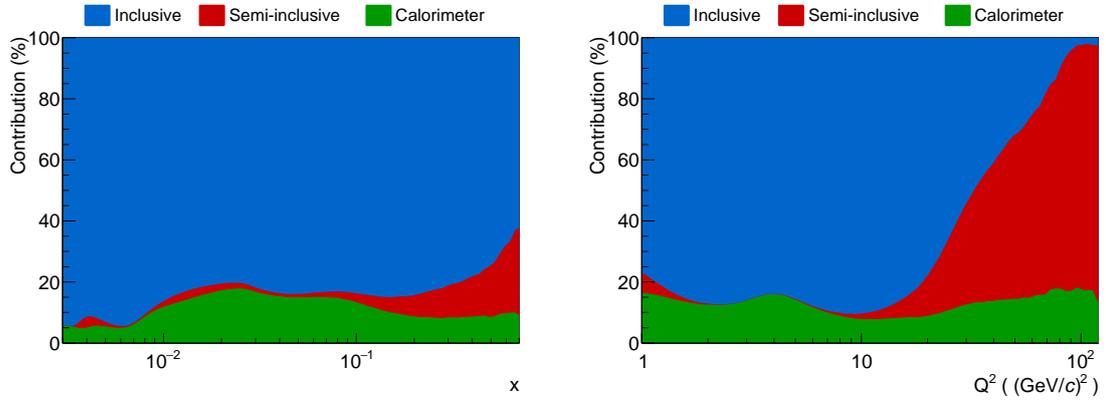
Figure 64: 2011 data. The relative contribution from the "inclusive", "semi-inclusive" and pure calorimeter triggers as a function of Bjorken-x (left) and the photon virtuality (right).
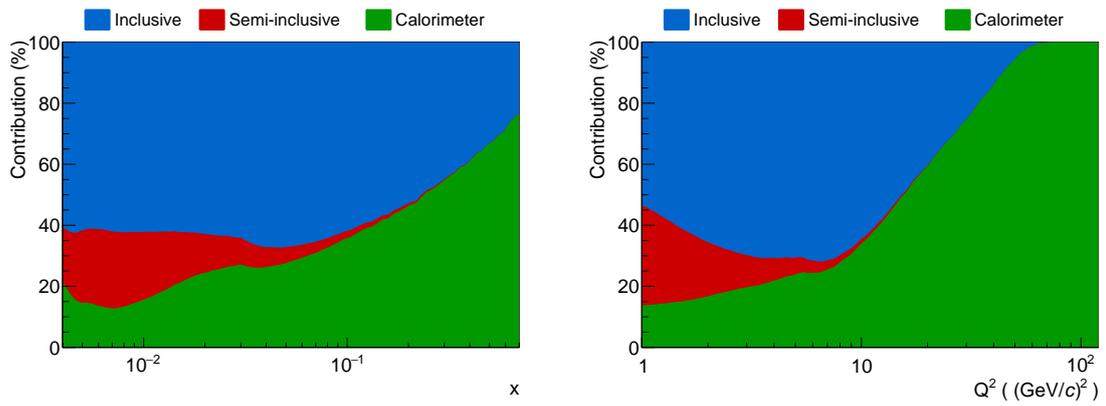


Figure 65: 2006 data. The relative contribution from the "inclusive", "semi-inclusive" and pure calorimeter triggers as a function of Bjorken-x (left) and the photon virtuality (right).

to lower values of the photon virtuality, whereas "semi-inclusive" and pure calorimeter triggered events are dominant at high photon virtualities. In Figure 67, the relative contributions from the different triggers are shown for the data taken in 2006 and in Figure 66 for the data taken in 2011.
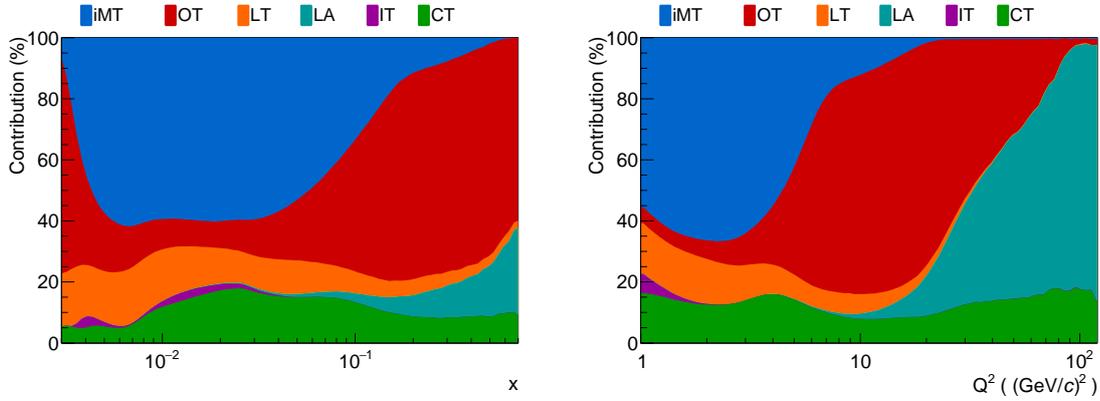
Figure 66: 2011 data. The relative contribution from the individual triggers as a function of Bjorken-x (left) and the photon virtuality (right).
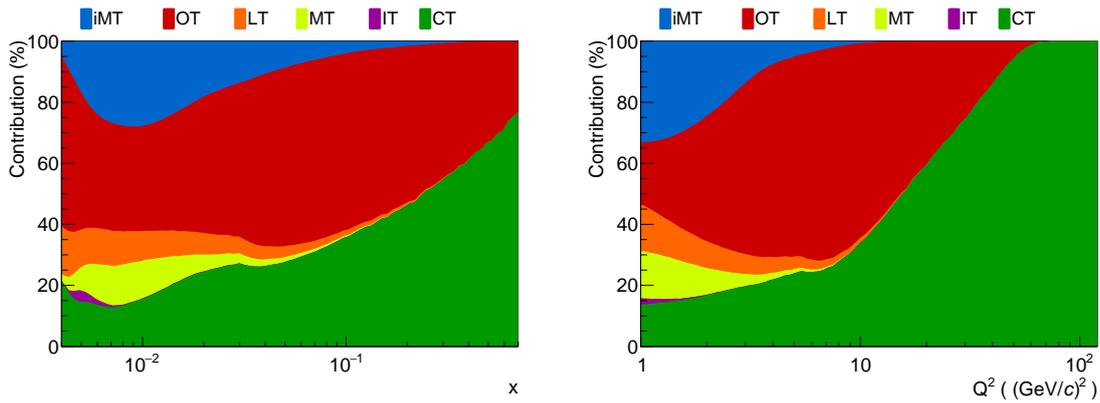
Figure 67: 2006 data. The relative contribution from the individual triggers as a function of Bjorken-x (left) and the photon virtuality (right).

The number of events obtained from the data taken in 2011 after all selection cuts is $77 \cdot 10^6$. This is about the same amount of events as used in the analysis of the data taken in 2007 where $93 \cdot 10^6$ events were selected. The difference in the number of events is caused by the increased beam momentum in 2011, which results in a lower beam intensity. The increased beam momentum results in a shift of the kinematic range of the data towards lower values of Bjorken-x and higher photon virtualities. The kinematic coverage of the 2006 and 2011 data is shown in Figure 68. In the case of the data taken in 2006 the final amount of events is $46 \cdot 10^6$. This increases the statistics used in the calculation of the asymmetry A_1^d compared to the data set from the 2002-2004 data taking by about 50%.
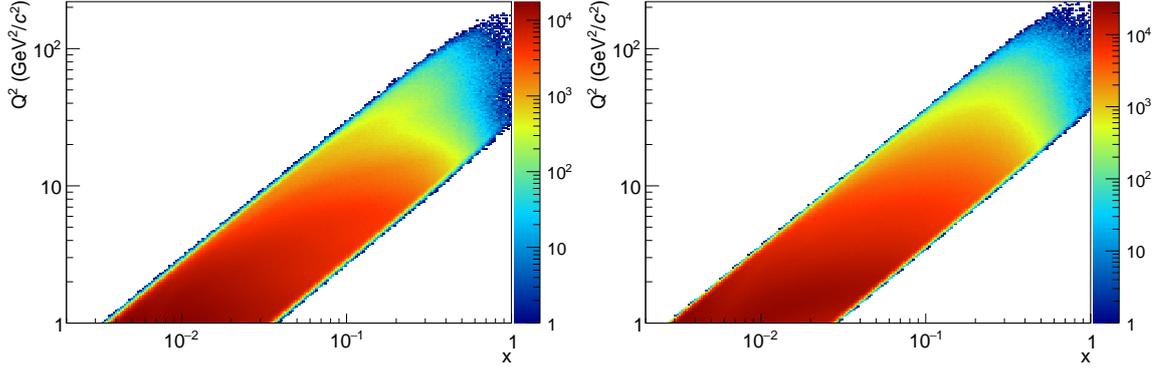
Figure 68: Kinematic coverage of the 2006 (left) and 2011 (right) data in Bjorken-x and the photon virtuality.

5.2 FALSE ASYMMETRIES

The size of the measured raw asymmetries, extracted from the counting rates is rather small and only about 2.5% at largest Bjorken-x in the case of the proton. The size of the measured photon-nucleon asymmetry is rather large. The measured raw asymmetry is shown together with the measured photon-nucleon asymmetry without any corrections in Figure 69.
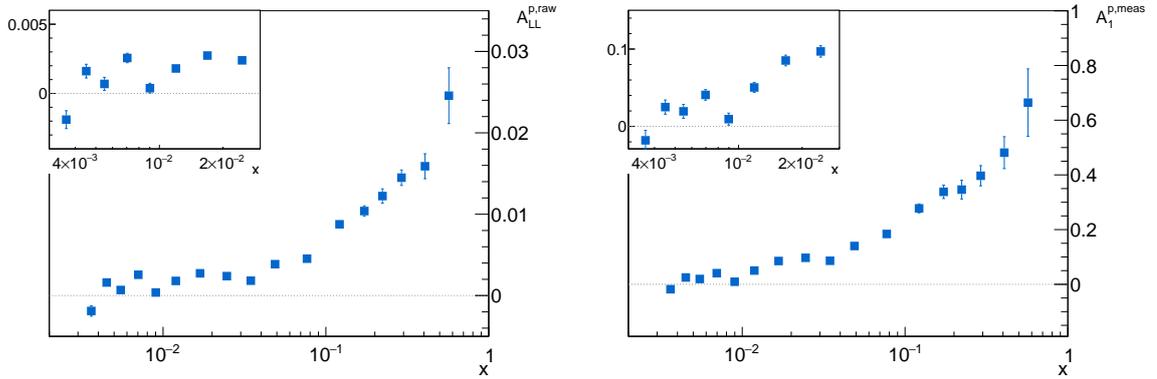
Figure 69: Left: Measured raw asymmetry as a function of Bjorken-x obtained from the 2011 proton data. Right: Measured photon-nucleon asymmetry without any corrections.

First, the assumption for a cancellation of the acceptance in the calculation of the asymmetry is tested. This is done using the data. The studies presented in this section are performed in order to determine the size of the systematic uncertainty compared to the statistical precision of the data. In addition, the various contributions from the inputs used in the calculation to the systematic uncertainty are given at the end of this section. These can be identified from the equation containing the different contributions to the one photon exchange asymmetry

$$A_1^{1\gamma} = \frac{1}{fDP_BP_T}A_{LL}^{raw} - \left(\frac{\eta A_2}{\rho} + A_1^{RC} + A_{false}\right) \, . \tag{157}$$

Contributions from, for example, spin-1 nucleons in the target in the case of the proton asymmetry are not shown. The studies on the acceptance cancellation focus on the contribution of false asymmetries, whereas the contributions from spin-dependent radiative corrections, A_1^{RC}, and the contribution from the asymmetry A_2 are small.

5.2.1 *Different data groupings*

The data from one year of data taking are split into different weeks that consist of groups of stable data taking. These groups contain the data recorded before and after a rotation of the solenoid field. Two ways for combining the groups are used, which are explained in Section 4.3. Here, the results for the asymmetry are compared using the consecutive grouping and a global grouping, where the asymmetry is calculated for the full year at once. This test shows false asymmetries connected to changes in the spectrometer. The result obtained from both groupings is shown in Figure 70 for the data from 2006 and 2011. No significant difference between both methods is visible. For the analysis, the consecutive grouping is chosen.
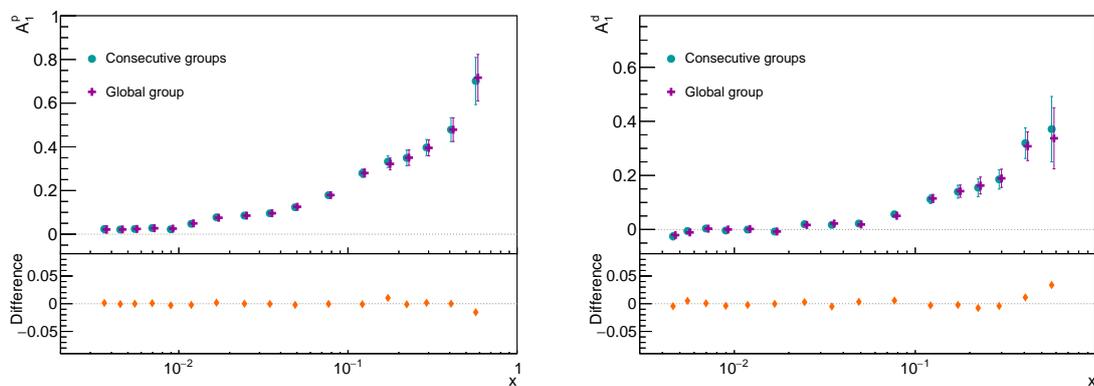
Figure 70: Result for the asymmetry A_1^p (left) obtained from the 2011 data and A_1^d (right) obtained from the 2006 data using two different ways for combining the various periods. The results for the global grouping are slightly shifted for better visibility.

5.2.2 *Direct search for false asymmetries*

A direct way to find hints on false asymmetries is using such groupings of the data, which results in no physics asymmetry. In such cases deviations from zero can be interpreted as a hint on the presence of false asymmetries. For these test, different groupings are used, which are explained in the following sections. Two different ways are used to investigate such effects.

5.2.2.1 *Using fake configurations*

Usually the data are combined using groups containing a rotation of the solenoid field. Those groups contain the data taken close in time, for example during one or two days. Due to the solenoid field rotation, for each target cell data with both polarisation directions exist. In order to test for the presence of false asymmetries the data are combined using

the data from adjacent groups, which have the same polarisation direction of the cells. The difference between the two groupings is illustrated in Figure 71 for a two cell target together with the direction of the solenoid field. Using such a grouping results in a
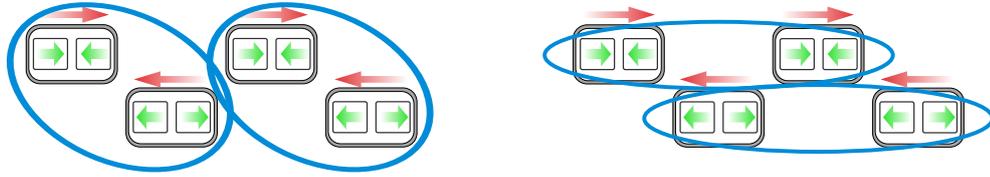
Figure 71: Illustration on how the fake configurations (right) are formed compared to the consecutive ones (left). The green arrows correspond to the polarisation direction of the target cells and the red ones show the direction of the solenoid field. The blue circles illustrate how the groups are formed.

zero physics asymmetry and can show false asymmetries, which are connected to a time dependence of the acceptance. The asymmetries obtained from the two years of data taking are shown in Figure 72. In both cases the asymmetry is compatible with zero, as expected. The χ^2 probability for the asymmetries to be compatible with zero is in the case of the 2011 data 34% for the "inclusive" sample and 54% for the "semi-inclusive" sample. The probabilities for the case of the 2006 data are 45% and 67% respectively.
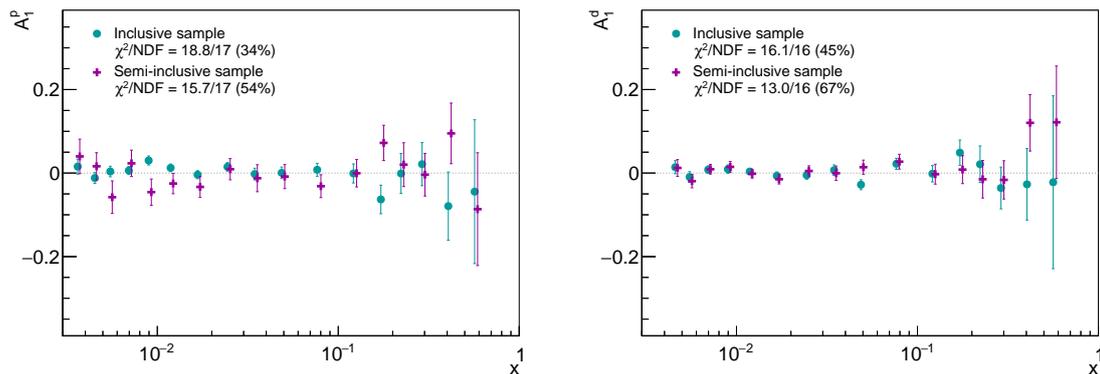
Figure 72: Result for the asymmetry obtained from the data using fake configurations. The results for the "semi-inclusive" sample are slightly shifted for better visibility and the χ^2 for both samples to be compatible with zero is given. Left: Results for the 2011 data taking. Right: Results for the 2006 data taking.

5.2.2.2 *Using the target cells*

Another possibility to form a physics asymmetry, which is zero, can be obtained by combining the data from target cells with the same polarisation direction. The simplest way to combine the cells is shown in Figure 73. For the asymmetry calculation two groups are formed. One is formed by using the two outer cells of a three cell target and the second one is formed by using the central cell, which has to be divided artificially into two equally sized cells. This results in a zero asymmetry as always data with the same polarisation direction is used. For the two new groupings, a non zero asymmetry hints on possible acceptance differences or on possible problems with the homogeneity of the target polar-
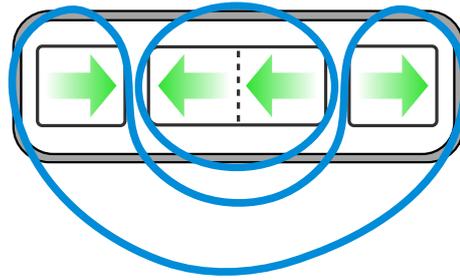
Figure 73: Illustration on combining the data inside one group using target cells with the same polarisation direction. The central cell has to be artificially be divided into two cells. The green arrows represent the polarisation direction of the target cells.

isation. Both asymmetries are obtained separately for the two years of data taking for the two samples and are shown in Figure 74 for the 2006 data and in Figure 75 for the 2011 one. All are found to be in agreement with zero within their statistical uncertainties.
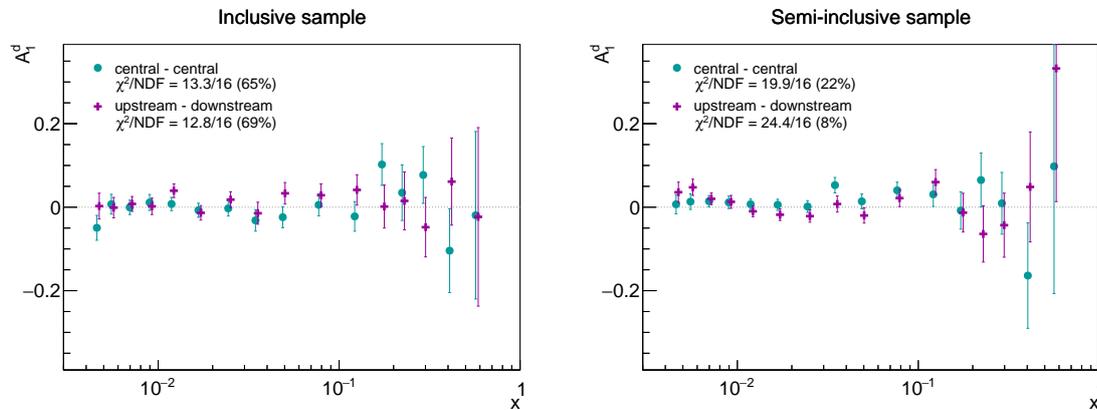
Figure 74: Results for the asymmetries obtained from the 2006 data combining target cells with the same polarisation direction. The results for the combination of the outer cells are slightly shifted for better visibility and the χ^2 for both samples to be compatible with zero is given. Left: Results for the "inclusive" sample. Right: Result for the "semi-inclusive" sample.

The χ^2 probability for the asymmetries obtained from the 2006 data and the 2011 data are listed in Table 14 for all combinations. The χ^2 probability for the asymmetries to be compatible with zero is in the case of combining the outer cells lower than for combining the central cells. This effect is produced by a larger acceptance difference between both outer cells compared to the central one. A better cancellation is obtained when calculation the photon-nucleon asymmetry from all target cells combined.

5.2.3 *Compatibility between the two microwave settings*

As the polarisation direction in each target cell is changed by changing the direction of the solenoid field, the relative direction between the polarisation and the field direction remains the same. This might also change the acceptance for both directions. In order to cancel such an influence, once in 2006 and 2011 the target polarisation was destroyed. Afterwards the target polarisation was rebuild with a different relative direction between
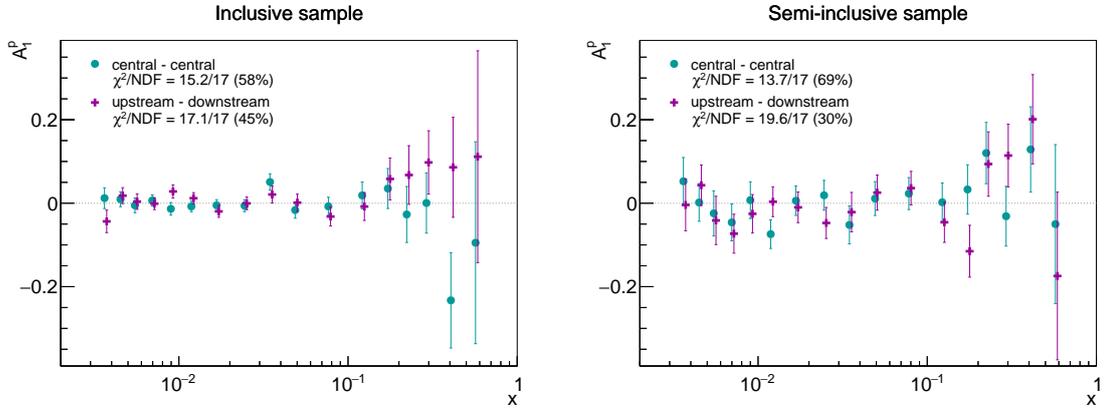
Figure 75: Results for the asymmetries obtained from the 2011 data combining target cells with the same polarisation direction. The results for the combination of the outer cells are slightly shifted for better visibility and the χ^2 for both samples to be compatible with zero is given. Left: Results for the "inclusive" sample. Right: Result for the "semi-inclusive" sample.

Table 14: χ^2 probabilities for the asymmetries obtained from combining the outer or central cells to be compatible with zero. The probabilities are shown for the 2006 and 2011 data for both samples.

	2006		2011	
SAMPLE	OUTER CELLS	CENTRAL CELL	OUTER CELLS	CENTRAL CELL
Inclusive	69%	65%	45%	58%
Semi-inclusive	8%	22%	30%	69%

the polarisation and the solenoid field using the microwave frequencies connected to the new polarisation direction (see Section 3.2). In this way, possible systematic effects connected to the relative direction can be cancelled. This divides the data taking year in two separate periods with the same relative direction, for which the asymmetry is calculated separately. The two periods are labelled plus and minus. The weeks of data taking belonging to each of the two periods are listed in Table 15. The results for the asymmetry

Table 15: Sharing of data between the two microwave periods in 2006 and 2011. In both years only one reversal was done.

YEAR	−	+
2006	W32 W33 W34 W35 W36 W37	W40 W41 W42 W43 W44 W45 W46
2011	W25 W27 W30 W31 W32 W33 (W34)	W36 W38 W39 W41 W43

are compared with one another and are shown in Figure 76 for the data taken in 2006 and in Figure 77 for the data taken in 2011 for the "inclusive" and "semi-inclusive" samples. In these figures also the difference between both groups is shown. It shows no hints for a possible false asymmetry for neither the "inclusive" nor the "semi-inclusive" sample. Possible false asymmetries connected to the direction of the solenoid field cancel in the combination of the two microwave periods.
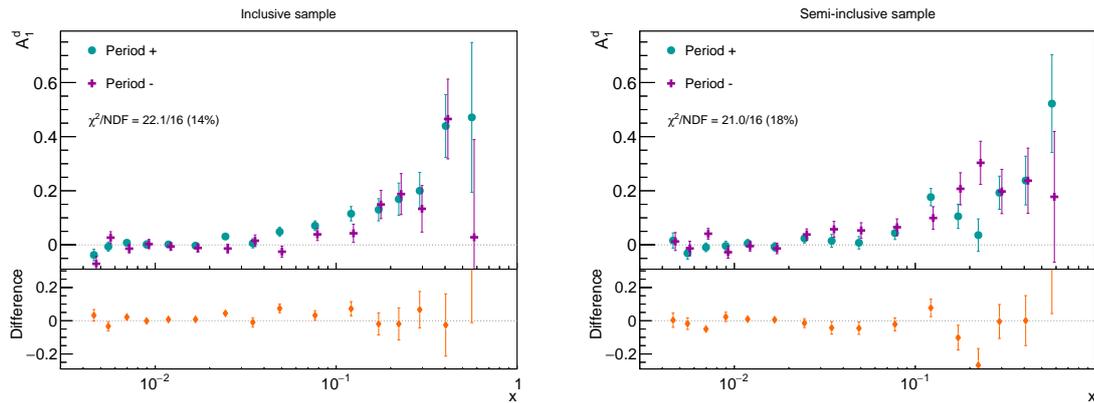
Figure 76: Results for A_1^d obtained from the 2006 data for the two periods with different microwave settings. The difference between both results is shown on the bottom. The results for period − are slightly shifted for better visibility and the χ^2 for both samples to be compatible with one another is given.

5.2.4 *Further studies for systematic effects*

Beyond the studies already mentioned before, additional test were performed. A test checking the stability of the detector was performed by calculating the asymmetry separately in distinguished parts of the spectrometer depending on the direction of the scattered muon. The asymmetry obtained for the case that the scattered muon is detected in the left half is compared to the case that the scattered muon is detected in the right half. Also the case where the scattered muon is detected in the upper part is compared to the case
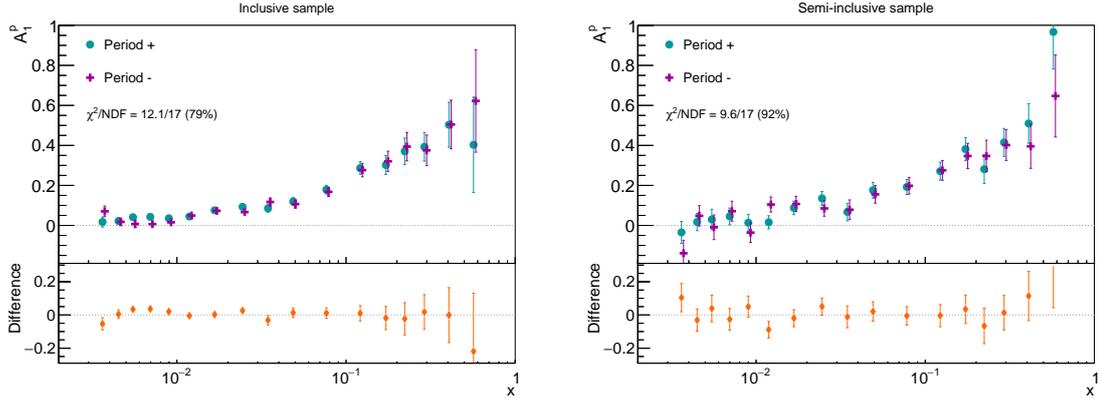
Figure 77: Results for A_1^p obtained from the 2011 data for the two periods with different microwave settings. The difference between both results is shown on the bottom. The difference between both results is shown on the bottom. The results for period $-$ are slightly shifted for better visibility and the χ^2 for both samples to be compatible with one another is given.

that the muon is detected in the lower part. In both cases no hint for false asymmetries was found. As the experimental hall of the COMPASS experiment is located on the surface, temperature difference between day and night are present. In order to test whether these temperature changes that lead to some changes in the detector performance have an influence on the extracted asymmetry, the results for the asymmetry are compared for samples recorded during the day and during the night. No hints for systematic effects are found. A test similar to the comparison of the two groups with different microwave settings was performed based on the solenoid field direction. Here, the data groups with the same direction of the solenoid field are combined. This test should show up possible correlations between the acceptance and the direction of the solenoid field. No hints on false asymmetries were found.

5.2.5 *Upper limit on false asymmetries*

From all the tests described before, no hint on false asymmetries were found using different combinations of the data. In order to obtain an upper limit on possible false asymmetries, a statistical method is used. This method uses the so called "pulls" distribution. A pull r_i is calculated as difference between the asymmetry ($A_{1,i}$) obtained for a certain group using the consecutive grouping and the result obtained by combining all groups ($\overline{A}_1$) using the weighted mean, normalised to the statistical uncertainty of the individual asymmetry:

$$r_i = \frac{A_{1,i} - \overline{A}_1}{\Delta A_{1,i}^{stat}} \ . \tag{158}$$

Here, i denotes the different groups. The method is described in Reference [107]. In absence of false asymmetries, the obtained distribution should be a Gaussian distribution centred at zero with a standard deviation of one. A broadening of such distribution can be used to estimate the upper limit for the presence of false asymmetries. The pulls distributions are obtained using the 39 groups used for the 2011 data and the 33 groups

used for the analysis of the 2006 data. For each of those groups two asymmetries are obtained ("inclusive" and "semi-inclusive" sample) and used to calculate the pulls. Their distribution is shown for each Bjorken-x bin in Figure 78 for the data taken in 2006 and in Figure 79 for the data taken in 2011.
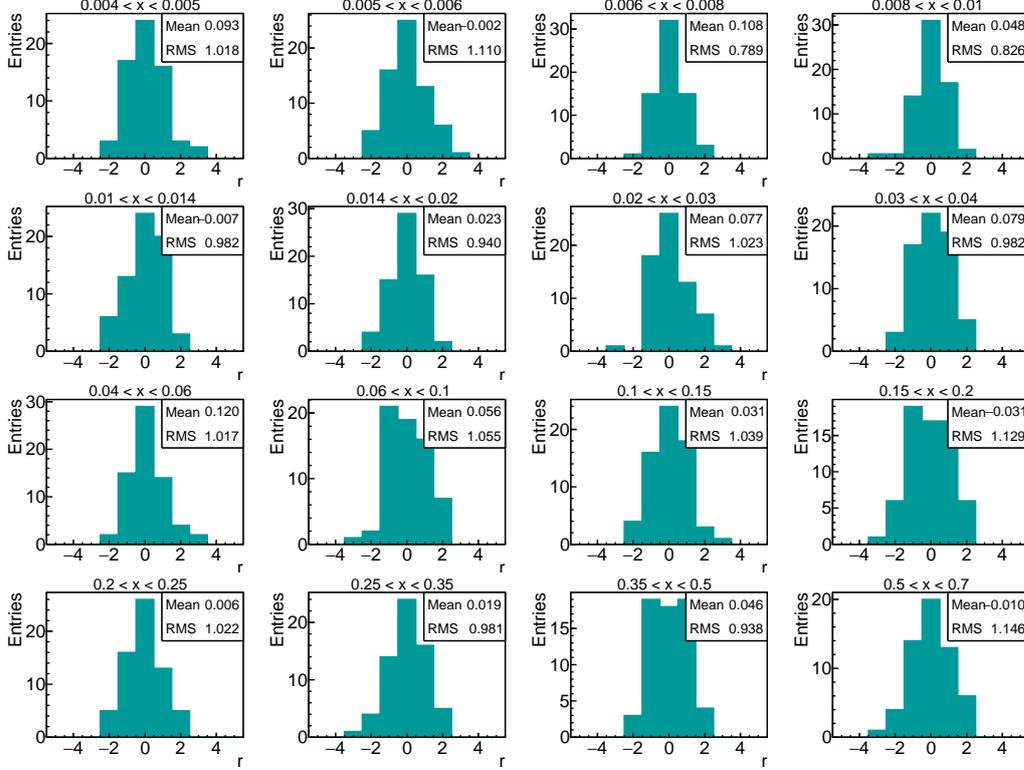
Figure 78: Pulls distributions obtained from the data taken in 2006 for each Bjorken-x bin. The results from the two samples of the 33 periods are shown.

For each Bjorken-x bin in both years the mean value and the standard deviation of the distribution is calculated. All are in agreement with the expected value, giving no hint towards time dependent effects on the asymmetry. The results for the mean value and standard deviation in each bin is used to calculate an upper limit for the systematic uncertainty due to false asymmetries. In principle, the standard deviation of a pull, σ_{tot}, has two contributions. The first, σ_{stat}, represents the one from statistics, which is equal to one. The second, σ_{syst}, leads to a possible broadening due to systematic effects,

$$\sigma_{tot}^2 = \sigma_{stat}^2 + \sigma_{syst}^2 \ . \tag{159}$$

The upper limit for the standard deviation of the pulls distribution is obtained from the data. As the standard deviation can also be smaller than one the upper limit, σ_{tot}^{lim}, is estimated using the uncertainty of the standard deviation $(\Delta\sigma_{tot})$ and the total standard deviation (σ_{tot})

$$\sigma_{tot}^{lim} = \Delta\sigma_{tot} + \mathrm{Max}\,(1, \sigma_{tot}) \ . \tag{160}$$

From this upper limit, a limit for the uncertainty on possible false asymmetries is than given by

$$\sigma^{syst} = \sqrt{(\Delta\sigma_{tot} + \mathrm{Max}\,(1, \sigma_{tot}))^2 - 1} \ . \tag{161}$$
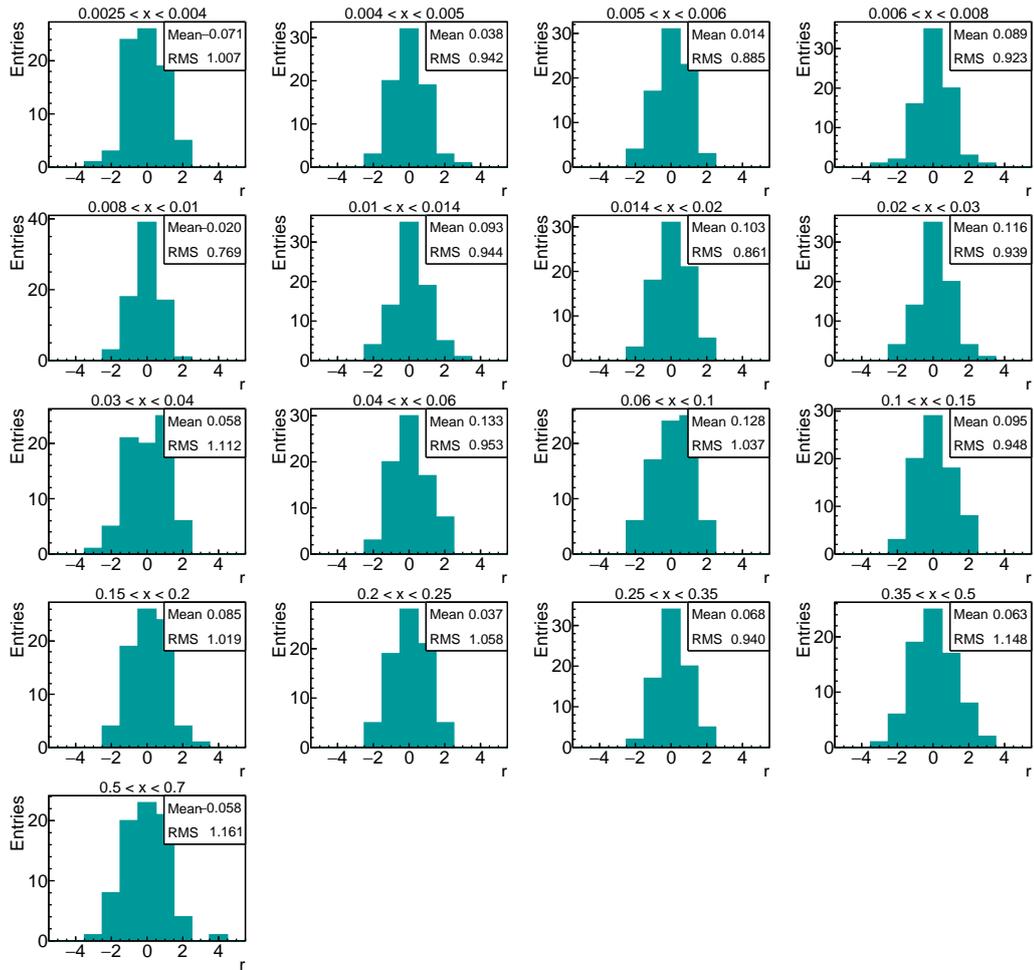
Figure 79: Pulls distributions obtained from the data taken in 2011 for each Bjorken-x bin. The results from the two samples of the 39 periods are shown.

5.2.6 *Bias due to semi-inclusive triggers*

Using "semi-inclusive" triggers in the calculation of the inclusive asymmetry A_1 might introduce a bias. At large Bjorken-x, the invariant mass of the hadronic final state is smaller than at low Bjorken-x. Therefore, only a small number of hadrons is produced. Due to the different detection probabilities for charged and neutral hadrons, a possible bias can be introduced as the fragmentation of up quarks into charged hadrons is more abundant than the one of down quarks. This results into a bias due to different contributions from up and down quarks to the asymmetry [88]. This influence can be determined using a Monte Carlo simulation. This method was already used by SMC and the influence was been found to be negligible [88]. The program used for this analysis is called POLDIS [108]. It uses the LEPTO [109] Monte Carlo generator to generate events. Afterwards a weight is calculated for each event based on parton helicity distributions and unpolarised parton distributions. The Fortran code of the most recent version was converted to C++ for easier access to the various functions and to add support for various sets of helicity distributions and unpolarised parton distribution functions. In the version used by SMC, an external LEPTO generator was used. It is replaced in order to use already existing Monte Carlo data, which were generated using the COMPASS setup of 2011 with a proton target.

5.2.6.1 *Method*

POLDIS uses information from the LEPTO generator stored in a block of LEPTO information. It contains information on the kind of interaction and the quark interacting with the virtual photon. In addition, the kinematic variables are also stored and are accessed by POLDIS. These information are used to calculate the asymmetry as follows:

1. Get information on the process, the target and the quark (LST 22,24,25)

2. Get the polarised and unpolarised PDFs for the Bjorken-x and photon virtuality of the process

3. Select the PDFs for the quark flavour in this reaction

4. Calculate cross section ratio R and the depolarisation factor D

5. Calculate the asymmetry A_{LL} for this process

6. Calculate the asymmetry $A_1^i = A_{LL} \cdot q(x, Q^2)/\Delta q(x, Q^2)/D$

7. Calculate the mean value of the asymmetry A_1^i for all events

The calculation of A_{LL} depends on the type of interaction, which occurred. In POLDIS the following processes are considered in the calculation:

- $\gamma q \longrightarrow q$

- $\gamma q \longrightarrow qg$

- $\gamma q \longrightarrow q\bar{q}$

- $\gamma q \longrightarrow q\bar{q}$ (Heavy quarks)

The conversion from the Fortran code into C++ allowed to update the implemented parton distributions. The C++ version contains additional sets of helicity distributions and unpolarised parton distribution functions. This version supports the following parton distribution functions:

- Unpolarised parton distributions
    - MSTW [110] (LO and NLO)
    - NNPDF 3.0 [111] (LO and NLO)

- Helicity distributions
    - AAC [50] (LO and NLO)
    - BB [112] (LO and NLO)
    - BB 2010 [113] (NLO)
    - DNS 2005 [114] (LO and NLO)
    - GRSV [115] (LO and NLO)
    - LSS 2001 [116] (LO and NLO)
    - LSS 2005 [117] (LO and NLO)
    - LSS 2006 [118] (NLO)
    - LSS 2010 [119] (NLO)
    - NNPDF(pol) 1.1 [120] (NLO)
    - COMPASS (NLO)

Three of the parton helicity distributions do not differentiate between the various flavours of the sea quarks. In the case of the BB parametrisations the valence distributions for up and down quarks is available together with a sea quark distribution. For the COMPASS fit (described in Chapter 7) the assumption $\Delta s = \Delta \bar{s}$ is used and only the sum of quark and antiquark distributions is obtained. Here, the assumption that the sea quark helicity distributions are the same for each flavour is used for the calculation. For the cross section ratio R different parametrisations can be used:

- $R = 0$

- R NMC [121]

- R 1990 [122]

- R 1998 [94]

5.2.6.2 *Results for the 2011 setup*

The influence of "semi-inclusive" triggers on the asymmetry A_1^p was tested using an existing Monte Carlo simulation of the 2011 setup with a proton target. From these data the generator information are extracted and stored for the analysis using POLDIS. All events are split into two classes based on the trigger, which would have triggered the event, similar to the selection done for real data (see Section 5.1). In the case of the presence of an

"inclusive" trigger bit, the event is added to the "inclusive" sample. In the case of no "inclusive" trigger and the presence of a "semi-inclusive" bit or only the calorimeter trigger bit is set, the event is added to the "semi-inclusive" sample. Both samples are processed in POLDIS and the asymmetry is calculated using different parton distributions. An example for the calculated asymmetry using the unpolarised parton distributions from MSTW and the polarised ones from GRSV2000 in next-to-leading and leading order is shown in Figure 80.
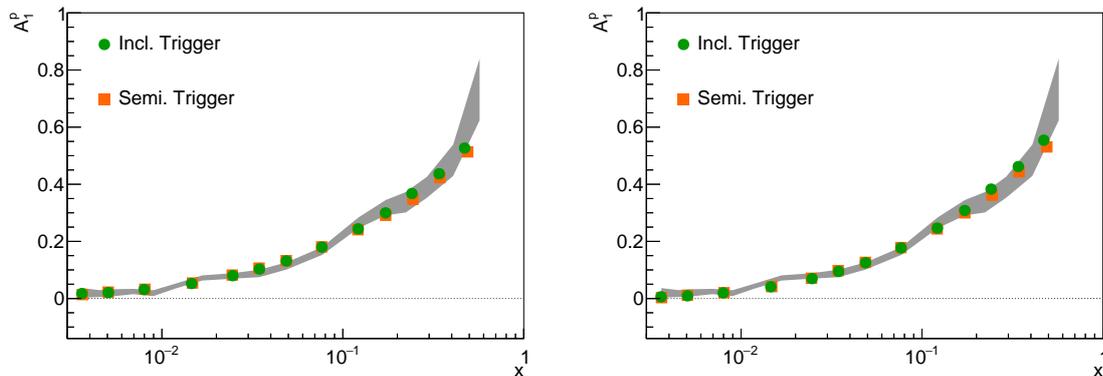
Figure 80: Comparison between A_1^p obtained from POLDIS using the parton distribution functions from MSTW and the helicity distributions from GRSV for "inclusive" and "semi-inclusive" trigger. Left: Results using leading order sets. Right: Results using next-to-leading order sets. The grey band indicates the results for A_1 from the 2011 data with its statistical uncertainty.

The asymmetry is obtained for all implemented parton distributions. The difference between the result obtained from "inclusive" and "semi-inclusive" sample is shown in Figure 81. The difference is compared to the statistical uncertainty of the 2011 data. The Monte Carlo simulation of the 2011 setup is done in leading order. Therefore, the results obtained using leading order parton distributions are used for the estimate of the bias. From these results only small offset is found by including "semi-inclusive" triggers in the extraction of the asymmetry. The offset between both samples is below $\sim 0.1 \Delta A_{1,\text{stat}}^p$. This contributions will be neglected in the systematic uncertainty of A_1 as the offset depends on the combination of the various parton distributions. Using different parton distributions smaller offsets can be found. In addition, the contribution from the "semi-inclusive" sample to the full data set is much smaller than the one from the inclusive sample (see Table 13) and no hint on an offset is found by comparing the results from the data for both samples.

5.2.7 *Additional sources of systematic uncertainties*

So far only two contributions to the systematic uncertainty of A_1 are discussed. Additional contributions to the systematic uncertainty are due to the external inputs used in the extraction of the asymmetry. They can be split in an additive and a multiplicative contribution. From Equation 157, the contributions to the additive and multiplicative part can
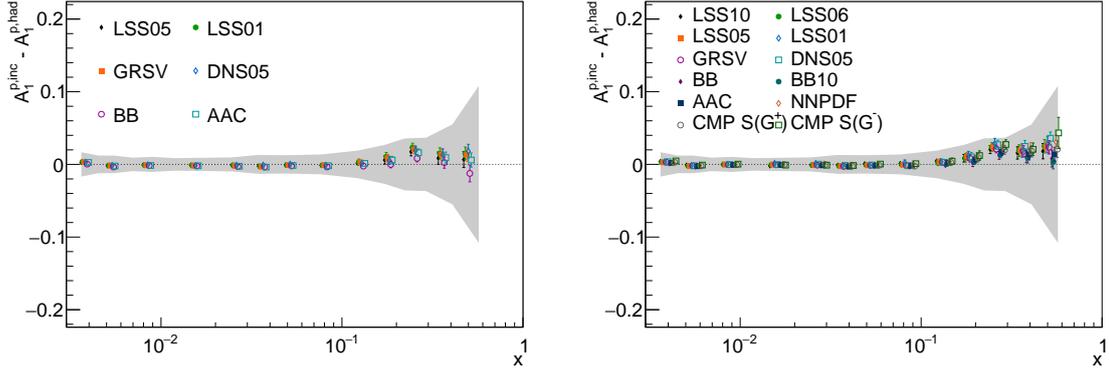
Figure 81: Comparison between the statistical uncertainties of the 2011 data (grey band) and the difference between the asymmetry obtained by using only "inclusive" or "semi-inclusive" triggers. The results for various parton distributions are shown. Left: Results using leading order sets. Right: Results using next-to-leading order sets.

be identified. The multiplicative part contains the uncertainties on the target and beam polarisation and the uncertainties on the depolarisation factor and dilution factor,

$$\Delta A_1^{\text{mult}} = A_1 \sqrt{\left(\frac{\Delta P_B}{P_B}\right)^2 + \left(\frac{\Delta P_T}{P_T}\right)^2 + \left(\frac{\Delta f}{f}\right)^2 + \left(\frac{\Delta D(R)}{D(R)}\right)^2} \,. \tag{162}$$

Here, the assumption is made, that corrections to the measured asymmetry are small, which will be shown in Sections 5.3.1 and 5.5.1. The contributions to the additive part of the uncertainty are due neglecting the transverse asymmetry A_2, the uncertainty on the spin-dependent radiative corrections and possible false asymmetries,

$$\Delta A_1^{\text{add}} = \sqrt{\left(\frac{\eta}{\rho} A_2\right)^2 + \left(\Delta A_1^{\text{RC}}\right)^2 + \left(\Delta A_{\text{false}}\right)^2} \,. \tag{163}$$

5.2.7.1 *Multiplicative contributions*

The contributions to the multiplicative contribution, which have no kinematic dependence, can be used as a normalisation uncertainty. These are uncertainties connected to the target and beam polarisation (described in Section 4.4.1). The uncertainty on the beam polarisation is the same for all years as it is obtained from a Monte Carlo simulation of the beamline. It is in the order of 5%. In the case of the target polarisation the uncertainty depends on the year. The uncertainty depends on the temperature measurements of the target and the measurement of the NMR signal. This is summarised in Reference [69] for the data taking in 2011. The uncertainty on the target polarisation is 3.5% for the 2011 data and 5% in the case of the 2006 data. The uncertainty of depolarisation factor and dilution factor (see Sections 4.4.4 and 4.4.5) is also part of the multiplicative uncertainty but depend on the kinematics. The uncertainty on the depolarisation factor is given by the parametrisation of the longitudinal to transverse polarised photon absorption cross section $R = \sigma_L/\sigma_T$. The resulting uncertainty of the depolarisation factor is between 2% and 3% for both years depending on the kinematics. In the case of the dilution factor the uncertainty is caused by uncertainties on the contributions and the weight of the

different materials present in the target. In addition, the uncertainties on the cross section ratios and the radiative corrections used in the calculation of the dilution factor contribute to the uncertainty. The resulting uncertainty is about $2-3\%$ and also has a kinematic dependence. The total multiplicative uncertainty is about 8% in the case of the 2006 data and about 7% in the case of the 2011 data.

5.2.7.2 *Additive contributions*

During the calculation of the asymmetry A_1, the contribution from the transverse asymmetry A_2, which enters via the factor ηA_2, was neglected. The factor η is given by

$$\eta = \frac{y\left((1+\gamma^2 y/2)\,(2-y) - 2y^2 m^2/Q^2\right)}{y^2\,(1-2m^2/Q^2)\,(1+\gamma^2)\,2\,(1+R)\,(1-y-\gamma^2 y^2/4)}\ . \tag{164}$$

Here, $\gamma = 2Mx/\sqrt{Q^2}$, the lepton mass m and the proton mass M are used. This contribution was neglected due to the small size of A_2 in the kinematic range of COMPASS and the small size of the factor η (see Section 2.9). The factor η is below 0.1. The contribution to the uncertainty was calculated for each data point using the size of A_2 from Reference [38]. Based on this measurement, $A_2^p = 0.05$ for $x < 0.5$ and $A_2^p = 0.1$ for $x \geqslant 0.5$ are assumed. In the case of the deuteron measurement the size of A_2^d is assumed to be 0.02 for $x < 0.15$, 0.05 for $0.15 < x < 0.55$ and 0.2 for the high Bjorken-x region. The uncertainty obtained is below 10^{-2}.

Another contribution to the systematic uncertainty is the uncertainty on the spin-dependent radiative corrections (see Section 4.4.8). These are calculated using POLRAD [104], their size is shown later in Sections 5.3.1 and 5.5.1. Within this program a parametrisation of the asymmetry A_1 is used to obtain the corrections. Varying the parameters results in different corrections to the asymmetry. From these changes the uncertainty of this contribution is estimated to be

$$\Delta A_1^{RC} = 0.1 \cdot \mathrm{Max}\left(|A_{1,\mathrm{incl}}^{RC}|, |A_{1,\mathrm{semi\text{-}incl}}^{RC}|\right) \tag{165}$$

as the largest difference was in the order of 10%. The resulting uncertainty on the asymmetry is below 10^{-3}.

5.2.8 *Contribution to the systematic uncertainty of g_1*

For the calculation of the spin-dependent structure function $g_1 = A_1 F_2/(2x(1+R))$ from the asymmetry A_1 two additional contributions have to be considered, the structure function F_2 (see Section 4.4.2) and the cross section ratio R (see Section 4.4.3). The uncertainty on F_2 is taken from the parametrisation of SMC [88] and amounts to about 2%. The uncertainty of the cross section ratio R also contributes to the uncertainty of the depolarisation factor. Therefore, this uncertainty is recalculated for the spin-dependent structure function using the quantity

$$h = D\,(1+R) \tag{166}$$

in the calculation of the systematic uncertainty instead. The size of this contribution is shown in Figure 82 compared to the size of the systematic contribution taking into account both contributions separately.
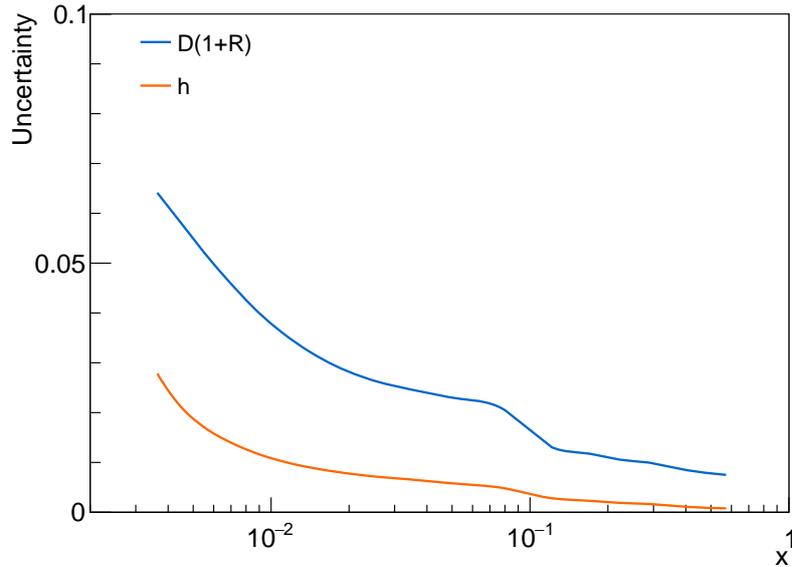
Figure 82: Illustration of the size of the systematic uncertainty from taking into account the uncertainties on the depolarisation factor and the cross section ratio R independently and in a combined way.

5.2.9 *Calculation of the full systematic uncertainty*

From the two previously discussed contributions to the systematic uncertainty the full systematic uncertainty is calculated:

$$\Delta A_1^{\text{syst}} = \sqrt{\left(\Delta A_1^{\text{mult}}\right)^2 + \left(\Delta A_1^{\text{add}}\right)^2} \tag{167}$$

In the case of the spin-dependent structure function, the multiplicative contribution is modified to take into account the additional contribution from the spin-independent structure function and the contribution from the depolarisation factor is exchanged by the combined contribution from the cross section ratio R and the depolarisation factor. The size of the different contributions to the systematic uncertainty of the asymmetry are summarised in Table 16. The contributions to the spin-dependent structure function are summarised in Table 17.

The relative contributions from all contributions to the systematic uncertainty are shown in Figure 83 and Figure 84 for the data taken in 2006 and 2011. Here, also the relative contributions for the spin-dependent structure function are shown in addition to the ones for the asymmetry. In both cases, the upper limit on the presence of false asymmetries is the largest contribution from the systematic uncertainty.

5.3 ASYMMETRY RESULTS USING A PROTON TARGET

The asymmetry A_1^{p} using a proton target was measured by COMPASS in 2007 [106] using a 160 GeV/c muon beam. Here, the results from the data taken in 2011 are presented. Due to the increased beam energy in 2011, larger photon virtualities and smaller Bjorken-x values are reached compared to the 2007 data. This is shown in Figure 85.

Table 16: Summary for the systematic uncertainty of A_1 for the data taken in 2006 and 2011.

		2006	2011
Beam polarisation	$\Delta P_B/P_B$	5%	5%
Target polarisation	$\Delta P_T/P_T$	5%	3.5%
Depolarisation factor	$\Delta D(R)/D(R)$	$2-3\%$	$2-3\%$
Dilution factor	$\Delta f/f$	$2-3\%$	2%
Total	ΔA_1^{mult}	$\simeq 0.08 \cdot A_1^d$	$\simeq 0.07 \cdot A_1^p$
False asymmetry	ΔA_1^{false}	$< 0.75 \cdot \sigma_{stat}$	$< 0.84 \cdot \sigma_{stat}$
Transverse asymmetry	$\eta \cdot \Delta A_2$	$< 10^{-2}$	$< 10^{-2}$
Rad. corrections	ΔA_1^{RC}	$10^{-5} - 10^{-3}$	$10^{-4} - 10^{-3}$

Table 17: Summary for the systematic uncertainty of g_1 for the data taken in 2006 and 2011.

		2006	2011
Beam polarisation	$\Delta P_B/P_B$	5%	5%
Target polarisation	$\Delta P_T/P_T$	5%	3.5%
Factor $h = D(1+R)$	$\Delta h/h$	$0-3\%$	$0-3\%$
Dilution factor	$\Delta f/f$	$2-3\%$	2%
Structure function F_2	$\Delta F_2/F_2$	2%	2%
Total	ΔA_1^{mult}	$\simeq 0.09 \cdot g_1^d$	$\simeq 0.08 \cdot g_1^p$
False asymmetry		$< 0.75 \cdot \sigma_{stat}$	$< 0.84 \cdot \sigma_{stat}$
Transverse asymmetry		$< 10^{-3}$	$< 10^{-2}$
Rad. corrections		$10^{-5} - 10^{-3}$	$10^{-4} - 10^{-2}$
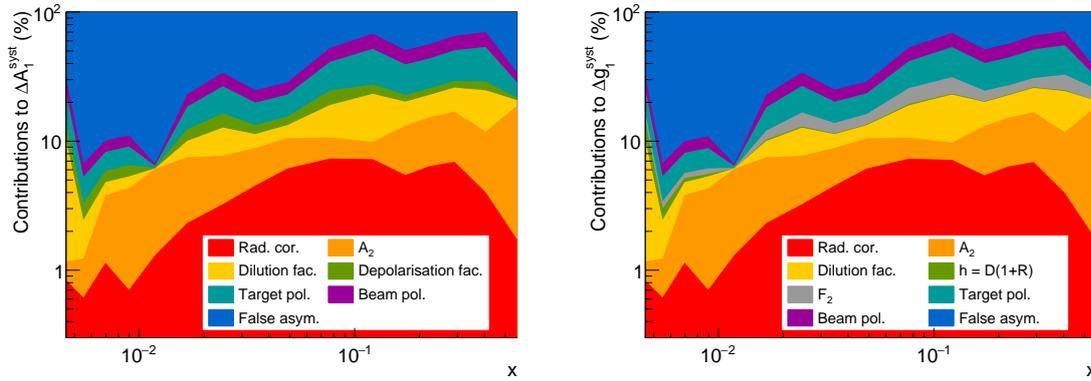
Figure 83: Relative contributions to the full systematic uncertainty for the data taken in 2006. Left: Contributions in the case of the asymmetry A_1^d. Right: Contributions in the case of the structure function g_1^d.
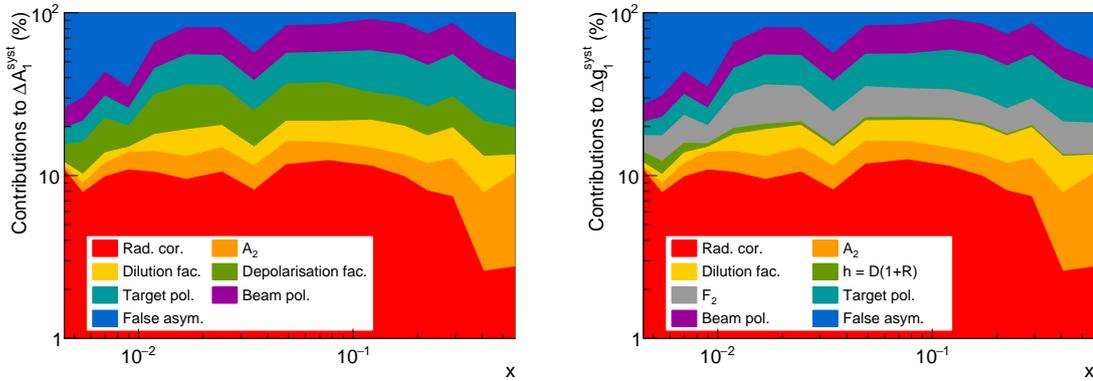
Figure 84: Relative contributions to the full systematic uncertainty for the data taken in 2011. Left: Contributions in the case of the asymmetry A_1^p. Right: Contributions in the case of the structure function g_1^p.
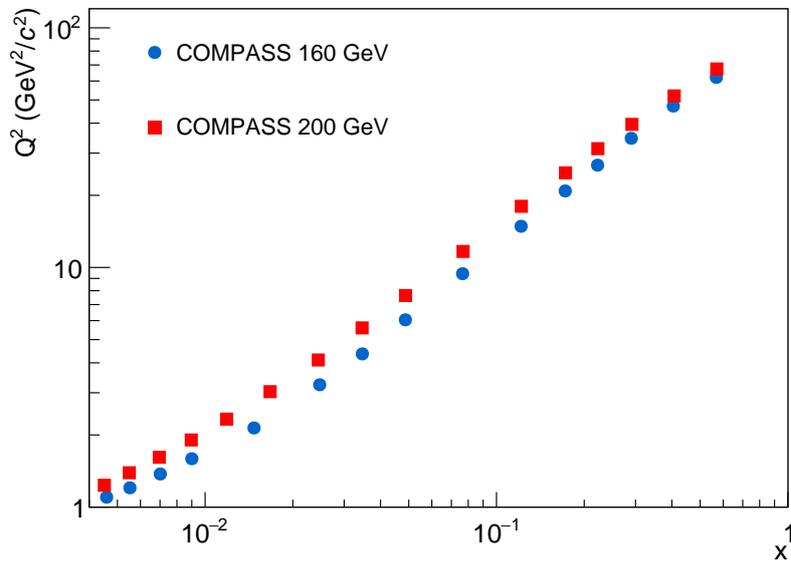
Figure 85: Comparison between the mean values of the photon virtuality and Bjorken-x for the 2011 and 2007 proton data.

As described in Section 5.1, the asymmetry obtained from the "inclusive" and "semi-inclusive" sample is shown in Figure 86. The inset shows the region of low Bjorken-x where the the asymmetry is small. The results from both samples agree well with one an-
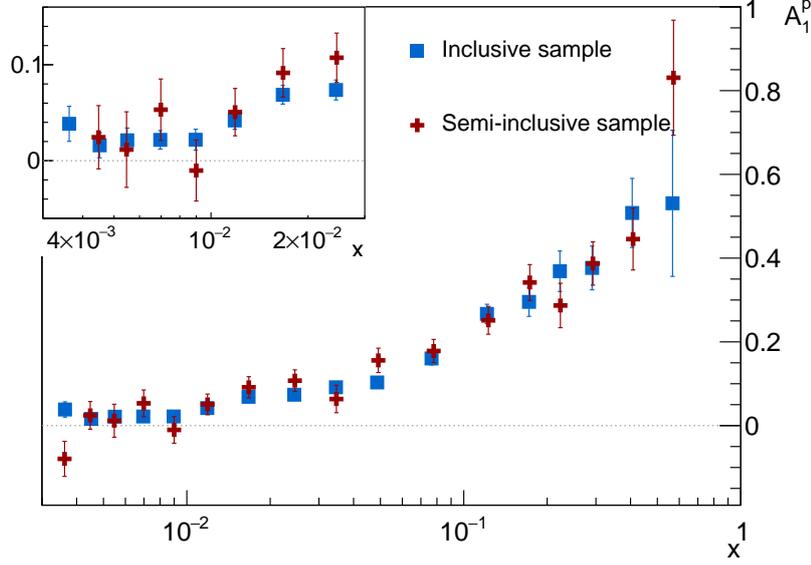
Figure 86: Results for the asymmetry A_1^p as a function of Bjorken-x obtained for the "inclusive" and "semi-inclusive" sample from the 2011 data.

other. The χ^2 probability is 34%. This supports the assumption that no false asymmetries are introduced by using also "semi-inclusive" trigger for the extraction of the inclusive asymmetry. Before obtaining the final results for the asymmetry, some corrections have to be applied.

5.3.1 Corrections to the asymmetry

The results from the "inclusive" and "semi-inclusive" sample can be combined after applying the spin-dependent radiative correction calculated using POLRAD (see Section 4.4.8). This correction has to be applied first due to different contribution to this correction for both samples and differences in the kinematics. The absolute and the relative size of this contribution is shown in Figure 87. The largest correction is in the order of 0.026. This correction is small but, important compared to the statistical precision of the measurement. As the difference between the correction for the "inclusive" and the "semi-inclusive" sample are small, the conclusion on the agreement between both results remains valid.

The second correction takes into account the presence of nitrogen-14 in the target, which is a spin-1 nucleus and introduces an additional asymmetry on top of the one from the protons. The calculation of this correction is described in Section 4.4.6. This results in a modification of Equation 157:

$$A_1^p = \frac{1}{f D P_B P_T} A_1^{p,meas} - \left(\frac{\eta A_2^p}{\rho} + A_1^{p,RC} + A_{false} \right) - C_2 \frac{\sigma_d}{\sigma_p} A_1^d \,, \tag{168}$$
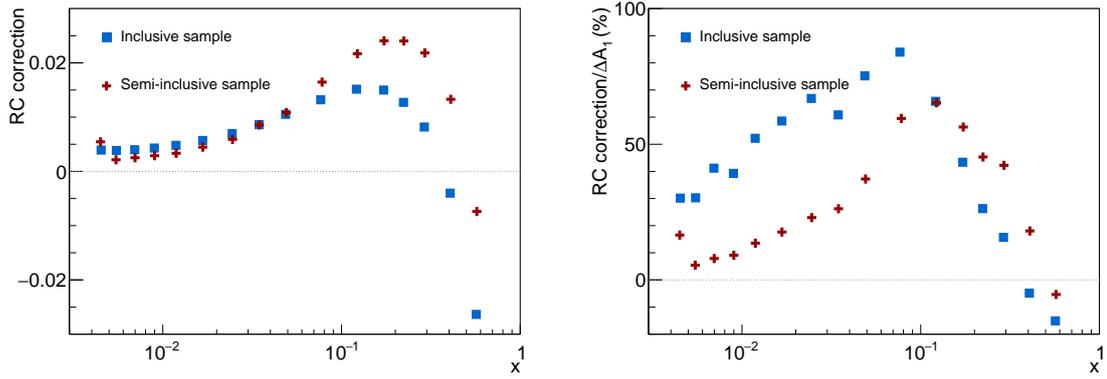
Figure 87: Spin-dependent radiative corrections in bins of Bjorken-x for the "inclusive" and "semi-inclusive" sample. Left: Absolute size. Right: Relative size compared to the statistical uncertainty.

where the A_1^{RC} are the radiative corrections and the term containing A_1^d is the correction for the presence of nitrogen-14. The size of the correction is shown in Figure 88. The largest correction is about 20% of the statistical uncertainty at high x.
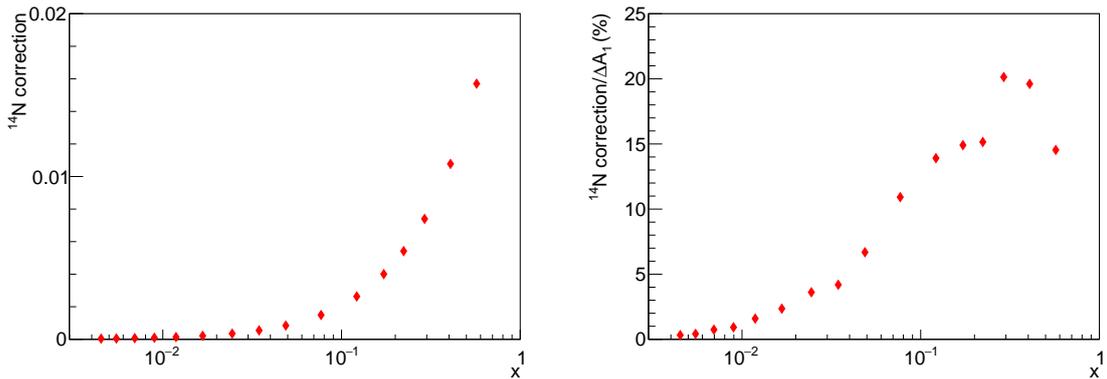
Figure 88: Correction to the asymmetry due to the presence of nitrogen-14 in bins of Bjorken-x. Left: Absolute size. Right: Relative size compared to the statistical uncertainty.

5.3.2 Final results

The final results for the longitudinal double spin asymmetry A_1^p obtained with the $200\,\mathrm{GeV}/c$ muon beam are shown in Figure 89 as a function of Bjorken-x at their measured Q^2 together with the results from 2007. The asymmetry is small and close to zero at low values of Bjorken-x and increases towards higher values. This behaviour is expected from the definition of the asymmetry using the cross sections for scattering photons of nucleons with a total spin of $1/2$ and $3/2$ (see Section 2.9). The results from the 2011 data agrees well with the results from the 2007 data over the full kinematic range. Even though, they are measured at slightly different kinematics.

The statistical precision of the COMPASS data is good enough to allow a two dimensional determination of the asymmetry in bins of Bjorken-x and photon virtuality. The
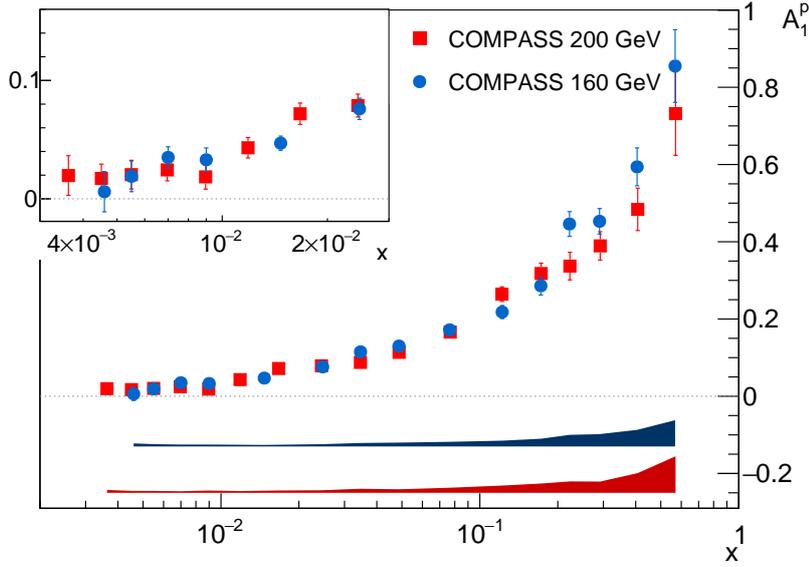
Figure 89: Results for the asymmetry A_1^p as a function of Bjorken-x for the data sample from 2011 and 2007.

result is shown in Figure 90. Here again, the results from the 2007 data set are shown. The good agreement is obvious. The comparison also illustrates that measuring with the increased beam energy in 2011 results in higher values of the photon virtuality in every Bjorken-x bin compared to the 2007 data. The data shows no significant dependence on the photon virtuality for all Bjorken-x bins.

5.3.3 *Comparison with the world data*

The COMPASS data are compared to the world data on the asymmetry A_1^p. This is shown in Figure 91. All data points are shown at their measured kinematics. The results from the 2011 data taking improve the statistical precision at low Bjorken-x where only a few data sets are available. Except for the measurement of COMPASS, only results of SMC [88] are present in this region. Good agreement between the new results obtained with the 200 GeV/c muon beam and the world data is visible, which supports the weak dependence of A_1^p on the photon virtuality in a larger kinematic range due to the lower beam energies of the other experiments. For example, at HERMES an electron beam with 27.5 GeV was used and at CLAS an electron beam with energies between 1.6 GeV and 5.7 GeV.

5.4 STRUCTURE FUNCTION RESULTS USING A PROTON TARGET

The results on the asymmetry are used to obtain the spin-dependent structure function g_1 of the proton using $g_1^p = A_1^p F_2^p/(2x(1 + R))$ (see Section 2.9). Here, the F_2 parametrisation of SMC [88] was used together with a modified version of the R parametrisation from Reference [94]. In the literature two representations are used to show the results for the spin-dependent structure function. Either the structure function is shown, which increases the uncertainties at low Bjorken-x, or the structure function is multiplied by Bjorken-x,
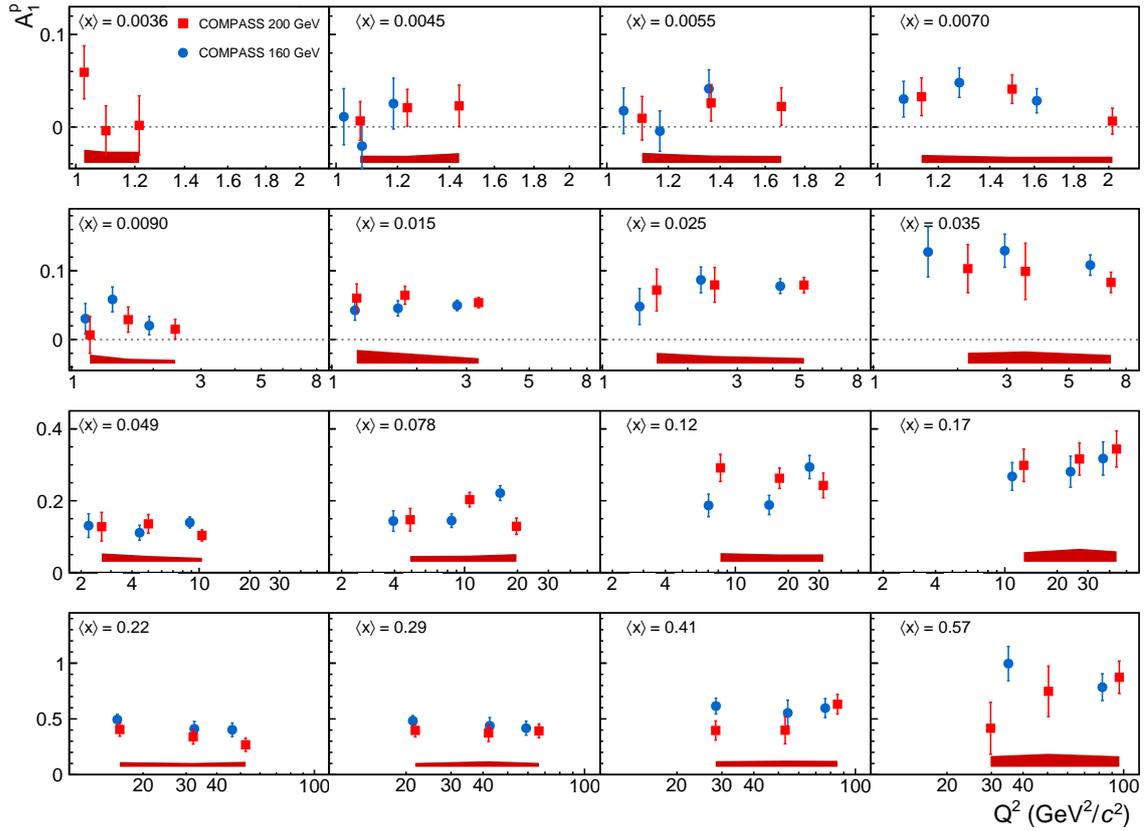
Figure 90: Results for the asymmetry A_1^p as a function of the photon virtuality for each Bjorken-x bin.
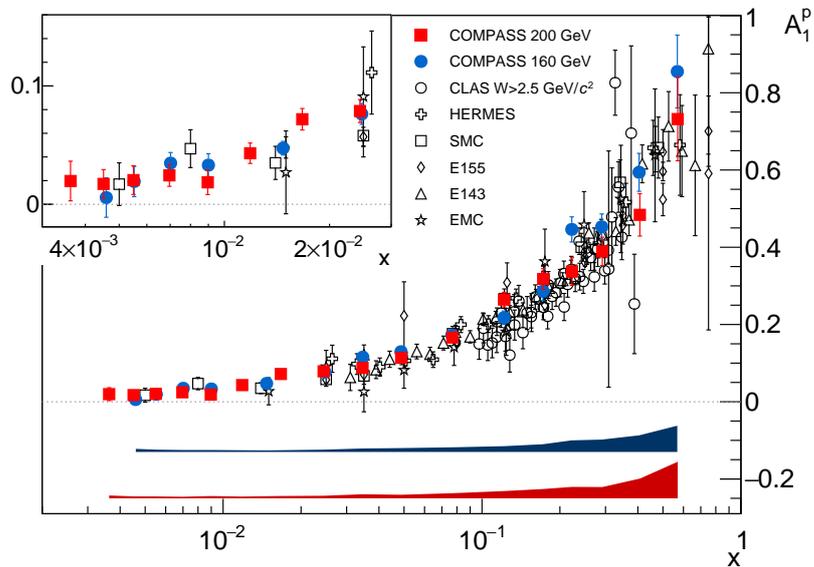
Figure 91: Results for the Bjorken-x dependence of the asymmetry A_1^p from COMPASS compared to the world data at their measured kinematics. The shown data are from CLAS [123], E143 [124], E155 [125], EMC [13], HERMES [126] and SMC [88]

which is closer to the measured asymmetry. Both representations for the spin-dependent structure function g_1^p are shown in Figure 92 as a function of Bjorken-x.
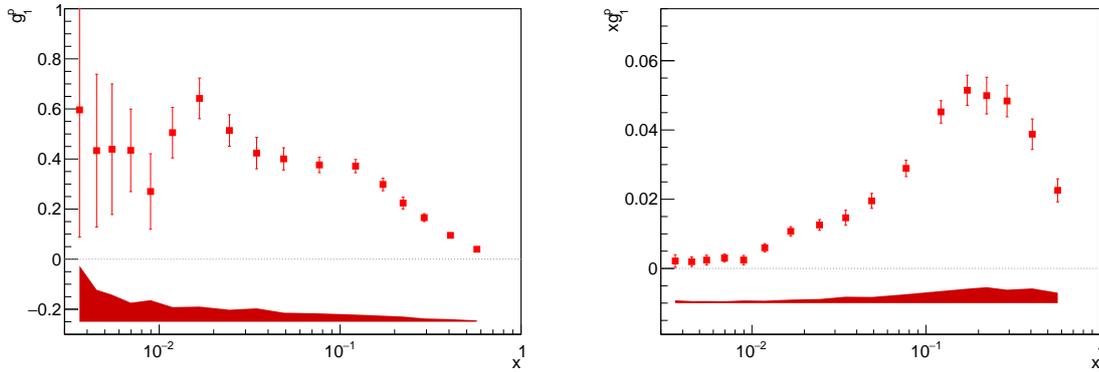
Figure 92: Results for the structure function g_1^p (left) and xg_1^p (right) as a function of x.

A comparison with the previous results for g_1^p using the 160 GeV/c muon beam and the results from SMC using the 190 GeV/c muon beam is shown in Figure 93. For the comparison some COMPASS bins at low Bjorken-x are combined to use a similar binning compared to that of SMC. In this comparison, the good statistical precision of the new data set obtained with the 200 GeV/c muon beam is visible. The figure also shows that the structure function is positive at low Bjorken-x and seems to approach a constant value. The results for the structure function and the asymmetry obtained using the 200 GeV/c muon beam are given in the appendix in Table 38 for the Bjorken-x dependence and in Tables 39 and 40 for the two dimensional binning.
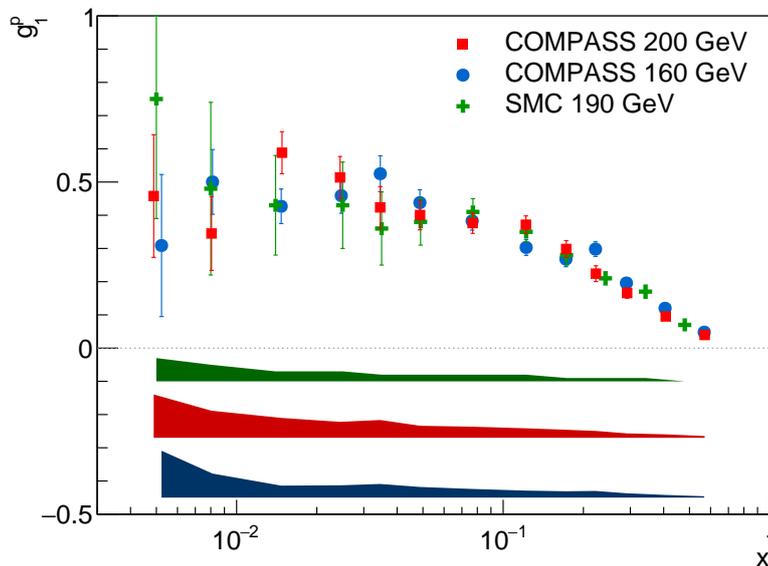
Figure 93: Results for the spin-dependent structure function g_1^p obtained from the COMPASS data using the 200 GeV/c and 160 GeV/c muon beam compared to the results from SMC [88] using the 190 GeV/c muon beam.

Results for the deuteron asymmetry A_1^d were already obtained by COMPASS from the 2002-2004 data taking [105]. In Figure 94 the mean values of the photon virtuality is shown as a function of Bjorken-x for the 2006 data. They are compared to the ones of the 2002-2004 data. Good agreement between the two results is seen at low Bjorken-x. Towards higher values of Bjorken-x, the data taken in 2006 show an slightly higher mean value of the photon virtuality compared to the data taken in 2002-2004. This increase is not due to an increase beam energy as it is the case for the new proton data set, see Table 11. Both data sets are obtained using the 160 GeV/c muon beam. The increase is achieved by improvements in the trigger acceptance at larger photon virtualities.
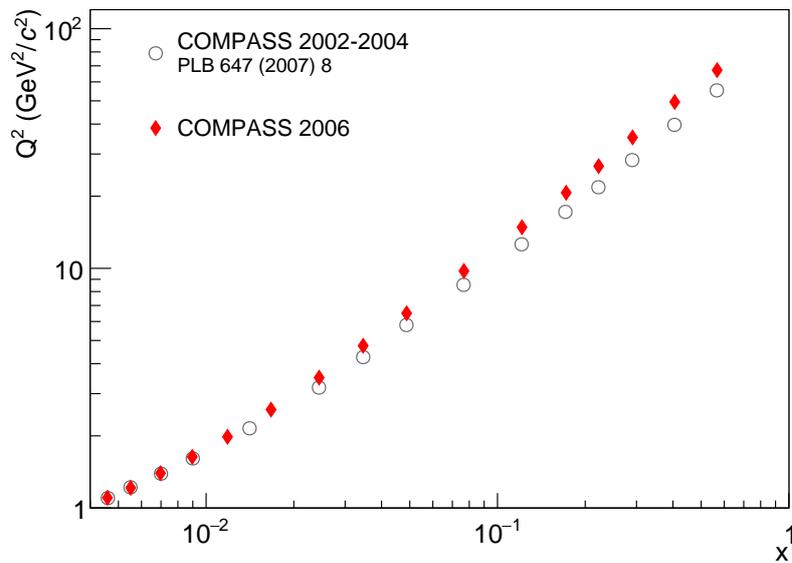
Figure 94: Comparison between the mean values of the photon virtuality in bins of Bjorken-x for the 2002-2004 and 2006 deuteron data.

The results for the asymmetry A_1^d from the 2006 data are obtained separately for two samples (see Section 5.1). A comparison between the results from the two samples is shown in Figure 95. They agree well with one another. The χ^2 probability is 30% giving no hint towards any false asymmetry introduced by including "semi-inclusive" triggers in the measurement of the inclusive asymmetry. This is expected from studies performed by SMC [88].

5.5.1   *Corrections to the asymmetry*

As already explained for the proton case, spin-dependent radiative corrections have to be applied to both samples. The size of the correction is shown in Figure 96. The largest correction is in the order of 0.017, which is only a small correction but still sizeable compared to the statistical uncertainty of this measurement.

Similar to the proton case, the deuteron asymmetry has to be corrected for the presence of polarisable spin-1/2 nuclei in the target, which introduce an additional asymmetry on
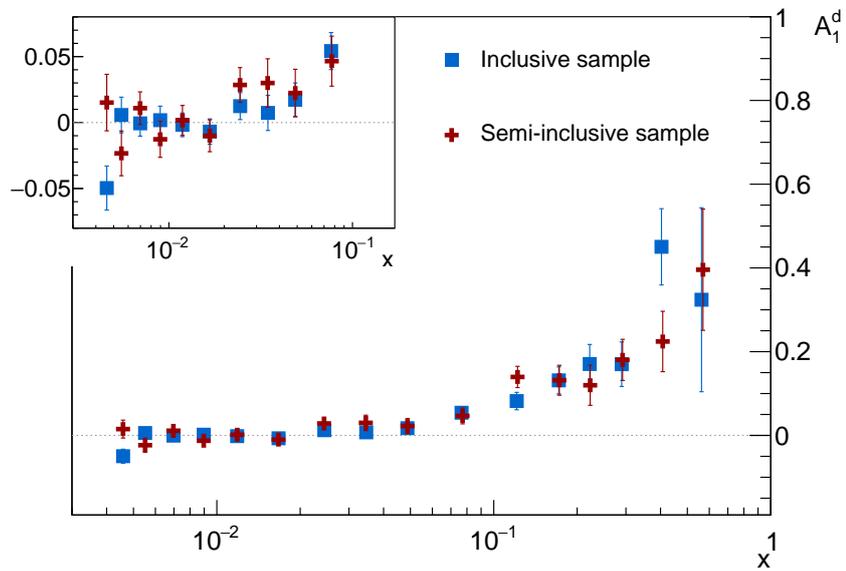
Figure 95: Results for the asymmetry A_1^d as a function of the Bjorken-x obtained for the "inclusive" and "semi-inclusive" sample from the 2006 data.
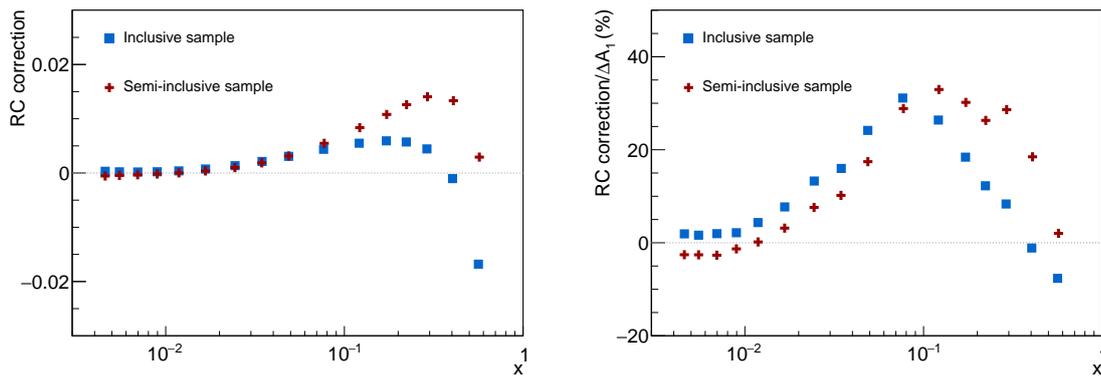
Figure 96: Spin-dependent radiative corrections as a function of Bjorken-x for the "inclusive" and "semi-inclusive" sample. Left: Absolute size. Right: Relative size compared to the statistical uncertainty.

top of the deuteron one. The calculation of this correction is described in Section 4.4.7. The size of the correction is shown in Figure 97. It is larger at high Bjorken-x than at low Bjorken-x. The largest correction is in the order of 0.014, which corresponds to about 12% of the statistical uncertainty.
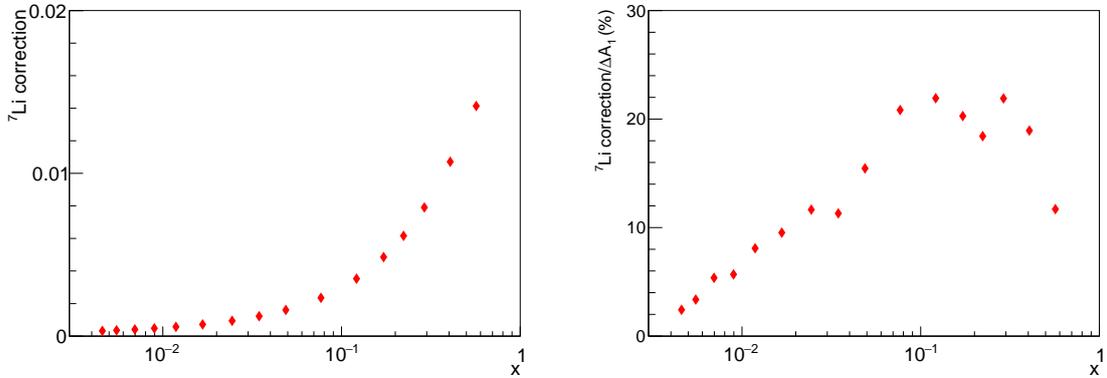
Figure 97: Correction due to lithium-7 to the asymmetry as a function of Bjorken-x. Left: Absolute size. Right: Relative size compared to the statistical uncertainty.

5.5.2 *Comparison with the 2002-2004 results*

The aim of the analysis of the 2006 data is to increase the precision of the results from the 2002-2004 data by combining both results. A comparison is shown in Figure 98. This comparison shows good agreement between the two data sets. From a χ^2 test using the statistical uncertainty a probability of 63% is obtained.
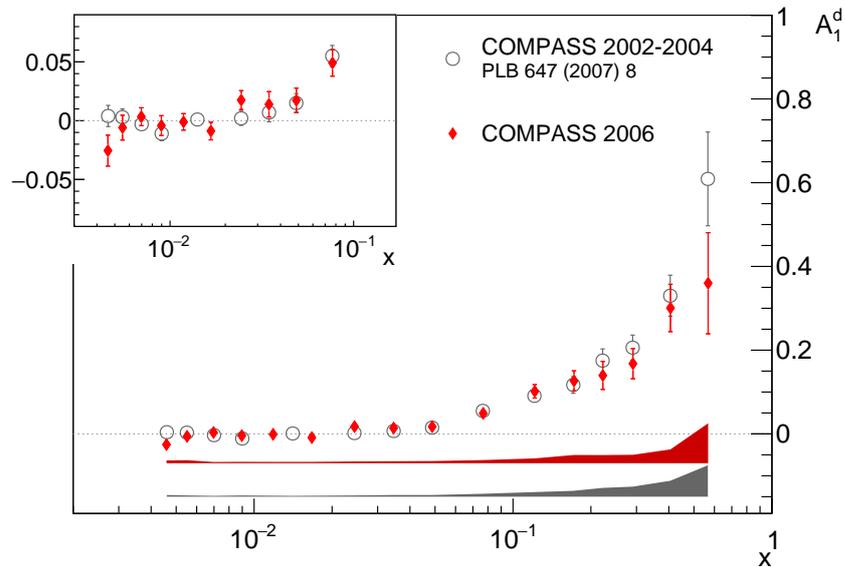
Figure 98: Comparison between the results for the asymmetry A_1^d as a function of Bjorken-x obtained from the 2002-2004 data and the 2006 data .

5.5.3 Final results

The final results for the asymmetry A_1^d are obtained by combining the 2002-2004 data set with the 2006 one. This is done using the weighted mean. The new data set improves the statistics for the asymmetry by about 50%. The obtained result is shown in Figure 99 as a function of Bjorken-x.
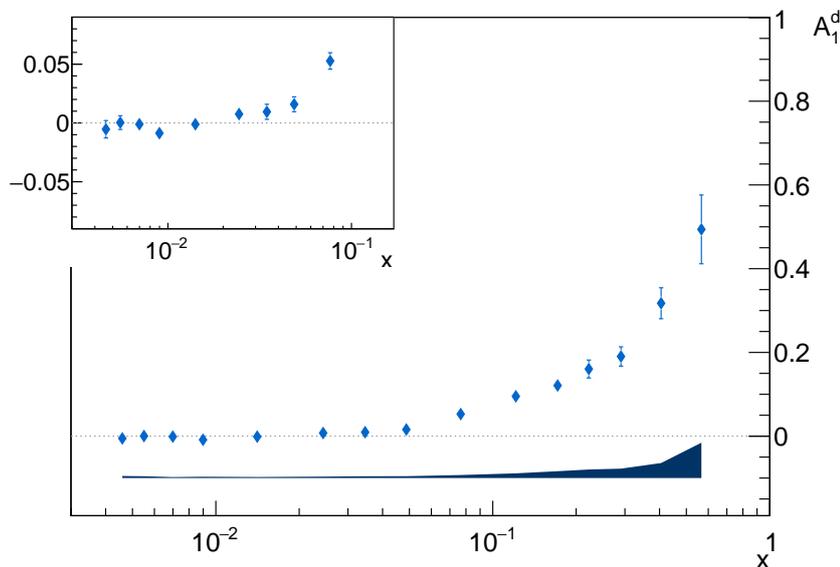
Figure 99: Results for the asymmetry A_1^d as a function of Bjorken-x obtained from the full deuteron data set.

The asymmetry is compatible with zero for $x < 0.02$ and increases towards a value of 0.5 at largest Bjorken-x. As expected, the deuteron asymmetry is considerably smaller than the proton asymmetry. Due to the good statistics, the results for the asymmetry is obtained in a two dimensional binning. In each bin in Bjorken-x the dependence on the photon virtuality is studied. The results are shown in Figure 100. As for A_1^p, no significant dependence on the photon virtuality is found in any Bjorken-x bin.

5.5.4 Comparison with the world data

The final results for the asymmetry A_1^d of the deuteron is compared to the world data in Figure 101. This comparison shows good agreement between all data sets, even though they are shown at their measured kinematics. This indicates the weak dependence of the asymmetry on the photon virtuality, again a large kinematic range is covered due to lower beam energies of the other experiments. The figure also shows the good statistical precision of the new data set. This is of special interest at low Bjorken-x, where only results from SMC [88] and HERMES [126] exists, which have large uncertainties compared to those of the final COMPASS result.
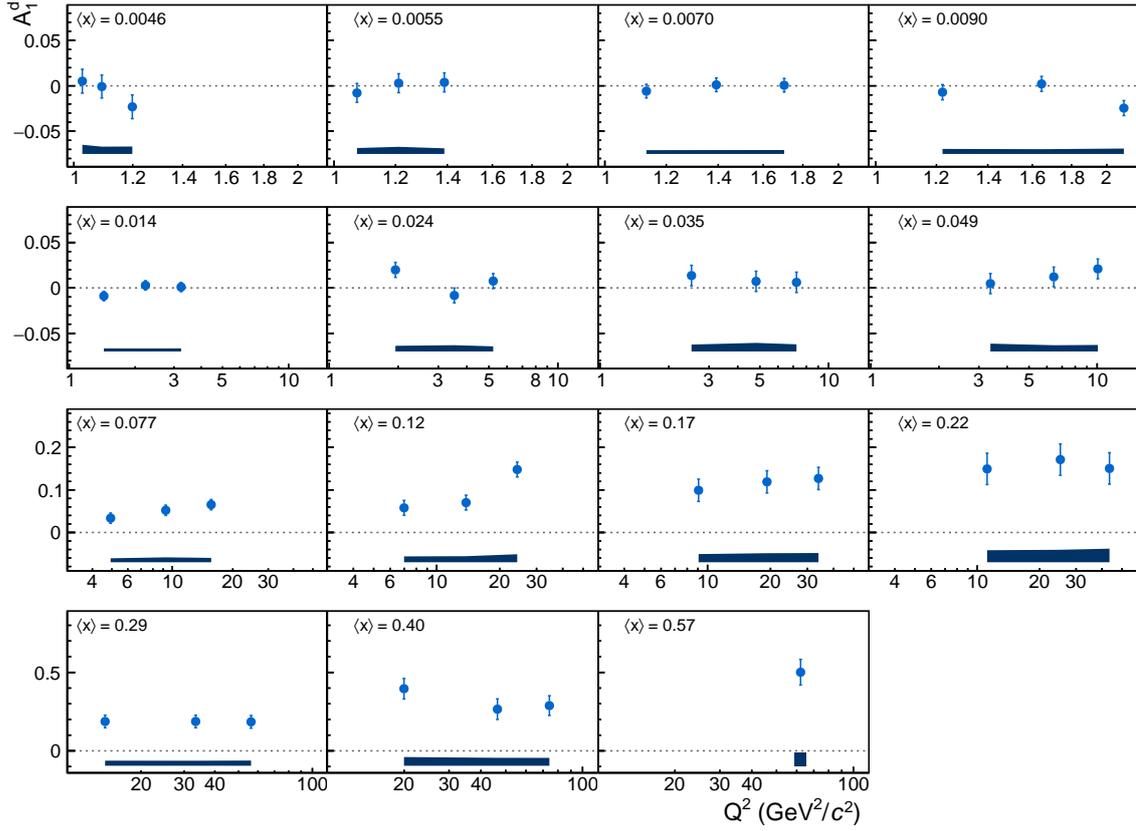
Figure 100: Results for the asymmetry A_1^d as a function of the photon virtuality for each Bjorken-x bin.
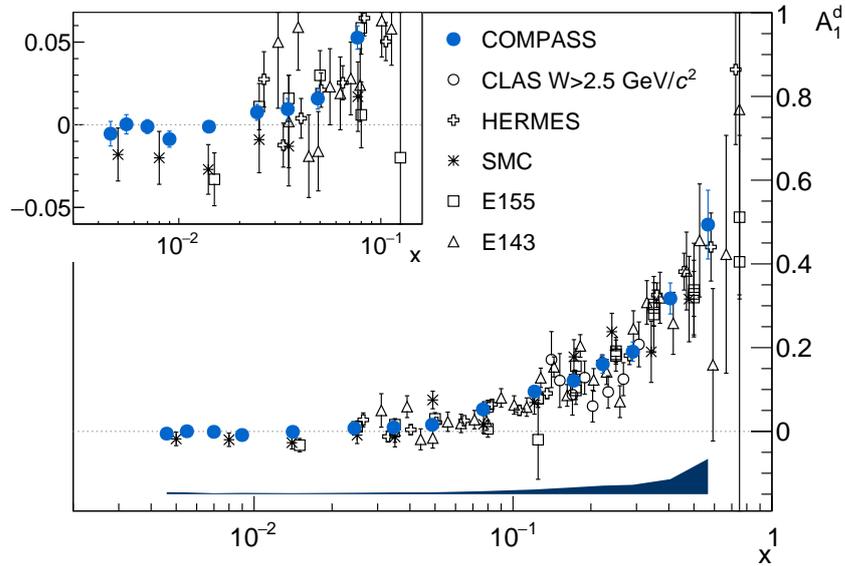
Figure 101: Results for the asymmetry A_1^d from COMPASS compared to the world data at their measured kinematics. The shown data are from CLAS [123], E143 [124], E155 [127], HERMES [126] and SMC [88]

The spin-dependent structure function of the deuteron is obtained in a way similar to the one of the proton (see section 5.4) by using the relation $g_1^d = A_1^d F_2^d / (2x(1+R))$. The results for the spin-dependent structure function are shown in Figure 102 as a function of Bjorken-x in the two representation commonly used in literature.
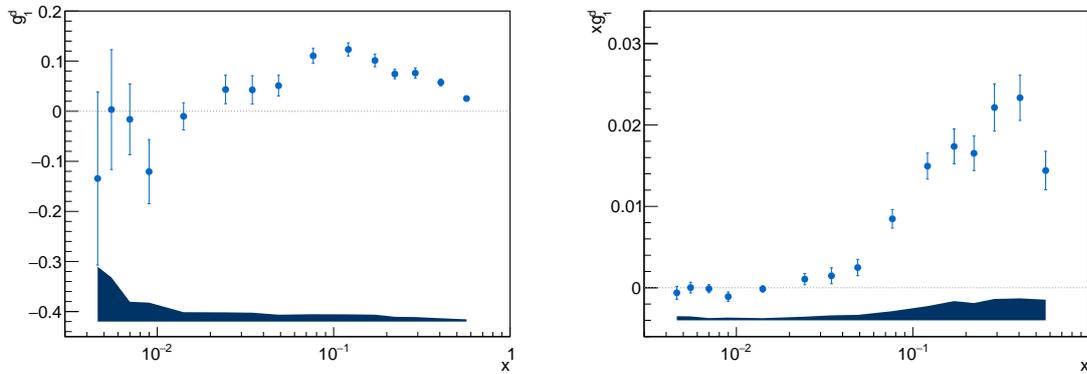
Figure 102: Results for the structure function g_1^d (left) and xg_1^d (right) as a function of Bjorken-x for the full deuteron data set.

At low Bjorken-x, the combined results are consistent with zero. The χ^2 probability for a compatibility with zero calculated using the five data points at lowest Bjorken-x is 50%. This is interesting when comparing the results to the ones from SMC. They had found hints for possible large negative values of the structure function at such low values of Bjorken-x, albeit they had large statistical uncertainties. The comparison is shown in Figure 103. For this comparison, the four COMPASS data points at lowest Bjorken-x are combined in pairs using the weighted mean to have the same binning as SMC. The figure shows once more the good statistical precision of the combined deuteron data set. The results for the structure function and the asymmetry for the combined deuteron data are given in Tables 44, 45 and 46 in the appendix. In addition the results obtained from the 2006 data set alone are given in Tables 41, 42 and 43.
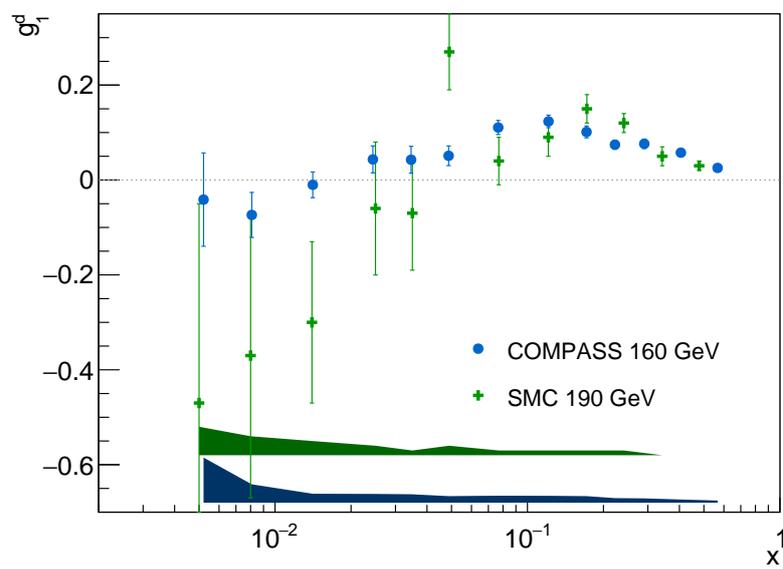
Figure 103: Results for the spin-dependent structure function g_1^d from the combined COMPASS deuteron data using the 160 GeV/c muon beam compared to the results from SMC [88] using the 190 GeV/c muon beam.

ASYMMETRY AT LOW PHOTON VIRTUALITIES

In a second analysis of the 2007/11 proton data, events with low photon virtualities, $Q^2 < 1\,(\text{GeV}/c)^2$, are selected. Due to the correlation between photon virtuality and Bjorken-x, the data with low photon virtuality cover the range of low Bjorken-x. The results obtained from these data allow to study the non-perturbative region and provide input to theoretical predictions. The results using the deuteron data are already published in Reference [95].

6.1 DATA SELECTION

The data selection was performed using the full data taken in 2007 and 2011 without any preselection, as no significant rejection would be achieved by removing only events with high photon virtualities.

6.1.1 *Selection for the A_1 analysis*

The cuts applied to the data are similar to the ones applied in the case of the analysis of high photon virtualities (see Section 5.1). The selected events have a primary vertex with a reconstructed incoming and scattered muon. The beam momentum was restricted to the range of $\pm 20\,\text{GeV}/c$ around the nominal beam momentum for the 2007 data and a range of $\pm 15\,\text{GeV}/c$ for the 2011 data. The latter one was chosen due to the range of validity of the parametrisation of the beam polarisation. Events with no measured beam momentum were discarded. In order to equalised the beam flux in each of the target cells, the incoming muon was required to cross all target cells assuming no interaction. The range in the relative virtual photon energy is the same as for the analysis at high photon virtualities, $0.1 < y < 0.9$. The lower limit removes events, which are hard to reconstruct, while the upper limit removes events where large radiative corrections have to be applied. The range of the photon virtuality is restricted to $Q^2 < 1\,\text{GeV}/c^2$. In addition, events with $\log_{10}(x) < -4.4$ are removed. The Bjorken-x cut was also applied in the case of the deuteron data [95]. It is applied as the relative uncertainty of the depolarisation factor increases at such low Bjorken-x and the mean values of Bjorken-x become a bias. This was studied in Reference [107] using the deuteron data.

At low photon virtualities the scattering angle of the muon are very small. This results in a bad vertex resolution. Therefore, at least one additional hadron is required in the vertex in order to improve the vertex resolution. Afterwards, the vertex is required to be inside of one of the target cells. The requirement of an additional hadron results in a semi-inclusive measurement. These kinds of events are similar to the "semi-inclusive" sample of the analysis at high photon virtualities. The bias introduced by performing a semi-inclusive measurement was studied using Monte Carlo simulations. It was found to be small [88]. The bias is expected to be negligible since at low Bjorken-x the invariant mass of the hadronic final state is large, which results in a large number of hadrons. This results

also in the use of the "semi-inclusive" radiative corrections, which are much smaller in this kinematics than the "inclusive" ones. The kinematic coverage of the 2007 and 2011 data is shown in Figure 104 as a function of Bjorken-x and the photon virtuality.
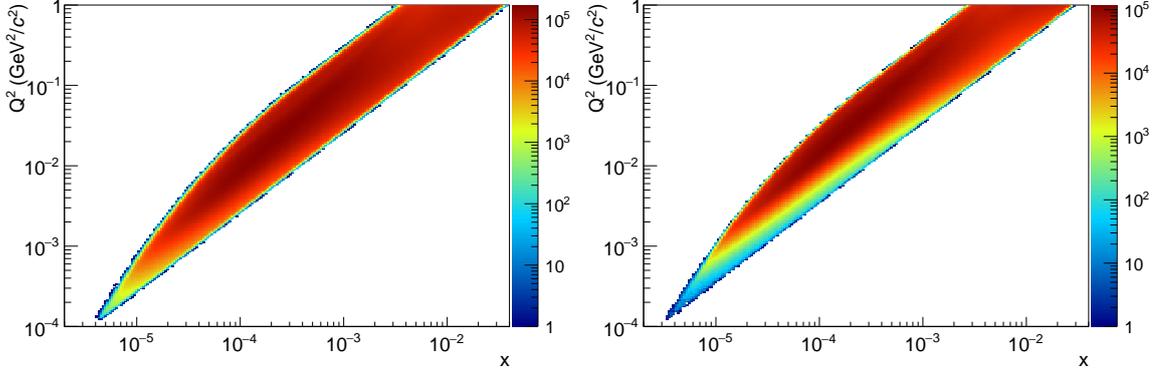
Figure 104: Kinematic coverage of the 2007 (left) and 2011 (right) data in Bjorken-x and the photon virtuality.

6.1.2 Target cuts

A stricter radial cut on the vertex position inside the target is applied in contrast to analysis at the high photon virtualities. The stricter cut of $r < 1.8\,\mathrm{cm}$ was applied instead of $r < 1.9\,\mathrm{cm}$ for consistency with the deuteron analysis. It was increased to ensure that the interaction took place inside of a target cell as the accuracy is worse at low scattering angles. In addition, a cut on the χ^2 of the vertex position is applied:

$$\chi^2 \leqslant \mathrm{NDF} + 3 \cdot \sqrt{2\mathrm{NDF}} \,. \tag{169}$$

This cut is motivated by the mean value of the χ^2 distribution and its variance $\sigma^2 = 2\,\mathrm{NDF}$. Therefore, this cut corresponds to the upper limit of the 3σ range.

6.1.3 Removal of muon electron scattering events

At low Bjorken-x, events in which the incoming muon is scattered of an electron instead of the target nucleon appear. The Bjorken-x for such events is $x = m_e/m_p \approx 5.5 \cdot 10^{-4}$. These events are no deep inelastic scattering events and have to be removed. As the kinematics of such events is well defined and the electron track is in direction of the virtual photon, a cut on the angle of the outgoing track with respect to the virtual photon is applied. The angle is multiplied by the charge of the outgoing particle. The cut was only applied to events with one track in addition to the scattered muon. As also a contribution from muon-electron scattering is found in events with two additional outgoing tracks, the cut is also applied for those events. No cut is applied in the case of more than two outgoing tracks as no contribution of muon-electron-scattering was observed. The distribution of the angle is shown in Figure 105. The cut is applied for the range of $-3.6 < \log_{10}(x) < -3.0$ and removes the following range:

- $-0.005 < q\theta^* < 0.002$ in the case of one outgoing track
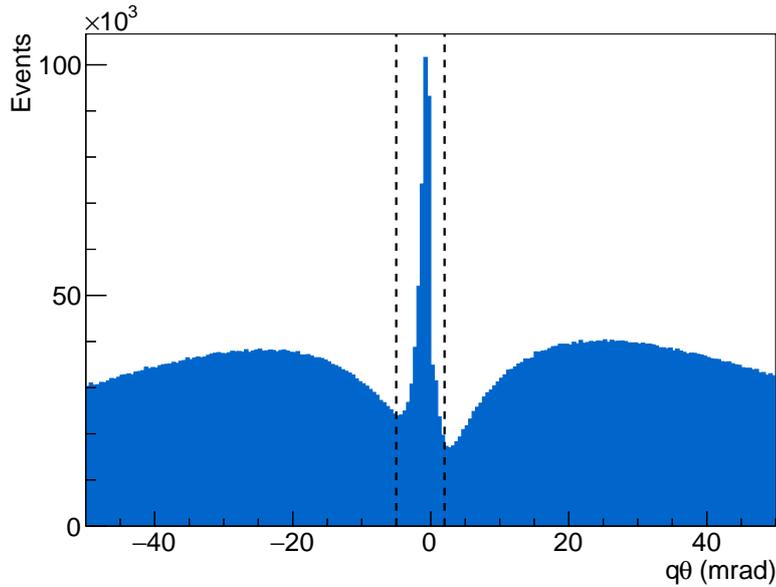
Figure 105: Distribution of the angle qθ of the outgoing track with respect to the virtual photon. The peak around zero indicates events where the muon is scattered off electrons. The applied cut is indicated by a dashed line.

- $-0.001 < q\theta^* < 0.000$ in the case of two outgoing track.

The result of these cuts is shown in Figure 106, where the photon virtuality is shown as a function of Bjorken-x before and after applying the cut. The cuts remove the peak in this distribution corresponding to muon-electron-scattering.
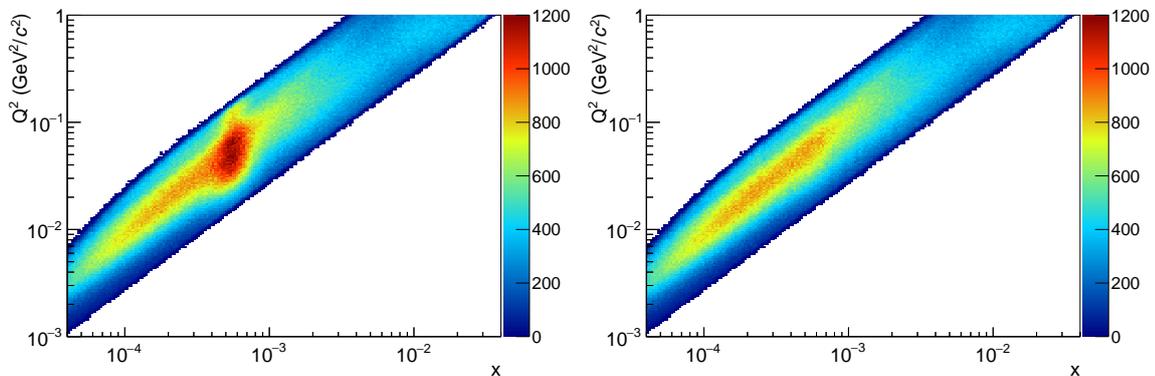
Figure 106: Effect of the cuts for the removal of muon-electron-scattering events. Left: Before applying the cut. The peak correspond to muon-electron-scattering. Right: After applying the cut.

6.1.4   *Good hadron selection*

The cuts for selecting good hadrons are applied to ensure that the additional track in the vertex is produced in the muon nucleon interaction. They are also applied in order to

be consistent with the analysis of the deuteron data. They remove ghost tracks, poorly reconstructed tracks and possible halo muons. Therefore, the following cuts were applied for the hadrons:

- Has measured momentum

- $z_{last} > 350\,cm$

- $0.1 < z_h = \frac{E_h}{\nu} < 1$

- In 2007: $P_h < 140\,GeV/c$

- In 2011: $P_h < 180\,GeV/c$

- $X/X_0 < 15$ and $z_{last} < 3500\,cm$

The first three cuts ensure that the track was well reconstructed and is no ghost track. Ghost tracks are artefacts introduced during the reconstruction and correspond to no real particle. The good reconstructed tracks should have a well defined momentum, which is also ensured by the cut on the last measured position. Tracks with a last measured position before the first spectrometer magnet are removed. For such tracks a momentum measurement is possible using the solenoid field of the target or the fringe field in between SM1 and the target solenoid. The uncertainty on the momentum of such tracks is large. Therefore, they are not used. The three remaining cuts remove tracks that are considered to be muons. The momentum cuts remove halo muons, which have momenta close to the nominal beam momentum. Possible muons are also removed by applying a cut on the amount of radiation length passed by the track. They are also removed by the requirement that the last measured position is in in front of the absorber at $z = 3500\,cm$.

6.1.5 *Effect of the different cuts*

The amount of events passing the various cuts is shown in Table 18 for the data taken in 2007 and 2011. The larger amount of rejected events in 2011 after the selection of a primary vertex compared to 2007 is caused by a change in the reconstruction program, as already explained in the case of the data selection for the high photon virtuality analysis in Section 5.1. The relative contributions from the various trigger is shown in Figure 107 as a function of Bjorken-x and Figure 108 as a function of the photon virtuality. The inner trigger is much more important for this analysis than in the case of high photon virtualities (see Section 5.1).

6.2 FALSE ASYMMETRIES

Similar systematic studies as in the case of high photon virtualities are performed (see Section 5.2) for the asymmetry at low photon virtualities. The measured raw asymmetry and the photon nucleon asymmetry without any correction are shown in Figure 109 for the data from 2007. The raw asymmetry is only about $5 \cdot 10^{-3}$, whereas the photon nucleon asymmetry is about 1%. A search for hints on false asymmetries, which are for example caused by misalignment of detectors, is performed. In these test also the acceptance cancellation assumed for the asymmetry calculation is tested. This is done by testing the

Table 18: Effect of the data selection for the analysis at low photon virtualities. The last two rows show the cuts, which are applied after the data selection.

CUT	2007		2011	
	EVENTS/10^6	(%)	EVENTS/10^6	(%)
Reconstructed Events	5635	100.0	11559	100.0
Physics trigger	5568	98.8	10957	94.8
Primary vertex	5476	97.2	6991	60.5
Scattered muon	1952	34.6	1680	14.5
Additional track(s)	1209	21.4	909	7.9
Primary vertex inside the target	975	17.2	669	5.8
Vertex quality	791	14.0	438	3.8
y cuts	716	12.7	401	3.5
Beam momentum cut	662	11.8	392	3.4
μe rejection	650	11.5	370	3.2
Good hadron	541	9.6	298	2.6
Equalise beam flux	532	9.4	295	2.6
$Q^2 < 1\,(\text{GeV/c})^2$	471	8.4	241	2.1
$\log_{10}(x) \geqslant -4.4$	447	7.9	229	2.0
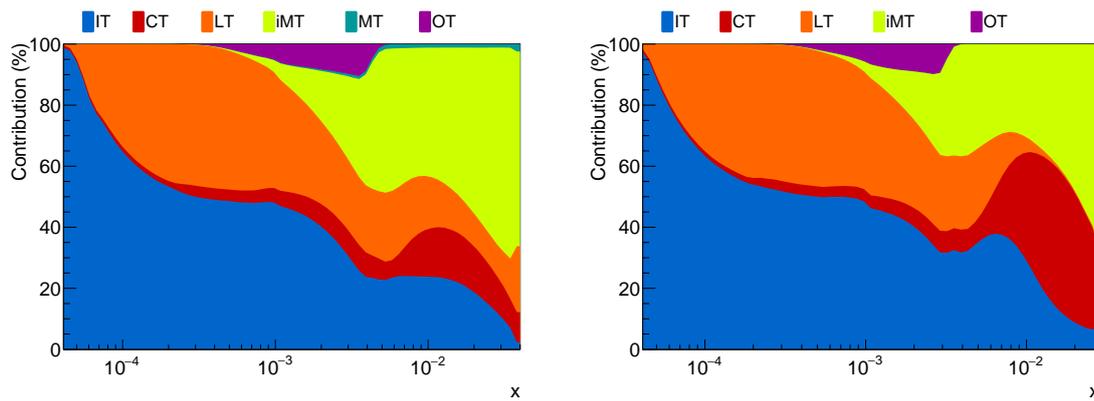
Figure 107: Relative contributions from the various triggers as a function of Bjorken-x for the data taken in 2007 (left) and in 2011 (right).
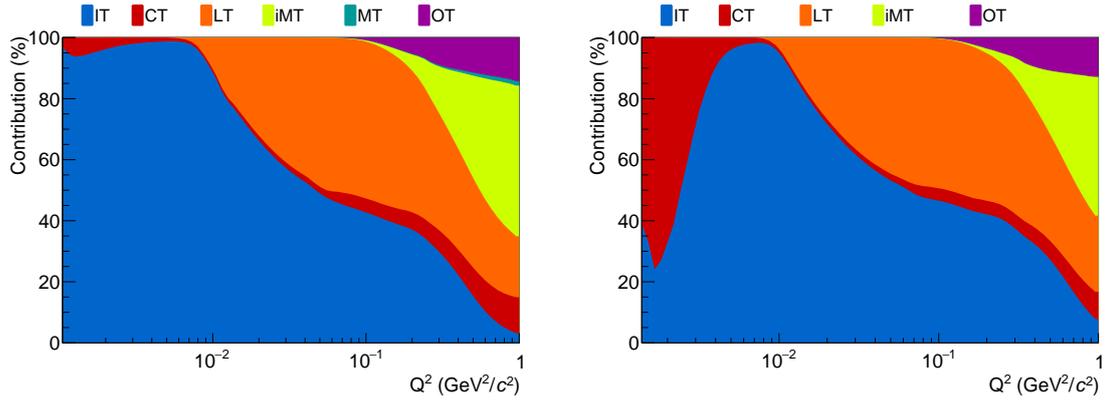
Figure 108: Relative contributions from the various triggers as a function of the photon virtuality for the data taken in 2007 (left) and in 2011 (right).

compatibility between the various groups and by using two methods for grouping them in a different way. An upper limit on the presence of false asymmetries is obtained from studying possible time dependent effects.
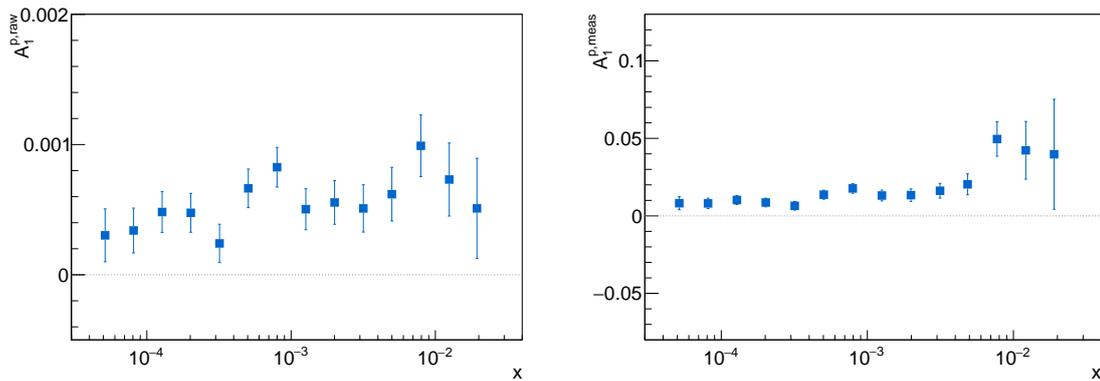
Figure 109: Left: Measured raw asymmetry as a function of Bjorken-x obtained from the 2007 proton data. Right: Measured photon-nucleon asymmetry without any corrections.

6.2.1 Compatibility between two microwave settings

The data from each year is split into two microwave periods. They arise from the destruction of the polarisation of each target cell followed by a repolarisation with a different microwave frequency. The microwave frequency is chosen such that the relative direction between the solenoid field and the target polarisation is changed (see Section 3.2). This is done to cancel systematic effects related to the direction of the solenoid field. The weeks of data taking belonging to each period are listed in Table 19. The data taking in 2011 was split into two periods by the so called "microwave reversal", whereas the data taking in 2007 is split into three periods, where two periods have the same solenoid field direction and are merged into one period. For the periods, the asymmetry is calculated and compared in order to search for false asymmetries due to the solenoid field direction. The results are shown in Figure 110 for the 2007 data as a function of Bjorken-x and the virtual

Table 19: Sharing of data between the two microwave periods in 2007 and 2011. In 2011 only one reversal was performed, whereas in 2007 two were performed.

YEAR	−	+
2007	W35 W36 W37 W38	W32 W33 W34 W44 W45
2011	W25 W27 W30 W31 W32 W33 (W34)	W36 W38 W39 W41 W43

photon energy and in Figure 111 for the 2011 data. For both data takings no hint on a possible false asymmetry was observed.
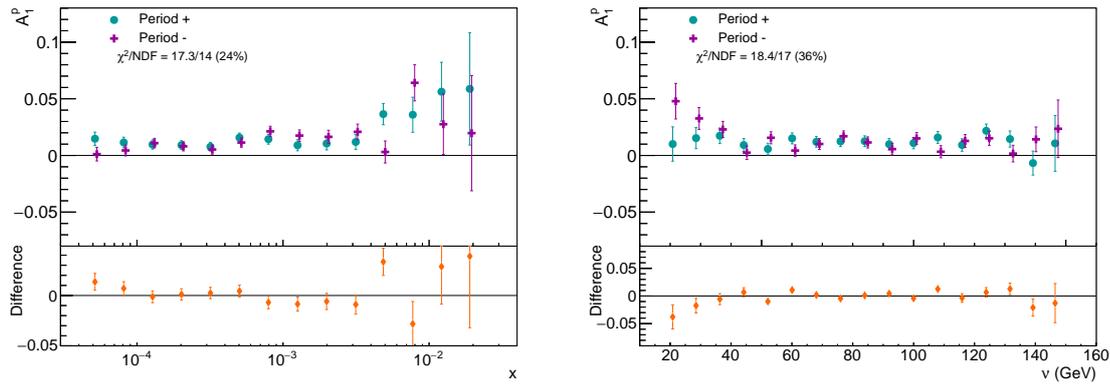
Figure 110: 2007 data. Results for A_1^p for two periods with different microwave settings. The results for period − are slightly shifted for better visibility and the χ^2 for both samples to be compatible with one another is given. Left: Results as a function of Bjorken-x. Right: Results as a function of the virtual photon energy.
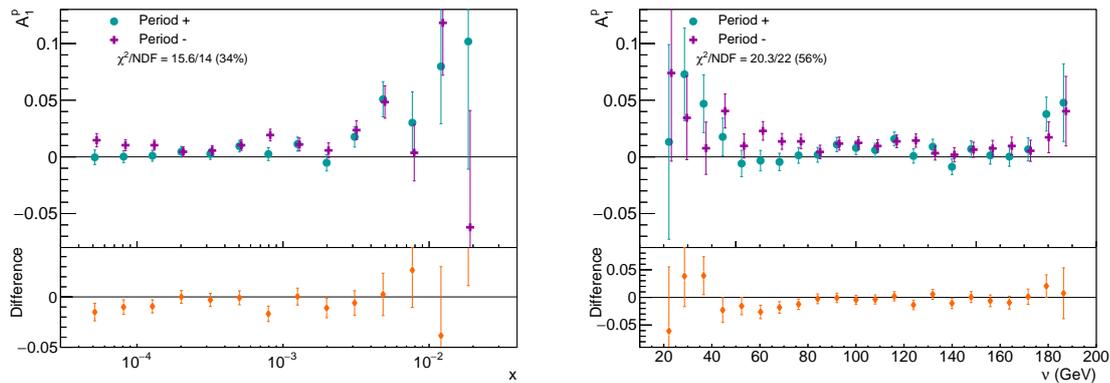
Figure 111: 2011 data. Results for A_1^p for two periods with different microwave settings. The results for period − are slightly shifted for better visibility and the χ^2 for both samples to be compatible with one another is given. Left: Results as a function of Bjorken-x. Right: Results as a function of the virtual photon energy.

6.2.2   *Search for false asymmetries using fake configurations*

A direct search on false asymmetries is performed by grouping the data such that the resulting physics asymmetry is expected to be zero. The same method used for the data at high photon virtualities (see Section 5.2.2.1) is also applied here. In order to search for false asymmetries new groups are build, which contain data with the same polarisation directions in each target cell. This was illustrated in Figure 71. The results for the asymmetry obtained using such a grouping is shown in Figure 112 for the data from both years. In both cases the asymmetry is compatible with zero. For the 2007 data the χ^2 probability is 97% for the binning in Bjorken-x and 84% for the binning in the virtual photon energy. In the case of the 2011 data the probabilities are 65% and 18%.
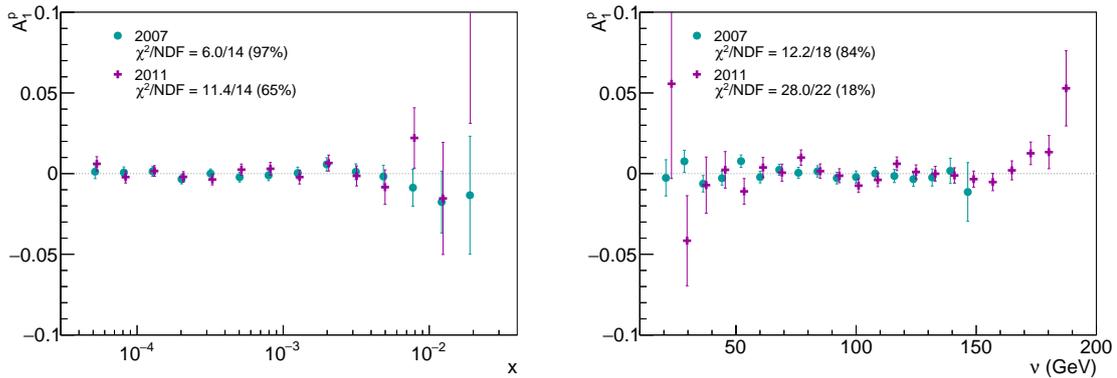
Figure 112: Results for the asymmetry obtained using fake configurations. The results of the 2011 data taking are slightly shifted for better visibility and the χ^2 for the results from both years to be compatible with zero is given. Left: Results as a function of Bjorken-x. Right: Results as a function of the virtual photon energy.

6.2.3   *Search for false asymmetries using the target cells*

Another possibility for a direct search on false asymmetries is to combine data from target cells with the same polarisation direction. The resulting asymmetry is expected to be zero. The same method for combining the data from the different cells is used as in the case of high photon virtualities described in Section 5.2.2.2. The data from the two outer cells are combined. In addition, the central cell is artificially split into two parts of equal length. The asymmetry obtained from the 2007 data is shown in Figure 113 as a function of Bjorken-x and the virtual photon energy and for the 2011 data in Figure 114. The χ^2 probability of the asymmetries being compatible with zero are listed in Table 20. In the 2007 data no hint for the presence of false asymmetries is found. In the case of the 2011 data hints are found. As the obtained false asymmetries have an opposite sign at least a partial cancellation of this effect is expected. In addition, no further hints on false asymmetries are found in other systematic studies.
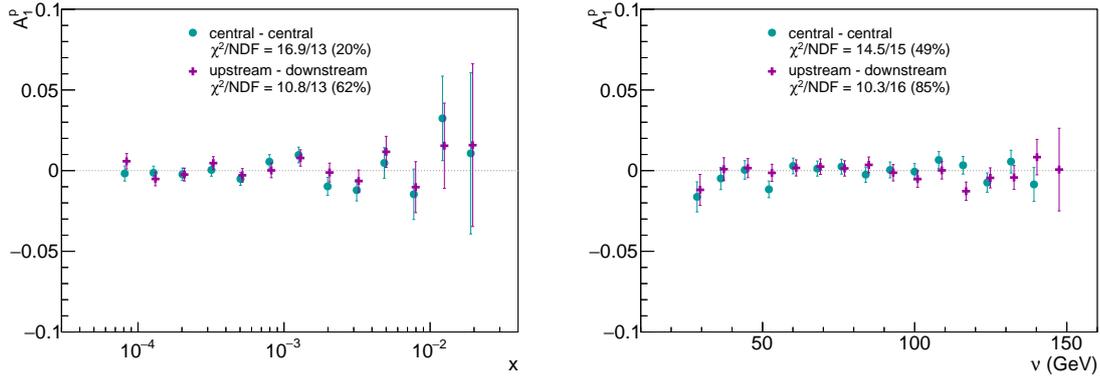
Figure 113: Results for the asymmetry obtained from the 2007 data combining data from target cells with the same polarisation direction. The results for the combination of the outer cells are slightly shifted for better visibility and the χ^2 for both samples to be compatible with zero is given. Left: Results as a function of Bjorken-x. Left: Results as a function of the virtual photon energy.
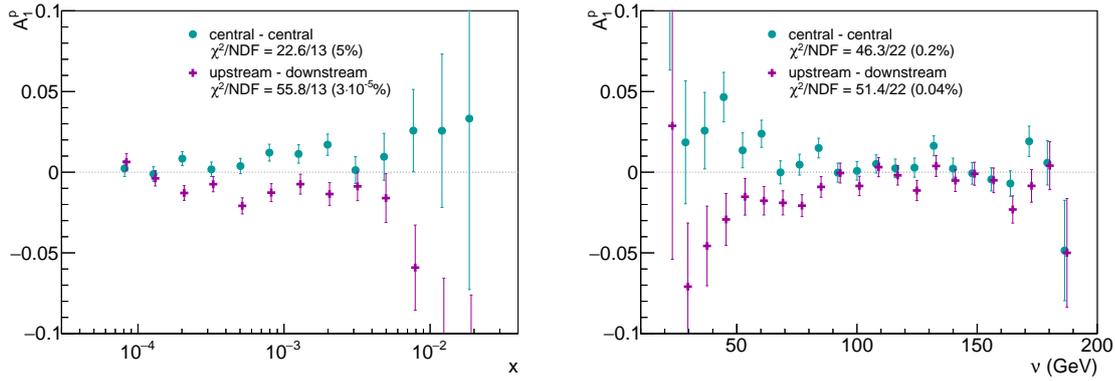
Figure 114: Results for the asymmetry obtained from the 2011 data combining data from target cells with the same polarisation direction. The results for the combination of the outer cells are slightly shifted for better visibility and the χ^2 for both samples to be compatible with zero is given. Left: Results as a function of Bjorken-x. Left: Results as a function of the virtual photon energy.

Table 20: χ^2 probabilities for the asymmetries obtained from combining the outer or central cells to be compatible with zero. The probabilities are shown for the 2007 and 2011 data for the binning in Bjorken-x and the virtual photon energy.

| | 2007 | | 2011 | |
BINNING	OUTER CELLS	CENTRAL CELL	OUTER CELLS	CENTRAL CELL
x	62%	20%	$3 \cdot 10^{-5}$%	5%
ν	85%	49%	0.04%	0.2%

6.2.4 *Further test*

Beyond the studies already mentioned before, further studies are performed similar to the analysis at high photon virtualities described in Section 5.2.4. Here, a study on a possible dependence of the asymmetry on the day-night effects is performed. Such an dependence may arise due to temperature differences between day and night in the experimental hall. No hints are found. The stability of the spectrometer was studied by calculating the asymmetry separately in distinguished parts of the spectrometer based on the direction of the scattered muon. The results where the muon was detected in the left or right part of the spectrometer are compared. Also the results where the muon was detected in the top or bottom part are compared. In both cases no hint on false asymmetries are found.

6.2.5 *Limit on false asymmetries*

In order to obtain an upper limit for the presence of false asymmetries, the same method as described in Section 5.2.5 is used. The pulls are calculated for each of the 39 groups used for the 2011 data and for the 23 groups used for the 2007 data. The obtained distributions are shown in Figure 115 for the 2007 data and in Figure 116 for the 2011 data.
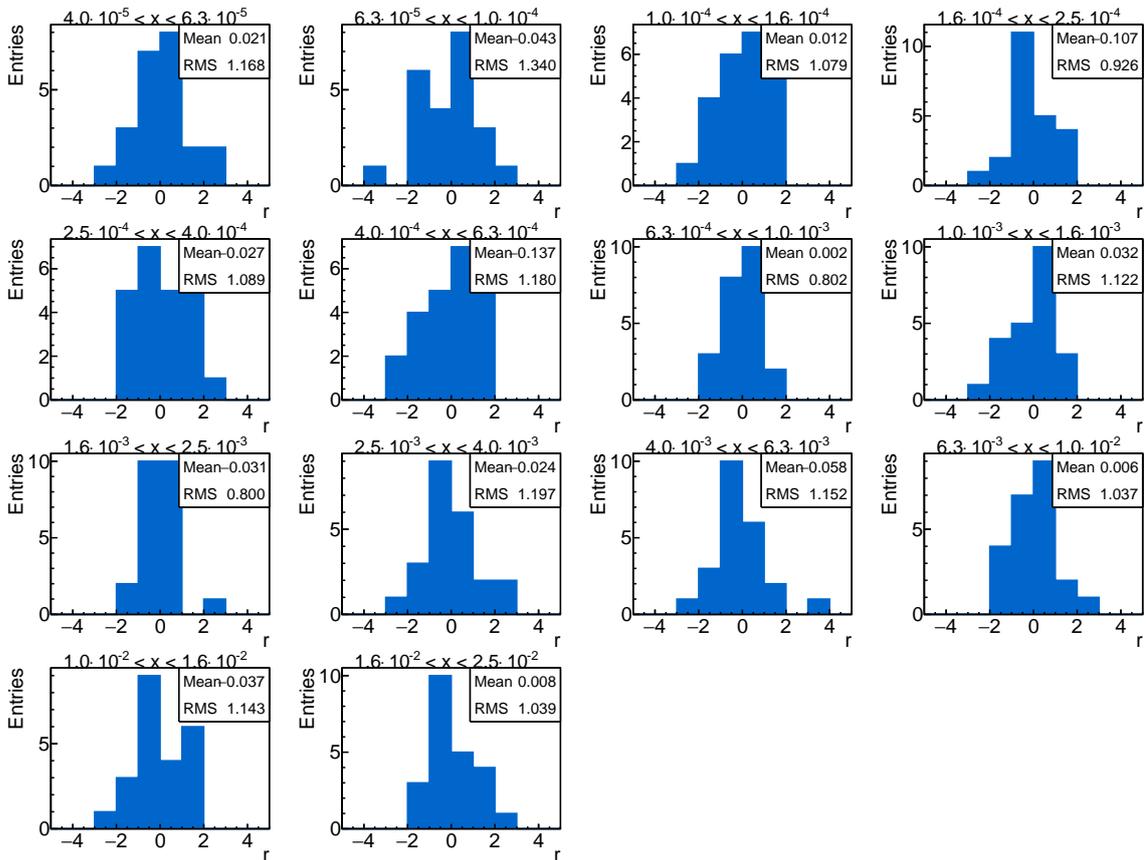
Figure 115: Pulls distributions obtained from the 2007 data for each Bjorken-x bin. The results from all 23 groups are used.

For each bin in the data from both years the mean value and the standard deviation of the distribution is calculated. All of them are in agreement with the expected behaviour of
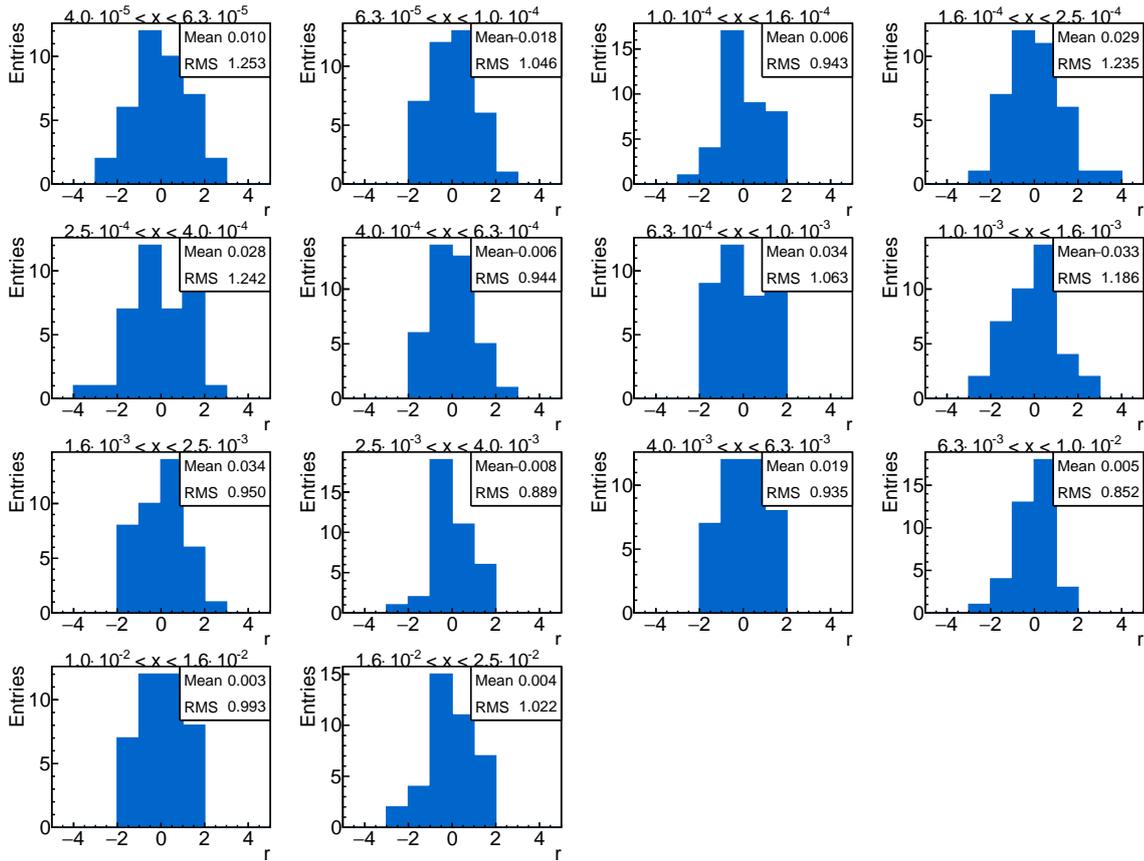
Figure 116: Pulls distributions obtained from the 2011 data for each Bjorken-x bin. The results from all 39 groups are used.

a Gaussian distribution centred at zero with a width of $\sigma = 1$. The results for the standard deviation (σ_{tot}) and its uncertainty ($\Delta\sigma_{tot}$) are used to calculate the upper limit for the presence of false asymmetries:

$$\sigma^{syst} = \sqrt{(\Delta\sigma_{tot} + \mathrm{Max}\,(1, \sigma_{tot}))^2 - 1} \, . \tag{170}$$

The limit on the systematic uncertainty from the presence of possible false asymmetries is about $0.97 \cdot \Delta A_1^{stat}$. The slightly larger value compared to the case of the analysis at high photon virtualities is caused by the smaller number of groups. At high photon virtualities, for each group two pulls are calculated from the two samples. Here, only one sample exists.

6.2.6 *Additional sources of systematic uncertainties*

The contribution to the systematic uncertainty discussed so far only consider possible false asymmetries. Other contributions are due to external inputs used in the calculation. These were already discussed in more detail for the asymmetry at high photon virtualities in Section 5.2.7. The contributions to the systematic uncertainty are split again into two parts. The multiplicative part contains the uncertainties related to the dilution and depolarisation factors and the beam and target polarisations. The additive part contains the contributions from the uncertainty on spin-dependent radiative corrections, from possible false asymmetries and from neglecting A_2 in the determination of A_1. The upper limit for A_2^p was taken from Reference [128]. Here, the value of the asymmetry at the lowest measured Bjorken-x is used. The different contributions to the systematic uncertainty are listed in Table 21. The relative size of the contributions to the systematic uncertainty is shown in Figure 117 for the 2007 data and in Figure 118 for the 2011 data. Compared to the analysis at high photon virtualities, the uncertainty on the depolarisation factor is larger. It is about $32 - 44\%$. This is related to the uncertainty on the parametrisation of the cross section ration R, which is poorly known in the kinematic range of the data and the uncertainty is based on an estimate.

Table 21: Summary for the systematic uncertainty on A_1 for the data taken in 2007 and 2011.

		2007	2011
Beam polarisation	$\Delta P_B / P_B$	5%	5%
Target polarisation	$\Delta P_T / P_T$	2%	3.5%
Depolarisation factor	$\Delta D(R)/D(R)$	$4 - 30\%$	$4 - 30\%$
Dilution factor	$\Delta f / f$	5%	5%
Total	ΔA_1^{mult}	$\simeq (0.09 - 0.30) \cdot A_1^p$	$\simeq (0.09 - 0.30) \cdot A_1^p$
False asymmetry	A_1^{false}	$< 0.92 \cdot \sigma_{stat}$	$< 0.97 \cdot \sigma_{stat}$
Transverse asymmetry	$\eta \cdot \Delta A_2$	$< 10^{-3}$	$< 10^{-3}$
Rad. corrections	ΔA_1^{RC}	$10^{-5} - 10^{-4}$	$10^{-5} - 10^{-4}$

In the case of the structure function g_1^p, two additional contributions have to be taken into account. The modification on the systematic uncertainty are similar to the ones de-
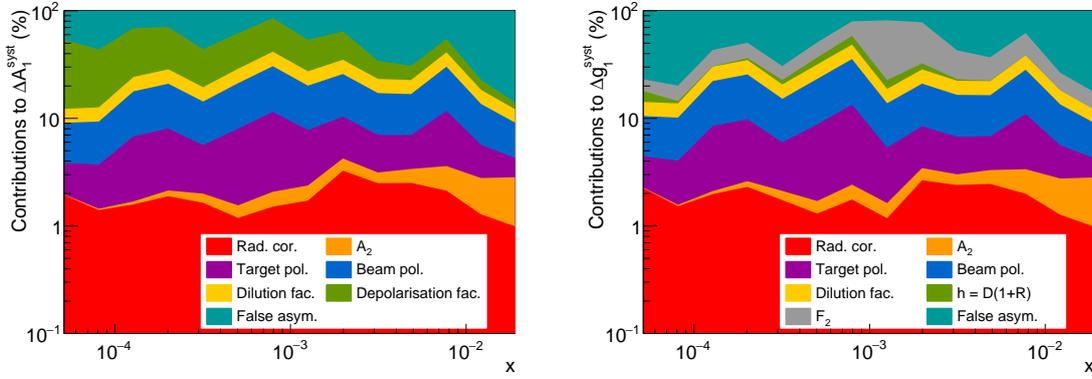
Figure 117: Relative contributions to the full systematic uncertainty of the data taken in 2007. Left: Contributions to the asymmetry A_1^p. Right: Contributions to the structure function g_1^p.
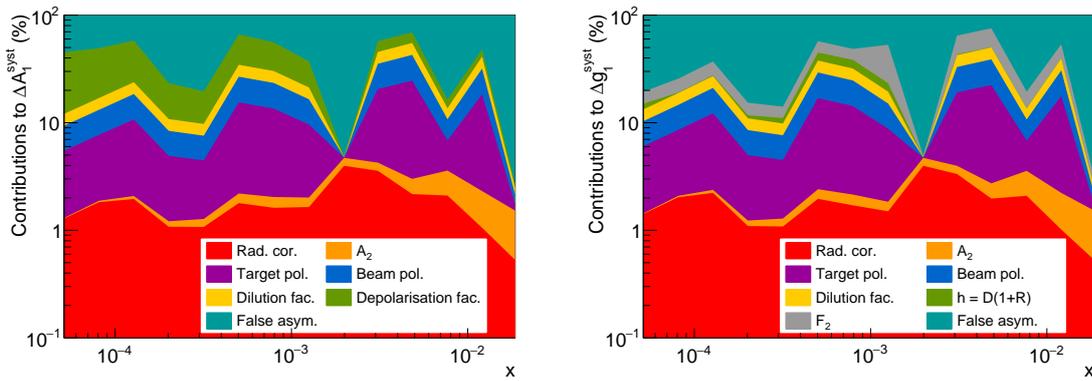
Figure 118: Relative contributions to the full systematic uncertainty of the data taken in 2011. Left: Contributions to the asymmetry A_1^p. Right: Contributions to the structure function g_1^p.

scribed in Section 5.2.8. One contribution is connected to the parametrisation of the spin-independent structure function. The largest difference between the different parametrisations is used to estimate its size:

$$\Delta F_2^p = \frac{\text{Max}\left(F_{2,i}^p - F_2^p, F_{2,j}^p - F_2^p, \ldots\right)}{2} \; . \tag{171}$$

Here, F_2^p is the parametrisation used in the calculation of the spin-dependent structure function and $F_{2,i}^p$, $F_{2,j}^p$ are the other available parametrisations. They are described in Section 4.4.2. In addition, the uncertainty on the parametrisation of the cross section ratio R has to be considered. This quantity is also used in the calculation of the depolarisation factor. Therefore, parts of the uncertainty would be taken into account twice. For this reason, the uncertainty on both contributions is combined by using the quantity $h = D \cdot (1 + R)$. The size of the uncertainty is shown in Figure 119 where it is compare to the size of the systematic uncertainty taking into account both contributions separately. Especially at low Bjorken-x a large cancellation is visible. The different contributions to the systematic uncertainty of g_1 are listed in Table 22.
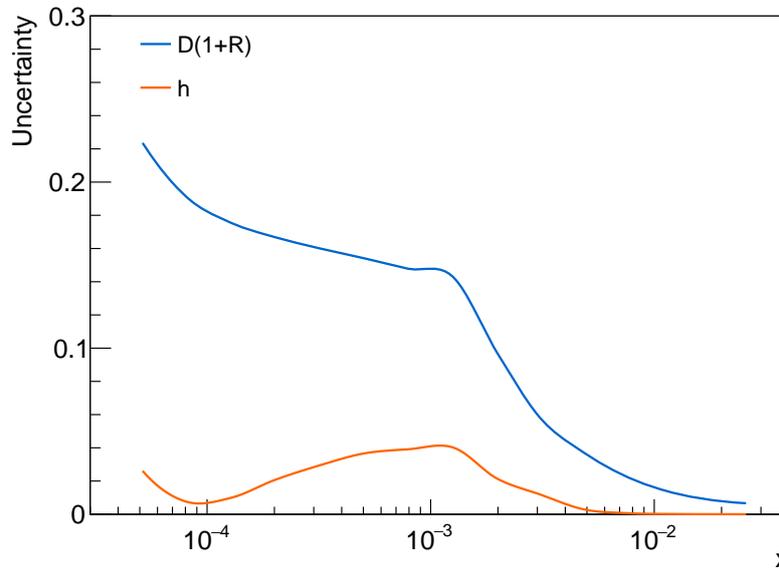
Figure 119: Size of the systematic uncertainty connected to the depolarisation factor and the cross section ratio R. It is shown once for the calculation using the combination of both and once for the calculation using them separately.

6.3   RESULTS FROM THE PROTON DATA

The asymmetries are obtained as a function of Bjorken-x and as a function of the virtual photon energy. The mean values of the photon virtualities are shown for both cases in Figure 120 in each bin. The results for both years of data taking are compared. The comparison shows the effect of the increased beam energy in 2011. The mean values for the photon virtualities are larger in each Bjorken-x bin in the case of the 2011 data than the ones of the 2007 data. Also higher virtual photon energies are accessible.

Table 22: Summary for the systematic uncertainty on g_1 for the data taken in 2007 and 2011.

		2007	2011
Beam polarisation	$\Delta P_B/P_B$	5%	5%
Target polarisation	$\Delta P_T/P_T$	2%	3.5%
Factor $h = D(1 + R)$	$\Delta h/h$	$0 - 6\%$	$0 - 5\%$
Dilution factor	$\Delta f/f$	5%	5%
Structure function F_2	$\Delta F_2/F_2$	$7 - 18\%$	$7 - 20\%$
Total	ΔA_1^{mult}	$\simeq (0.10 - 0.32) \cdot A_1^p$	$\simeq (0.10 - 0.21) \cdot g_1^p$
False asymmetry		$< 0.92 \cdot \sigma_{stat}$	$< 0.97 \cdot \sigma_{stat}$
Transverse asymmetry		$< 10^{-2}$	$< 10^{-2}$
Rad. corrections		$10^{-3} - 10^{-2}$	$10^{-3} - 10^{-2}$
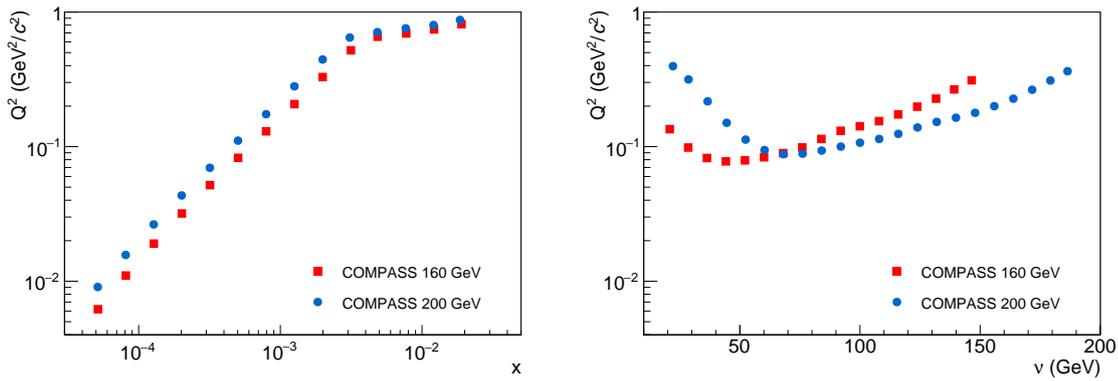
Figure 120: Mean values of the photon virtuality in bins of Bjorken-x obtained for the 2007 data and 2011 data (left) and in bins of the virtual photon energy (right).

6.3.1 *Corrections to the asymmetry*

In contrast to the extraction of the asymmetry at high photon virtualities, the asymmetry at low photon virtualities is only extracted from a "semi-inclusive" sample, due to the requirement of the additional hadron. The necessary corrections, which have to be applied, remain the same. They are described for the asymmetry at high photon virtualities in Sections 5.3.1 and 5.5.1. The correction due to spin-dependent radiative effects is calculated using POLRAD, which is described in Section 4.4.8. In order to ensure that the obtained correction to the asymmetry is still valid at low photon virtualities, the parametrisation of the asymmetry used by POLRAD is compared to the results from the data. The comparison is shown in Figure 121 for both years of data taking. The results from the data of both years show a reasonable agreement with the parametrisation. Therefore, the spin-
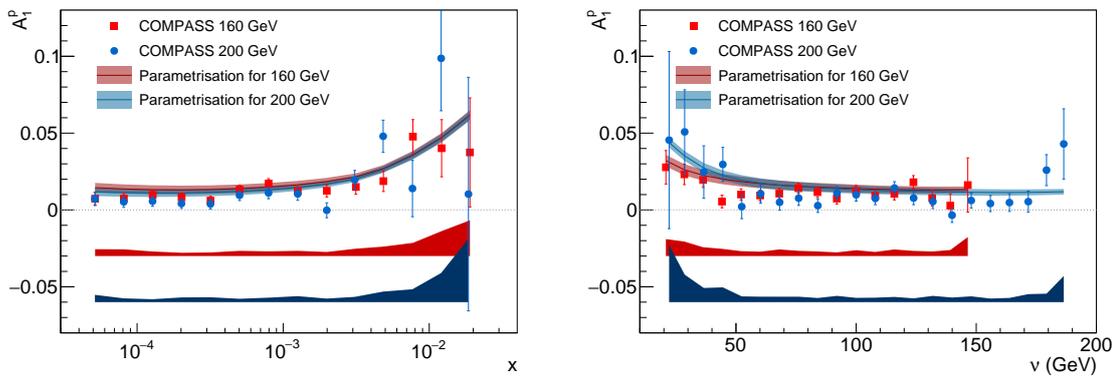
Figure 121: Comparison between the parametrisation of the asymmetry used by POLRAD and the results from the data. Left: In bins of Bjorken-x. Right: In bins of the virtual photon energy.

dependent radiative correction from POLRAD are used to correct the asymmetry. The absolute and relative size of the correction are shown in Figures 122 and 123. This correction is small but important compared to the statistical precision. The largest correction is about 25% of the statistical uncertainty.

The second correction takes into account the presence of nitrogen-14 inside the target material. The correction is described in Section 4.4.6. It is necessary since nitrogen-14 is a spin-1 nucleus that introduces an additional asymmetry on top of the one from proton. Therefore, the correction is proportional to the size of the deuteron asymmetry. For the deuteron asymmetry, a parametrisation of the world data is used. It was obtained by COMPASS and is described in Reference [129]. This parametrisation is given by

$$A_1^d(x) = (x^\alpha - \gamma^\alpha)\left(1 - e^{-\beta x}\right) \ . \tag{172}$$

Here, the parameters are $\alpha = 1.158 \pm 0.024$, $\beta = 125.1 \pm 115.7$ and $\gamma = 0.018 \pm 0.0038$. The absolute and relative size of the correction obtained for the two data sets are shown in Figures 124 and 125. The largest relative size of this correction is about 1% of the statistical uncertainty.
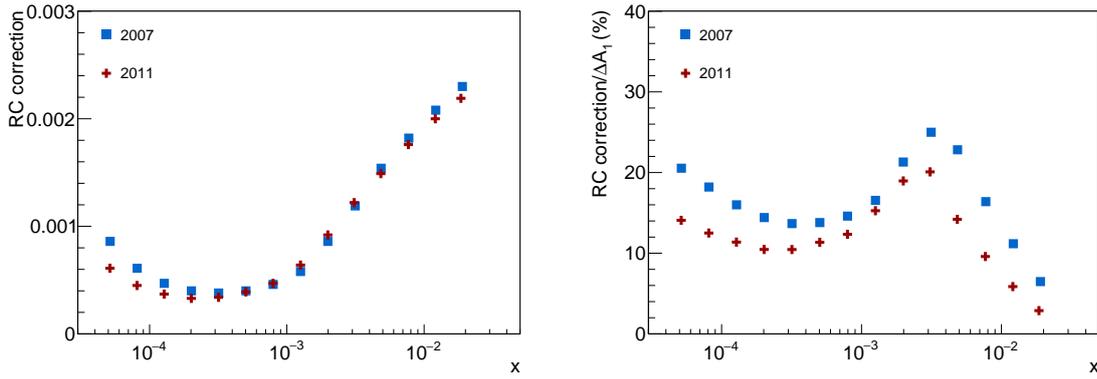
Figure 122: Correction to the asymmetry due to polarised radiative effects in bins of Bjorken-x. Left: absolute size of the correction. Right: Relative size of the correction compared to the statistical uncertainty.
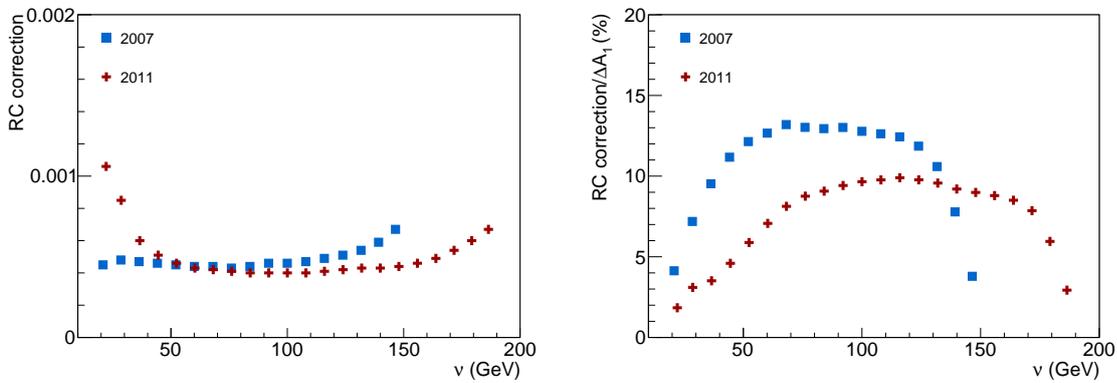
Figure 123: Correction to the asymmetry due to polarised radiative effects in bins of the virtual photon energy. Left: absolute size of the correction. Right: Relative size of the correction compared to the statistical uncertainty.
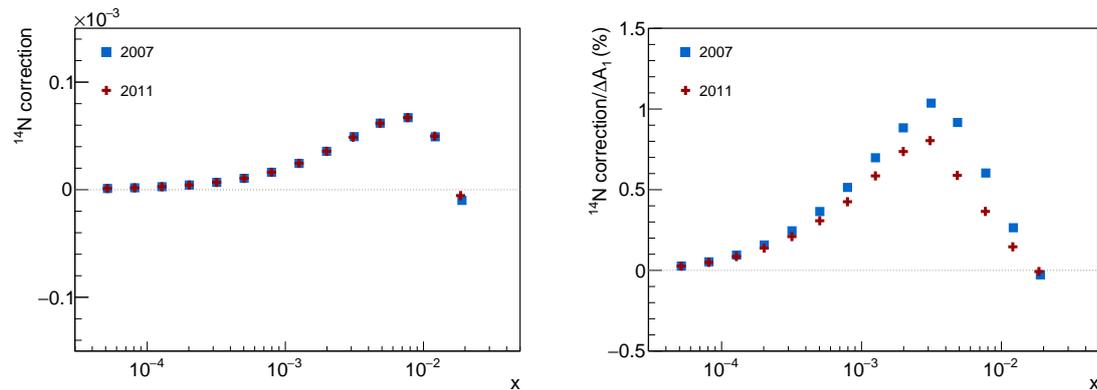
Figure 124: Correction to the asymmetry due to the presence of nitrogen-14 in the target in bins of Bjorken-x. Left: Absolute size. Right: Relative size compared to the statistical uncertainty.
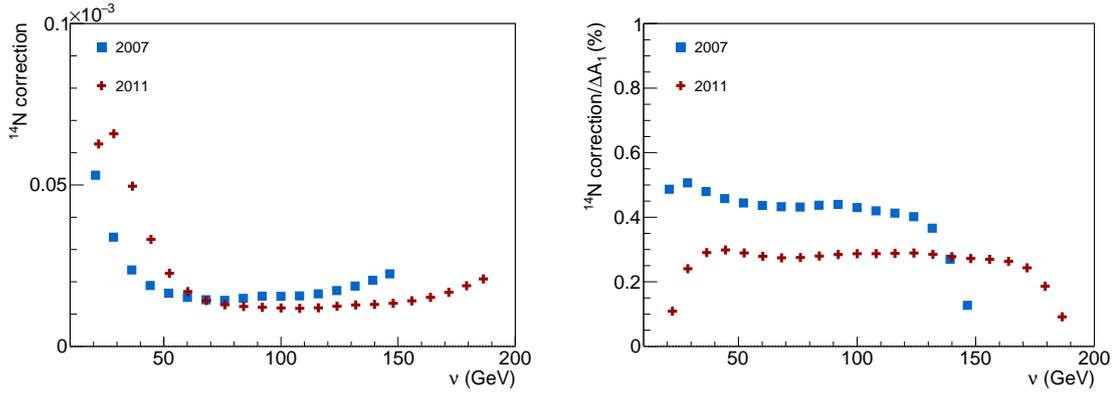
Figure 125: Correction to the asymmetry due to the presence of nitrogen-14 in the target in bins of the virtual photon energy. Left: Absolute size. Right: Relative size compared to the statistical uncertainty.

6.3.2 *Final results for the asymmetry and the structure function*

The final results for the asymmetry A_1^p from both years of data taking are obtained as a function of Bjorken-x and the virtual photon energy. The results are shown in Figure 126. The asymmetry has a finite size of about 1% and is larger than zero. It is significantly different from zero within its small statistical uncertainty. The asymmetry shows no dependence on the virtual photon energy, whereas a small increase at larger Bjorken-x is visible.
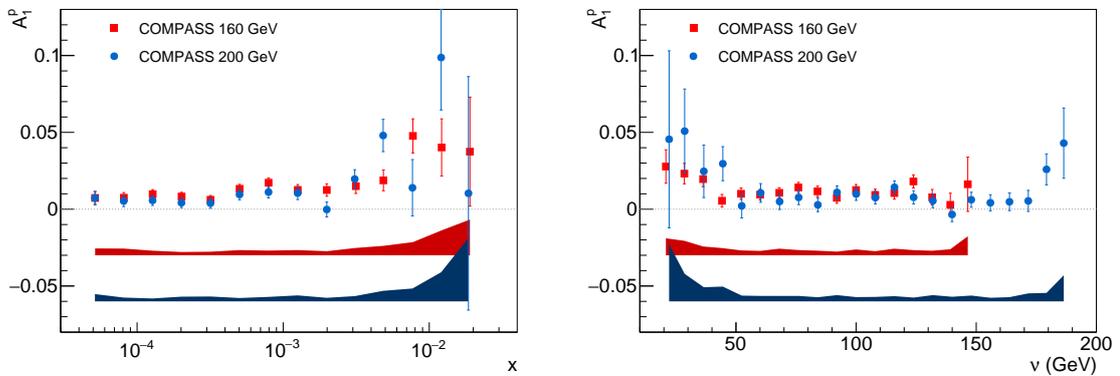
Figure 126: Results for the asymmetry A_1^p obtained at low photon virtualities in bins of Bjorken-x (left) and the virtual photon energy (right).

The results for the asymmetry are shown together with the results for the asymmetry obtained at high photon virtualities (see Chapter 5) in Figure 127. The results at low photon virtualities show a good continuation towards lower Bjorken-x.

The spin-dependent structure function g_1 is obtained from the results for the asymmetry A_1 in the same way as at high photon virtualities using $g_1^p = A_1^p F_2^p / (2x(1 + R))$ (see Sections 2.9 and 5.4). Here, again the modified parametrisation of R, described in Section 4.4.3 is used together with parametrisation of the structure functions F_2^p valid at low photon virtualities. Mainly the parametrisation from SMC [88] and a parametrisation
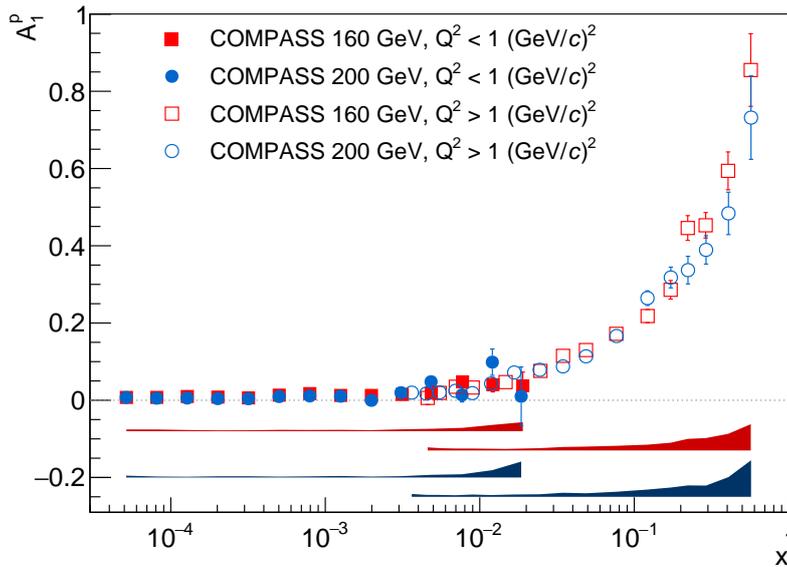
Figure 127: Results for the asymmetry A_1^p obtained at low and high photon virtualities.

based on the generalised vector meson dominance model [90, 91] are used (see also Section 4.4.2). The results obtained for the spin-dependent structure function are shown in Figure 128. Here, a positive value of about 0.5 is obtained for the structure function in the whole range of Bjorken-x and the virtual photon energy.
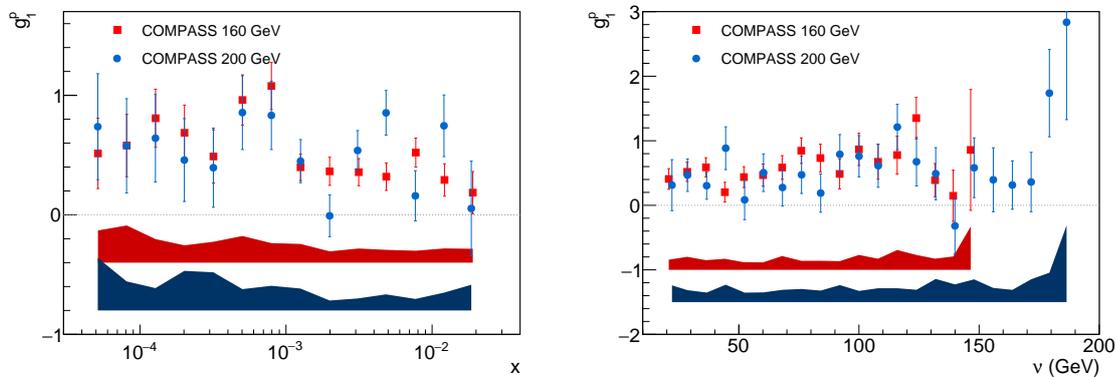
Figure 128: Results for the spin-dependent structure function in bins of Bjorken-x (left) and the virtual photon energy (right).

The results agree with predictions of a phenomenological model [54] using the generalised vector meson dominance model. The model contains in addition to the partonic contribution also a contribution from light vector mesons (see Section 2.13). In this prediction requires a large negative contribution from the vector mesons is needed in the kinematic range of COMPASS. This is consistent with previous analysis as also shown in Reference [54].

6.3.3 *Comparison with the world data*

The results for the asymmetry obtained from the two years of data taking is compared to results from other experiments at such low values of Bjorken-x. Here, only results from SMC [130] and Hermes [131] exist. This comparison is shown in Figure 129. It shows the good statistical precision of the new 2007 data and 20011 data compared to the previous results.
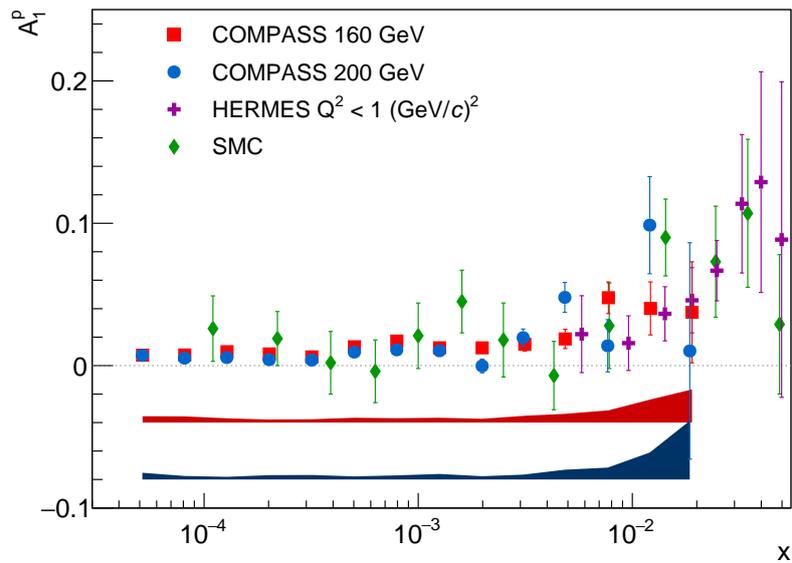
Figure 129: Comparison of the 2007 data and 2011 data with results from SMC and HERMES at low values of the Bjorken-x and $Q^2 < 1\,(\mathrm{GeV}/c)^2$.

FURTHER RESULTS USING THE EXTRACTED ASYMMETRIES

NLO QCD FIT

The results for the spin-dependent structure function of the proton and deuteron presented in Chapter 5 are used together with the world data on the spin-dependent structure functions of the proton, neutron and deuteron in a next-to-leading order QCD fit. The QCD fit allows to extract the parton helicity distributions. These can be used to determine the contribution of the quark spins to the total spin of the nucleon as well as the contribution of the gluon spins.

7.1 INPUT DATA

The world data on spin-dependent structure functions consists of the experimental results obtained using a proton, deuteron or ^{3}He target. They are given either as asymmetry A_1, ratio g_1/F_1 or structure function g_1. The results for the spin-dependent structure function obtained by the different experiments are not used as an input for the QCD fit. They may result in an additional systematic uncertainty caused by the use of various parametrisations for the spin-independent structure function. Instead, the asymmetry A_1 or the ratio g_1/F_1 is used. If the asymmetry is used as an input, it is converted into the ratio g_1/F_1 using the kinematic factor $\sqrt{1+\gamma^2} = \sqrt{1+4M^2x^2/Q^2}$ (see also Section 2.9). From the ratio g_1/F_1, the spin-dependent structure function is calculated using the same parametrisation of the spin-independent structure function F_1 for all data sets. The spin-independent structure function F_1 is calculated from a parametrisation of the cross section ratio R and a parametrisation of the spin-independent structure function F_2. These two parametrisations are described in Sections 4.4.3 and 4.4.2.

All available experimental data sets are listed in Table 23 with the quantity used in the QCD fit. For each data set, the results obtained in bins of Bjorken-x and photon virtuality are used, if they were available, in order to cover a large kinematic range. This was done in order to be as sensitive as possible to scaling violations, which are used to determine the gluon helicity distribution. For the QCD fit, not all data points were used. Data points with low invariant hadronic final state masses are excluded in order to avoid possible effects due to higher twist, as, for example, contributions to the spin-dependent structure function, which are proportional to $1/Q^2$ and therefore not described by the DGLAP equations, or corrections due to the finite mass of the nucleon. Theses effects were studied, for example, in Reference [136]. The data points with $W^2 < 10\,(\text{GeV}/c^2)^2$ were removed. The number of remaining data points are also listed in Table 23 for each data set. Introducing this cut removes the results of CLAS and Hall-A from the QCD fit, which were obtained using a polarised electron beam with an energy between $1.6\,\text{GeV}$ and $5.7\,\text{GeV}$. In total, the cut removed 241 out of the 736 data points from the QCD fit. The kinematic coverage of all data sets is shown in Figure 130 for the spin-dependent structure function of the proton, neutron and deuteron. In addition, also the kinematic range removed by the cut on the invariant hadronic final state mass is shown.

Table 23: List of available experimental data sets in DIS. For each data set, the number of data points before and after the W^2 cut are listed together with the extracted function.

EXPERIMENT	EXTRACTED FUNCTION	NUMBER OF POINTS		REFERENCE
		NO CUT	W^2 CUT	
CLAS	g_1^d/F_1^d	89	0	[123]
CLAS	g_1^p/F_1^p	59	0	[123]
COMPASS 160 GeV	A_1^d	43	43	This work
COMPASS 160 GeV	A_1^p	44	44	[106]
COMPASS 200 GeV	A_1^p	51	51	This work
E142	A_1^n	8	6	[132]
E143	g_1^d/F_1^d	82	54	[124]
E143	g_1^p/F_1^p	82	54	[124]
E154	A_1^n	11	11	[133]
E155	g_1^d/F_1^d	24	22	[127]
E155	g_1^p/F_1^p	23	21	[125]
EMC	A_1^p	10	10	[13]
Hall A	g_1^n/F_1^n	3	0	[134]
HERMES	A_1^d	37	24	[126]
HERMES	A_1^p	37	24	[126]
HERMES	A_1^n	9	7	[135]
SMC	A_1^d	65	65	[88]
SMC	A_1^p	59	59	[88]
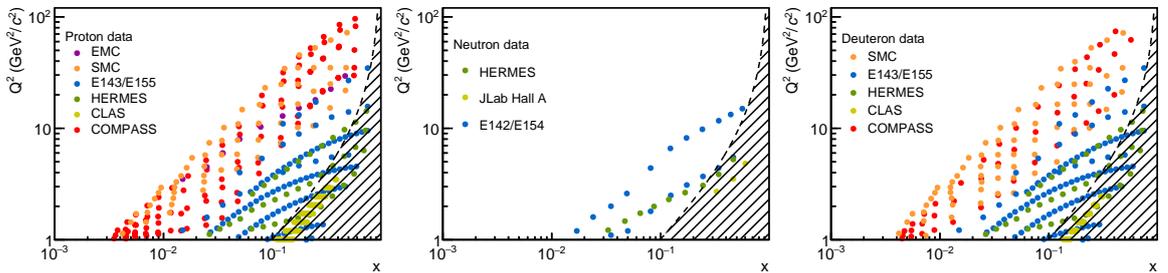
Figure 130: Kinematic coverage in Bjorken-x and photon virtuality of the DIS world data on the spin-dependent structure function of the proton (left), the neutron (centre) and the deuteron (right). The dashed area indicates the kinematic range with $W^2 < 10\,(\text{GeV}/c^2)^2$.

The original code for the extraction of the parton helicity distributions from the world data on the spin-dependent structure function was developed by SMC [137]. A modified version was also used by COMPASS [105] before. In these codes, the QCD fit is performed in the $\overline{\text{MS}}$ scheme. It uses the DGLAP equations (see Section 2.7.2) to perform the evolution of the parton helicity distributions and therefore also for the evolution of the spin-dependent structure function. Their values are calculated on a grid in Bjorken-x and photon virtuality, which covers the range of the experimental data. This method is described in Reference [138]. It differs from the method used by most of the other QCD fits where the DGLAP equations are solved in the Mellin space (see, for example, in Reference [139]).

The COMPASS code was modified to take into account a normalisation uncertainty for each data set and the external inputs to the fit were updated. The external inputs include the unpolarised parton distribution functions and the calculation of the strong coupling constant. The modified code is used to extract the parton helicity distributions. In addition, studies were performed to evaluate the systematic uncertainty on the results of the QCD fit.

7.2.1 *Fitting function*

The spin-dependent structure function is expressed in next-to-leading order by combinations of the parton helicity distributions (see Section 2.7.2). These are the singlet combination $\Delta q^S(x, Q^2)$, the two non-singlet combinations $\Delta q_3(x, Q^2)$ and $\Delta q_8(x, Q^2)$ and the gluon helicity distribution $\Delta g(x, Q^2)$. The spin-dependent structure function of the proton or neutron is given by:

$$
\begin{aligned}
g_1^{p(n)}(x, Q^2) = \frac{1}{9} \Big(& C^S(Q^2) \otimes \Delta q^S(x, Q^2) \\
& + C^{NS}(Q^2) \otimes \left[\pm \frac{3}{4} \Delta q_3(x, Q^2) + \frac{1}{4} \Delta q_8(x, Q^2) \right] \\
& + C^g(Q^2) \otimes \Delta g(x, Q^2) \Big) .
\end{aligned}
\tag{173}
$$

Here, the spin-dependent structure function of the proton is obtained by using the positive term containing the non-singlet distribution Δq_3, and the spin-dependent structure function of the neutron is obtained by using the negative term. The coefficients C^S, C^{NS}, C^g are the Wilson coefficient functions. They are used in next-to-leading order from References [31, 32].

While the DGLAP equations only predict the dependence on the photon virtuality but not the dependence on Bjorken-x, a functional form depending on Bjorken-x must be assumed at a certain input scale Q_0^2. Using the DGLAP equations, this dependence is evolved to any other scale. The assumed functional form is similar to the description in

the spin-independent case. The following functional forms are used for the singlet helicity distribution, the non-singlet helicity distributions and the gluon helicity distribution:

$$\Delta q^S(x) = \eta^S \frac{x^{\alpha^S}(1-x)^{\beta^S}(1+\gamma^S x + \rho^S \sqrt{x})}{\int_0^1 x^{\alpha^S}(1-x)^{\beta^S}(1+\gamma^S x + \rho^S \sqrt{x}) dx} \ , \tag{174}$$

$$\Delta g(x) = \eta_g \frac{x^{\alpha_g}(1-x)^{\beta_g}(1+\gamma_g x + \rho_g \sqrt{x})}{\int_0^1 x^{\alpha_g}(1-x)^{\beta_g}(1+\gamma_g x + \rho_g \sqrt{x}) dx} \ , \tag{175}$$

$$\Delta q_3(x) = \eta_3 \frac{x^{\alpha_3}(1-x)^{\beta_3}}{\int_0^1 x^{\alpha_3}(1-x)^{\beta_3} dx} \ , \tag{176}$$

$$\Delta q_8(x) = \eta_8 \frac{x^{\alpha_8}(1-x)^{\beta_8}}{\int_0^1 x^{\alpha_8}(1-x)^{\beta_8} dx} \ . \tag{177}$$

Here, the parameters α_i describe the behaviour at low Bjorken-x, the parameters β_i the behaviour at larger Bjorken-x and the parameters γ_i and ρ_i allow for a zero crossing for more flexibility. In addition, the integral in the denominator of each function is introduced as normalisation. Thus the parameters η_i are the first moments of the corresponding function. In total 16 parameters are used. Assuming SU(2) and SU(3) flavour symmetry, the first moments of the non-singlet helicity distributions are fixed by the baryon decay constants and are not used as a free parameter in the fit (see also Section 2.11).

7.2.2 χ^2 function

The QCD fit to the world data on the spin-dependent structure function performs a χ^2 minimisation. The χ^2 function is given by:

$$\chi^2 = \sum_{n=1}^{N_{Exp}} \left[\sum_{i=1}^{N_n^{Data}} \underbrace{\left(\frac{g_1^{Fit}(x_i, Q_i^2) - \mathcal{N}_n\, g_1^{Data}(x_i, Q_i^2)}{\mathcal{N}_n\, \sigma_i} \right)^2}_{\text{Statistics}} + \underbrace{\left(\frac{1 - \mathcal{N}_n}{\delta \mathcal{N}_n} \right)^2}_{\text{Normalisations}} \right] + \chi^2_{\text{Positivity}} \ . \tag{178}$$

The χ value receives three different contributions. The first one is the usual contribution taking into account the difference between the value of the spin-dependent structure function from the fit, g_1^{Fit}, and its measured value, g_1^{Data}, with its statistical uncertainty, σ_i. This contribution is modified to take into account a normalisation factor $\mathcal{N}_n$ for each experiment. The normalisation factors are used as a free parameter in the QCD fit for each experiment. In order to constrain these parameters, the second contribution to the χ^2 value penalises large deviations from one. It takes into account the normalisation uncertainty $\delta \mathcal{N}_n$ given by the experiments either within their publication or estimated from the uncertainty of the beam and target polarisation. The remaining contributions to the systematic uncertainty, which are, for example, related to false asymmetries, are not taken into account in the fit since they are correlated locally and their correlation is in general not known. The third contribution to the χ^2 value constrains the high Bjorken-x behaviour of the parton helicity distributions by applying a positivity condition to all parton helicity distributions. The latter should be smaller than their unpolarised counterparts:

$$|\Delta q(x) + \Delta \bar{q}(x)| < q(x) + \bar{q}(x) \ , \tag{179}$$

$$|\Delta g(x)| < g(x) \ . \tag{180}$$

This constraint is strictly only valid in leading order. It was shown in Reference [140] that it can be also used in next-to-leading order since the corrections are small compared to the uncertainty on the parton helicity distributions for $x \gtrsim 0.01$. In the case of the QCD fit, the additional term $\chi^2_{\text{Positivity}}$ is calculated for all Bjorken-x larger than 0.1. The same form as used by LSS [141] is used for this contribution:

$$\chi^2_{\text{positivity}} = \exp\left(k \cdot \left(|\Delta q(x)| - q(x)\right)\right) . \tag{181}$$

Here, the factor k determines the strength of the positivity constraint. It has to be chosen such that violations are still suppressed while the fit is not dominated by the positivity constraint. The parton distribution functions are taken from MSTW [110]. The positivity constraint is only applied at the lowest scale, $Q^2 = 1\,(\text{GeV}/c)^2$, in the fit since once it is satisfied, it is conserved at all scales by the evolution to larger photon virtualities [142].

7.2.3 *Strength of the positivity constraint*

In order to find an appropriate value for the factor k in the positivity constraint, the QCD fit was repeated several times changing the strength within the range of $k = 50$ to $k = 1000$. The effect of increasing the strength of the positivity constraint is shown in Figure 131 in the case of the results for the down quark helicity distribution. The results are shown for the two functional forms chosen later on (see Section 7.4.1). By increasing
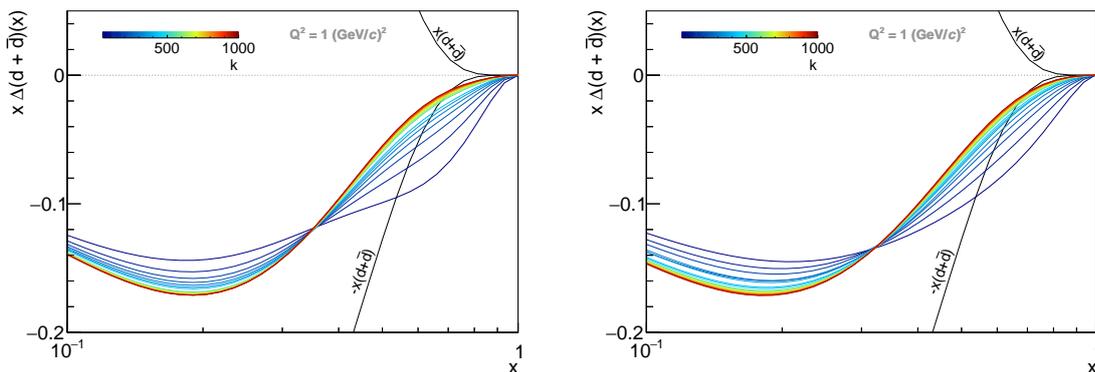
Figure 131: Effect of the increasing strength of the positivity constraint on the down quark helicity distribution. The results are shown at a fixed photon virtuality of $Q^2 = 1\,(\text{GeV}/c^2)^2$ for the two solutions of the QCD fit. Left: Solution $S(G^-)$. Right: Solution $S(G^+)$.

the strength of the positivity constraint, the resulting down quark helicity distribution gets closer to the unpolarised one. This also results in a larger contribution to the χ^2 value from the positivity constraint. The size of the different contributions to the reduced $\chi^2 = \chi^2/\text{NDF}$ value, which takes into account the number of degrees of freedom, is shown in Figure 132 as a function of the strength of the positivity constraint. For a large strength of the positivity constraint ($k \sim 1000$), no significant improvement on the size of the violation of the positivity constraint is found at large Bjorken-x compared to a medium strength ($k \sim 600$) while the χ^2 value of the QCD fit is further increased. Therefore, a medium strength ($k = 600$) of the positivity constraint is used in further QCD fits.
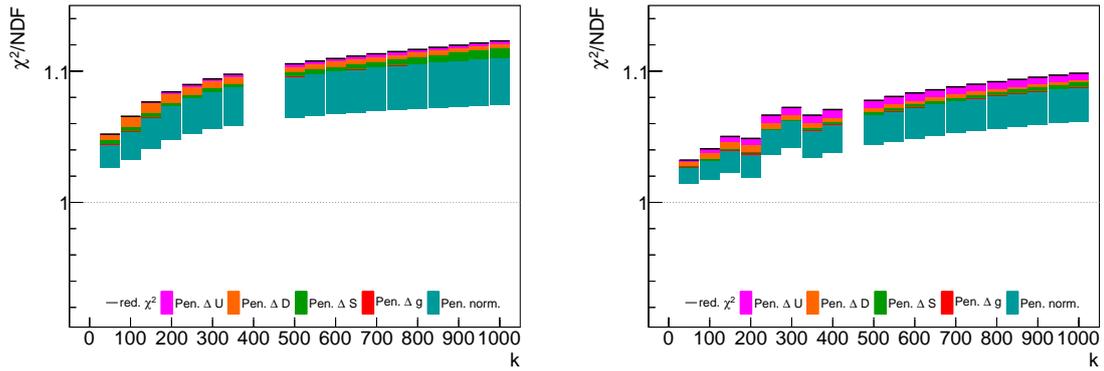
Figure 132: Effect of the strength of the positivity constraint on the reduced χ^2 value of the QCD fit. The various contributions from the positivity constraint and the normalisation to the reduced χ^2 value are shown. The black line indicates the reduced χ^2 value of the full fit. Left: Solution $S(G^-)$. Right: Solution with $S(G^+)$.

7.3 STATISTICAL UNCERTAINTY OF THE QCD FIT

Several methods exist to propagate the statistical uncertainties from data to the results of the fit. Three widely used methods are the Lagrange multiplier [143], the Hessian method [144] and the Monte Carlo sampling [145]. Here, the Monte Carlo sampling method is used due to its simplicity in calculating the statistical uncertainty at each point of the grid in Bjorken-x and photon virtuality.
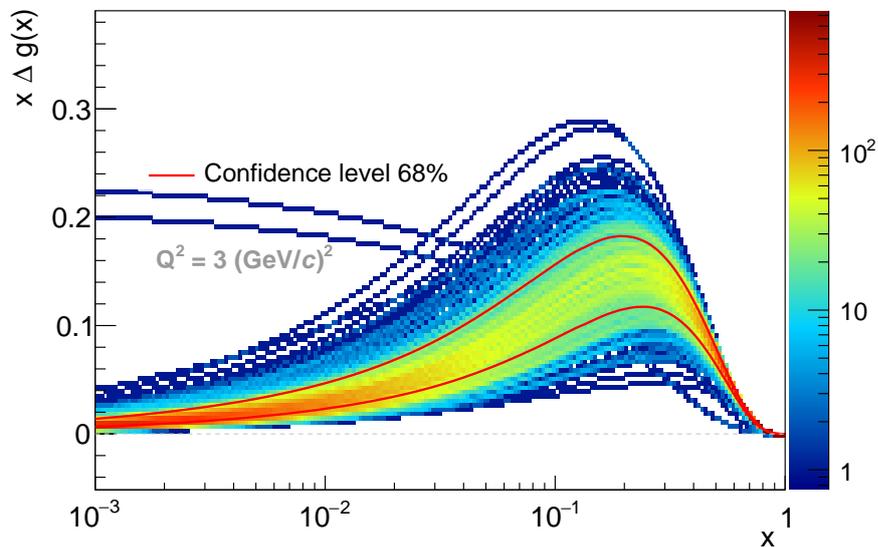
Figure 133: Illustration of the calculation of the statistical uncertainty using the Monte Carlo sampling method. The results of the QCD fit for 1000 replicas are shown together with the red lines indicating the 1σ range around the mean value of this distribution.

For the Monte Carlo sampling method a set of 1000 replicas is created. These are obtained by creating new data sets as an input to the QCD fit. The new data sets are obtained

by randomly varying the measured values for the spin-dependent structure function according to a Gaussian distribution. The mean value of the Gaussian distribution is given by the measured value of the spin-dependent structure function and the width of the Gaussian distribution is given by the statistical uncertainty. The distribution of the results for the gluon helicity distribution from all replicas is shown in Figure 133 at a fixed photon virtuality for the solution $S(G^+)$, which will be explained later. The results of the various fits are used to obtain a mean value and the root-mean-square of the distribution at each point in Bjorken-x and photon virtuality. The root-mean-square of the distribution is also indicated in Figure 133 by two red lines. Note that the obtained uncertainty bands are not necessarily symmetric around the original distribution. This method can easily be extended to calculate the statistical uncertainty on any quantity derived from such distributions. It can, for example, be used to calculate the uncertainty on the first moment of the various parton helicity distributions or the structure function.

7.4 SELECTION OF THE PARAMETRISATION

The functional forms described before allow for a complex description of the singlet and gluon helicity distribution. In order to determine, which parameters are necessary in the QCD fit of the spin-dependent structure function, the dependence on different functional forms of the singlet and gluon helicity distribution is studied. From this study, not only the functional forms for the final QCD fits are obtained, also a contribution to the systematic uncertainty is obtained.

7.4.1 *Choice of the functional forms*

The Bjorken-x dependence of the parton helicity distributions given in Equations 174-177 assumes at least two parameters describing the low and high Bjorken-x behaviour. In the case of the singlet helicity distribution and the gluon helicity distribution also a zero crossing can be allowed by using the parameters γ and ρ as a free parameter. For the QCD fit, the parameter describing the high Bjorken-x behaviour of the gluon helicity distribution is fixed to the value of the parton distribution function from Reference [110]. This will be explained in Section 7.4.2.

The influence on the parameters allowing a zero crossing of the functional shapes is studied in several fits. Fits including the parameters γ^S, ρ^S, γ_g and ρ_g as a free parameter or fixing them to zero were performed. The result of those fits is shown in Figure 134 for the Bjorken-x dependence of the gluon and singlet helicity distribution together with the χ^2 value of the fit.

The χ^2 value of all fits that converge is comparably good. The obtained shape and size of the singlet helicity distribution is quite similar between the various assumed functional shapes, whereas the result for the gluon helicity distribution changes drastically. Negative values for the first moment of the gluon helicity distribution are obtained as well as positive ones and also some close to zero. This test illustrates that the gluon helicity distribution is not well constrained by the deep inelastic scattering data alone. However, the impact on the spin-dependent structure functions is small.

From this test, two functional shapes were chosen for the final results of the QCD fit. These two solutions represent the two extreme cases for possible solutions. All other
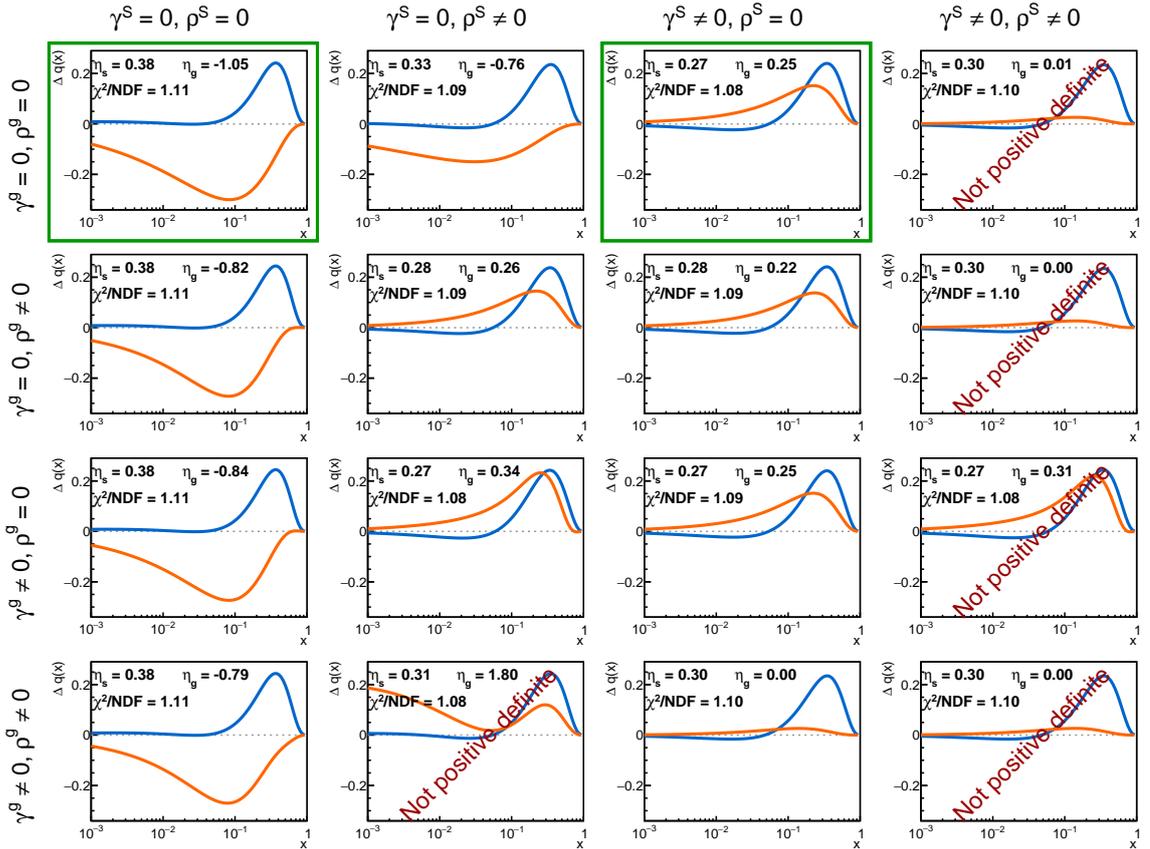
Figure 134: Results of the QCD fit for various functional forms are shown at $Q^2 = 3\,(\text{GeV}/c)^2$. The blue curve represents $\Delta q^S(x)$, the orange one $\Delta g(x)$. The first moment of these distributions at the input scale and the χ^2 value are given for comparison. The solutions shown in panels one and three of the first row (surrounded by green boxes) represent the two solutions $S(G^-)$ and $S(G^+)$.

obtained results are in between those two results and the range covered by those solutions will be part of the systematic uncertainty. The solution with all γ and ρ parameters fixed to zero named $S(G^-)$, which results in a negative gluon polarisation, is chosen and the solution with γ^S as a free parameter named $S(G^+)$, which results in a positive gluon distribution. In the following sections, the systematic studies are performed using only these two solutions and their influence is compared to the difference between the extreme solutions.

7.4.2 *High Bjorken-x behaviour of the gluon helicity distribution*

The data used in the QCD fit are not very sensitive to the high Bjorken-x behaviour of the gluon helicity distribution. This is tested by performing various fits with different values for the parameter β_g. The dependence of the χ^2 value of the QCD fit on the parameter is shown in Figure 135 for a range of β_g between 1 and 10. The dependence is shown for both solutions of the QCD fit. No significant dependence of the χ^2 value is visible except for $\beta_g < 2.5$ where an increase is visible. The effect on the singlet helicity distribution
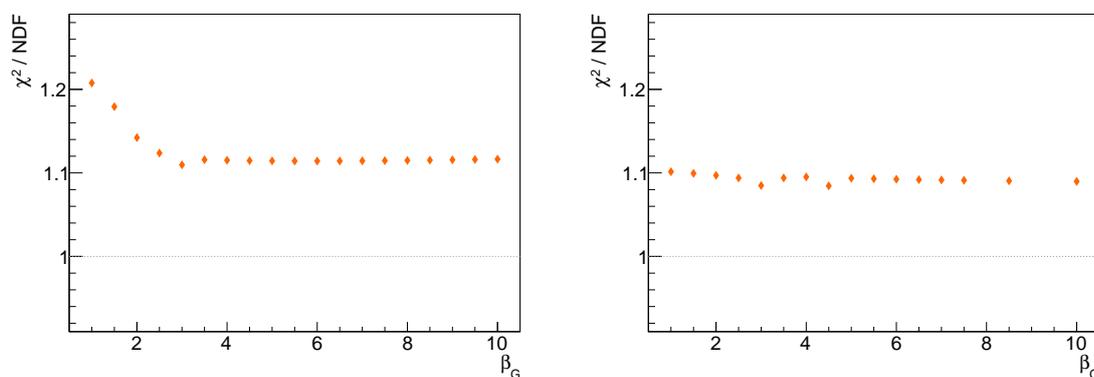
Figure 135: Dependence of the χ^2 value of the two solutions of the QCD fit on the value of β_g. Left: Dependence for the solution $S(G^-)$. Right: Dependence for the solution $S(G^+)$.

and the gluon helicity distribution is shown in Figure 136 for the solution $S(G^-)$ of the QCD fit with a negative gluon polarisation. In the case of the singlet helicity distribution, only a small difference between all solutions is visible for small values of β_g, which also correspond to an increased χ^2 value. In the case of the gluon helicity distribution, also the solutions for small values of β_g show larger differences. The difference between the other solutions is caused by the positivity constraint, which has to be fulfilled at high Bjorken-x. This results in values close to zero. This study confirms that data used in the QCD fit are not very sensitive to the high Bjorken-x behaviour of the gluon helicity distribution. It was chosen to fix the parameter β_g to the value of the unpolarised gluon distribution from Reference [110] used in the positivity constraint.

7.5 SYSTEMATIC STUDIES

Several systematic studies on the results of the QCD fit were performed. The aim of these studies is to estimate the systematic uncertainty of the fit due to the used method. The
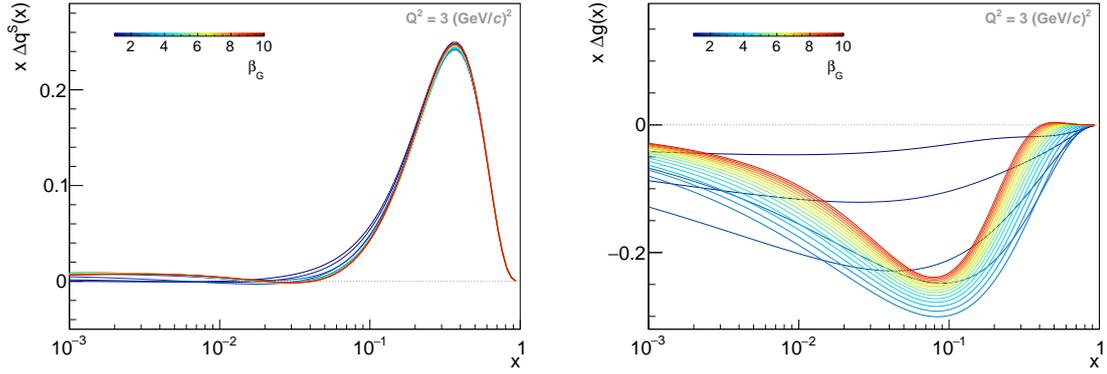
Figure 136: Dependence of the singlet helicity distribution (left) and the gluon helicity distribution (right) on β_g. The results are shown at $Q^2 = 3\,(\text{GeV}/c)^2$ for the solution $S(G^-)$.

results of these studies are compared to the contribution from the choice of the functional form.

7.5.1   *Input scale*

The functional forms for the parton helicity distributions were defined at an input scale of $Q_0^2 = 1\,(\text{GeV}/c)^2$. As there is no reason to prefer any input scale, it can be chosen freely. In order to test the influence of the chosen input scale on the results of the QCD fit, several fits were performed using various input scales. The results of the various fits are shown in Figure 137 for the solution $S(G^-)$ and in Figure 138 for the solution $S(G^+)$. The results for the singlet and gluon helicity distribution are shown at fixed photon virtuality of $3\,(\text{GeV}/c)^2$ for various input scales ranging from $1\,(\text{GeV}/c)^2$ to $63\,(\text{GeV}/c)^2$. The effect is similar to changing the functional form at an fixed input scale and agrees with the range covered by two extreme solutions. The χ^2 of the QCD fits are similar good.
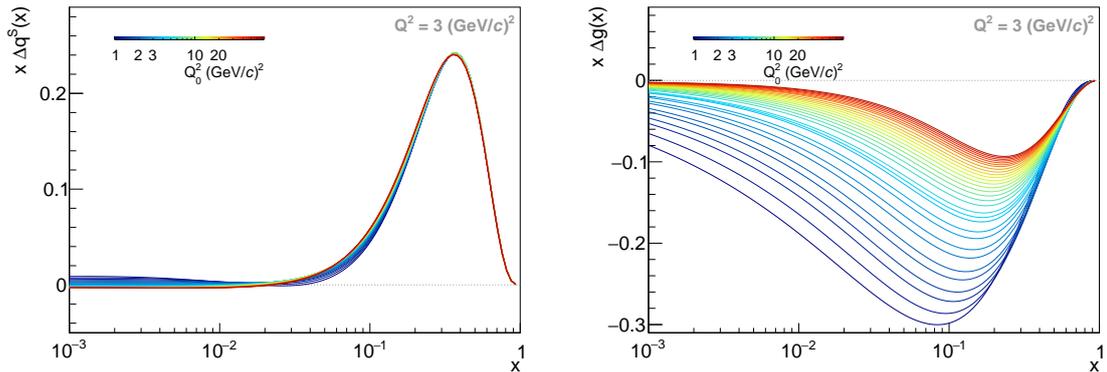
Figure 137: Influence of changing the input scale on the the singlet (left) and gluon helicity distribution (right) shown at $Q^2 = 3\,(\text{GeV}/c)^2$ for the solution $S(G^-)$ of the QCD fit.

Changing the input scale results only in a small change of the singlet helicity distribution. Also, the first moment shows no significant change. At $Q^2 = 3\,(\text{GeV}/c^2)$, it changes from $\Delta\Sigma = 0.344$ for an input scale of $1\,(\text{GeV}/c)^2$ to $\Delta\Sigma = 0.337$ for an input scale of
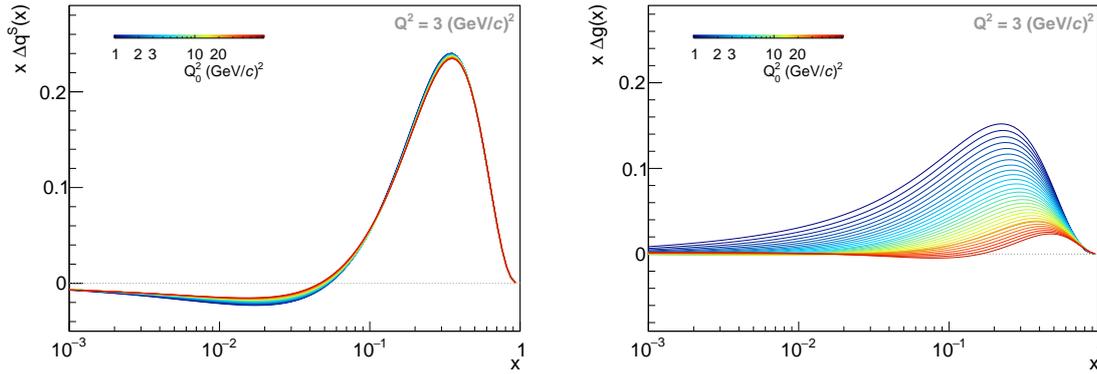
Figure 138: Influence of changing the input scale on the the singlet (left) and gluon helicity distribution (right) shown at $Q^2 = 3\,(\text{GeV}/c)^2$ for the solution $S(G^+)$ of the QCD fit.

$63\,(\text{GeV}/c)^2$ for the solutions $S(G^-)$ and from $\Delta\Sigma = 0.268$ to $\Delta\Sigma = 0.274$ for the other solution. The small changes visible at low and medium Bjorken-x compensate one another in the calculation of the first moment.

A different behaviour is obtained in the case of the gluon helicity distribution. The results show a strong dependence on the input scale. This is also reflected in the first moments. In the case of the solutions $S(G^-)$, the first moment at $Q^2 = 3\,(\text{GeV}/c^2)$ changes from $\Delta G = -1.36$ for an input scale of $Q_0^2 = 1\,(\text{GeV}/c)^2$ to $\Delta G = -0.25$ for an input scale of $Q_0^2 = 63\,(\text{GeV}/c)^2$. For the other solution of the QCD fit, the first moment changes from $\Delta G = 0.43$ to $\Delta G = 0.03$. This test confirms that the gluon helicity distribution is not well constrained in the QCD fit.

7.5.2 *Dependence on the parton distribution functions*

By introducing the positivity constraint to the QCD fit of the world data on the spin-dependent structure function, a dependence on the parton distribution functions is introduced. The MSTW collaboration provides 41 sets for the parton distribution functions [146]. These sets contain the optimal set and solutions corresponding to a certain increase in the χ^2, while moving along an eigenvector. Here, the solutions for the 68% confidence level are used. Using the lower and upper limit on the parton distribution functions, the QCD fit was repeated to evaluate their influence on the parton helicity distributions. This influence is shown for the up, down and strange quark helicity distributions in Figure 139. The uncertainty of the parton distribution functions has a very small influence on the parton helicity distributions of the up and down quarks. The effect is below the statistical uncertainty of the QCD fit. In the case of the strange quark helicity distribution, a stronger dependence is visible in between the two extreme solutions, which is already covered by the systematic uncertainty.

7.5.3 *Dependence on the data set*

Calculation using perturbative QCD seem to be valid for $Q^2 > 1\,(\text{GeV}/c)^2$, even though in current QCD fits to spin-independent data data points with photon virtualities close to
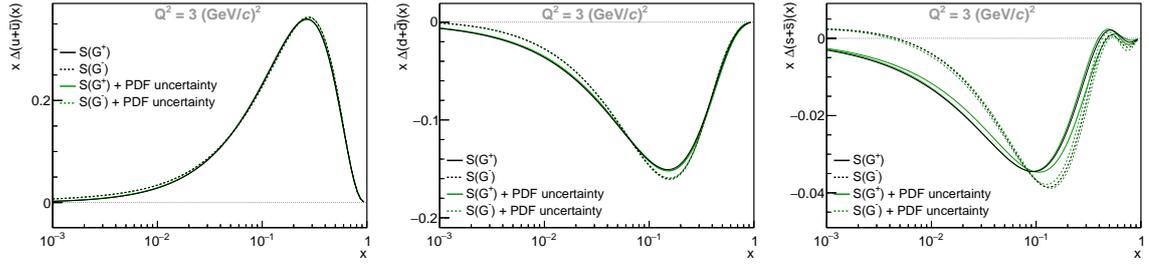
Figure 139: Influence of the uncertainty of the parton distribution functions on the results for the up (left), down (middle) and strange (right) quark helicity distribution for the two solutions $S(G^+)$ (solid) and $S(G^-)$ (dashed).

$Q^2 = 1\,(\text{GeV}/c)^2$ are excluded in order to ensure perturbative QCD to be valid. In the case of the fit by MSTW [110] the data from deep inelastic scattering with photon virtualities below $2\,(\text{GeV}/c)^2$ are rejected for the extraction of the parton distribution functions. These were also rejected in order to avoid large contributions from higher twist and also higher orders. In order to see whether an effect is visible in the case of the spin-dependent deep inelastic scattering data, the QCD fit was repeated removing data points with photon virtuality below $2\,(\text{GeV}/c)^2$. The comparison between the results of the QCD fit with and without those data points is shown in Figure 140. Removing the data points has no influence on the results of the QCD fit. But removing those data points from the QCD fit
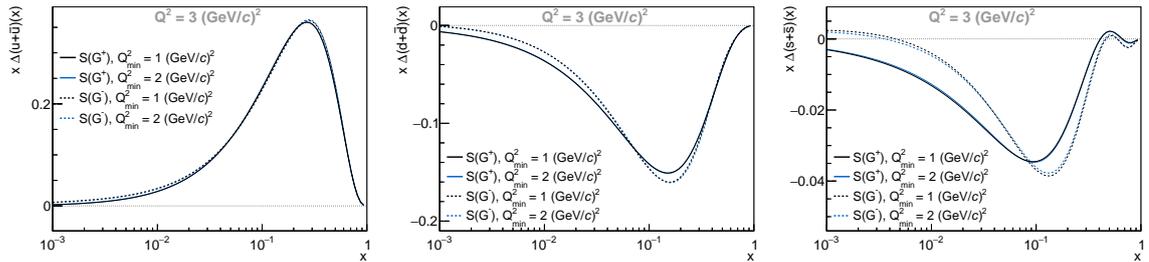
Figure 140: Influence of removing the the data point with $Q^2 \leqslant 2\,(\text{GeV}/c)^2$ from the QCD fit on the results for the up (left), down (middle) and strange (right) quark helicity distribution for the two solutions $S(G^+)$ (solid) and $S(G^-)$ (dashed).

results in the loss of 127 data points. This reduces the statistical precision of the QCD fit. In addition, the removed data points cover the region of lowest Bjorken-x in the fit. Thus the QCD fit is only valid in the Bjorken-x range from 0.007 to 0.8. As no influence on the results of the QCD fit was found, the data points are kept in the QCD fit.

7.6 RESULTS

The studies described in Section 7.4 show that two functional forms remain, which represent the two extreme cases for all possible solutions. The solution $S(G^-)$ uses a parametrisation that does not allows a zero crossing for the singlet helicity distribution at the input scale of $Q_0^2 = 1\,(\text{GeV}/c)^2$. It yields a negative gluon helicity distribution at the input scale. The solution $S(G^+)$ uses a parametrisation that allows a zero crossing of the singlet

helicity distribution at the input scale. It yields a positive gluon helicity distribution at the input scale.

7.6.1 *Parameters of the QCD fit*

The parameters of the two solutions of the QCD fit are given in Table 24 together with their χ^2 values. In both cases, the χ^2 values of the QCD fit is close to the number of degrees of freedom indicating a good description of the deep inelastic scattering data.

Table 24: Parameters of the NLO QCD fits obtained at $Q_0^2 = 1\,(\text{GeV}/c)^2$ for the two functional forms. The parameters marked with an asterisk are fixed.

PARAMETERS	SOLUTION $S(G^+)$	SOLUTION $S(G^-)$
η_g	0.25 ± 0.19	-1.05 ± 0.18
α_g	0.72 ± 0.64	-0.36 ± 0.12
β_g	3.0225^*	3.0225^*
η_{si}	0.274 ± 0.024	0.383 ± 0.012
α_{si}	-0.260 ± 0.061	1.40 ± 0.12
β_{si}	3.01 ± 0.11	3.50 ± 0.16
γ_{si}	-12.7 ± 1.1	0^*
α_3	0.018 ± 0.034	0.049 ± 0.034
β_3	2.690 ± 0.063	2.741 ± 0.066
α_8	0.261 ± 0.089	0.377 ± 0.078
β_8	2.54 ± 0.18	2.65 ± 0.14
χ^2/ndf	$509.2/470$	$522.6/471$

In addition, also the different contributions to the χ^2 values from the various experiments are of interest. They are listed for both solutions of the QCD fit in Tables 25, 26 and 27 for the proton, deuteron and neutron data respectively together with the normalisation factors obtained. For all experiments a good χ^2 value is obtained compared to the number of provided data points together with normalisation factors, which are in agreement with unity. The only experiment where the normalisation factor differs from unity is the proton data set from the E155 experiment. A normalisation factor of 1.16 ± 0.02 was found. The need of an additional normalisation factor for this particular data set is already known since it is already suggested within their paper [125]. They suggested the use of a normalisation factor of $1.08 \pm 0.03_{\text{stat}} \pm 0.08_{\text{syst}}$, which is in agreement with the one found in these QCD fits. Using the normalisation factor still results in an increased χ^2. The increased χ^2 is causes mainly by two data points, which account for about 50% of the χ^2.

Table 25: List of experimental data sets for the spin-dependent structure function of the proton. For each experiment, the number of data points, the χ^2 contribution and the normalisation factor is given for the two solutions of the QCD fit.

EXPERIMENT	NUMBER OF POINTS	χ^2		Normalisation	
		$S(G^+)$	$S(G^-)$	$S(G^+)$	$S(G^-)$
COMPASS 160 GeV	44	51.5	49.6	1.00 ± 0.03	0.99 ± 0.03
COMPASS 200 GeV	51	43.7	43.2	1.03 ± 0.03	1.02 ± 0.03
E143	54	47.6	49.1	1.05 ± 0.02	1.08 ± 0.02
E155	21	51.7	50.8	1.16 ± 0.02	1.16 ± 0.02
EMC	10	5.3	4.7	1.03 ± 0.07	1.02 ± 0.07
HERMES	24	14.0	16.2	1.07 ± 0.03	1.10 ± 0.03
SMC	59	55.0	55.4	1.02 ± 0.03	1.01 ± 0.03

Table 26: List of experimental data sets for the spin-dependent structure function of the deuteron. For each experiment, the number of data points, the χ^2 contribution and the normalisation factor is given for the two solutions of the QCD fit.

EXPERIMENT	NUMBER OF POINTS	χ^2		Normalisation	
		$S(G^+)$	$S(G^-)$	$S(G^+)$	$S(G^-)$
COMPASS 160 GeV	43	48.0	59.0	1.02 ± 0.04	1.00 ± 0.04
E143	54	60.7	58.2	0.99 ± 0.04	1.01 ± 0.04
E155	22	18.7	17.8	1.00 ± 0.04	1.00 ± 0.04
HERMES	24	28.0	27.0	0.98 ± 0.04	1.01 ± 0.04
SMC	65	58.9	61.4	1.00 ± 0.04	1.00 ± 0.04

Table 27: List of experimental data sets for the spin-dependent structure function of the neutron. For each experiment, the number of data points, the χ^2 contribution and the normalisation factor is given for the two solutions of the QCD fit.

EXPERIMENT	NUMBER OF POINTS	χ^2		Normalisation	
		$S(G^+)$	$S(G^-)$	$S(G^+)$	$S(G^-)$
E142	6	1.1	1.1	1.01 ± 0.07	0.98 ± 0.07
E154	11	5.5	7.2	1.06 ± 0.04	1.06 ± 0.04
HERMES	7	1.6	1.2	1.01 ± 0.07	1.00 ± 0.07

7.6.2 *Parton helicity distributions*

Results of the QCD fits for the parton helicity distributions of the three lightest quark flavours can be extracted from the results for the singlet and the two non-singlet helicity distributions. They are shown together with the results for the singlet and the gluon helicity distribution in Figure 141. Here, the darker bands correspond to the statistical uncertainty of the two solutions described in Section 7.3 and the lighter bands correspond to the combined statistical and systematic uncertainty described in Sections 7.4 and 7.5. The figure also shows that the statistical uncertainty of the fit is small compared to its systematic uncertainty. It also shows that the parton helicity distributions of the up and down quarks are well constrained by the QCD fit. The strange quark and down quark helicity distributions are negative and the up quark helicity distribution is positive in both solutions of the QCD fit. This agrees with the expectation from the magnetic moment of the quarks that spins of the up quarks are aligned parallel to the nucleon spin and the ones of the down and strange quarks are aligned antiparallel. The solutions for the three quark flavours differ from zero for $x \gtrsim 0.001$, whereas the singlet helicity distribution is compatible with zero for $x < 0.07$. The gluon helicity distribution is not well constrained, as already discussed in Section 7.4.
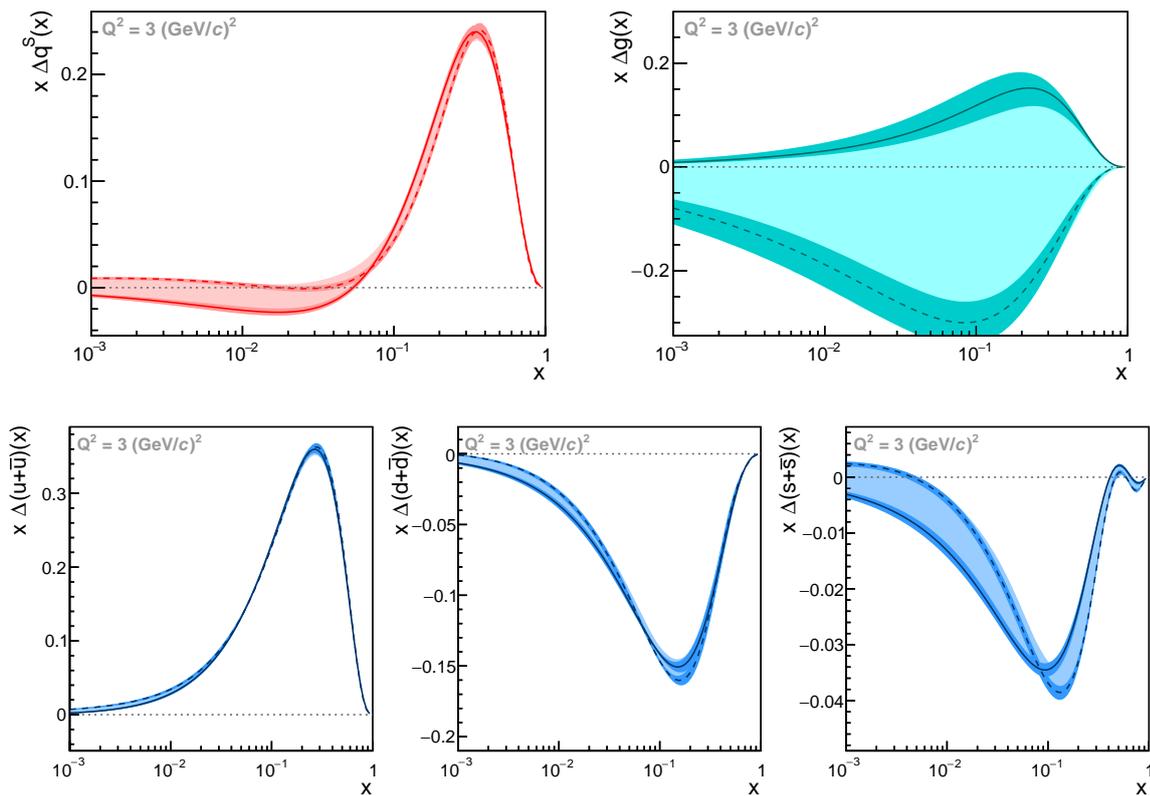
Figure 141: Results from the QCD fits shown at $Q^2 = 3\,(\text{GeV}/c)^2$. Top left: Singlet helicity distribution. Top right: Gluon helicity distribution. Bottom: $x(\Delta q + \Delta \bar{q})$ for u, d and s flavour going from left to right. For each distribution, the two extreme solutions corresponding to the two different functional forms are shown.

The results for the spin-dependent structure function of the proton and deuteron obtained from the QCD fit are compared to the world data in Figures 142 and 143. Here, all data sets listed in Table 23 are shown. An extrapolation of the results of the QCD fit for the kinematic range of $W^2 < 10\,(\mathrm{GeV}/c^2)^2$, which was excluded from the fit, is indicated by a dashed lines. These comparisons also show the contribution of the new data sets obtained by the COMPASS experiment to the world data. They show that COMPASS is the only experiment capable of measuring the spin-dependent structure function with a good statistical precision even at low Bjorken-x. At high Bjorken-x these results extend the measured range towards larger photon virtualities.

The results of the QCD fit are also used to obtain the contribution of the quark spins to the total spin of the nucleon, which is given by the first moment of the singlet helicity distribution. The individual contributions of the various flavours can also be obtained. They are given in Table 28 together with the result for the gluon. The ranges take into account the statistical and systematic uncertainty of the QCD fit. Note that the first moments of the individual flavours are not independent of one another since the first moments of the non-singlet distributions were fixed. The contribution of the gluon spin to the total spin of the nucleon is not well constrained by the QCD fits.

Table 28: Range for the first moments of the parton helicity distributions obtained from the QCD fits at $Q^2 = 3\,(\mathrm{GeV}/c)^2$.

FIRST MOMENT	VALUE
$\Delta\Sigma$	$[0.25, 0.35]$
$\Delta u + \Delta \bar{u}$	$[0.82, 0.85]$
$\Delta d + \Delta \bar{d}$	$[-0.45, -0.42]$
$\Delta s + \Delta \bar{s}$	$[-0.11, -0.08]$
ΔG	$[-1.5, 0.4]$

7.6.3 *Comparison with direct measurements of the gluon polarisation*

Even though the gluon helicity distribution is not constrained by the QCD fit, the result can be compared to the results of direct measurements using the photon-gluon-fusion process. This production mechanism is studied in reactions containing charmed mesons [147] or high-p_T hadrons [148–151]. These results are obtained mainly at leading order. For the analysis using charmed mesons also a next-to-leading order result was obtained. The comparison is shown in Figure 144. These results are in agreement with the results of the QCD fit. They might favour a solution with a positive gluon polarisation. This impression is caused by the latest COMPASS result obtained in leading order [151]. This result has small statistical and systematic uncertainties and favours a positive gluon polarisation.
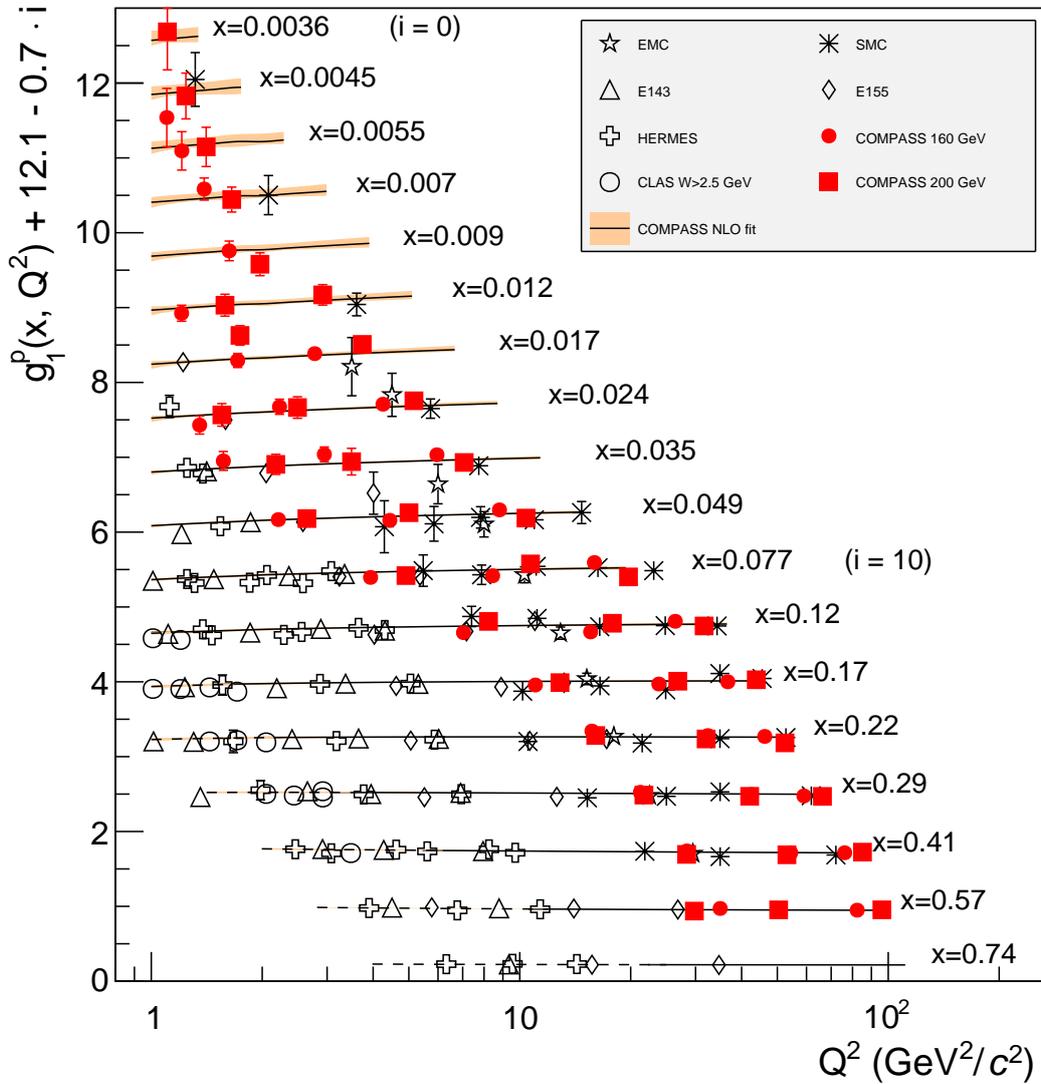
Figure 142: Results of the QCD fit on the spin-dependent structure function of the proton. The curves are given as a function of the photon virtuality for several values of Bjorken-x and are compared to the data. The orange band illustrates the domain covered by the two extreme solutions including the statistical and systematic uncertainty. An extrapolation for $W^2 < 10\,(\text{GeV}/c^2)^2$ is indicated by a dashed line.
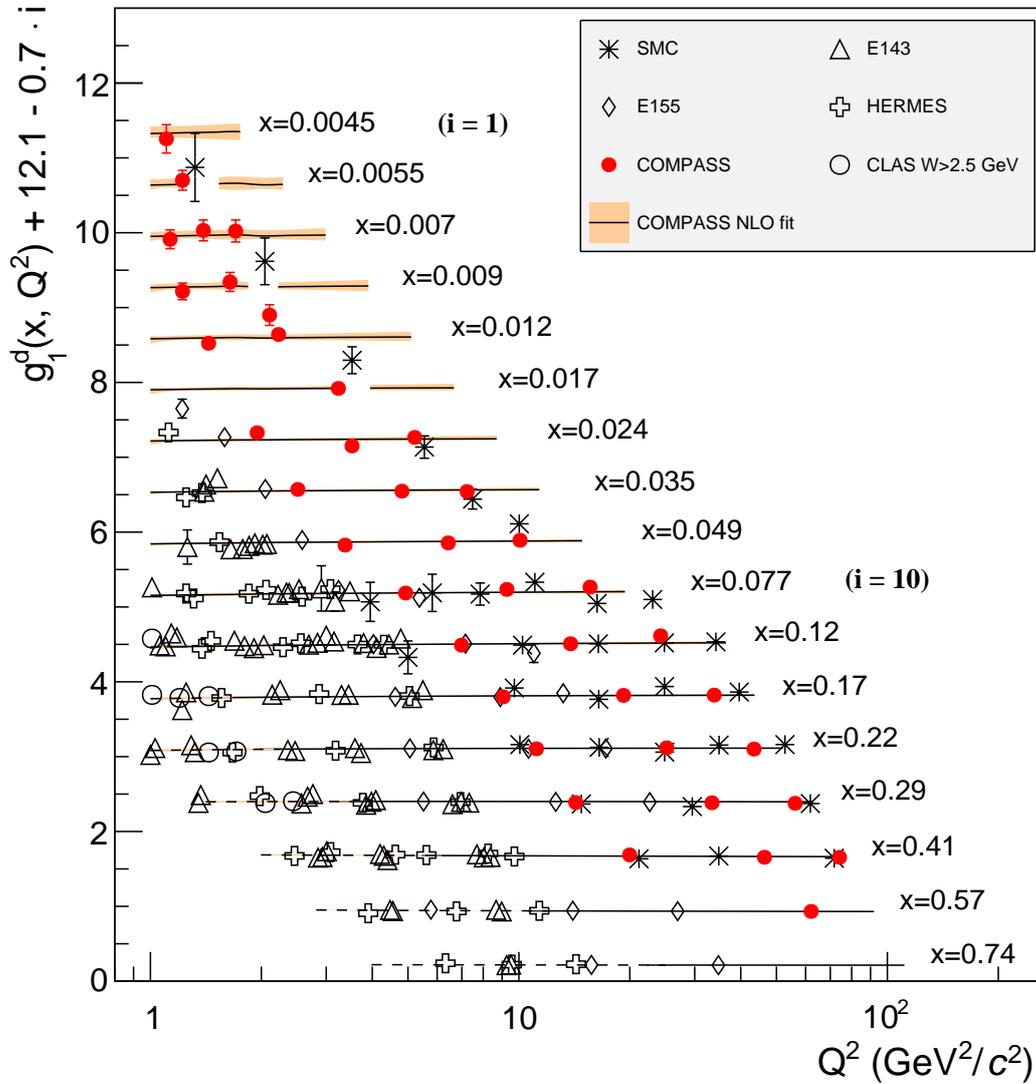
Figure 143: Results of the QCD fit on the spin-dependent structure function of the deuteron. The curves are given as a function of the photon virtuality for several values of Bjorken-x and are compared to the data. The orange band illustrates the domain covered by the two extreme solutions including the statistical and systematic uncertainty. An extrapolation for $W^2 < 10\,(\text{GeV}/c^2)^2$ is indicated by a dashed line.
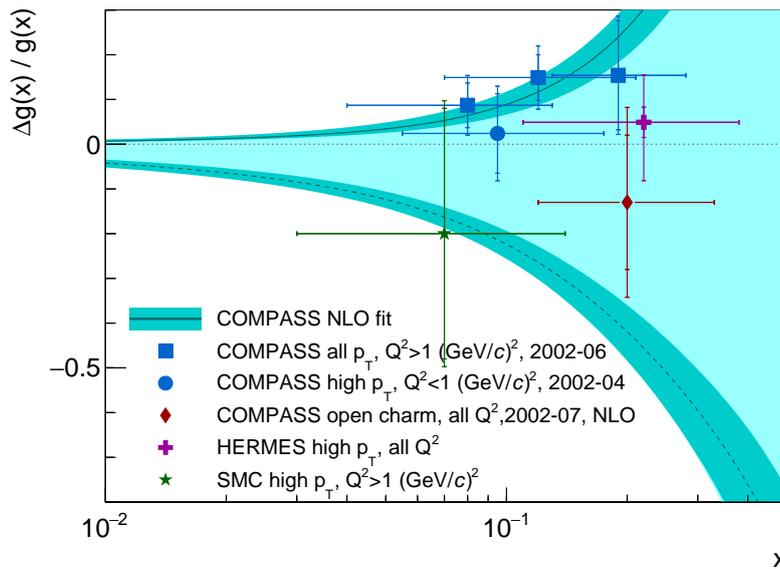
Figure 144: Comparison between the two solution of the QCD fit on the gluon helicity distribution and direct measurements. The direct measurements of COMPASS [150, 151], HERMES [148] and SMC [149] obtained in leading order from high p_T hadrons and from open charm muoproduction at COMPASS [147] in next-to-leading order are shown.

7.6.4 *Comparison with other global QCD fits*

The results for the parton helicity distributions are compared to the result of other recent QCD fits by AAC [152], BB [113] and LSS [119, 153] in Figure 145. Different inputs were used for the various QCD fits. In the case of the 2014 version of LSS and the 2010 version of BB only deep inelastic scattering data were used. For the 2010 version of LSS also results from semi-inclusive deep inelastic scattering were used. The 2008 version of AAC used in addition to the deep inelastic scattering data also results from RHIC. In addition, different methods were used in order to perform the QCD fit.

For the up quark helicity distribution, all results agree well with one another. The results for the down quark helicity distribution agree with one another. A slightly more negative down quark helicity distribution at $x \sim 0.2$ is obtained from the results of the QCD fit presented in this thesis compared to the other QCD fits. For the strange quark helicity distribution very large difference are found. One of the reasons is the inclusion of semi-inclusive deep inelastic scattering data. Their effect on the strange quark helicity distributions is visible in the two results of LSS. The results from the 2008 version includes semi-inclusive deep inelastic scattering data, whereas the 2014 version does not. Without such data, the strange quark helicity distribution is determined mainly by the SU(3) flavour symmetry, which fixes the first moment to a negative value. Including the semi-inclusive deep inelastic scattering data, the QCD fits become sensitive to the parton helicity distributions of the individual quark flavours. They also introduce a new dependence on the fragmentation functions, which describe the hadronisation of a quark. The results for the gluon helicity distribution shows a large spread between the various results.
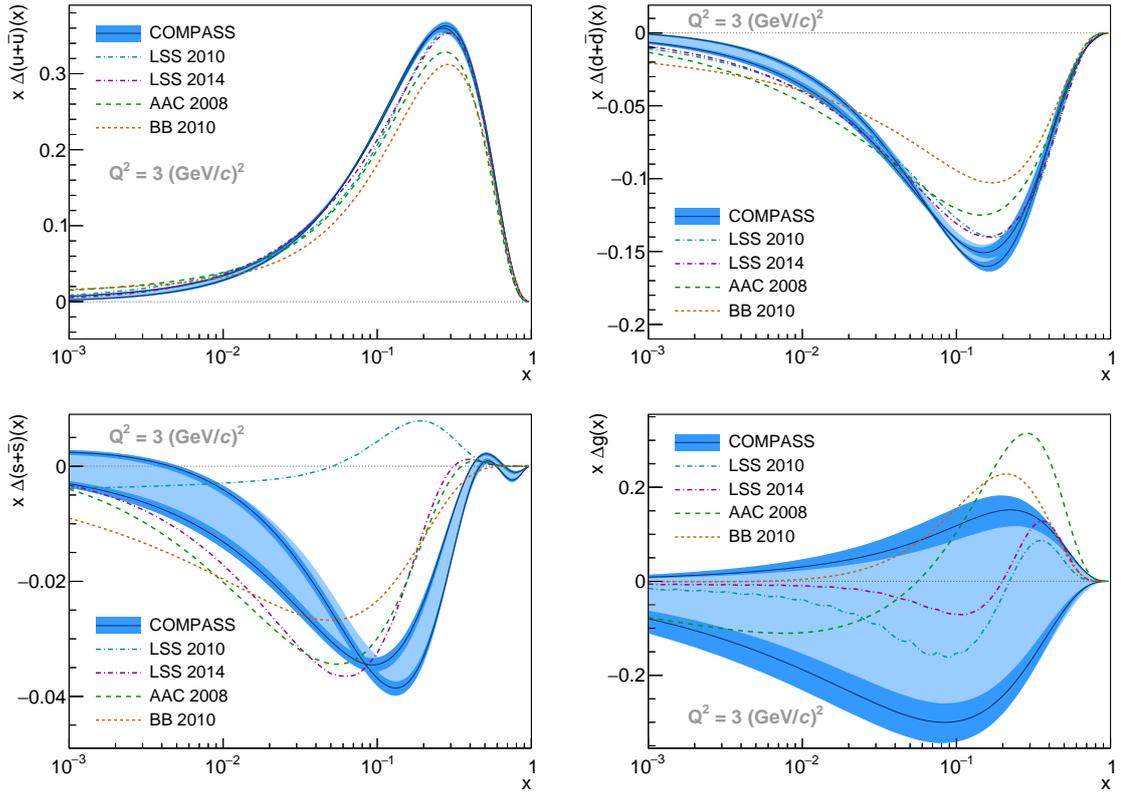
Figure 145: Comparison between various results from other QCD fits to the world data on the parton helicity distributions. Top left: Up quark helicity distribution. Top right: Down quark helicity distribution. Bottom left: Strange quark helicity distribution. Bottom right: Gluon helicity distribution.

They also show that the gluon helicity distribution is not well constrained by the present data.

7.7 TARGET MASS CORRECTION

The results of the QCD fit can be improved by taking into account higher twist effects. These are in general not known except for the correction due to the finite mass of the nucleon. This correction contributes at lower photon virtualities and high Bjorken-x. It can be calculated by introducing the Nachtmann variable

$$\xi = \frac{2x}{1 + (1 + 4M^2x^2/Q^2)^{1/2}} \,,$$
(182)

which represents a modified Bjorken-x variable. Using this variable, the spin-dependent structure function taking into account the target mass correction is given by [154]:

$$
\begin{aligned}
g_{1,\mathrm{TMC}}(x, Q^2) =& \frac{x}{\xi} \frac{g_1(\xi, Q^2)}{(1 + 4M^2x^2/Q^2)^{3/2}} \\
& + \frac{4M^2x^2}{Q^2} \frac{x + \xi}{\xi (1 + 4M^2x^2/Q^2)^2} \int_\xi^1 \frac{d\xi_1}{\xi_1} g_1(\xi_1, Q^2) \\
& - \frac{4M^2x^2}{Q^2} \frac{2 - 4M^2x^2/Q^2}{2 (1 + 4M^2x^2/Q^2)^{5/2}} \int_\xi^1 \frac{d\xi_1}{\xi_1} \int_{\xi_1}^1 \frac{d\xi_2}{\xi_2} g_1(\xi_2, Q^2) \,.
\end{aligned}
$$
(183)

Here, integrations over the full Bjorken-x range of the spin-dependent structure function have to be calculated. Introducing these modification to the spin-dependent structure function, the QCD fit was repeated. The size of the target mass correction to the spin-dependent structure function is shown in Figure 146 for two photon virtualities and for both solutions of the QCD fit. The figure shows the expected behaviour for the target mass
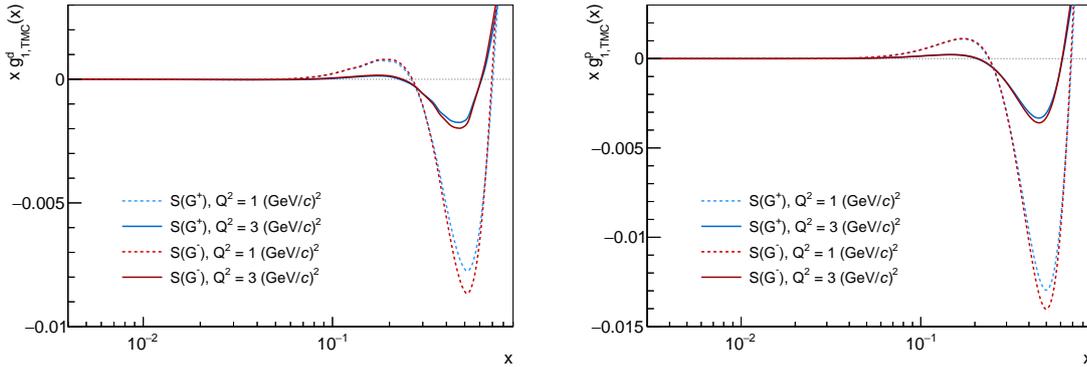
Figure 146: Size of the target mass correction to the spin-dependent structure function of the deuteron (left) and the proton (right) calculated for the two solutions of the QCD fit.

corrections. The largest correction is applied at high Bjorken-x. The correction is larger at small photon virtualities compared to the correction at larger ones. Figure 147 shows the comparison between the spin-dependent structure function of the proton and deuteron with and without the target mass correction. In addition, also the results of the QCD

fit without the target mass correction is shown. Here, the Bjorken-x dependence of the target mass correction is again visible. Comparing the results of the QCD fit including the target mass correction and the results from the QCD fit without the correction agreement is found for the result for the structure function the case of the solution $S(G^+)$. In the case of the solution $S(G^-)$ small differences are visible also at low Bjorken-x.
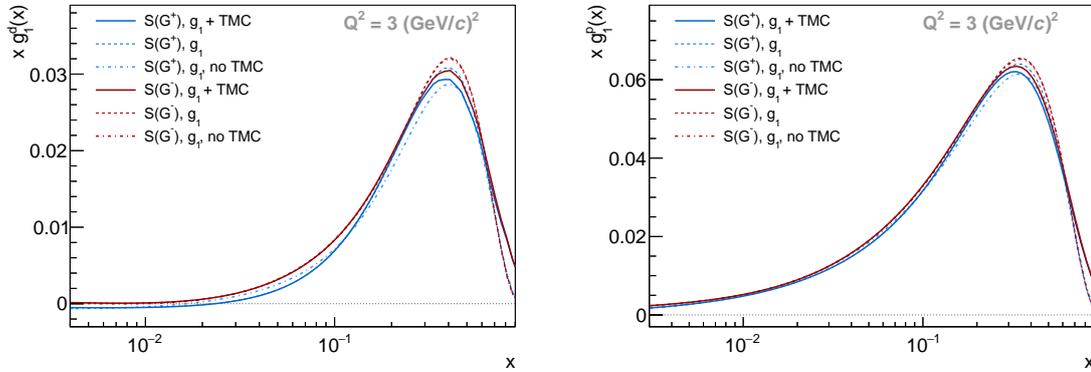
Figure 147: Comparison between the results of the QCD fit without the target mass correction (g_1, no TMC) and the results of the QCD fit including the target mass correction for the spin-dependent structure function with ($g_1 + TMC$) and without (g_1) the correction. Left: Spin-dependent structure function of the deuteron. Right: Spin-dependent structure function of the proton.

FIRST MOMENTS AND SUM RULES

The new results for the spin-dependent structure functions of the proton and the deuteron are used to calculate the first moments of these structure functions. The first moments are also used to test QCD sum rules like the Ellis-Jaffe sum rule and the Bjorken sum rule. The sum rules are discussed in Section 2.11. In addition, the first moment of the spin-dependent structure function of the deuteron is used to evaluate the contribution from the quark spins to the total spin of the nucleon, which can be compared to the results of the QCD fit.

8.1 FIRST MOMENTS

The new results for the spin-dependent structure functions of the proton and the deuteron (described in Chapter 5) allow for a precise determination of their first moments. The calculation also makes use of the results of the NLO QCD fit described before in Chapter 7. The first moments are defined by:

$$\Gamma_1^{p,d}(Q^2) = \int_0^1 g_1^{p,d}(x, Q^2)dx .$$ (184)

8.1.1 *Method and results*

In order to calculate first moments, the results for the spin-dependent structure functions of the proton and deuteron as measured by COMPASS (see Chapter 5 and Reference [106]) are evolved to common $Q^2 = 3\,(\text{GeV}/c)^2$. They are also moved to the centre of the corresponding bin in Bjorken-x. The evolution was performed using the results of the QCD fit. A comparison between the spin-dependent structure function and the result of the QCD fit is shown in Figure 148 at $Q^2 = 3\,(\text{GeV}/c)^2$.

The truncated first moment

$$\Gamma_1^{trunc} = \int_{x_1}^{x_2} g_1 dx ,$$ (185)

which covers the measured Bjorken-x range, is calculated from the data points. In order to obtain the first moment Γ_1 covering the full Bjorken-x range the missing contributions for the low Bjorken-x region and the high Bjorken-x region are estimated using an extrapolation of the spin-dependent structure function from the QCD fit. For the first moment of the spin-dependent structure functions of the proton and the nucleon, the results for the three Bjorken-x ranges are shown in Table 29. The results for the nucleon are obtained from the spin-dependent structure function of the deuteron by correcting for the D-state admixture in the deuteron:

$$\Gamma_1^N(Q^2) = \int_0^1 \frac{g_1^d(x, Q^2)}{1 - 1.5\omega_D}dx$$ (186)
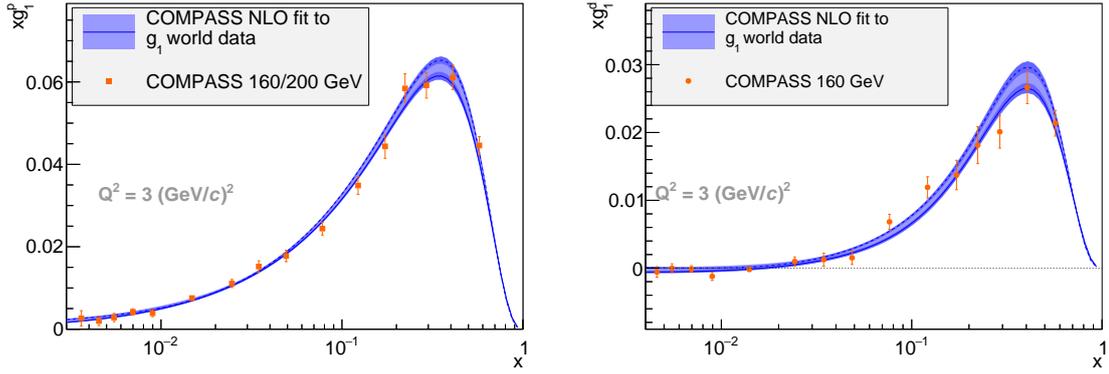
Figure 148: Comparison between the spin-dependent structure function of the proton (left) and deuteron (right) and the results for these structure functions of the QCD fit. The results are shown at a photon virtuality of $3\,(\text{GeV}/c)^2$.

Table 29: Contribution to the first moments of g_1 at $Q^2 = 3\,(\text{GeV}/c)^2$ with statistical uncertainties. The limits in parentheses are applied for the calculation of Γ_1^N.

BJORKEN-X RANGE	Γ_1^P	Γ_1^N
$0 - 0.0025\ (0.004)$	0.0023	-0.0003
$0.0025\ (0.004) - 0.7$	0.134 ± 0.003	0.045 ± 0.002
$0.7 - 1.0$	0.0025	0.0014

with $\omega_D = 0.05 \pm 0.02$ [155]. The table shows that the largest contribution to the first moment is given by the measured Bjorken-x range. It accounts for 96.5% in the case of the proton data and 97.5% in the case of the deuteron data. The extrapolation of the spin-dependent structure functions towards $x = 0$ and $x = 1$ accounts only for 3.5% in the case of the first moment of the proton and 2.5% for the first moment of the nucleon.

The dependence of the truncated first moments of the spin-dependent structure function of the proton and nucleon is shown in Figure 149 as a function of the lower limit in Bjorken-x. The comparison also illustrates that the largest contribution to the first moments is given by the measured data. The difference between the results obtained by using the results from the two solutions of the QCD fit is also shown, which is of about the same size for both first moments. The evolution uncertainty connected to the QCD fit of the first moments is obtained from the results for the first moments using the two solutions of the QCD fit. The mean value of both results is used for the final first moment. The difference between the final first moment and the solutions of the QCD fit is used as an evolution uncertainty of the first moment in the measured region. In addition, half of the full range covered by the two solutions of the QCD fit for the extrapolations is used in the evolution uncertainty. Two other possibilities to estimate the contribution from the extrapolation towards $x = 0$ are shown in Section 8.1.3, even though the low Bjorken-x range not covered by the data is quite small. This can be seen in the insets of Figure 149 where a zoom to the low Bjorken-x range is shown for the structure function on a linear scale.
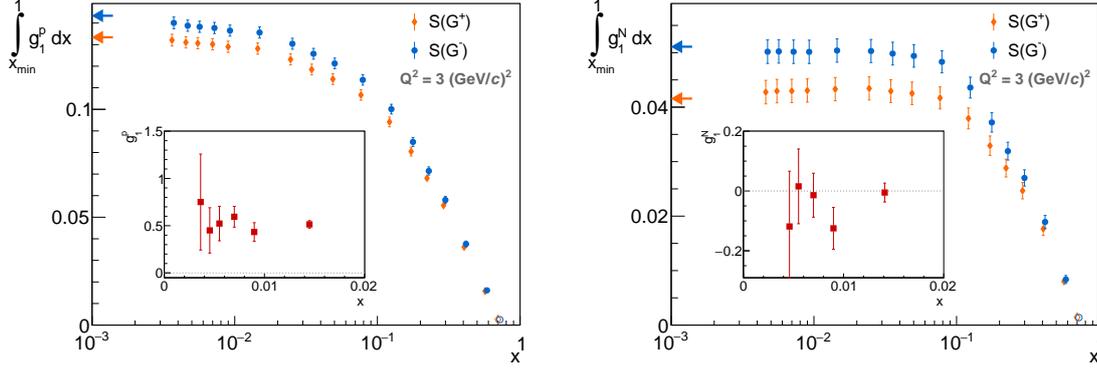
Figure 149: Dependence of the truncated first moment on the lower Bjorken-x limit for the two solutions of the QCD fit. The open circle at $x = 0.7$ is obtained from the QCD fit. Left: Dependence for the truncated first moment of g_1^p. Right: Dependence for the truncated first moment of g_1^d.

The systematic uncertainty of the first moment is calculated taking into account the multiplicative uncertainties of the structure functions. They include the uncertainty on the beam polarisation, the target polarisation, the dilution factor, the depolarisation factor and the spin-independent structure function. In the case of Γ_1^N also the uncertainty on ω_D is taken into account. The additive contribution to the systematic uncertainty of the structure functions are not taken into account as they cancel to a large amount in the calculation of the first moment. The largest additive contribution is the uncertainty due to the presence of a possible false asymmetry, whereas the other additive contributions are very small and can be neglected. No hints for false asymmetries were found in various systematic studies (see Section 5.2) and an upper limit was obtained by studying time dependent effects. From this test, the upper limit is obtained based on the statistical fluctuations. As no hint for the presence of false asymmetries is found, this contribution cancels in the calculation of first moments.

The results for the full first moments are shown in Table 30 together with their uncertainties. In this table also the result for the spin-dependent structure function of the neutron is given. It is calculated from the spin-dependent structure function of the proton and the nucleon using:

$$g_1^n = 2g_1^N - g_1^p = 2\frac{g_1^d}{1 - 1.5\omega_D} - g_1^p . \tag{187}$$

Table 30: First moments of the spin-dependent structure function at $Q^2 = 3\,(\text{GeV}/c)^2$.

	Γ_1	$\delta\Gamma_1^{stat}$	$\delta\Gamma_1^{syst}$	$\delta\Gamma_1^{evol}$
Proton	0.138	±0.003	±0.009	±0.005
Nucleon	0.046	±0.002	±0.004	±0.005
Neutron	−0.046	±0.005	±0.011	±0.005

8.1.2 *Dependence on the QCD fit*

For the calculation of the first moments, results of the QCD fit were used. Instead also the results from other QCD fits to the world data on the spin-dependent structure function can be used. A comparison between the results from various QCD fits on the spin-dependent structure function of the proton and the nucleon is shown in Figure 150. The results from those fits were also used in the calculation of the first moments. The obtained first moments are shown in Figure 151 and compared to the result using the COMPASS fit with its evolution uncertainty as the statistical and systematic uncertainty are the same. In the case of the first moment of the proton, all the results agree with one another. Even though the results obtained using the QCD fit from AAC [50], DNS [114] and the 2006 version of LSS [118] show some larger difference. In the case of AAC the difference is caused by low values for the structure function at low Bjorken-x, whereas the difference from the 2006 version of LSS and DNS is caused by artefacts at low Bjorken-x. In the case of LSS the structure function becomes zero, whereas in the case of DNS the structure function becomes quite large at very small Bjorken-x. In the case of the first moment of the nucleon using most of the other QCD fits results in a lower value for the first moment, except for such QCD fits, which have artefacts at low Bjorken-x. The lower value for the first moments obtained by using most of the QCD fits is caused by the low Bjorken-x behaviour of the structure function obtained in those QCD fits. They favour a negative value for the structure function, which is not indicated by the data.
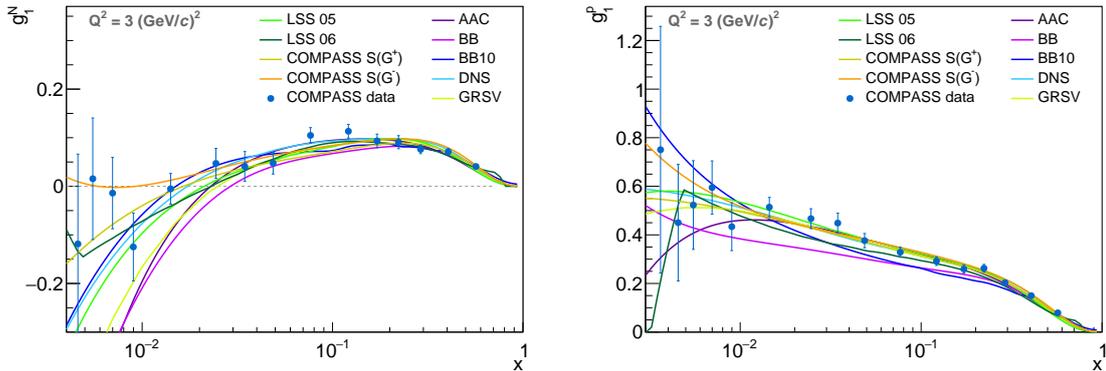
Figure 150: The structure functions g_1^N (left) and g_1^P (right) as a function of Bjorken-x for $Q^2 = 3 \, (\text{GeV}/c)^2$ obtained in different QCD fits. The results from AAC [50], BB [112], BB2010 [113], DNS2000 [114], GRSV [115], LSS2005 [117] and LSS2006 [118] are shown.

8.1.3 *Dependence on the extrapolations for low and high Bjorken-x*

In order to test a possible influence on the unknown contribution of the low Bjorken-x region to the first moment of the spin-dependent structure function, various methods are used to evaluate its contribution. Similar studies were also performed by E143 [124]. The evaluation of the first moment, as described before, used the results from the QCD fit to the world data to extrapolate the spin-dependent structure function towards the low Bjorken-x region. An uncertainty connected to this extrapolation is already part of the evolution uncertainty of the first moment. In addition, a fit was performed using the
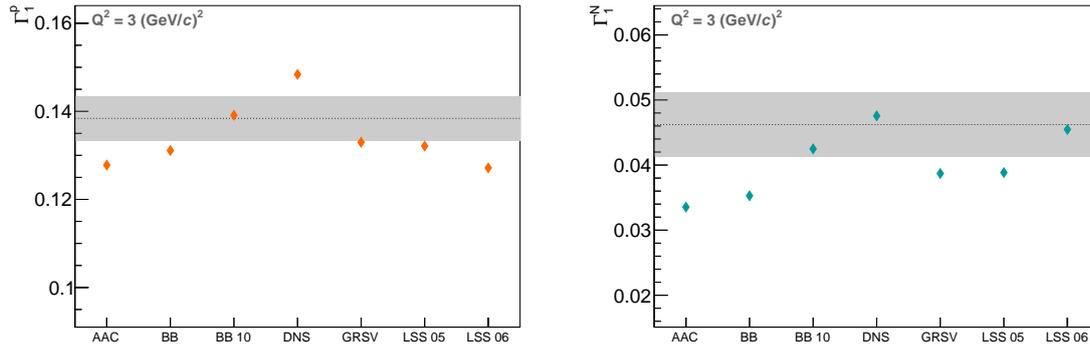
Figure 151: Results for the first moment of the spin-dependent structure function of the proton (left) and the nucleon (right) obtained using various QCD fits. The results are compared to the COMPASS result with its evolution uncertainty indicated by the band.

spin-dependent structure function in the kinematic range with Bjorken-x below 0.1. Using these data points at $Q^2 = 3\,(\text{GeV}/c)^2$, two different fits were performed. The first one assumes a Regge like behaviour of the spin-dependent structure function, $g_1 = a \cdot x^b$, and the second one assumes a $\ln(1/x)$ behaviour at low Bjorken-x. The results from both fits are shown in Figure 152 together with the measured values for the spin-dependent structure function of the proton and deuteron. The parameters and χ^2 of the fits are given in Table 31.
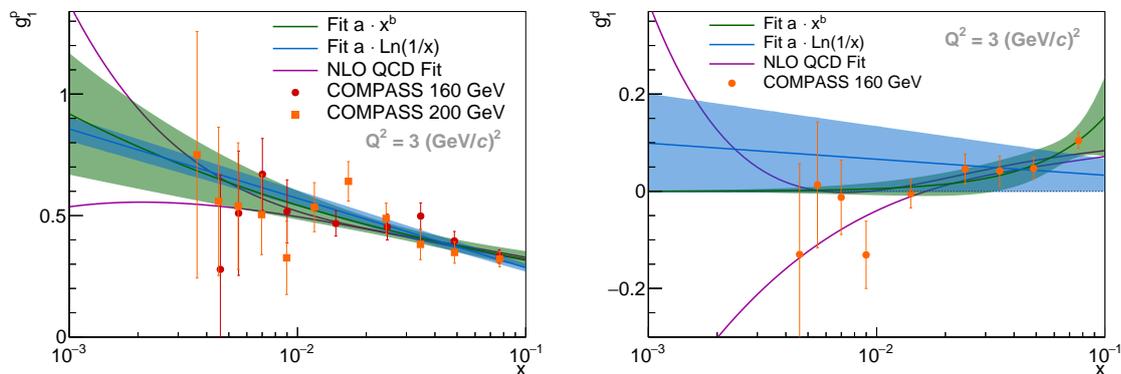
Figure 152: Comparison between the spin-dependent structure function of the proton (left) and the nucleon (right) and the results of the two fits of the low Bjorken-x range. Also the results from the QCD fit are shown.

The proton data is described well by both models. In the case of the deuteron data, only the Regge like behaviour results in a good fit. The model assuming a $\ln(1/x)$ dependence does not describe the low Bjorken-x data points ($\chi^2/\text{NDF} \approx 4$). Using the results of the fits, the contribution to the first moment is calculated. They are shown in Table 32 together with the results obtained from the two solutions of the QCD fit. The contributions obtained for the low Bjorken-x region are very similar for the QCD fit and the two models. Their differences are always within the range already covered by the two solutions of the

Table 31: Fitted parameter and χ^2 values for the various fits to the low Bjorken-x range of the spin-dependent structure function.

	PROTON		NUCLEON	
	$a \cdot x^{-b}$	$a \cdot \ln(1/x)$	$a \cdot x^{-b}$	$a \cdot \ln(1/x)$
a	0.189 ± 0.028	0.124 ± 0.004	4.4 ± 7.1	0.014 ± 0.003
b	-0.229 ± 0.042	—	1.45 ± 0.61	—
χ^2/NDF	$13.1/18$	$12.9/19$	$5.5/7$	$33.8/8$

QCD fit. Therefore, no additional uncertainty has to be assigned to the first moments connected to the low Bjorken-x extrapolation.

Table 32: Contribution from the low Bjorken-x region to the first moment of the spin-dependent structure function. Several methods are used to evaluate its size.

	QCD FIT			FIT TO THE DATA	
	$S(G^+)$	$S(G^-)$	MEAN	$a \cdot x^{-b}$	$a \cdot \ln(1/x)$
Proton	0.0013	0.0033	0.0023	0.0024	0.0022
Nucleon	-0.0015	0.0010	-0.0003	$2 \cdot 10^{-6}$	0.0004

8.2   ELLIS-JAFFE SUM RULE

The first moments of the spin-dependent structure function can be used to test the Ellis-Jaffe sum rule. In the case of the COMPASS data, the first moments Γ_1^p and Γ_1^N are calculated at $Q^2 = 3\,(\text{GeV}/c)^2$. In addition, the first moments calculated by SMC [88] and EMC [13] at $Q^2 \approx 10\,(\text{GeV}/c)^2$, by E155 [125, 127] and Hermes [126] at $Q^2 \approx 5\,(\text{GeV}/c)^2$ and by E143 [124] at $Q^2 \approx 3\,(\text{GeV}/c)^2$ are used. The results from all of these experiments are compared to the prediction of the Ellis-Jaffe sum rule

$$\Gamma_1^{p(n)} = \frac{1}{12} C^{NS} \left(\pm a_3 + \frac{1}{3} a_8 \right) + \frac{1}{9} C^S a_0 \,. \tag{188}$$

It predicts the first moments for the case that the flavour singlet axial charge a_0 is not known by assuming $a_0 = a_8$ (see Section 2.11.2). In the case of the first moment of the nucleon, the term containing the axial charge a_3 cancels. Here, the value for the axial charge a_8 from the two parameter fit described in Section 2.12 is used together with value from the neutron β decay for the axial charge a_3.

The prediction of the Ellis-Jaffe sum rule in next-to-leading order and the measured first moments are shown in Figure 153 as a function of the photon virtuality and given in Table 33. The uncertainty on the prediction from the Ellis-Jaffe sum rule takes into account the uncertainties on the axial charges. In both cases, the experimental results show a large deviation from the sum rule. The difference between the prediction and the experimental data is of the order of 2.0 to 4.8 standard deviations for the proton data, and of the order of 2.5 to 4.3 standard deviations for the deuteron data.
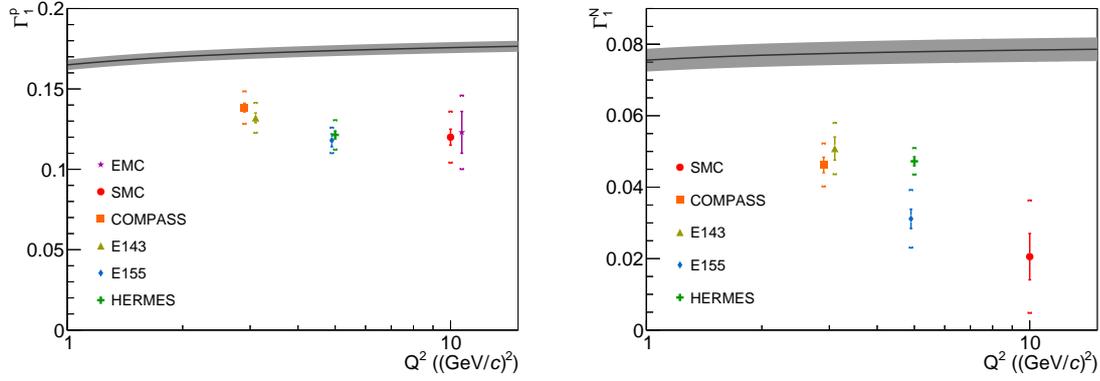
Figure 153: Comparison between the first moment of g_1^p (left) and g_1^N (right) and the prediction of the Ellis-Jaffe sum rule. The uncertainties correspond to the statistical uncertainty and the combined total uncertainty of the measured first moments.

Table 33: Results for the first moments of the spin-dependent structure functions from various experiments compared to the prediction from the Ellis-Jaffe sum rule. The given uncertainties are the statistical and the systematic ones and, if available, the evolution uncertainty from the QCD fit. Note that for the COMPASS result already the results for the nucleon is given.

EXPERIMENT	Q^2	FIRST MOMENT	EJS PREDICTION
COMPASS (N)	$3\,(\mathrm{GeV/c})^2$	$0.046 \pm 0.002 \pm 0.004 \pm 0.005$	0.077 ± 0.003
COMPASS (p)	$3\,(\mathrm{GeV/c})^2$	$0.138 \pm 0.003 \pm 0.009 \pm 0.005$	0.171 ± 0.003
E143 (d)	$3\,(\mathrm{GeV/c})^2$	$0.047 \pm 0.003 \pm 0.006$	0.071 ± 0.003
E143 (p)	$3\,(\mathrm{GeV/c})^2$	$0.132 \pm 0.003 \pm 0.009$	0.171 ± 0.003
E155 (d)	$5\,(\mathrm{GeV/c})^2$	$0.029 \pm 0.003 \pm 0.007$	0.072 ± 0.003
E155 (p)	$5\,(\mathrm{GeV/c})^2$	$0.118 \pm 0.004 \pm 0.007$	0.173 ± 0.003
HERMES (d)	$5\,(\mathrm{GeV/c})^2$	$0.044 \pm 0.001 \pm 0.002$	0.072 ± 0.003
HERMES (p)	$5\,(\mathrm{GeV/c})^2$	$0.121 \pm 0.003 \pm 0.009$	0.173 ± 0.003
SMC (d)	$10\,(\mathrm{GeV/c})^2$	$0.019 \pm 0.006 \pm 0.003 \pm 0.013$	0.072 ± 0.003
SMC (p)	$10\,(\mathrm{GeV/c})^2$	$0.120 \pm 0.005 \pm 0.006 \pm 0.014$	0.175 ± 0.003
EMC (p)	$10.7\,(\mathrm{GeV/c})^2$	$0.123 \pm 0.013 \pm 0.019$	0.175 ± 0.003

This violation shows that a contribution from the spins of the strange quarks to the total spin of the nucleon is needed, which was neglected in the prediction of the Ellis-Jaffe sum rule by assuming $a_0 = a_8$. Parts of the violations might also be connected to the treatment of the extrapolations towards $x = 0$ and $x = 1$, especially since the kinematic range of EMC, HERMES, E143 and E155 only covers Bjorken-x down to $\sim 10^{-2}$. The Bjorken-x range covered by the data of the various experiments is given in Table 34. The extrapolation towards low Bjorken-x was performed in most cases using results of a QCD fit to the available world data on the spin-dependent structure function and therefore depends strongly on the statistical fluctuations of the data points at lowest Bjorken-x. In the case of EMC only the simple assumption that the spin-dependent structure function remains constant was used. In the case of SMC, even though a large range in Bjorken-x is covered, the data points at lowest Bjorken-x hints towards a negative value of the spin-dependent structure function of the nucleon. This resulted in a smaller value of the first moment.

The confirmation of a contribution of the spins of the strange quarks to the nucleon spin is given by the QCD fit where also the axial charges a_3 and a_8 are used. A small contribution of about $8-11\%$ from the spins of the strange quarks is found.

Table 34: Bjorken-x range covered by the various experiments.

EXPERIMENT	BJORKEN-x RANGE
COMPASS (d)	$4.0 \cdot 10^{-3} - 0.7$
COMPASS (p)	$2.5 \cdot 10^{-3} - 0.7$
E143	$3.0 \cdot 10^{-2} - 0.7$
E155	$1.0 \cdot 10^{-2} - 0.9$
HERMES	$2.1 \cdot 10^{-2} - 0.9$
SMC	$3.0 \cdot 10^{-3} - 0.7$
EMC	$1.0 \cdot 10^{-2} - 0.7$

8.3   EXTRACTION OF THE FLAVOUR-SINGLET AXIAL CHARGE

The test of the Ellis-Jaffe sum rule showed that a contribution from the strange quark spins to the total spin of the nucleon exists. Therefore, Equation 188 can be used to calculate the flavour singlet axial charge a_0 using the first moment of the nucleon. The flavour-singlet axial charge a_0 is of special interest since it is identified with the contribution from the quark spins to the total spin of the nucleon in the $\overline{\text{MS}}$ scheme, since in the $\overline{\text{MS}}$ factorisation scheme the first moment of the gluon coefficient function vanishes. Therefore, the first moment of the spin-dependent structure function of the nucleon does not depend on the gluon helicity distribution. It only depends on the axial charges a_0 and a_8. It can be calculated from the first moment as follows:

$$a_0(Q^2) = \frac{1}{C_1^{\text{Si}}(Q^2)} \left[9\Gamma_1^N - \frac{1}{4} a_8 C_1^{\text{NS}}(Q^2) \right] . \tag{189}$$

Here, $C_1^{Si}(Q^2)$ and $C_1^{NS}(Q^2)$ are the singlet and non-singlet Wilson coefficients, which are used in next-to-leading order. Assuming SU(3) flavour symmetry the value $a_8 = 3F - D = 0.587 \pm 0.025$ from Section 2.12 is used. Using the next-to-leading order values $C_1^{Si}(Q^2) = C_1^{NS}(Q^2) = 0.893$ with $\alpha_s = 0.337 \pm 0.012$ at $Q^2 = 3\,(\text{GeV}/c)^2$ in addition to the results for the first moment shown in Section 8.1, the flavour-singlet axial charge is calculated:

$$a_0(Q^2 = 3\,(\text{GeV}/c)^2) = 0.32 \pm 0.02_{\text{stat}} \pm 0.04_{\text{syst}} \pm 0.05_{\text{evol}} \,. \tag{190}$$

The evolution uncertainty is obtained from the first moment. Thus, it also contains contributions from the poorly gluon helicity distribution. The systematic uncertainty takes the uncertainty on a_8 into account in addition to the one of the first moment. The evolution uncertainty is the largest contribution to the uncertainty on the flavour-singlet axial charge. The experimental uncertainties are all smaller. Comparing the result for the flavour-singlet axial charge with the result of the QCD fit given in Table 28 shows a good agreement between both results with similar precision.

Using the axial charge $a_3 = 1.2723 \pm 0.0023$ [18], the contributions from the up, down and strange quark spins to the total spin of the nucleon can be calculated separately. The relations between the axial charges and the various flavours are already given in Section 2.11 and are repeated here:

$$a_0 = (\Delta u + \Delta \bar{u}) + (\Delta d + \Delta \bar{d}) + (\Delta s + \Delta \bar{s}) \,, \tag{191}$$

$$a_3 = (\Delta u + \Delta \bar{u}) - (\Delta d + \Delta \bar{d}) \,, \tag{192}$$

$$a_8 = (\Delta u + \Delta \bar{u}) + (\Delta d + \Delta \bar{d}) - 2(\Delta s + \Delta \bar{s}) \,. \tag{193}$$

Using these relations, the various contributions can be calculated:

$$(\Delta u + \Delta \bar{u})(Q^2 = 3\,(\text{GeV}/c)^2) = 0.840 \pm 0.007_{\text{stat}} \pm 0.014_{\text{syst}} \pm 0.016_{\text{evol}} \,, \tag{194}$$

$$(\Delta d + \Delta \bar{d})(Q^2 = 3\,(\text{GeV}/c)^2) = -0.432 \pm 0.007_{\text{stat}} \pm 0.014_{\text{syst}} \pm 0.016_{\text{evol}} \,, \tag{195}$$

$$(\Delta s + \Delta \bar{s})(Q^2 = 3\,(\text{GeV}/c)^2) = -0.089 \pm 0.007_{\text{stat}} \pm 0.018_{\text{syst}} \pm 0.016_{\text{evol}} \,. \tag{196}$$

The uncertainties take into account the same contributions as the uncertainties of the flavour singlet charge. In the case of the systematic uncertainty also the uncertainty on a_3 is taken into account. These results are also in agreement with the results of the QCD fit with similar precision.

8.4 BJORKEN SUM RULE

The results for the spin-dependent structure functions of the proton and deuteron can also be used to evaluate the non-singlet spin-dependent structure function:

$$g_1^{NS}(x, Q^2) = 2(g_1^P(x, Q^2) - g_1^N(x, Q^2)) \,. \tag{197}$$

This structure function is interesting since its evolution is independent of the gluon helicity distribution (see Section 2.7.2) and its first moment can be used to test the Bjorken sum rule, which is described in Section 2.11.1:

$$\Gamma_1^{NS}(Q^2) = \int_0^1 g_1^{NS}(x, Q^2)dx = \frac{1}{6}\left|\frac{g_A}{g_V}\right| C_1^{NS}(Q^2) \,. \tag{198}$$

Here, $C_1^{NS}(Q^2)$ is the non-singlet Wilson coefficient and $g_A/g_V = a_3$ is the ratio of the weak axial and vector coupling constants (see also Equation 192).

8.4.1   *Method and results*

In order to calculate the non-singlet structure function, the results for the spin-dependent structure function of the proton and deuteron, described in Chapter 5 and the results for the spin-dependent structure function of the proton from Reference [106] are used. The kinematics of these data sets is shown in Figure 154. The mean value for the photon virtuality is different for the three data sets at the same measured Bjorken-x. In order to correct for this difference, the results of the QCD fit to the world data is used to evolve all data points to the photon virtuality of the corresponding data point of the 160 GeV proton data. One additional data point at $x = 0.0036$ exists in the case of the proton data. In order to calculate the non-singlet structure function, the corresponding value of the spin-dependent structure function of the deuteron is taken from the QCD fit to the world data.
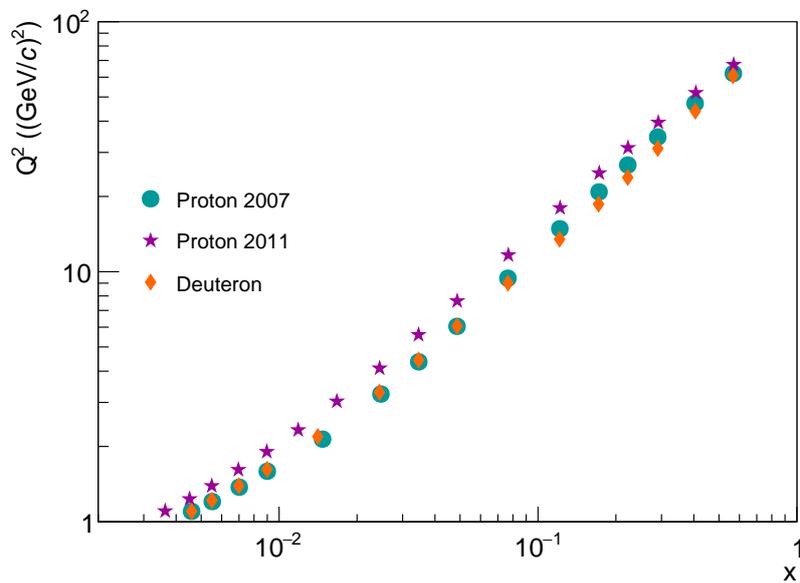
Figure 154: Kinematics of the data sets used for the calculation of the non-singlet spin-dependent structure function.

The calculation of the first moment of the non-singlet structure function differs from the one presented before. Instead of using the results of the QCD fit to the world data to evolve all data points to a common photon virtuality, the independence of the evolution of the non-singlet structure function on the gluon helicity distribution is used. The NLO QCD fit described in Chapter 7 is repeated using only the non-singlet structure function as an input. In this fit only the non-singlet helicity distribution $\Delta q_3 = \Delta u + \Delta \bar{u} - (\Delta d + \Delta \bar{d})$ is needed to calculate the non-singlet structure function:

$$g_1^{NS}(x, Q^2) = \frac{1}{6} \int_x^1 \frac{dx'}{x'} C^{NS}\left(\frac{x}{x'}, Q^2\right) \Delta q_3(x', Q^2) . \tag{199}$$

The non-singlet structure function can be described by a functional form with three parameters, $\Delta q_3 = \eta_3 x^{\alpha_3}(1-x)^{\beta_3}/N$ where N is the normalisation, as discussed in Section 7.2.1. Their results are given in Table 35 together with the χ^2 of the fit. A comparison

between the non-singlet structure function and the results of the non-singlet fit is shown in Figure 155 at $Q^2 = 3\,(\text{GeV}/c)^2$. The calculation of the statistical uncertainty of the non-singlet fit is done in the same way as already described in Section 7.3 for the QCD fit to the world data.

Figure 155: Values of $xg_1^{NS}(x)$ at $Q^2 = 3\,(\text{GeV}/c)^2$ compared to the non-singlet NLO QCD fit using COMPASS data only. The errors are statistical only. The open square at lowest x is obtained with g_1^d taken from the NLO QCD fit.
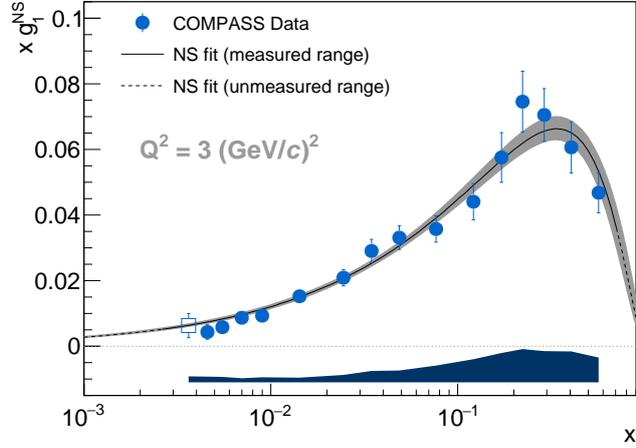
Table 35: Results of the non-singlet fit performed at an input scale of $Q_0^2 = 1\,(\text{GeV}/c)^2$ with their statistical uncertainty.

PARAM.	VALUE
η_3	1.30 ± 0.05
α_3	-0.13 ± 0.07
β_3	1.9 ± 0.3
χ^2/NDF	$7.8/13$

The results of the non-singlet fit are used to evolve all data points to a common photon virtuality of $3\,(\text{GeV}/c)^2$ before calculating the first moment. The contributions from the unmeasured region is calculated using an extrapolation of the non-singlet structure function from the non-singlet fit. The uncertainty on the extrapolations is estimated using the statistical uncertainty of the non-singlet fit as it is the largest uncertainty of the fit. The contributions to the first moment for the various Bjorken-x ranges are given in Table 36. The dependence of the truncated first moment of the non-singlet structure function on the lower Bjorken-x limit is shown in Figure 156.

The data yield a contribution of 93.2% to the first moment, while the low Bjorken-x and high Bjorken-x extrapolation contribute 3.5% and 3.3% respectively. The uncertainty of the extrapolation is taken into account as part of the systematic uncertainty. The full first moment of the non-singlet structure function is

$$\Gamma_1^{NS}(Q^2 = 3\,(\text{GeV}/c)^2) = 0.191 \pm 0.007_{\text{stat}} \pm 0.014_{\text{syst}} \,. \tag{200}$$

The systematic uncertainty of the first moment is larger than the statistical one. It accounts in addition to the extrapolation uncertainty for the uncertainty on the target polarisation, the dilution factor, the depolarisation factor and the spin-independent structure function. The contributions are listed in Table 37 for all data sets. The largest contribution is the uncertainty on the beam polarisation. The normalisation uncertainty of the non-singlet fit is given by the multiplicative uncertainties of the spin-dependent structure function. These are already included in the systematic uncertainty. The contributions from the systematic uncertainties of the proton data are larger than the ones from the deuteron data due to
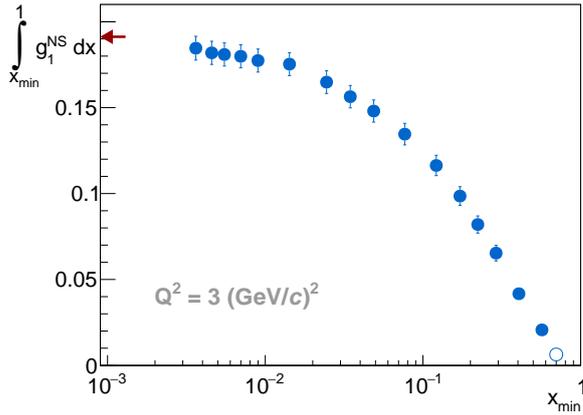
Figure 156: Values of $\int_{x_{min}}^{1} g_1^{NS} dx$ as a function of x_{min}. The open circle at $x = 0.7$ is obtained from the fit. The arrow on the left side shows the value for the full range, $0 < x < 1$.

Table 36: First moment Γ_1^{NS} at $Q^2 = 3\,(GeV/c)^2$ from the COMPASS data with only statistical uncertainties. Contributions from the unmeasured regions are estimated from the NLO fit to g_1^{NS}

X RANGE	Γ_1^{NS}
$0 - 0.0025$	0.0066 ± 0.0008
$0.0025 - 0.7$	0.178 ± 0.007
$0.7 - 1.0$	0.0063 ± 0.0019
$0 - 1$	0.191 ± 0.007

Table 37: Contributions to the systematic uncertainties from the various data sets.

	DEUTERON 160 GeV	PROTON 160 GeV	PROTON 200 GeV
Beam polarisation P_B		5%	
Structure function F_2		2%	
Target polarisation P_T	5%	2%	3.5%
Depolarisation factor D	2%	2%	2%
Dilution factor f	2%	1%	2%
Combined (P_T, D, f)	6%	3.6%	

the different magnitude of the spin-dependent structure function. Contributions from the non-singlet fit and the evolutions to a common photon virtuality are negligible.

Using the non-singlet Wilson coefficient in next-to-leading order, $C_1^{NS} = 0.893$, the ratio of the weak coupling constants is obtained from the first moment:

$$\left| \frac{g_A}{g_V} \right|_{NLO} = 1.29 \pm 0.05_{stat} \pm 0.10_{syst} . \tag{201}$$

Comparing this result to the one obtained from the neutron β decay $|g_A/g_V| = 1.2723 \pm 0.0023$ [18], provides a validation of the Bjorken sum rule with an accuracy of 9%. The influence of the perturbative order on the result is shown in Section 8.4.5 as the experimental result includes all perturbative orders.

8.4.2 *Scale dependence*

The ratio of the weak coupling constants should be independent on the scale used for its calculation. This can be tested by changing the scale at which the non-singlet fit is

performed and the scale at which the ratio is calculated. This test was performed for various scales between $1 \, (\mathrm{GeV}/c)^2$ and $30 \, (\mathrm{GeV}/c)^2$. The results are shown in Figure 157, where the difference between the result obtained at a certain scale and the result obtained at $Q^2 = 1 \, (\mathrm{GeV}/c)^2$ is shown. Only a very small dependence on the scale is seen, which is negligible compared to any uncertainty. This confirms the expected scale independence of the result.
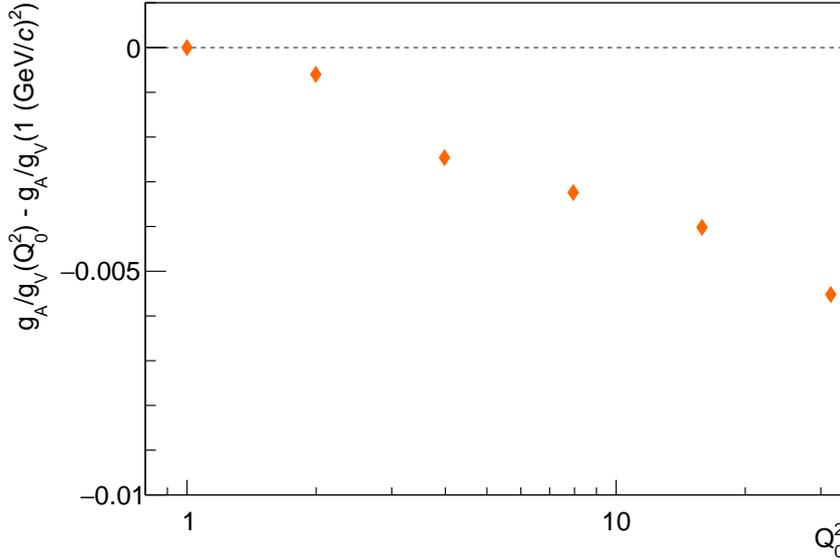
Figure 157: Dependence of the ratio of the weak coupling constants on the scale used for its calculation. For each scale the difference to the ratio obtained at $Q^2 = 1 \, (\mathrm{GeV}/c)^2$ is shown.

8.4.3 *Systematic studies on the non-singlet fit*

The systematic uncertainty of the non-singlet fit can be studied using similar methods as for the QCD fit to the world data (see Section 7.5). The input scale, at which the Bjorken-x dependence is fitted, was changed from $1 \, (\mathrm{GeV}/c)^2$ to $63 \, (\mathrm{GeV}/c)^2$. The influence on the non-singlet structure function is shown in Figure 158. Hardly any dependence on the non-singlet structure function is found. Its dependence is negligible compared to the statistical uncertainty of the non-singlet fit.

The dependence of the non-singlet fit on the functional form is tested by using the parameter γ_3 (see also Section 7.2) as an additional free parameter in the fit. This changes the Bjorken-x dependence to

$$\Delta q_3(x) = \eta_3 \frac{x^{\alpha_3}(1-x)^{\beta_3}(1+\gamma_3 x)}{\int_0^1 x^{\alpha_3}(1-x)^{\beta_3}(1+\gamma_3 x)\mathrm{d}x} \; . \tag{202}$$

The comparison between the results from the non-singlet fit with γ_3 as a free parameter and fixed to zero is shown in Figure 159 showing small differences at low Bjorken-x and differences at large Bjorken-x. However, using this fit does not change the value for the
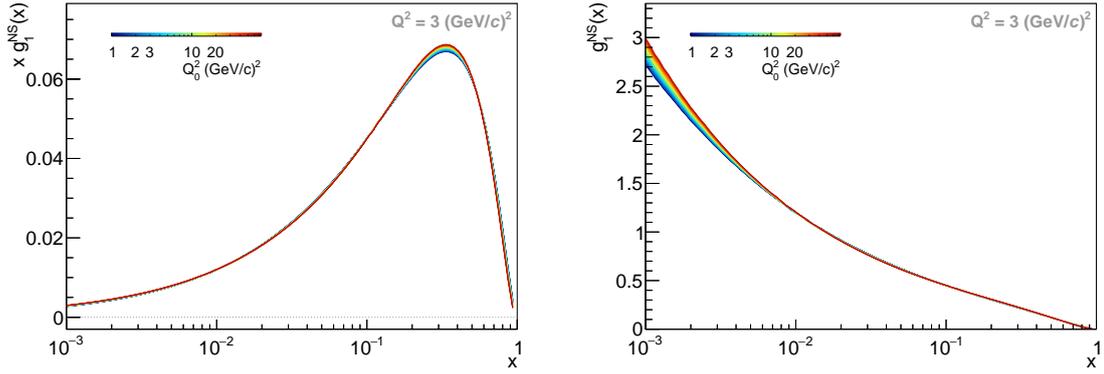
Figure 158: Dependence of the result for the non-singlet structure function on the input scale. The results for the non-singlet structure function are shown at $Q^2 = 3 \, (\text{GeV}/c)^2$.

first moment. Using instead of γ_3 the parameter ρ_3 would result in a similar shape for the non-singlet structure function since it also allows for a zero crossing.
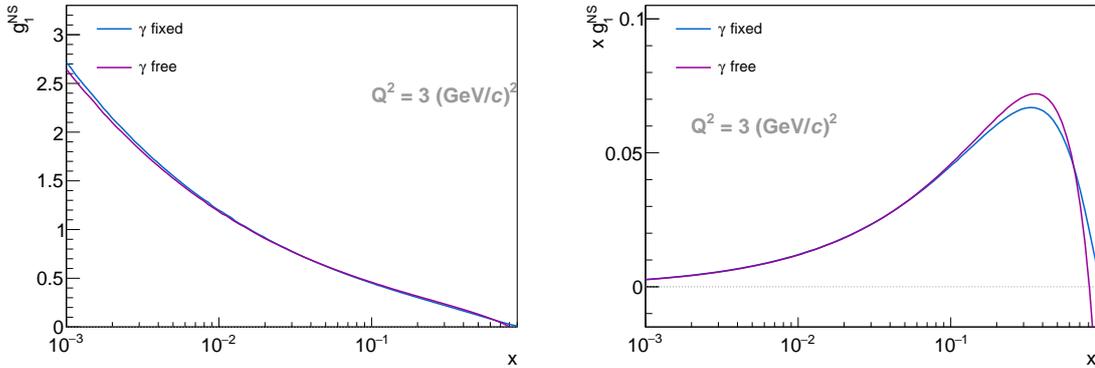
Figure 159: Dependence of the non-singlet fit on the functional shape. The results for the non-singlet structure function are shown for γ_3 as a free parameter of the fit or fixed to zero.

8.4.4 *Dependence on the QCD fit*

The results of the other NLO QCD fits to the world data, which are discussed in Section 8.1.2, can be used to evaluate the influence of the QCD fit on the ratio of the weak coupling constants. The results from these QCD fits are used to calculate the non-singlet structure function. The systematic uncertainty of these fit are larger than the one of the direct fit of the non-singlet structure function. The comparison between the results of the non-singlet fit and the other QCD fits is shown in Figure 160. The results of the 2006 version of LSS shows again the artefact at low Bjorken-x. The results from the other QCD fits agree with the results of the non-singlet fit. However, the QCD fits show a larger value of the non-singlet structure function at low Bjorken-x. Using these QCD fits for the evolution and extrapolation, the ratio of the weak coupling constants is calculated. The difference between the results and the value obtained from the neutron β decay are shown in Fig-
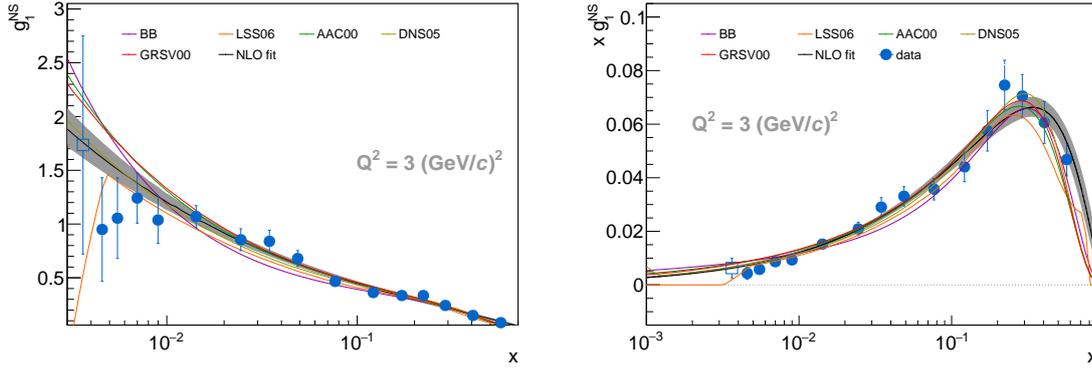
Figure 160: Comparison between the non-singlet fit and the results from various QCD fits to the world data. The results from AAC [50], BB [112], DNS [114], GRSV [115] and the 2006 version from LSS [118] are shown.

ure 161. Most of the obtained ratios of the weak coupling constants using the other QCD fits are slightly larger compared to the one presented in this thesis due to the differences at low Bjorken-x. The ratio of the weak coupling constant obtained using the 2006 version by LSS results in a slightly lower value. This is caused by the artefact at low Bjorken-x. The ratio of the weak coupling constant obtained using BB results in a slightly larger value due to a different Bjorken-x dependence.

Comparing the COMPASS data at low Bjorken-x with the non-singlet fit also shows that the data might favour an even smaller contribution from the low Bjorken-x extrapolation. Using a constant value given by the five lowest data points in Bjorken-x, the low Bjorken-x extrapolation would be about 0.003. This would results in a smaller value of the first moment and therefore also an smaller value for g_A/g_V, which would be closer to the value obtained from the neutron β decay.

8.4.5 *Dependence on the perturbative order*

Since it is not possible to perform the QCD fit and the non-singlet fit in next-to-next-to-leading order, the influence of increasing the perturbative order cannot be estimated. Instead, an upper limit can be obtained from a leading order calculation. The difference between the leading order and the next-to-leading order result should be larger than the one between next-to-leading order and next-to-next-to-leading order. The results for a leading order calculation of the non-singlet structure function in each component and the next-to-leading order calculation are shown in Figure 162. This also results in a change of the first moment and therefore also the result for the ratio of the weak coupling constants. The result in leading order is

$$\left|\frac{g_A}{g_V}\right|_{LO} = 1.19 \pm 0.04_{stat} \pm 0.09_{syst} .\tag{203}$$

The difference between the leading order and next-to-leading order result given in Equation 201 is in the order of the systematic uncertainty.
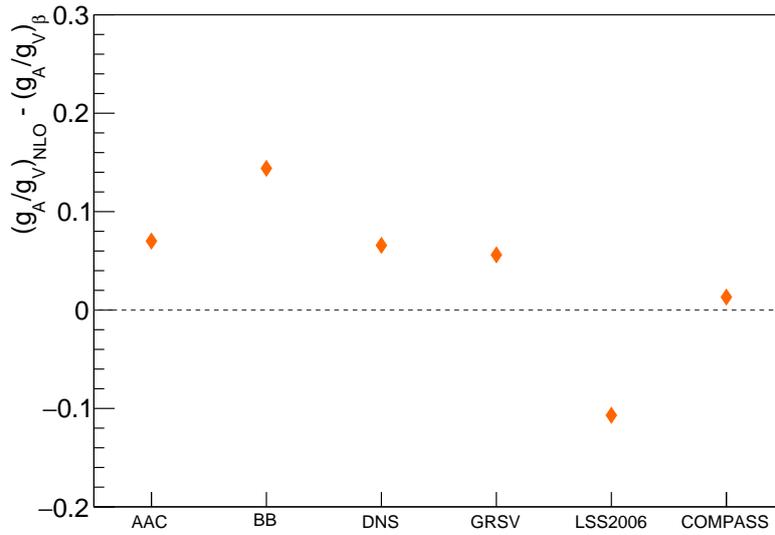
Figure 161: Dependence of the ratio of the weak coupling constants on the QCD fit used in their calculation. The grey line indicates the result obtained from the neutron β decay [18].
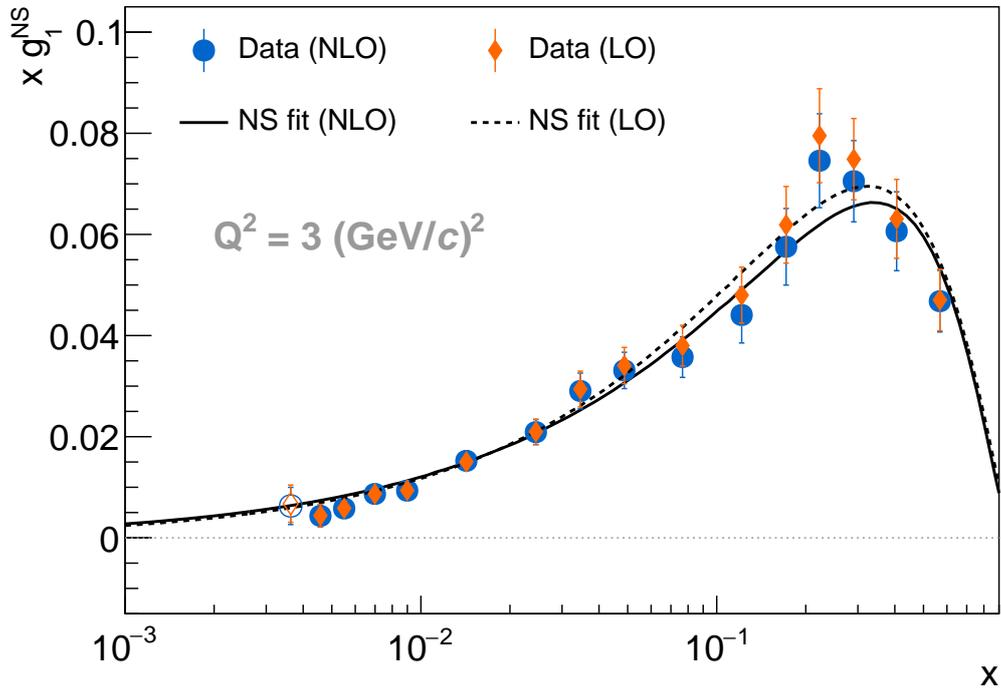
Figure 162: Comparison between the result from the non-singlet fit performed at leading order and next-to-leading order. Also the influence on the non-singlet structure function calculated from the experimental data is shown at a fixed photon virtuality of 3 $(\text{GeV}/c)^2$.

8.5 SUMMARY FIRST MOMENTS

The results for the first moments presented in Section 8.1 are shown as a function of the first moment of the spin-dependent structure function of the proton and the neutron in Figure 163. The figure shows in addition the result for the first moment of the non-singlet structure function described in Section 8.4. The results for the first moment of
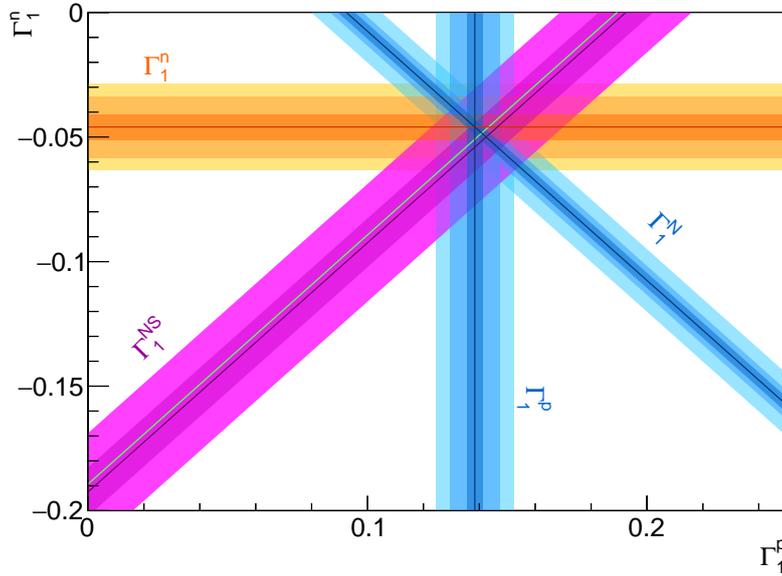
Figure 163: Results for the first moments of the spin-dependent structure functions. The dark lines represent the calculated value. The dark band represent the statistical uncertainty, the lighter bands the combined statistical and systematic uncertainty and the lightest ones the combined statistical, systematic and evolution uncertainty. The green line correspond to the prediction of the first moment of the non-singlet structure function, Γ_1^{NS} using the ratio of the weak coupling constants [18].

the spin-dependent structure function of the proton and nucleon are two independent measurements, whereas the first moment of the spin-dependent structure function of the neutron is the result of Equation 187. The first moment of the spin-dependent non-singlet structure function is in good agreement with the other first moments. Note that it is not fully independent. Even though a different method was used for its calculation, which is independent of the poorly known gluon helicity distribution. In addition to these results also a prediction for the first moment of the spin-dependent non-singlet structure function from the ratio of the weak coupling constants obtained from the neutron β decay is shown. It shows good agreement with the results from the COMPASS data and also agrees well with the intersection of the bands representing the first moment of the spin-dependent structure function of the proton and nucleon.

CONCLUSION

SUMMARY AND CONCLUSION

The COMPASS experiment is investigating the composition of the nucleon spin. This is studied in scattering of polarised muons on a polarised fixed target. In 2002-2004 and in 2006 a polarised lithium deuteride target was used to investigate the longitudinal double spin asymmetry and the spin-dependent structure function of the deuteron. The spin-dependent structure function and longitudinal double spin asymmetry of the proton were studied in 2007 and 2011 using a polarised ammonia target. For the measurement in 2011 the beam momentum was increased from $160\,\text{GeV/c}$ to $200\,\text{GeV/c}$.

In this thesis, the longitudinal double spin asymmetry and spin-dependent structure function are presented in two different kinematic regions, namely at low photon virtualities, $Q^2 < 1\,(\text{GeV/c})^2$, and at high photon virtualities, $Q^2 > 1\,(\text{GeV/c})^2$. The asymmetry at low photon virtualities is extracted using the data from the 2007 and 2011 data taking. The asymmetry shows a positive non-zero asymmetry even at low Bjorken-x. This differs from the results obtained from the deuteron data, which are compatible with zero. The statistical precision of the measurements is significant increased compared to the results of SMC and HERMES, which are the only other experiments that obtained results for this kinematic range. The results agree with predictions from a phenomenological model [54] based on generalised vector meson dominance. It requires a large negative contributions from light vector mesons in addition to the partonic contribution.

At high photon virtualities, the COMPASS data sets cover a large range in Bjorken-x from about $4 \cdot 10^{-3}$ up to 0.7 and in the photon virtuality up to about $150\,(\text{GeV/c})^2$. The results from the 2006 deuteron data taking on the spin-dependent structure function and the longitudinal double spin asymmetry are used to increase the statistics of the 2002-2004 deuteron data taking by about 50%. The results for the spin-dependent structure function and the longitudinal double spin asymmetry of the proton obtained from the 2011 data set completes the previous results from the 2007 proton data taking. It allows to extend the kinematic range covered by the world data. The Bjorken-x range is extended towards lower values down to $x = 0.0025$ and the photon virtuality range is extended towards higher values up to $Q^2 \simeq 190\,(\text{GeV/c})^2$. Both results improve the statistical precision on the spin-dependent structure function compared to SMC, which was the only experiment able to cover this kinematic range previously. The results represent the final COMPASS results on the spin-dependent structure function of the proton and the deuteron.

The results for the spin-dependent structure function of the proton and deuteron from deep inelastic scattering are used together with the world data on the spin-dependent structure function of the proton, deuteron and neutron in a NLO QCD fit. This fit allows the extraction of the parton helicity distributions. Studies on the functional form result in two extreme solutions for the QCD fit, which cover all possible solutions in between. This study shows together with the study on the dependence on the input scale that the systematic uncertainty on the results from such fits is larger than the statistical and experimental systematic uncertainty of the helicity distributions. The contribution from quark spins to the nucleon spin is obtained from the QCD fit to be in the range of 25% to 35%

at $Q^2 = 3 \, (\text{GeV}/c)^2$. The contribution from the gluon spins to the nucleon spin is not well constrained. This is also illustrated in the comparison with other QCD fits showing various different functional shapes. The QCD fit including the new measurements confirms the results of the previous COMPASS QCD fit with a much more refined systematic treatment. In order to improve the results for such QCD fits additional inputs are needed. Compared to the spin-independent structure function, the kinematic coverage of the spin-dependent structure function is limited. Further improvements would require either collider data at low Bjorken-x and high photon virtualities or the inclusion of results from other processes like proton-proton collisions, which needs a more elaborate QCD analysis method.

The results for the spin-dependent structure function of the proton and deuteron are also used to calculate their first moments. In their calculation the results from the QCD fit are used to evaluate the contribution of the unmeasured region and to evolve the data points to a common photon virtuality. The first moments obtained at $Q^2 = 3 \, (\text{GeV}/c)^2$ are $\Gamma_1^P = 0.138 \pm 0.003_{\text{stat}} \pm 0.009_{\text{syst}} \pm 0.005_{\text{evol}}$ and $\Gamma_1^N = 0.046 \pm 0.002_{\text{stat}} \pm 0.004_{\text{syst}} \pm 0.005_{\text{evol}}$. In both cases, a contribution of about 94% is given by the measured data. The measured first moments violate the Ellis-Jaffe sum rule. This confirms the already known violation of the Ellis-Jaffe sum rule. Using the first moments of the spin-dependent structure function of the nucleon, the singlet axial charge is calculated, $a_0 = 0.32 \pm 0.02_{\text{stat}} \pm 0.04_{\text{syst}} \pm 0.05_{\text{evol}}$. It is identified in the $\overline{\text{MS}}$ scheme with the contribution from quark spins to the nucleon spin. In this scheme, the first moment of the spin-dependent structure function of the nucleon is independent of the contribution from the gluon helicity distribution. Also, the contribution from the various quark flavours is calculated. The results using only the COMPASS data agree with the results from the QCD fit with a similar statistical precision. The largest uncertainty of these results is the evolution uncertainty, which is connected to the uncertainty of the QCD fit. It is mainly given by the poorly known gluon helicity distribution, even though the first moment is independent of it. As, stated before, this can only be improved by new measurements at very low Bjorken-x in order to observe the evolution in this kinematic range in order to constrain the gluon helicity distribution. The contribution from such measurements to the first moments is with about $1 - 2\%$ very small.

Using the results for the spin-dependent structure function of the proton and deuteron together, the non-singlet structure function is calculated. This structure function is of special interest, since its evolution is decoupled from the gluon helicity distribution. Its first moment is used to test the Bjorken sum rule. For the calculation of the first moment the results of a non-singlet QCD fit to the COMPASS data is used for the evolution of the data points. The resulting first moment is $\Gamma_1^{\text{NS}} = 0.191 \pm 0.007_{\text{stat}} \pm 0.014_{\text{syst}}$. Also here the largest contribution of about 92% is given by the data. The inclusion of the results from the 2011 data reduced the contribution from the unmeasured low Bjorken-x region by about 30% and also reduced the statistical error by 23%. Also the systematic uncertainty was slightly reduced by about 7%. The ratio of the weak coupling constants obtained from the first moment is $|g_A/g_V|_{\text{NLO}} = 1.29 \pm 0.05_{\text{stat}} \pm 0.10_{\text{syst}}$, which represents a validation of the Bjorken sum rule at the level of 9%.

APPENDIX

A

RESULTS FROM THE PROTON DATA AT HIGH PHOTON VIRTUALITIES

The results for the longitudinal double spin asymmetry and the spin-dependent structure function obtained from the 2011 data using a 200 GeV/c muon beam are given in the following tables as a function of the Bjorken-x and as a function of Bjorken-x and the photon virtuality.

Table 38: Results for the asymmetry A_1^p and spin-dependent structure function g_1^p obtained from the 2011 data set using a 200 GeV/c muon beam in bins of Bjorken-x.

x range	$\langle x \rangle$	$\langle y \rangle$	$\langle Q^2 \rangle$	A_1^p	g_1^p
0.003 − 0.004	0.0036	0.800	1.10	$0.020 \pm 0.017 \pm 0.007$	$0.60 \pm 0.51 \pm 0.22$
0.004 − 0.005	0.0045	0.726	1.23	$0.017 \pm 0.012 \pm 0.005$	$0.43 \pm 0.31 \pm 0.13$
0.005 − 0.006	0.0055	0.677	1.39	$0.020 \pm 0.012 \pm 0.005$	$0.44 \pm 0.26 \pm 0.11$
0.006 − 0.008	0.0070	0.629	1.61	$0.0244 \pm 0.0093 \pm 0.0041$	$0.43 \pm 0.16 \pm 0.08$
0.008 − 0.010	0.0090	0.584	1.91	$0.019 \pm 0.010 \pm 0.006$	$0.27 \pm 0.15 \pm 0.09$
0.010 − 0.014	0.0119	0.550	2.33	$0.0431 \pm 0.0086 \pm 0.0045$	$0.512 \pm 0.10 \pm 0.06$
0.014 − 0.020	0.0167	0.518	3.03	$0.0719 \pm 0.0091 \pm 0.0060$	$0.642 \pm 0.081 \pm 0.061$
0.020 − 0.030	0.0244	0.492	4.11	$0.0788 \pm 0.0097 \pm 0.0065$	$0.514 \pm 0.063 \pm 0.048$
0.030 − 0.040	0.0346	0.477	5.60	$0.088 \pm 0.013 \pm 0.010$	$0.424 \pm 0.063 \pm 0.054$
0.040 − 0.060	0.0488	0.464	7.64	$0.114 \pm 0.013 \pm 0.009$	$0.401 \pm 0.044 \pm 0.036$
0.060 − 0.100	0.0768	0.450	11.7	$0.166 \pm 0.014 \pm 0.013$	$0.376 \pm 0.031 \pm 0.033$
0.100 − 0.150	0.122	0.432	18.0	$0.264 \pm 0.019 \pm 0.019$	$0.372 \pm 0.027 \pm 0.029$
0.150 − 0.200	0.173	0.415	24.8	$0.318 \pm 0.027 \pm 0.024$	$0.298 \pm 0.025 \pm 0.024$
0.200 − 0.250	0.223	0.404	31.3	$0.337 \pm 0.036 \pm 0.030$	$0.224 \pm 0.024 \pm 0.021$
0.250 − 0.350	0.292	0.389	39.6	$0.389 \pm 0.037 \pm 0.029$	$0.166 \pm 0.016 \pm 0.013$
0.350 − 0.500	0.407	0.366	52.0	$0.484 \pm 0.055 \pm 0.051$	$0.095 \pm 0.011 \pm 0.010$
0.500 − 0.700	0.570	0.339	67.3	$0.73 \pm 0.11 \pm 0.09$	$0.0396 \pm 0.0058 \pm 0.0053$

Table 39: Results for the asymmetry A_1^p and spin-dependent structure function g_1^p obtained from the 2011 data set using a 200 GeV/c muon beam in bins of Bjorken-x and photon virtuality.

x range			$\langle x \rangle$	$\langle y \rangle$	$\langle Q^2 \rangle$	A_1^p	g_1^p
0.003	—	0.004	0.0035	0.771	1.03	$0.059 \pm 0.029 \pm 0.014$	$1.79 \pm 0.87 \pm 0.45$
0.003	—	0.004	0.0036	0.798	1.10	$-0.004 \pm 0.027 \pm 0.012$	$-0.13 \pm 0.81 \pm 0.37$
0.003	—	0.004	0.0038	0.840	1.22	$0.003 \pm 0.032 \pm 0.012$	$0.06 \pm 0.98 \pm 0.37$
0.004	—	0.005	0.0044	0.641	1.07	$0.006 \pm 0.021 \pm 0.008$	$0.15 \pm 0.50 \pm 0.19$
0.004	—	0.005	0.0045	0.730	1.24	$0.021 \pm 0.030 \pm 0.008$	$0.53 \pm 0.51 \pm 0.20$
0.004	—	0.005	0.0046	0.817	1.44	$0.023 \pm 0.023 \pm 0.011$	$0.60 \pm 0.59 \pm 0.28$
0.005	—	0.006	0.0055	0.540	1.11	$0.009 \pm 0.024 \pm 0.011$	$0.18 \pm 0.46 \pm 0.21$
0.005	—	0.006	0.0055	0.661	1.36	$0.026 \pm 0.020 \pm 0.008$	$0.56 \pm 0.42 \pm 0.18$
0.005	—	0.006	0.0056	0.795	1.68	$0.022 \pm 0.020 \pm 0.008$	$0.51 \pm 0.47 \pm 0.18$
0.006	—	0.008	0.0069	0.442	1.14	$0.033 \pm 0.021 \pm 0.009$	$0.50 \pm 0.32 \pm 0.14$
0.006	—	0.008	0.0069	0.580	1.50	$0.041 \pm 0.016 \pm 0.007$	$0.71 \pm 0.27 \pm 0.12$
0.006	—	0.008	0.0071	0.757	2.02	$0.006 \pm 0.014 \pm 0.007$	$0.12 \pm 0.27 \pm 0.13$
0.008	—	0.010	0.0089	0.349	1.17	$0.007 \pm 0.027 \pm 0.013$	$0.08 \pm 0.32 \pm 0.16$
0.008	—	0.010	0.0089	0.483	1.62	$0.029 \pm 0.018 \pm 0.007$	$0.40 \pm 0.25 \pm 0.10$
0.008	—	0.010	0.0090	0.710	2.41	$0.015 \pm 0.014 \pm 0.006$	$0.24 \pm 0.23 \pm 0.09$
0.010	—	0.014	0.0116	0.278	1.21	$0.044 \pm 0.026 \pm 0.013$	$0.41 \pm 0.24 \pm 0.12$
0.010	—	0.014	0.0117	0.401	1.75	$0.040 \pm 0.017 \pm 0.011$	$0.42 \pm 0.18 \pm 0.11$
0.010	—	0.014	0.0120	0.656	2.92	$0.044 \pm 0.011 \pm 0.005$	$0.56 \pm 0.14 \pm 0.07$
0.014	—	0.020	0.0164	0.206	1.26	$0.087 \pm 0.034 \pm 0.015$	$0.58 \pm 0.22 \pm 0.12$
0.014	—	0.020	0.0165	0.313	1.92	$0.100 \pm 0.021 \pm 0.011$	$0.77 \pm 0.16 \pm 0.09$
0.014	—	0.020	0.0168	0.605	3.74	$0.063 \pm 0.011 \pm 0.006$	$0.60 \pm 0.10 \pm 0.06$
0.020	—	0.030	0.0239	0.177	1.55	$0.072 \pm 0.031 \pm 0.016$	$0.36 \pm 0.15 \pm 0.08$
0.020	—	0.030	0.0240	0.280	2.49	$0.080 \pm 0.025 \pm 0.011$	$0.45 \pm 0.14 \pm 0.07$
0.020	—	0.030	0.0246	0.575	5.16	$0.079 \pm 0.011 \pm 0.008$	$0.545 \pm 0.078 \pm 0.061$

Table 40: Results for the asymmetry A_1^p and spin-dependent structure function g_1^p obtained from the 2011 data set using a 200 GeV/c muon beam in bins of Bjorken-x and photon virtuality.

x RANGE	$\langle x \rangle$	$\langle y \rangle$	$\langle Q^2 \rangle$	A_1^p	g_1^p
0.030 — 0.040	0.0341	0.173	2.18	$0.103 \pm 0.035 \pm 0.016$	$0.39 \pm 0.13 \pm 0.06$
0.030 — 0.040	0.0343	0.272	3.50	$0.099 \pm 0.041 \pm 0.018$	$0.43 \pm 0.18 \pm 0.08$
0.030 — 0.040	0.0347	0.559	7.07	$0.083 \pm 0.015 \pm 0.013$	$0.421 \pm 0.075 \pm 0.066$
0.040 — 0.060	0.0473	0.151	2.65	$0.128 \pm 0.040 \pm 0.024$	$0.37 \pm 0.12 \pm 0.07$
0.040 — 0.060	0.0480	0.283	5.00	$0.136 \pm 0.026 \pm 0.016$	$0.449 \pm 0.086 \pm 0.057$
0.040 — 0.060	0.0492	0.575	10.4	$0.103 \pm 0.015 \pm 0.011$	$0.378 \pm 0.057 \pm 0.043$
0.060 — 0.100	0.0740	0.184	4.91	$0.147 \pm 0.032 \pm 0.016$	$0.308 \pm 0.066 \pm 0.036$
0.060 — 0.100	0.0754	0.390	10.7	$0.203 \pm 0.020 \pm 0.017$	$0.465 \pm 0.047 \pm 0.043$
0.060 — 0.100	0.0800	0.664	19.7	$0.129 \pm 0.023 \pm 0.022$	$0.293 \pm 0.052 \pm 0.050$
0.100 — 0.150	0.119	0.190	8.23	$0.291 \pm 0.038 \pm 0.024$	$0.397 \pm 0.051 \pm 0.035$
0.100 — 0.150	0.121	0.402	17.8	$0.263 \pm 0.028 \pm 0.021$	$0.372 \pm 0.040 \pm 0.031$
0.100 — 0.150	0.125	0.676	31.7	$0.243 \pm 0.034 \pm 0.021$	$0.337 \pm 0.048 \pm 0.031$
0.150 — 0.200	0.171	0.209	12.9	$0.299 \pm 0.045 \pm 0.027$	$0.279 \pm 0.042 \pm 0.026$
0.150 — 0.200	0.172	0.419	26.9	$0.316 \pm 0.045 \pm 0.036$	$0.298 \pm 0.042 \pm 0.035$
0.150 — 0.200	0.175	0.667	43.8	$0.344 \pm 0.050 \pm 0.029$	$0.318 \pm 0.047 \pm 0.029$
0.200 — 0.250	0.222	0.200	16.1	$0.405 \pm 0.060 \pm 0.043$	$0.273 \pm 0.041 \pm 0.030$
0.200 — 0.250	0.222	0.385	32.1	$0.340 \pm 0.066 \pm 0.035$	$0.227 \pm 0.044 \pm 0.024$
0.200 — 0.250	0.224	0.624	52.4	$0.268 \pm 0.060 \pm 0.045$	$0.174 \pm 0.039 \pm 0.030$
0.250 — 0.350	0.289	0.209	21.7	$0.397 \pm 0.057 \pm 0.035$	$0.177 \pm 0.025 \pm 0.016$
0.250 — 0.350	0.290	0.387	42.1	$0.374 \pm 0.077 \pm 0.050$	$0.160 \pm 0.034 \pm 0.022$
0.250 — 0.350	0.296	0.602	66.3	$0.392 \pm 0.062 \pm 0.035$	$0.159 \pm 0.025 \pm 0.015$
0.350 — 0.500	0.403	0.195	28.4	$0.396 \pm 0.086 \pm 0.051$	$0.085 \pm 0.018 \pm 0.011$
0.350 — 0.500	0.405	0.350	53.1	$0.40 \pm 0.12 \pm 0.06$	$0.079 \pm 0.024 \pm 0.011$
0.350 — 0.500	0.413	0.556	85.1	$0.631 \pm 0.088 \pm 0.054$	$0.114 \pm 0.016 \pm 0.010$
0.500 — 0.700	0.561	0.143	29.8	$0.42 \pm 0.23 \pm 0.10$	$0.028 \pm 0.016 \pm 0.007$
0.500 — 0.700	0.567	0.238	50.4	$0.75 \pm 0.23 \pm 0.12$	$0.044 \pm 0.013 \pm 0.007$
0.500 — 0.700	0.575	0.457	96.1	$0.87 \pm 0.15 \, pm0.09$	$0.0429 \pm 0.0071 \pm 0.0048$

B

RESULTS FROM THE DEUTERON DATA AT HIGH PHOTON
VIRTUALITIES

The results for the asymmetry A_1^d and spin-dependent structure function g_1^d obtained by using only the 2006 data set with a 160 GeV/c muon beam. The tables contain the results with their statistical and systematic uncertainty.

Table 41: Results for the asymmetry A_1^d ans spin-dependent structure function g_1^d obtained from the 2006 deuteron data set using a 160 GeV/c muon beam in bins of Bjorken-x.

x range	$\langle x \rangle$	$\langle y \rangle$	$\langle Q^2 \rangle ((\text{GeV/c})^2)$	A_1^d	g_1^d
0.003 − 0.004	0.0039	0.863	1.03	$-0.020 \pm 0.051 \pm 0.033$	$-0.5 \pm 1.4 \pm 0.9$
0.004 − 0.005	0.0046	0.799	1.10	$-0.026 \pm 0.013 \pm 0.007$	$-0.59 \pm 0.30 \pm 0.15$
0.005 − 0.006	0.0055	0.738	1.21	$-0.006 \pm 0.011 \pm 0.007$	$-0.12 \pm 0.21 \pm 0.14$
0.006 − 0.008	0.0070	0.679	1.40	$0.0034 \pm 0.0076 \pm 0.0029$	$0.05 \pm 0.12 \pm 0.05$
0.008 − 0.010	0.0090	0.624	1.63	$-0.0042 \pm 0.0084 \pm 0.0033$	$-0.06 \pm 0.11 \pm 0.04$
0.010 − 0.014	0.0118	0.583	1.98	$-0.0010 \pm 0.0070 \pm 0.0031$	$-0.011 \pm 0.076 \pm 0.033$
0.014 − 0.020	0.0167	0.548	2.57	$-0.0088 \pm 0.0075 \pm 0.0032$	$-0.072 \pm 0.062 \pm 0.026$
0.020 − 0.030	0.0244	0.521	3.50	$0.0175 \pm 0.0080 \pm 0.0041$	$0.105 \pm 0.049 \pm 0.025$
0.030 − 0.040	0.0346	0.505	4.75	$0.014 \pm 0.011 \pm 0.005$	$0.062 \pm 0.048 \pm 0.021$
0.040 − 0.060	0.0488	0.491	6.49	$0.017 \pm 0.010 \pm 0.005$	$0.057 \pm 0.034 \pm 0.017$
0.060 − 0.100	0.0767	0.468	9.75	$0.049 \pm 0.011 \pm 0.007$	$0.104 \pm 0.024 \pm 0.016$
0.100 − 0.150	0.121	0.445	14.8	$0.102 \pm 0.016 \pm 0.012$	$0.132 \pm 0.021 \pm 0.015$
0.150 − 0.200	0.172	0.433	20.7	$0.126 \pm 0.024 \pm 0.020$	$0.107 \pm 0.020 \pm 0.017$
0.200 − 0.250	0.222	0.429	26.7	$0.140 \pm 0.033 \pm 0.020$	$0.081 \pm 0.019 \pm 0.011$
0.250 − 0.350	0.291	0.430	35.2	$0.168 \pm 0.036 \pm 0.020$	$0.060 \pm 0.013 \pm 0.007$
0.350 − 0.500	0.406	0.429	49.5	$0.301 \pm 0.057 \pm 0.033$	$0.0466 \pm 0.0088 \pm 0.0052$
0.500 − 0.700	0.567	0.415	67.1	$0.36 \pm 0.12 \pm 0.10$	$0.0146 \pm 0.0049 \pm 0.0039$

Table 42: Results for the asymmetry A_1^d ans spin-dependent structure function g_1^d obtained from the 2006 deuteron data set using a 160 GeV/c muon beam in bins of Bjorken-x and photon virtuality.

x range	$\langle x \rangle$	$\langle y \rangle$	$\langle Q^2 \rangle ((GeV/c)^2)$	A_1^d	g_1^d
0.003 — 0.004	0.0038	0.854	1.01	$-0.05 \pm 0.10 \pm 0.05$	$-1.3 \pm 2.8 \pm 1.3$
0.003 — 0.004	0.0039	0.860	1.02	$0.099 \pm 0.084 \pm 0.049$	$2.7 \pm 2.3 \pm 1.3$
0.003 — 0.004	0.0039	0.872	1.06	$-0.122 \pm 0.083 \pm 0.066$	$-3.3 \pm 2.2 \pm 1.8$
0.004 — 0.005	0.0045	0.764	1.02	$0.022 \pm 0.024 \pm 0.018$	$0.50 \pm 0.56 \pm 0.41$
0.004 — 0.005	0.0045	0.795	1.09	$-0.046 \pm 0.022 \pm 0.010$	$-1.07 \pm 0.50 \pm 0.23$
0.004 — 0.005	0.0047	0.835	1.20	$-0.044 \pm 0.023 \pm 0.010$	$-1.02 \pm 0.53 \pm 0.24$
0.005 — 0.006	0.0055	0.658	1.07	$-0.021 \pm 0.018 \pm 0.009$	$-0.39 \pm 0.34 \pm 0.16$
0.005 — 0.006	0.0055	0.739	1.21	$0.002 \pm 0.019 \pm 0.013$	$0.05 \pm 0.37 \pm 0.26$
0.005 — 0.006	0.0056	0.818	1.38	$0.001 \pm 0.018 \pm 0.008$	$0.02 \pm 0.38 \pm 0.16$
0.006 — 0.008	0.0069	0.560	1.14	$-0.010 \pm 0.013 \pm 0.005$	$-0.15 \pm 0.20 \pm 0.08$
0.006 — 0.008	0.0069	0.682	1.39	$0.020 \pm 0.013 \pm 0.006$	$0.34 \pm 0.22 \pm 0.09$
0.006 — 0.008	0.0072	0.789	1.70	$-0.000 \pm 0.013 \pm 0.006$	$-0.00 \pm 0.22 \pm 0.10$
0.008 — 0.010	0.0089	0.467	1.23	$0.021 \pm 0.015 \pm 0.006$	$0.25 \pm 0.18 \pm 0.08$
0.008 — 0.010	0.0089	0.623	1.65	$0.007 \pm 0.015 \pm 0.006$	$0.09 \pm 0.20 \pm 0.08$
0.008 — 0.010	0.0091	0.774	2.11	$-0.039 \pm 0.014 \pm 0.008$	$-0.56 \pm 0.21 \pm 0.11$
0.010 — 0.020	0.0131	0.395	1.47	$-0.0060 \pm 0.0090 \pm 0.0038$	$-0.051 \pm 0.077 \pm 0.032$
0.010 — 0.020	0.0135	0.585	2.27	$0.0042 \pm 0.0089 \pm 0.0037$	$0.041 \pm 0.087 \pm 0.036$
0.010 — 0.020	0.0157	0.713	3.30	$-0.0122 \pm 0.0088 \pm 0.0038$	$-0.116 \pm 0.084 \pm 0.037$
0.020 — 0.030	0.0239	0.310	2.10	$0.036 \pm 0.014 \pm 0.008$	$0.188 \pm 0.074 \pm 0.043$
0.020 — 0.030	0.0241	0.528	3.73	$-0.013 \pm 0.014 \pm 0.010$	$-0.078 \pm 0.087 \pm 0.064$
0.020 — 0.030	0.0253	0.724	5.44	$0.029 \pm 0.014 \pm 0.007$	$0.190 \pm 0.091 \pm 0.043$

Table 43: Results for the asymmetry A_1^d ans spin-dependent structure function g_1^d obtained from the 2006 deuteron data set using a 160 GeV/c muon beam in bins of Bjorken-x and photon virtuality.

X RANGE			$\langle x \rangle$	$\langle y \rangle$	$\langle Q^2 \rangle ((GeV/c)^2)$	A_1^d	g_1^d
0.030	—	0.040	0.0342	0.283	2.73	$0.009 \pm 0.019 \pm 0.009$	$0.034 \pm 0.074 \pm 0.034$
0.030	—	0.040	0.0344	0.504	5.11	$0.011 \pm 0.019 \pm 0.014$	$0.051 \pm 0.086 \pm 0.064$
0.030	—	0.040	0.0352	0.721	7.56	$0.021 \pm 0.019 \pm 0.010$	$0.104 \pm 0.090 \pm 0.046$
0.040	—	0.060	0.0477	0.266	3.58	$-0.001 \pm 0.019 \pm 0.012$	$-0.002 \pm 0.056 \pm 0.037$
0.040	—	0.060	0.0482	0.483	6.82	$0.026 \pm 0.017 \pm 0.008$	$0.088 \pm 0.059 \pm 0.025$
0.040	—	0.060	0.0504	0.709	10.6	$0.024 \pm 0.018 \pm 0.008$	$0.084 \pm 0.062 \pm 0.027$
0.060	—	0.100	0.0745	0.250	5.24	$0.023 \pm 0.020 \pm 0.009$	$0.047 \pm 0.039 \pm 0.017$
0.060	—	0.100	0.0756	0.459	10.1	$0.072 \pm 0.020 \pm 0.014$	$0.157 \pm 0.042 \pm 0.031$
0.060	—	0.100	0.0801	0.693	16.3	$0.051 \pm 0.020 \pm 0.009$	$0.109 \pm 0.042 \pm 0.020$
0.100	—	0.150	0.119	0.219	7.42	$0.058 \pm 0.028 \pm 0.012$	$0.073 \pm 0.035 \pm 0.015$
0.100	—	0.150	0.120	0.427	15.0	$0.076 \pm 0.028 \pm 0.013$	$0.100 \pm 0.037 \pm 0.017$
0.100	—	0.150	0.125	0.686	25.2	$0.171 \pm 0.028 \pm 0.021$	$0.221 \pm 0.036 \pm 0.027$
0.150	—	0.200	0.171	0.199	9.70	$0.071 \pm 0.042 \pm 0.018$	$0.059 \pm 0.035 \pm 0.015$
0.150	—	0.200	0.171	0.415	20.8	$0.155 \pm 0.041 \pm 0.025$	$0.132 \pm 0.035 \pm 0.021$
0.150	—	0.200	0.175	0.685	35.4	$0.153 \pm 0.042 \pm 0.025$	$0.127 \pm 0.035 \pm 0.021$
0.200	—	0.250	0.221	0.188	11.9	$0.152 \pm 0.058 \pm 0.027$	$0.089 \pm 0.034 \pm 0.016$
0.200	—	0.250	0.222	0.412	26.8	$0.212 \pm 0.058 \pm 0.030$	$0.123 \pm 0.034 \pm 0.017$
0.200	—	0.250	0.225	0.683	45.5	$0.052 \pm 0.058 \pm 0.032$	$0.029 \pm 0.033 \pm 0.018$
0.250	—	0.350	0.288	0.186	15.3	$0.193 \pm 0.063 \pm 0.030$	$0.072 \pm 0.024 \pm 0.011$
0.250	—	0.350	0.288	0.424	35.7	$0.174 \pm 0.063 \pm 0.029$	$0.064 \pm 0.023 \pm 0.010$
0.250	—	0.350	0.297	0.676	59.5	$0.138 \pm 0.063 \pm 0.030$	$0.046 \pm 0.021 \pm 0.010$
0.350	—	0.500	0.401	0.190	21.6	$0.432 \pm 0.099 \pm 0.054$	$0.075 \pm 0.017 \pm 0.010$
0.350	—	0.500	0.402	0.430	50.7	$0.279 \pm 0.098 \pm 0.047$	$0.044 \pm 0.016 \pm 0.008$
0.350	—	0.500	0.415	0.663	81.5	$0.196 \pm 0.098 \pm 0.045$	$0.027 \pm 0.014 \pm 0.006$
0.500	—	0.700	0.567	0.377	67.1	$0.36 \pm 0.12 \pm 0.10$	$0.0146 \pm 0.0049 \pm 0.0039$

The results for the asymmetry A_1^d and spin-dependent structure function g_1^d obtained from the combined COMPASS deuteron data set obtained by using a 160 GeV/c muon beam.

Table 44: Results for the asymmetry A_1^d ans spin-dependent structure function g_1^d obtained from the combined deuteron data set using a 160 GeV/c muon beam in bins of Bjorken-x.

x RANGE	$\langle x \rangle$	$\langle Q^2 \rangle ((GeV/c)^2)$	A_1^d	g_1^d
0.004 — 0.005	0.0046	1.10	$-0.0054 \pm 0.0074 \pm 0.0048$	$-0.13 \pm 0.17 \pm 0.11$
0.005 — 0.006	0.0055	1.22	$0.0003 \pm 0.0058 \pm 0.0043$	$0.00 \pm 0.12 \pm 0.09$
0.006 — 0.008	0.0070	1.39	$-0.0011 \pm 0.0042 \pm 0.0023$	$-0.016 \pm 0.071 \pm 0.040$
0.008 — 0.010	0.0090	1.62	$-0.0087 \pm 0.0049 \pm 0.0031$	$-0.121 \pm 0.064 \pm 0.038$
0.010 — 0.020	0.0141	2.19	$-0.0011 \pm 0.0032 \pm 0.0024$	$-0.010 \pm 0.027 \pm 0.019$
0.020 — 0.030	0.0244	3.29	$0.0075 \pm 0.0048 \pm 0.0034$	$0.043 \pm 0.028 \pm 0.018$
0.030 — 0.040	0.0346	4.43	$0.0095 \pm 0.0064 \pm 0.0042$	$0.043 \pm 0.028 \pm 0.018$
0.040 — 0.060	0.0487	6.06	$0.0159 \pm 0.0063 \pm 0.0044$	$0.051 \pm 0.021 \pm 0.014$
0.060 — 0.100	0.0766	9.00	$0.0527 \pm 0.0070 \pm 0.0072$	$0.111 \pm 0.015 \pm 0.015$
0.100 — 0.150	0.121	13.5	$0.095 \pm 0.010 \pm 0.011$	$0.123 \pm 0.013 \pm 0.014$
0.150 — 0.200	0.171	18.6	$0.121 \pm 0.015 \pm 0.016$	$0.101 \pm 0.013 \pm 0.014$
0.200 — 0.250	0.222	23.8	$0.160 \pm 0.022 \pm 0.020$	$0.0744 \pm 0.0096 \pm 0.0096$
0.250 — 0.350	0.290	31.1	$0.190 \pm 0.023 \pm 0.022$	$0.076 \pm 0.010 \pm 0.009$
0.350 — 0.500	0.405	43.9	$0.317 \pm 0.037 \pm 0.036$	$0.0576 \pm 0.0069 \pm 0.0067$
0.500 — 0.700	0.567	60.8	$0.494 \pm 0.082 \pm 0.084$	$0.0254 \pm 0.0042 \pm 0.0045$

Table 45: Results for the asymmetry A_1^d ans spin-dependent structure function g_1^d obtained from the combined deuteron data set using a $160\,\mathrm{GeV/c}$ muon beam in bins of Bjorken-x and photon virtuality.

x RANGE			$\langle x \rangle$	$\langle Q^2 \rangle ((\mathrm{GeV/c})^2)$	A_1^d	g_1^d
0.004	−	0.005	0.0045	1.03	$0.005 \pm 0.013 \pm 0.010$	$0.12 \pm 0.30 \pm 0.23$
0.004	−	0.005	0.0046	1.09	$-0.001 \pm 0.013 \pm 0.008$	$-0.02 \pm 0.29 \pm 0.19$
0.004	−	0.005	0.0047	1.20	$-0.023 \pm 0.013 \pm 0.008$	$-0.54 \pm 0.30 \pm 0.19$
0.005	−	0.006	0.0055	1.07	$-0.008 \pm 0.010 \pm 0.007$	$-0.15 \pm 0.20 \pm 0.12$
0.005	−	0.006	0.0055	1.21	$0.003 \pm 0.010 \pm 0.008$	$0.06 \pm 0.21 \pm 0.16$
0.005	−	0.006	0.0056	1.39	$0.004 \pm 0.011 \pm 0.006$	$0.08 \pm 0.22 \pm 0.14$
0.006	−	0.008	0.0069	1.13	$-0.0058 \pm 0.0075 \pm 0.0042$	$-0.09 \pm 0.11 \pm 0.06$
0.006	−	0.008	0.0069	1.39	$0.0011 \pm 0.0075 \pm 0.0043$	$0.02 \pm 0.12 \pm 0.07$
0.006	−	0.008	0.0072	1.70	$0.0007 \pm 0.0075 \pm 0.0043$	$0.01 \pm 0.13 \pm 0.07$
0.008	−	0.010	0.0089	1.22	$-0.0070 \pm 0.0084 \pm 0.0055$	$-0.08 \pm 0.10 \pm 0.07$
0.008	−	0.010	0.0089	1.65	$0.0021 \pm 0.0083 \pm 0.0052$	$0.03 \pm 0.11 \pm 0.07$
0.008	−	0.010	0.0091	2.11	$-0.0245 \pm 0.0083 \pm 0.0059$	$-0.36 \pm 0.12 \pm 0.09$
0.010	−	0.020	0.0132	1.44	$-0.0090 \pm 0.0051 \pm 0.0034$	$-0.076 \pm 0.043 \pm 0.029$
0.010	−	0.020	0.0135	2.23	$0.0028 \pm 0.0051 \pm 0.0033$	$0.027 \pm 0.050 \pm 0.032$
0.010	−	0.020	0.0156	3.24	$0.0009 \pm 0.0051 \pm 0.0034$	$0.009 \pm 0.049 \pm 0.033$
0.020	−	0.030	0.0239	1.95	$0.0198 \pm 0.0082 \pm 0.0062$	$0.101 \pm 0.042 \pm 0.032$
0.020	−	0.030	0.0240	3.53	$-0.0083 \pm 0.0082 \pm 0.0069$	$-0.051 \pm 0.050 \pm 0.042$
0.020	−	0.030	0.0253	5.22	$0.0075 \pm 0.0082 \pm 0.0056$	$0.048 \pm 0.053 \pm 0.037$
0.030	−	0.040	0.0342	2.51	$0.014 \pm 0.011 \pm 0.008$	$0.052 \pm 0.043 \pm 0.029$
0.030	−	0.040	0.0344	4.82	$0.007 \pm 0.011 \pm 0.009$	$0.033 \pm 0.051 \pm 0.043$
0.030	−	0.040	0.0352	7.24	$0.006 \pm 0.011 \pm 0.008$	$0.029 \pm 0.054 \pm 0.038$

Table 46: Results for the asymmetry A_1^d ans spin-dependent structure function g_1^d obtained from the combined deuteron data set using a $160\,\text{GeV/c}$ muon beam in bins of Bjorken-x and photon virtuality.

x range			$\langle x \rangle$	$\langle Q^2 \rangle ((\text{GeV/c})^2)$	A_1^d	g_1^d
0.040	—	0.060	0.0477	3.38	$0.005 \pm 0.011 \pm 0.009$	$0.014 \pm 0.032 \pm 0.025$
0.040	—	0.060	0.0482	6.43	$0.012 \pm 0.011 \pm 0.007$	$0.040 \pm 0.036 \pm 0.023$
0.040	—	0.060	0.0502	10.1	$0.021 \pm 0.011 \pm 0.007$	$0.072 \pm 0.037 \pm 0.025$
0.060	—	0.100	0.0744	4.93	$0.034 \pm 0.012 \pm 0.009$	$0.067 \pm 0.024 \pm 0.019$
0.060	—	0.100	0.0757	9.28	$0.052 \pm 0.012 \pm 0.012$	$0.111 \pm 0.026 \pm 0.025$
0.060	—	0.100	0.0796	15.6	$0.065 \pm 0.012 \pm 0.010$	$0.140 \pm 0.026 \pm 0.022$
0.100	—	0.150	0.119	6.99	$0.058 \pm 0.017 \pm 0.014$	$0.072 \pm 0.022 \pm 0.017$
0.100	—	0.150	0.120	13.8	$0.070 \pm 0.017 \pm 0.014$	$0.092 \pm 0.023 \pm 0.019$
0.100	—	0.150	0.124	24.2	$0.148 \pm 0.017 \pm 0.019$	$0.191 \pm 0.023 \pm 0.025$
0.150	—	0.200	0.171	9.06	$0.099 \pm 0.026 \pm 0.019$	$0.082 \pm 0.022 \pm 0.016$
0.150	—	0.200	0.171	19.2	$0.119 \pm 0.026 \pm 0.021$	$0.101 \pm 0.022 \pm 0.018$
0.150	—	0.200	0.174	33.9	$0.127 \pm 0.026 \pm 0.022$	$0.106 \pm 0.022 \pm 0.018$
0.200	—	0.250	0.221	11.2	$0.150 \pm 0.037 \pm 0.028$	$0.087 \pm 0.022 \pm 0.017$
0.200	—	0.250	0.221	25.2	$0.171 \pm 0.037 \pm 0.029$	$0.100 \pm 0.021 \pm 0.017$
0.200	—	0.250	0.224	43.5	$0.151 \pm 0.037 \pm 0.032$	$0.085 \pm 0.021 \pm 0.018$
0.250	—	0.350	0.287	14.3	$0.187 \pm 0.040 \pm 0.032$	$0.071 \pm 0.015 \pm 0.012$
0.250	—	0.350	0.288	33.4	$0.187 \pm 0.040 \pm 0.032$	$0.068 \pm 0.015 \pm 0.012$
0.250	—	0.350	0.295	56.2	$0.185 \pm 0.040 \pm 0.033$	$0.062 \pm 0.014 \pm 0.011$
0.350	—	0.500	0.400	20.0	$0.396 \pm 0.065 \pm 0.056$	$0.070 \pm 0.012 \pm 0.010$
0.350	—	0.500	0.402	46.4	$0.266 \pm 0.066 \pm 0.051$	$0.043 \pm 0.011 \pm 0.008$
0.350	—	0.500	0.411	74.1	$0.288 \pm 0.063 \pm 0.050$	$0.041 \pm 0.009 \pm 0.007$
0.500	—	0.700	0.569	62.1	$0.501 \pm 0.082 \pm 0.084$	$0.0204 \pm 0.0033 \pm 0.0035$

RESULTS FROM THE PROTON DATA AT LOW PHOTON VIRTUALITIES

The results for the asymmetry A_1^p ans spin-dependent structure function g_1^p obtained from the proton data set obtained by using the in 2007 and 2011 data. The results are given as a function of Bjorken-x and as a function of the virtual photon energy. The tables contain the results with their statistical and systematic uncertainty.

Table 47: Results for the asymmetry A_1^p and spin-dependent structure function g_1^p obtained from the 2007 data set in bins of Bjorken-x.

x range		$\langle x \rangle$	$\langle Q^2 \rangle$ (GeV^2/c^2)	A_1^p	g_1^p
$4.0 \cdot 10^{-5}$	$- \quad 6.3 \cdot 10^{-5}$	$5.16 \cdot 10^{-5}$	0.006	$0.0073 \pm 0.0042 \pm 0.0044$	$0.51 \pm 0.29 \pm 0.27$
$6.3 \cdot 10^{-5}$	$- \quad 1.0 \cdot 10^{-4}$	$8.12 \cdot 10^{-5}$	0.011	$0.0074 \pm 0.0034 \pm 0.0043$	$0.58 \pm 0.26 \pm 0.31$
$1.0 \cdot 10^{-4}$	$- \quad 1.6 \cdot 10^{-4}$	$1.28 \cdot 10^{-4}$	0.019	$0.0098 \pm 0.0029 \pm 0.0030$	$0.81 \pm 0.24 \pm 0.20$
$1.6 \cdot 10^{-4}$	$- \quad 2.5 \cdot 10^{-4}$	$2.02 \cdot 10^{-4}$	0.032	$0.0082 \pm 0.0028 \pm 0.0021$	$0.69 \pm 0.23 \pm 0.15$
$2.5 \cdot 10^{-4}$	$- \quad 4.0 \cdot 10^{-4}$	$3.18 \cdot 10^{-4}$	0.052	$0.0061 \pm 0.0028 \pm 0.0023$	$0.49 \pm 0.22 \pm 0.17$
$4.0 \cdot 10^{-4}$	$- \quad 6.3 \cdot 10^{-4}$	$5.03 \cdot 10^{-4}$	0.083	$0.0132 \pm 0.0029 \pm 0.0034$	$0.96 \pm 0.21 \pm 0.22$
$6.3 \cdot 10^{-4}$	$- \quad 1.0 \cdot 10^{-3}$	$7.94 \cdot 10^{-4}$	0.130	$0.0172 \pm 0.0032 \pm 0.0030$	$1.08 \pm 0.20 \pm 0.16$
$1.0 \cdot 10^{-3}$	$- \quad 1.6 \cdot 10^{-3}$	$1.26 \cdot 10^{-3}$	0.207	$0.0125 \pm 0.0035 \pm 0.0034$	$0.40 \pm 0.11 \pm 0.16$
$1.6 \cdot 10^{-3}$	$- \quad 2.5 \cdot 10^{-3}$	$1.99 \cdot 10^{-3}$	0.329	$0.0125 \pm 0.0040 \pm 0.0026$	$0.36 \pm 0.12 \pm 0.09$
$2.5 \cdot 10^{-3}$	$- \quad 4.0 \cdot 10^{-3}$	$3.15 \cdot 10^{-3}$	0.520	$0.0150 \pm 0.0048 \pm 0.0048$	$0.36 \pm 0.11 \pm 0.12$
$4.0 \cdot 10^{-3}$	$- \quad 6.3 \cdot 10^{-3}$	$4.86 \cdot 10^{-3}$	0.656	$0.0187 \pm 0.0067 \pm 0.0061$	$0.32 \pm 0.12 \pm 0.11$
$6.3 \cdot 10^{-3}$	$- \quad 1.0 \cdot 10^{-2}$	$7.73 \cdot 10^{-3}$	0.693	$0.048 \pm 0.011 \pm 0.009$	$0.52 \pm 0.12 \pm 0.10$
$1.0 \cdot 10^{-2}$	$- \quad 1.6 \cdot 10^{-2}$	$1.22 \cdot 10^{-2}$	0.743	$0.040 \pm 0.019 \pm 0.016$	$0.29 \pm 0.14 \pm 0.12$
$1.6 \cdot 10^{-2}$	$- \quad 2.5 \cdot 10^{-2}$	$1.90 \cdot 10^{-2}$	0.812	$0.037 \pm 0.036 \pm 0.023$	$0.19 \pm 0.18 \pm 0.12$

Table 48: Results for the asymmetry A_1^p and spin-dependent structure function g_1^p obtained from the 2011 data set in bins of Bjorken-x.

x range			$\langle x \rangle$	$\langle Q^2 \rangle$ (GeV^2/c^2)	A_1^p	g_1^p
$4.0 \cdot 10^{-5}$	–	$6.3 \cdot 10^{-5}$	$5.15 \cdot 10^{-5}$	0.009	$0.0072 \pm 0.0043 \pm 0.0047$	$0.74 \pm 0.44 \pm 0.44$
$6.3 \cdot 10^{-5}$	–	$1.0 \cdot 10^{-4}$	$8.10 \cdot 10^{-5}$	0.016	$0.0053 \pm 0.0036 \pm 0.0025$	$0.58 \pm 0.39 \pm 0.24$
$1.0 \cdot 10^{-4}$	–	$1.6 \cdot 10^{-4}$	$1.28 \cdot 10^{-4}$	0.026	$0.0057 \pm 0.0033 \pm 0.0019$	$0.64 \pm 0.37 \pm 0.19$
$1.6 \cdot 10^{-4}$	–	$2.5 \cdot 10^{-4}$	$2.01 \cdot 10^{-4}$	0.043	$0.0042 \pm 0.0032 \pm 0.0031$	$0.46 \pm 0.35 \pm 0.33$
$2.5 \cdot 10^{-4}$	–	$4.0 \cdot 10^{-4}$	$3.18 \cdot 10^{-4}$	0.070	$0.0039 \pm 0.0033 \pm 0.0032$	$0.39 \pm 0.33 \pm 0.32$
$4.0 \cdot 10^{-4}$	–	$6.3 \cdot 10^{-4}$	$5.03 \cdot 10^{-4}$	0.111	$0.0095 \pm 0.0034 \pm 0.0022$	$0.86 \pm 0.31 \pm 0.18$
$6.3 \cdot 10^{-4}$	–	$1.0 \cdot 10^{-3}$	$7.94 \cdot 10^{-4}$	0.174	$0.0111 \pm 0.0038 \pm 0.0029$	$0.83 \pm 0.29 \pm 0.21$
$1.0 \cdot 10^{-3}$	–	$1.6 \cdot 10^{-3}$	$1.26 \cdot 10^{-3}$	0.281	$0.0104 \pm 0.0042 \pm 0.0039$	$0.45 \pm 0.18 \pm 0.18$
$1.6 \cdot 10^{-3}$	–	$2.5 \cdot 10^{-3}$	$1.99 \cdot 10^{-3}$	0.444	$-0.0002 \pm 0.0049 \pm 0.0023$	$-0.01 \pm 0.17 \pm 0.08$
$2.5 \cdot 10^{-3}$	–	$4.0 \cdot 10^{-3}$	$3.09 \cdot 10^{-3}$	0.647	$0.0196 \pm 0.0061 \pm 0.0034$	$0.54 \pm 0.17 \pm 0.10$
$4.0 \cdot 10^{-3}$	–	$6.3 \cdot 10^{-3}$	$4.84 \cdot 10^{-3}$	0.709	$0.048 \pm 0.011 \pm 0.007$	$0.85 \pm 0.19 \pm 0.13$
$6.3 \cdot 10^{-3}$	–	$1.0 \cdot 10^{-2}$	$7.68 \cdot 10^{-3}$	0.757	$0.014 \pm 0.018 \pm 0.008$	$0.16 \pm 0.21 \pm 0.10$
$1.0 \cdot 10^{-2}$	–	$1.6 \cdot 10^{-2}$	$1.21 \cdot 10^{-2}$	0.801	$0.099 \pm 0.034 \pm 0.019$	$0.75 \pm 0.26 \pm 0.15$
$1.6 \cdot 10^{-2}$	–	$2.5 \cdot 10^{-2}$	$1.85 \cdot 10^{-2}$	0.874	$0.010 \pm 0.076 \pm 0.041$	$0.05 \pm 0.40 \pm 0.21$

Table 49: Results for the asymmetry A_1^p and spin-dependent structure function g_1^p obtained from the 2007 data set in bins of the virtual photon energy.

ν RANGE	$\langle \nu \rangle$	$\langle x \rangle$	$\langle Q^2 \rangle ((GeV/c)^2)$	A_1^P	g_1^P
16 — 24	20.8	$3.53 \cdot 10^{-3}$	0.135	$0.028 \pm 0.011 \pm 0.011$	$0.41 \pm 0.16 \pm 0.16$
24 — 32	28.5	$1.86 \cdot 10^{-3}$	0.099	$0.0232 \pm 0.0067 \pm 0.0094$	$0.52 \pm 0.15 \pm 0.20$
32 — 40	36.3	$1.22 \cdot 10^{-3}$	0.082	$0.0196 \pm 0.0049 \pm 0.0057$	$0.59 \pm 0.15 \pm 0.15$
40 — 48	44.2	$9.40 \cdot 10^{-4}$	0.078	$0.0055 \pm 0.0041 \pm 0.0047$	$0.20 \pm 0.15 \pm 0.17$
48 — 56	52.1	$8.10 \cdot 10^{-4}$	0.079	$0.0100 \pm 0.0037 \pm 0.0032$	$0.44 \pm 0.16 \pm 0.12$
56 — 64	60.1	$7.40 \cdot 10^{-4}$	0.083	$0.0094 \pm 0.0035 \pm 0.0028$	$0.47 \pm 0.17 \pm 0.12$
64 — 72	68.0	$7.01 \cdot 10^{-4}$	0.090	$0.0106 \pm 0.0033 \pm 0.0043$	$0.59 \pm 0.18 \pm 0.21$
72 — 80	76.0	$6.92 \cdot 10^{-4}$	0.099	$0.0142 \pm 0.0033 \pm 0.0034$	$0.85 \pm 0.20 \pm 0.14$
80 — 88	83.9	$7.24 \cdot 10^{-4}$	0.114	$0.0116 \pm 0.0034 \pm 0.0030$	$0.73 \pm 0.21 \pm 0.14$
88 — 96	92.0	$7.59 \cdot 10^{-4}$	0.131	$0.0074 \pm 0.0035 \pm 0.0024$	$0.49 \pm 0.23 \pm 0.13$
96 — 104	100.0	$7.56 \cdot 10^{-4}$	0.142	$0.0125 \pm 0.0036 \pm 0.0038$	$0.87 \pm 0.25 \pm 0.23$
104 — 112	107.9	$7.64 \cdot 10^{-4}$	0.155	$0.0093 \pm 0.0037 \pm 0.0027$	$0.67 \pm 0.27 \pm 0.17$
112 — 120	115.9	$7.97 \cdot 10^{-4}$	0.174	$0.0105 \pm 0.0039 \pm 0.0043$	$0.78 \pm 0.29 \pm 0.31$
120 — 128	123.9	$8.52 \cdot 10^{-4}$	0.198	$0.0180 \pm 0.0043 \pm 0.0034$	$1.35 \pm 0.32 \pm 0.23$
128 — 136	131.7	$9.20 \cdot 10^{-4}$	0.227	$0.0077 \pm 0.0051 \pm 0.0029$	$0.39 \pm 0.26 \pm 0.17$
136 — 144	139.2	$1.02 \cdot 10^{-3}$	0.266	$0.0028 \pm 0.0076 \pm 0.0039$	$0.15 \pm 0.40 \pm 0.21$
144 — 152	146.5	$1.13 \cdot 10^{-3}$	0.311	$0.016 \pm 0.018 \pm 0.012$	$0.86 \pm 0.94 \pm 0.67$

Table 50: Results for the asymmetry A_1^p and spin-dependent structure function g_1^p obtained from the 2011 data set in bins of the virtual photon energy.

ν RANGE	$\langle \nu \rangle$	$\langle x \rangle$	$\langle Q^2 \rangle ((\text{GeV/c})^2)$	A_1^p	g_1^p
16 — 24	22.2	$9.5541 \cdot 10^{-3}$	0.396	$0.046 \pm 0.058 \pm 0.037$	$0.31 \pm 0.40 \pm 0.26$
24 — 32	28.6	$5.9587 \cdot 10^{-3}$	0.316	$0.051 \pm 0.027 \pm 0.018$	$0.47 \pm 0.25 \pm 0.18$
32 — 40	36.6	$3.1960 \cdot 10^{-3}$	0.217	$0.025 \pm 0.017 \pm 0.009$	$0.30 \pm 0.21 \pm 0.15$
40 — 48	44.5	$1.8140 \cdot 10^{-3}$	0.150	$0.030 \pm 0.011 \pm 0.010$	$0.88 \pm 0.33 \pm 0.27$
48 — 56	52.4	$1.1526 \cdot 10^{-3}$	0.113	$0.0021 \pm 0.0078 \pm 0.0037$	$0.08 \pm 0.31 \pm 0.15$
56 — 64	60.3	$8.3596 \cdot 10^{-4}$	0.094	$0.0105 \pm 0.0061 \pm 0.0035$	$0.51 \pm 0.29 \pm 0.15$
64 — 72	68.2	$6.8775 \cdot 10^{-4}$	0.088	$0.0050 \pm 0.0052 \pm 0.0035$	$0.28 \pm 0.29 \pm 0.19$
72 — 80	76.1	$6.2092 \cdot 10^{-4}$	0.089	$0.0076 \pm 0.0047 \pm 0.0035$	$0.47 \pm 0.29 \pm 0.20$
80 — 88	84.1	$5.9263 \cdot 10^{-4}$	0.094	$0.0028 \pm 0.0044 \pm 0.0027$	$0.19 \pm 0.30 \pm 0.18$
88 — 96	92.0	$5.7928 \cdot 10^{-4}$	0.100	$0.0109 \pm 0.0042 \pm 0.0041$	$0.79 \pm 0.31 \pm 0.26$
96 — 104	100.0	$5.6950 \cdot 10^{-4}$	0.107	$0.0099 \pm 0.0041 \pm 0.0028$	$0.76 \pm 0.32 \pm 0.17$
104 — 112	108.0	$5.6287 \cdot 10^{-4}$	0.114	$0.0075 \pm 0.0041 \pm 0.0029$	$0.61 \pm 0.33 \pm 0.21$
112 — 120	116.0	$5.7146 \cdot 10^{-4}$	0.124	$0.0142 \pm 0.0041 \pm 0.0034$	$1.21 \pm 0.35 \pm 0.21$
120 — 128	123.9	$5.9694 \cdot 10^{-4}$	0.139	$0.0077 \pm 0.0043 \pm 0.0025$	$0.68 \pm 0.38 \pm 0.19$
128 — 136	131.9	$6.1668 \cdot 10^{-4}$	0.153	$0.0055 \pm 0.0045 \pm 0.0041$	$0.49 \pm 0.40 \pm 0.36$
136 — 144	139.9	$6.2467 \cdot 10^{-4}$	0.164	$-0.0034 \pm 0.0047 \pm 0.0030$	$-0.32 \pm 0.43 \pm 0.27$
144 — 152	147.9	$6.4238 \cdot 10^{-4}$	0.178	$0.0062 \pm 0.0049 \pm 0.0038$	$0.58 \pm 0.46 \pm 0.35$
152 — 160	155.9	$6.8267 \cdot 10^{-4}$	0.200	$0.0042 \pm 0.0052 \pm 0.0023$	$0.40 \pm 0.50 \pm 0.22$
160 — 168	163.8	$7.3842 \cdot 10^{-4}$	0.227	$0.0048 \pm 0.0058 \pm 0.0027$	$0.31 \pm 0.38 \pm 0.19$
168 — 176	171.7	$8.2114 \cdot 10^{-4}$	0.265	$0.0054 \pm 0.0069 \pm 0.0052$	$0.36 \pm 0.46 \pm 0.35$
176 — 184	179.3	$9.2117 \cdot 10^{-4}$	0.310	$0.026 \pm 0.010 \pm 0.006$	$1.74 \pm 0.68 \pm 0.46$
184 — 192	186.4	$1.0384 \cdot 10^{-3}$	0.363	$0.043 \pm 0.023 \pm 0.017$	$2.8 \pm 1.5 \pm 1.2$

BIBLIOGRAPHY

[1] E. Rutherford, Phil. Mag. Ser.6 **21**, 669 (1911). (Cited on page 3.)

[2] J. Chadwick, Proc. Roy. Soc. Lond. **A136**, 692 (1932). (Cited on page 3.)

[3] M. Gell-Mann, Phys. Lett. **8**, 214 (1964). (Cited on pages 3 und 13.)

[4] G. Zweig, in *DEVELOPMENTS IN THE QUARK THEORY OF HADRONS. VOL. 1. 1964 - 1978*, edited by D. Lichtenberg and S. P. Rosen (Hadronic Press, 1964), pp. 22–101, URL http://inspirehep.net/record/4674/files/cern-th-412.pdf. (Cited on pages 3 und 13.)

[5] J. E. Augustin et al. (SLAC-SP-017), Phys. Rev. Lett. **33**, 1406 (1974), [Adv. Exp. Phys.5,141(1976)]. (Cited on page 3.)

[6] J. J. Aubert et al. (E598), Phys. Rev. Lett. **33**, 1404 (1974). (Cited on page 3.)

[7] M. Breidenbach, J. I. Friedman, H. W. Kendall, E. D. Bloom, D. H. Coward, H. C. DeStaebler, J. Drees, L. W. Mo, and R. E. Taylor, Phys. Rev. Lett. **23**, 935 (1969). (Cited on pages 3 und 12.)

[8] R. P. Feynman, Phys. Rev. Lett. **23**, 1415 (1969). (Cited on pages 3 und 13.)

[9] R. Brandelik et al. (TASSO), Phys. Lett. **B86**, 243 (1979). (Cited on page 3.)

[10] M. J. Alguard et al., Phys. Rev. Lett. **41**, 70 (1978). (Cited on page 3.)

[11] G. Baum et al., Phys. Rev. Lett. **51**, 1135 (1983). (Cited on page 3.)

[12] F. E. Close and R. G. Roberts, Phys. Lett. **B316**, 165 (1993), hep-ph/9306289. (Cited on page 4.)

[13] J. Ashman et al. (EMC), Nucl. Phys. **B328**, 1 (1989). (Cited on pages 4, 27, 124, 156 und 182.)

[14] S. Stein, W. B. Atwood, E. D. Bloom, R. L. Cottrell, H. C. DeStaebler, C. L. Jordan, H. Piel, C. Y. Prescott, R. Siemann, and R. E. Taylor, Phys. Rev. **D12**, 1884 (1975). (Cited on pages 8 und 9.)

[15] M. Anselmino, A. Efremov, and E. Leader, Phys. Rept. **261**, 1 (1995), [Erratum: Phys. Rept.281,399(1997)], hep-ph/9501369. (Cited on pages 10 und 26.)

[16] B. Povh, K. Rith, C. Scholz, and F. Zetsche, *Teilchen und Kerne - Eine Einführung in die physikalischen Konzepte* (Springer, 2006), 7th ed. (Cited on pages 12 und 14.)

[17] J. D. Bjorken and E. A. Paschos, Phys. Rev. **185**, 1975 (1969). (Cited on page 13.)

[18] K. A. Olive et al. (Particle Data Group), Chin. Phys. **C38**, 090001 (2014). (Cited on pages 13, 16, 17, 28, 62, 64, 84, 185, 188, 192 und 193.)

[19] C. G. Callan, Jr. and D. J. Gross, Phys. Rev. Lett. **22**, 156 (1969). (Cited on page 14.)

[20] L. W. Whitlow, E. M. Riordan, S. Dasu, S. Rock, and A. Bodek, Phys. Lett. **B282**, 475 (1992). (Cited on page 16.)

[21] A. C. Benvenuti et al. (BCDMS), Phys. Lett. **B223**, 485 (1989). (Cited on page 16.)

[22] M. R. Adams et al. (E665), Phys. Rev. **D54**, 3006 (1996). (Cited on page 16.)

[23] M. Arneodo et al. (New Muon), Nucl. Phys. **B483**, 3 (1997), `hep-ph/9610231`. (Cited on page 16.)

[24] H. Abramowicz et al. (ZEUS, H1), Eur. Phys. J. **C75**, 580 (2015), `1506.06042[hep-ex]`. (Cited on page 16.)

[25] G. Altarelli, Phys. Rept. **81**, 1 (1982). (Cited on pages 17, 19 und 20.)

[26] W. A. Bardeen, A. J. Buras, D. W. Duke, and T. Muta, Phys. Rev. **D18**, 3998 (1978). (Cited on page 18.)

[27] G. Altarelli and G. Parisi, Nucl. Phys. **B126**, 298 (1977). (Cited on page 20.)

[28] W. Vogelsang, Nucl. Phys. **B475**, 47 (1996), `hep-ph/9603366`. (Cited on page 20.)

[29] R. Mertig and W. L. van Neerven, Z. Phys. **C70**, 637 (1996), `hep-ph/9506451`. (Cited on page 20.)

[30] S. D. Bass, *The Spin structure of the proton* (World Scientific, 2007), ISBN 978-981-270-946-2, URL `http://www.worldscibooks.com/physics/6558.html`. (Cited on page 21.)

[31] J. Kodaira, S. Matsuda, T. Muta, K. Sasaki, and T. Uematsu, Phys. Rev. **D20**, 627 (1979). (Cited on pages 21 und 157.)

[32] J. Kodaira, Nucl. Phys. **B165**, 129 (1980). (Cited on pages 21 und 157.)

[33] A. V. Manohar, in *Lake Louise Winter Institute: Symmetry and Spin in the Standard Model Lake Louise, Alberta, Canada, February 23-29, 1992* (1992), pp. 1–46, `hep-ph/9204208`. (Cited on page 21.)

[34] T. Pussieux and R. Windmolders, in *Internal spin structure of the nucleon. Proceedings, Symposium, SMC Meeting, New Haven, USA, January 5-6, 1994* (1995), pp. 212–234, URL `http://alice.cern.ch/format/showfull?sysnb=0206711`. (Cited on page 22.)

[35] L. N. Hand, Phys. Rev. **129**, 1834 (1963). (Cited on page 22.)

[36] J. Soffer and O. V. Teryaev, Phys. Lett. **B490**, 106 (2000), `hep-ph/0005132`. (Cited on page 23.)

[37] S. Wandzura and F. Wilczek, Phys. Lett. **B72**, 195 (1977). (Cited on page 23.)

[38] P. L. Anthony et al. (E155), Phys. Lett. **B553**, 18 (2003), `hep-ex/0204028`. (Cited on pages 23, 24 und 117.)

[39] P. L. Anthony et al. (E155), Phys. Lett. **B458**, 529 (1999), `hep-ex/9901006`. (Cited on page 24.)

[40] K. Abe et al. (E143), Phys. Rev. Lett. **76**, 587 (1996), `hep-ex/9511013`. (Cited on page 24.)

[41] D. Adams et al. (SMC), Phys. Lett. **B336**, 125 (1994), `hep-ex/9408001`. (Cited on page 24.)

[42] D. Adams et al. (SMC), Phys. Lett. **B396**, 338 (1997). (Cited on page 24.)

[43] P. Hoodbhoy, R. L. Jaffe, and A. Manohar, Nucl. Phys. **B312**, 571 (1989). (Cited on page 23.)

[44] R. D. Ball, S. Forte, and G. Ridolfi, Phys. Lett. **B378**, 255 (1996), `hep-ph/9510449`. (Cited on page 26.)

[45] S. A. Larin, T. van Ritbergen, and J. A. M. Vermaseren, Phys. Lett. **B404**, 153 (1997), `hep-ph/9702435`. (Cited on page 26.)

[46] S. A. Larin, Phys. Lett. **B334**, 192 (1994), `hep-ph/9403383`. (Cited on page 26.)

[47] P. A. Baikov, K. G. Chetyrkin, and J. H. Kuhn, Phys. Rev. Lett. **104**, 132004 (2010), `1001.3606[hep-ph]`. (Cited on page 26.)

[48] J. D. Bjorken, Phys. Rev. **148**, 1467 (1966). (Cited on page 27.)

[49] J. R. Ellis and R. L. Jaffe, Phys. Rev. **D9**, 1444 (1974), [Erratum: Phys. Rev.D10,1669(1974)]. (Cited on page 27.)

[50] Y. Goto et al. (Asymmetry Analysis), Phys.Rev. **D62**, 034017 (2000), `hep-ph/0001046`. (Cited on pages 27, 114, 180 und 191.)

[51] C. Caso et al. (Particle Data Group), Eur. Phys. J. **C3**, 1 (1998). (Cited on page 27.)

[52] J. Kwiecinski and B. Ziaja, Phys. Rev. **D60**, 054004 (1999), `hep-ph/9902440`. (Cited on page 28.)

[53] B. Badelek, J. Kiryluk, and J. Kwiecinski, Phys. Rev. **D61**, 014009 (2000), `hep-ph/9907569`. (Cited on page 29.)

[54] B. M. Badelek, J. Kwiecinski, and B. Ziaja, Eur. Phys. J. **C26**, 45 (2002), `hep-ph/0206188`. (Cited on pages 29, 151 und 197.)

[55] S. D. Drell and A. C. Hearn, Phys. Rev. Lett. **16**, 908 (1966). (Cited on page 29.)

[56] S. B. Gerasimov, Sov. J. Nucl. Phys. **2**, 430 (1966), [Yad. Fiz.2,598(1965)].

[57] M. Hosoda and K. Yamamoto, Progress of theoretical physics **36**, 425 (1966). (Cited on page 29.)

[58] P. Abbon et al. (COMPASS), Nucl. Instrum. Meth. **A577**, 455 (2007), `hep-ex/0703049`. (Cited on pages 33, 42, 45, 46, 47, 48, 51 und 58.)

[59] P. Abbon et al. (COMPASS), Nucl. Instrum. Meth. **A779**, 69 (2015), 1410. 1797[physics.ins-det]. (Cited on pages 33, 34, 36, 42 und 59.)

[60] L. Gatignon, *The m2 beam line for compass*, http://sba.web.cern.ch/sba/ BeamsAndAreas/M2/M2-OperatorCourse.pdf (2006). (Cited on page 34.)

[61] N. Doble, L. Gatignon, G. von Holtey, and F. Novoskoltsev, Nucl. Instrum. Meth. **A343**, 351 (1994). (Cited on pages 35, 37 und 87.)

[62] J. Ball et al., Nucl. Instrum. Meth. **A498**, 101 (2003). (Cited on page 37.)

[63] N. W. Schellingerhout, L. P. Kok, S. A. Coon, and R. M. Adam, Phys. Rev. **C48**, 2714 (1993), [Erratum: Phys. Rev.C52,439(1995)], nucl-th/9309012. (Cited on page 37.)

[64] J. Koivuniemi, N. Doshita, F. Gautheron, C. H. Hess, T. Iwata, Y. U. Kisselev, K. Kondo, W. Meyer, T. Michigami, and G. Reicherz, Journal of Physics: Conference Series **150**, 012023 (2009), URL http://dx.doi.org/10.1088/1742-6596/150/ 1/012023. (Cited on page 37.)

[65] A. Abragam and M. Goldman, Reports on Progress in Physics **41**, 395 (1978), URL http://dx.doi.org/10.1088/0034-4885/41/3/002. (Cited on page 38.)

[66] G. K. Mallot, Habilitation thesis, Mainz U. (1996), URL http://inspirehep.net/ record/1231276/files/1996_hab_mallot.pdf. (Cited on page 38.)

[67] N. Takabayashi, Ph.D. thesis, Nagoya U., Nagoya (2002), URL https://cds.cern. ch/record/1258401. (Cited on page 39.)

[68] B. Adeva et al. (SMC), Nucl. Instrum. Meth. **A419**, 60 (1998). (Cited on page 40.)

[69] J. Koivuniemi, N. Doshita, F. Gautheron, Y. Kisselev, K. Kondo, H. Matsuda, and M. Pesek (2013), COMPASS Note 2013-7. (Cited on pages 40 und 116.)

[70] I. Abt, S. Masciocchi, B. Moshous, T. Perschke, K. Riechmann, and W. Wagner, Nucl. Instrum. Meth. **A439**, 442 (2000). (Cited on page 48.)

[71] P. Schiavon (2011), progress report. (Cited on pages 52 und 53.)

[72] C. Bernet et al., Nucl. Instrum. Meth. **A550**, 217 (2005). (Cited on pages 53 und 56.)

[73] Du Fresne von Hohenesche, Nicolas, Ph.D. thesis, Mainz U. (2016), URL http:// publications.ub.uni-mainz.de/theses/volltexte/2015/100000552/index.html. (Cited on page 53.)

[74] J. Barth, J. Bernhard, E. Kabuß, N. du Fresne, and B. Veit (2016), COMPASS Note 2016-4. (Cited on page 55.)

[75] H. Fischer, J. Franz, A. Grunemaier, F. H. Heinsius, L. Hennig, K. Konigsmann, M. Niebuhr, T. Schmidt, H. Schmitt, and H. J. Urban, Nucl. Instrum. Meth. **A461**, 507 (2001), hep-ex/0010065. (Cited on page 58.)

[76] J. Baud, B. Couturier, C. Curran, J. Durand, E. Knezo, S. Occhetti, and O. Barring, CoRR **cs.OH/0305047** (2003), URL http://arxiv.org/abs/cs.OH/0305047. (Cited on page 58.)

[77] G. Roland, Nucl. Instrum. Meth. **A389**, 87 (1997). (Cited on page 58.)

[78] R. Fruhwirth, Nucl. Instrum. Meth. **A262**, 444 (1987). (Cited on page 60.)

[79] E. J. Wolin and L. L. Ho, Nucl. Instrum. Meth. **A329**, 493 (1993). (Cited on page 60.)

[80] Q. Curiel, V.Andrieux, Y.Bedfer, L.Capozza, F.Kunne, C.Marchand, and F.Sozzi (2013), COMPASS Note 2013-3. (Cited on pages 61 und 67.)

[81] F. Sozzi, Ph.D. thesis, Trieste U. (2007), URL `https://cds.cern.ch/record/1493519`. (Cited on page 67.)

[82] Q. M. Curiel Garcia, Ph.D. thesis, U. Paris-Sud (2014). (Cited on page 67.)

[83] J.-M. L. Goff (2004), COMPASS Note 2004-3. (Cited on page 79.)

[84] J. Pretz (2004), COMPASS Note 2004-11. (Cited on page 79.)

[85] C. Iselin, *Halo: A Computer Program to Calculate Muon Halo* (1974), CERN-74-17. (Cited on page 86.)

[86] B. Adeva et al. (SMC), Nucl. Instrum. Meth. **A343**, 363 (1994). (Cited on page 87.)

[87] D. Adams et al. (SMC), Nucl. Instrum. Meth. **A443**, 1 (2000). (Cited on page 87.)

[88] B. Adeva et al. (SMC), Phys. Rev. **D58**, 112001 (1998). (Cited on pages 87, 113, 117, 123, 124, 125, 126, 129, 130, 132, 133, 150, 156 und 182.)

[89] M. Arneodo et al. (New Muon), Nucl. Phys. **B487**, 3 (1997), `hep-ex/9611022`. (Cited on page 87.)

[90] J. Kwiecinski and B. M. Badelek, Z. Phys. **C43**, 251 (1989). (Cited on pages 88 und 151.)

[91] B. Badelek and J. Kwiecinski, Phys. Lett. **B295**, 263 (1992). (Cited on pages 88 und 151.)

[92] J. Bartels, K. J. Golec-Biernat, and H. Kowalski, Phys. Rev. **D66**, 014001 (2002), `hep-ph/0203258`. (Cited on page 88.)

[93] H. Abramowicz and A. Levy (1997), `hep-ph/9712415`. (Cited on page 89.)

[94] K. Abe et al. (E143), Phys. Lett. **B452**, 194 (1999), `hep-ex/9808028`. (Cited on pages 89, 114 und 123.)

[95] E. S. Ageev et al. (Compass), Phys. Lett. **B647**, 330 (2007), `hep-ex/0701014`. (Cited on pages 89, 99 und 133.)

[96] C. Adloff et al. (H1), Phys. Lett. **B393**, 452 (1997), `hep-ex/9611017`. (Cited on page 89.)

[97] K. Gustafsson (2003), COMPASS Note 2003-3. (Cited on pages 91 und 95.)

[98] B. Badelek (2010), COMPASS Note. (Cited on pages 91, 94 und 95.)

[99] D. Adams et al. (SMC), Phys. Rev. **D56**, 5330 (1997), `hep-ex/9702005`. (Cited on page 91.)

[100] A. A. Akhundov, D. Yu. Bardin, L. Kalinovskaya, and T. Riemann, Fortsch. Phys. **44**, 373 (1996), `hep-ph/9407266`. (Cited on pages 91 und 96.)

[101] D. Yu. Bardin and N. M. Shumeiko, Sov. J. Nucl. Phys. **29**, 499 (1979), [Yad. Fiz.29,969(1979)].

[102] A. A. Akhundov, D. Yu. Bardin, and N. M. Shumeiko, Sov. J. Nucl. Phys. **44**, 988 (1986), [Yad. Fiz.44,1517(1986)]. (Cited on pages 91 und 96.)

[103] C. Heppel, Private communication (2007). (Cited on pages 94 und 95.)

[104] I. Akushevich, A. Ilyichev, N. Shumeiko, A. Soroko, and A. Tolkachev, Comput. Phys. Commun. **104**, 201 (1997), `hep-ph/9706516`. (Cited on pages 96 und 117.)

[105] V. Yu. Alexakhin et al. (COMPASS), Phys. Lett. **B647**, 8 (2007), `hep-ex/0609038`. (Cited on pages 99, 126 und 157.)

[106] M. G. Alekseev et al. (COMPASS), Phys. Lett. **B690**, 466 (2010), `1001.4654[hep-ex]`. (Cited on pages 99, 118, 156, 177 und 186.)

[107] M. Stolarski, Ph.D. thesis, Warsaw U. (2006), URL `http://inspirehep.net/record/887033/files/Thesis-2006-Stolarski.pdf`. (Cited on pages 110 und 133.)

[108] A. Bravar, K. Kurek, and R. Windmolders, Comput. Phys. Commun. **105**, 42 (1997), `hep-ph/9704313`. (Cited on page 113.)

[109] G. Ingelman, A. Edin, and J. Rathsman, Comput. Phys. Commun. **101**, 108 (1997), `hep-ph/9605286`. (Cited on page 113.)

[110] A. Martin, W. Stirling, R. Thorne, and G. Watt, Eur.Phys.J. **C63**, 189 (2009), `0901.0002[hep-ph]`. (Cited on pages 114, 159, 161, 163 und 166.)

[111] R. D. Ball et al. (NNPDF), JHEP **04**, 040 (2015), `1410.8849[hep-ph]`. (Cited on page 114.)

[112] J. Blumlein and H. Bottcher, Nucl.Phys. **B636**, 225 (2002), `hep-ph/0203155`. (Cited on pages 114, 180 und 191.)

[113] J. Blumlein and H. Bottcher, Nucl. Phys. **B841**, 205 (2010), `1005.3113[hep-ph]`. (Cited on pages 114, 173 und 180.)

[114] D. de Florian, G. Navarro, and R. Sassot, Phys.Rev. **D71**, 094018 (2005), `hep-ph/0504155`. (Cited on pages 114, 180 und 191.)

[115] M. Gluck, E. Reya, M. Stratmann, and W. Vogelsang, Phys.Rev. **D63**, 094005 (2001), `hep-ph/0011215`. (Cited on pages 114, 180 und 191.)

[116] E. Leader, A. V. Sidorov, and D. B. Stamenov, Eur.Phys.J. **C23**, 479 (2002), `hep-ph/0111267`. (Cited on page 114.)

[117] E. Leader, A. V. Sidorov, and D. B. Stamenov, Phys.Rev. **D73**, 034023 (2006), `hep-ph/` `0512114`. (Cited on pages 114 und 180.)

[118] E. Leader, A. V. Sidorov, and D. B. Stamenov, Phys.Rev. **D75**, 074027 (2007), `hep-ph/` `0612360`. (Cited on pages 114, 180 und 191.)

[119] E. Leader, A. V. Sidorov, and D. B. Stamenov, Phys.Rev. **D82**, 114018 (2010), `1010.` `0574[hep-ph]`. (Cited on pages 114 und 173.)

[120] E. R. Nocera, R. D. Ball, S. Forte, G. Ridolfi, and J. Rojo (NNPDF), Nucl. Phys. **B887**, 276 (2014), `1406.5539[hep-ph]`. (Cited on page 114.)

[121] L. W. Whitlow, S. Rock, A. Bodek, E. M. Riordan, and S. Dasu, Phys. Lett. **B250**, 193 (1990). (Cited on page 114.)

[122] L. W. Whitlow, S. Rock, A. Bodek, E. M. Riordan, and S. Dasu, Phys. Lett. **B250**, 193 (1990). (Cited on page 114.)

[123] K. V. Dharmawardane et al. (CLAS), Phys. Lett. **B641**, 11 (2006), `nucl-ex/0605028`. (Cited on pages 124, 130 und 156.)

[124] K. Abe et al. (E143), Phys. Rev. **D58**, 112003 (1998), `hep-ph/9802357`. (Cited on pages 124, 130, 156, 180 und 182.)

[125] P. Anthony et al. (E155), Phys.Lett. **B493**, 19 (2000), `hep-ph/0007248`. (Cited on pages 124, 156, 167 und 182.)

[126] A. Airapetian et al. (HERMES), Phys.Rev. **D75**, 012007 (2007), `hep-ex/0609039`. (Cited on pages 124, 129, 130, 156 und 182.)

[127] P. Anthony et al. (E155), Phys.Lett. **B463**, 339 (1999), `hep-ex/9904002`. (Cited on pages 130, 156 und 182.)

[128] K. Abe et al. (E143), Phys. Rev. **D58**, 112003 (1998), `hep-ph/9802357`. (Cited on page 144.)

[129] V. Yu. Alexakhin et al. (COMPASS), Eur. Phys. J. **C52**, 255 (2007), `0704.1863[hep-ex]`. (Cited on page 148.)

[130] B. Adeva et al. (SMC), Phys. Rev. **D60**, 072004 (1999), [Erratum: Phys. Rev.D62,079902(2000)]. (Cited on page 152.)

[131] A. Airapetian et al. (HERMES), Phys. Rev. **D75**, 012007 (2007), `hep-ex/0609039`. (Cited on page 152.)

[132] P. Anthony et al. (E142), Phys.Rev. **D54**, 6620 (1996), `hep-ex/9610007`. (Cited on page 156.)

[133] K. Abe et al. (E154), Phys. Rev. Lett. **79**, 26 (1997), `hep-ex/9705012`. (Cited on page 156.)

[134] X. Zheng et al. (Jefferson Lab Hall A), Phys. Rev. Lett. **92**, 012004 (2004), `nucl-ex/` `0308011`. (Cited on page 156.)

[135] K. Ackerstaff et al. (HERMES), Phys.Lett. **B404**, 383 (1997), `hep-ex/9703005`. (Cited on page 156.)

[136] P. Jimenez-Delgado, A. Accardi, and W. Melnitchouk, Phys. Rev. **D89**, 034025 (2014), `1310.3734[hep-ph]`. (Cited on page 155.)

[137] B. Adeva et al. (SMC), Phys. Rev. **D58**, 112002 (1998). (Cited on page 157.)

[138] D. Fasching (1996), `hep-ph/9610261`. (Cited on page 157.)

[139] M. Stratmann and W. Vogelsang, Phys. Rev. **D64**, 114007 (2001), `hep-ph/0107064`. (Cited on page 157.)

[140] G. Altarelli, S. Forte, and G. Ridolfi, Nucl. Phys. **B534**, 277 (1998), `hep-ph/9806345`. (Cited on page 159.)

[141] D. B. Stamenov, Private communication (2014). (Cited on page 159.)

[142] S. Forte, M. L. Mangano, and G. Ridolfi, Nucl. Phys. **B602**, 585 (2001), `hep-ph/0101192`. (Cited on page 159.)

[143] D. Stump, J. Pumplin, R. Brock, D. Casey, J. Huston, J. Kalk, H. L. Lai, and W. K. Tung, Phys. Rev. **D65**, 014012 (2001), `hep-ph/0101051`. (Cited on page 160.)

[144] J. Pumplin, D. Stump, R. Brock, D. Casey, J. Huston, J. Kalk, H. L. Lai, and W. K. Tung, Phys. Rev. **D65**, 014013 (2001), `hep-ph/0101032`. (Cited on page 160.)

[145] W. T. Giele and S. Keller, Phys. Rev. **D58**, 094023 (1998), `hep-ph/9803393`. (Cited on page 160.)

[146] A. D. Martin, W. J. Stirling, R. S. Thorne, and G. Watt, Eur. Phys. J. **C64**, 653 (2009), `0905.3531[hep-ph]`. (Cited on page 165.)

[147] C. Adolph et al. (COMPASS), Phys. Rev. **D87**, 052018 (2013), `1211.6849[hep-ex]`. (Cited on pages 170 und 173.)

[148] A. Airapetian et al. (HERMES), JHEP **08**, 130 (2010), `1002.3921[hep-ex]`. (Cited on pages 170 und 173.)

[149] B. Adeva et al. (SMC), Phys. Rev. **D70**, 012002 (2004), `hep-ex/0402010`. (Cited on page 173.)

[150] E. S. Ageev et al. (COMPASS), Phys. Lett. **B633**, 25 (2006), `hep-ex/0511028`. (Cited on page 173.)

[151] C. Adolph et al. (COMPASS) (2015), `1512.05053[hep-ex]`. (Cited on pages 170 und 173.)

[152] M. Hirai and S. Kumano (Asymmetry Analysis), Nucl. Phys. **B813**, 106 (2009), `0808.0413[hep-ph]`. (Cited on page 173.)

[153] E. Leader, A. V. Sidorov, and D. B. Stamenov, Phys. Rev. **D91**, 054017 (2015), `1410.1657[hep-ph]`. (Cited on page 173.)

[154] J. Blumlein and A. Tkabladze, Nucl. Phys. **B553**, 427 (1999), `hep-ph/9812478`. (Cited on page 175.)

[155] R. Machleidt, K. Holinde, and C. Elster, Phys. Rept. **149**, 1 (1987). (Cited on page 178.)

PUBLICATIONS

Some ideas and figures have appeared previously in the following publications:

PUBLICATIONS

- *Final COMPASS results on the deuteron spin-dependent structure function g_1^d and the Bjorken sum rule*
  COMPASS Collaboration, arXiv:1612.00620 [hep-ex].

- *Final results on the spin dependent structure function g_1^d from COMPASS*
  M. Wilfert on behalf of the COMPASS Collaboration, PoS, **DIS2016** (2016) 228.

- *Results on longitudinal spin physics COMPASS*
  M. Wilfert on behalf of the COMPASS Collaboration, EPJ Web Conf. **112** (2016) 01023.

- *Results on longitudinal spin physics COMPASS*
  M. Wilfert on behalf of the COMPASS Collaboration, Nucl. Part. Phys. Proc. **270-272** (2016) 41.

- *The spin structure function g_1^p of the proton and a test of the Bjorken sum rule*
  COMPASS Collaboration, Phys. Lett. B **753** (2016) 18.

- *Estimation of the bias due to semi-inclusive trigger for $A_1^p(2011)$ and POLDIS*
  M. Wilfert, COMPASS note 2015-5.

- *Estimate of the systematic uncertainties for the 2007 A_1^p data in $x - Q^2$ bins*
  M. Wilfert, COMPASS note 2015-3.

- *New COMPASS results on the spin structure function g_1^p, and QCD fit*
  M. Wilfert on behalf of the COMPASS Collaboration, PoS, **DIS2014** (2014) 206.

PRESENTATIONS

- *Final COMPASS results on the spin dependent structure function* g_1^d *and* g_1^p (Invited talk)
  SPIN, Urbana-Champaign, Illinois, USA

- *Final results on the spin dependent structure function* g_1^d *from COMPASS* (Talk)
  DIS - XXIV, Hamburg, Germany

- *First results on the longitudinal double spin asymmetry for identified hadrons from the 2011 COMPASS data* (Talk)
  DPG Spring Meeting 2016, Darmstadt, Germany

- *Results on longitudinal spin physics COMPASS* (Talk)
  POETIC VI, Palaiseau, France

- *Results on longitudinal spin physics COMPASS* (Talk)
  QCD15, Montpellier, France

- *Improved LO extraction of the gluon polarisation using COMPASS data* (Talk)
  DPG Spring Meeting 2015, Heidelberg, Germany

- *New COMPASS results on the spin structure function* g_1^p *and QCD fit* (Talk)
  DIS - XXII, Warsaw, Poland

- *Results on the longitudinal double spin asymmetry* A_1^p *and* g_1^p *from the 2011 COMPASS data* (Talk)
  DPG Spring Meeting 2014, Frankfurt a. M., Germany

- *Results on* A_1^p *and* g_1^p *from 2011 COMPASS data* (Talk)
  SPIN-Praha-2013, Prague, Czech Republic

- *First results on the longitudinal double spin asymmetry* A_1^p *and* g_1^p *from the 2011 COMPASS data* (Talk)
  DPG Spring Meeting 2013, Dresden, Germany

DANKSAGUNG

LEBENSLAUF

Malte Christian Wilfert
Schubertstr. 43
D-55271 Stadecken-Elsheim

geboren am 09.08.86 in Darmstadt

STAATSANGEHÖRIGKEIT
Deutsch

STUDIUM

Oktober 2011	-	heute	Promotion in Physik
			Johannes Gutenberg-Universität Mainz
Juli 2011			Diplom mit Gesamtnote "sehr gut"
Juli 2010	-	Juli 2011	Diplomarbeit
			"Bestimmung von F_2^{cc} aus offener Charmproduktion bei COMPASS"
April 2006	-	Juli 2010	Studium der Physik
			Johannes Gutenberg-Universität Mainz

SCHULE

März 2006			Abitur mit Durchschnittsnote 2,0
September 1997	-	März 2006	Gymnasium Nieder-Olm
August 1993	-	Juli 1997	Grundschule Stadecken-Elsheim